The effects of gravity and patient positioning on lung mechanics: Investigation via poroelastic modelling.

Abigail Smith

University College London
Department of Mathematics
CHIMERA

A thesis submitted for the degree of
Doctor of Philosophy
December 2024

Declaration

I, Abigail Smith confirm that the work presented in this thesis is my own. Where information has been derived from other sources, I confirm that this has been indicated in the thesis.

Acknowledgements

I would first like to express my deepest gratitude to my supervisor, Professor Nick Ovenden, for his unwavering support and insightful guidance throughout this journey. His dedication and the many hours he invested in helping me navigate complex mathematical challenges have been invaluable. I am also profoundly grateful to my second supervisor, Professor Vanessa Diaz, whose constant stream of innovative ideas and practical solutions has been instrumental in shaping my research. I would like to extend my heartfelt thanks to the entire CHIMERA team, whose collaborative environment not only fostered creativity and innovation but also provided a wealth of expertise to help address the many questions that arose throughout my work.

My sincere appreciation goes to my wonderful friends whose support and understanding have been a source of strength, and my amazing partner for keeping me sane these last four years. Finally, I wish to express my profound gratitude to my family, especially my parents, whose unwavering love and encouragement have been a constant source of motivation. Their belief in my abilities and their encouragement to pursue my passion for mathematics have made this journey possible.

Contents

1 Abstract **17**

2 Impact Statement **19**

3 Introduction **21**

3.1 Literature Review 23

3.1.1 Clinical Context and Motivation: Patient Positioning in Critical Care 23

3.1.2 Physiological Mechanisms Influencing Regional Pulmonary Mechanics 26

3.1.3 Physiological Models of the Pulmonary System 33

3.1.4 Poroelasticity and its Application to Pulmonary Mechanics 43

3.1.5 Concluding Remarks 52

3.2 Outline of Modelling Chapters 54

4 Static Modelling of Lung Tissue Deformation **57**

4.1 Introduction 57

4.2 Tissue Deformation 57

4.3 Derivation of the Bar Equation 61

4.4 Lung Deformation in the Upright Position 63

4.5 Lung Deformation in the Horizontal Position 67

4.6 Comparing Deformation For Each Shape 70

4.7 Prone position 74

4.8 Alveolar Ventilation 78

4.9 Alveolar Perfusion 79

4.10 V/Q Ratio 80

4.11 Results 81

4.12 Concluding Remarks 84

5 Linear Poroelastic Lung Model 86

5.1 Introduction 86
5.2 Terzaghi's Problem 87
5.3 Derivation of The Governing Equations 94
5.4 Non-Dimensionalisation of the Equations 98
5.5 The Finite Difference Method 99
5.6 Model Validation 102
5.7 Source Problem 107
5.8 Patient Positioning in the Poroelastic Framework 110
5.9 Steady-State Solutions 113
5.10 Results for Patient Positioning 121
5.11 Concluding Remarks 125

6 Non-linear Poroelastic Lung Model 127

6.1 Introduction 127
6.2 Time-dependent Alveolar Recruitment 128
6.3 Non-Linear Porosity and Permeability Interactions 134
6.4 Neo-Hookean Hyperelasticity Governing Equations 144
6.5 Reduction to 1-Dimensional System 147
6.6 Results for the Neo-Hookean Hyper-poroelastic Model 150
6.7 Concluding Remarks 154

7 A Coupled Pulmonary Model based on Non-linear Poroelastics 158

7.1 Introduction 158
7.2 Connection to Upper Airways 160
7.3 Ventilation and Perfusion 167
7.4 Positions Comparison 176

7.5 Mechanical Power and VILI 185
7.6 Localised damage in the poroelastic model 198
7.7 Concluding Remarks 203

8 Conclusion **207**

8.1 Review 207
8.2 Novel Insights and Contributions to the Field of Pulmonary Mechanics 210
8.3 Future Work 213
  8.3.1 Modelling Complex Fluid Dynamics in the Airways 213
  8.3.2 Exploring Additional Patient Positions and Mobility . . . 214
  8.3.3 Increasing Physiological Accuracy of Lung Shape Analogy 214
  8.3.4 Heterogeneity Within Each Isogravitational Plane 215
  8.3.5 Modelling Different Pathophysiologies with Regional Characteristics 215
  8.3.6 Chest Wall and Diaphragm Considerations 216
  8.3.7 Validating with Experimental Data 216

9 Appendices **234**

9.1 Additional workings 234

List of Figures

1 Diagram representing West's theoretical three-zone model, which posits that pulmonary blood flow distribution is determined by the interplay of pulmonary arterial P_a, alveolar P_A, and pulmonary venous P_v pressures, with zones aligning vertically parallel to gravity. Zone 1 $P_A > P_a > P_v$ restricts blood flow, Zone 2 $P_a > P_A > P_v$ shows linear blood flow increase, and Zone 3 $P_a > P_v > P_A$ also shows linear blood flow increase but with a shallower gradient. [7]. 28

2 Schematic representation of strain-stress distribution and its impact on alveolar size distribution between the supine and prone position. The Slinky effect of a triangular-shaped spring suspended from its apex (supine position) causes higher strain and larger variation in the distribution of alveolar sizes due to the effects of gravity and a steeper stress production during mechanical inspiration in the upper lung regions. In contrast, suspending the spring by its base across a wider surface area (prone position) produces a more even strain and more homogeneous distribution of alveolar size that lessens inhomogeneity in stress development throughout the lungs during mechanical inspiration. Taken from [23]. 30

3 Reference diagram detailing various respiratory system pressures relevant to lung mechanics modelling. Key pressures include:, P_{awo} - airway opening pressure. P_{alv} - alveolar pressure. P_{pl} - intra-pleural pressure. P_{bs} - body surface pressure. P_{aw} - airway pressure. $P_{tp} = P_{alv} - P_{pl}$ - transpulmonary pressure. $P_{tt} = P_{alv} - P_{bs}$ - trans-thoracic pressure. $P_{ta} = P_{aw} - P_{alv}$ - trans-airway pressure. $P_{tr} = P_{awo} - P_{bs}$ - trans-respiratory pressure. taken from [34] 34

4 A simplistic model illustrating lung tissue deformation, representing the lung as a series of discrete alveolar sacs (masses m) connected by elastic springs, with deformation (x) occurring vertically. This model assumes the top and bottom of the lung are fixed, confining deformation internally. 58

5 Representation of lung deformation using a solid mechanics continuum approach. The left image shows the typical bar analogy, where the lung is modelled as a continuous solid bar with a volume load acting across its entirety, and fixed at both ends to ensure internal deformation. The right image provides a visual comparison to an anatomical lung shape. 60

6 A random, infinitely small element of the solid bar model, illustrating the normal force (N) acting upon it and the force of its own weight load $k(x)A$, used to derive the equilibrium equation for lung tissue deformation. 61

7 Three analogies for lung shape used in this paper. **A** represents a cylinder with radius r, **B** represents a cone with base radius r, **C** represents a truncated cone with base radius r_b and top radius r_t. Each shape has height L and is subject to weight load ρg. . . 64

8 Three analogies for lung shape used in this paper in the horizontal positions. **A** represents a cylinder with radius r, **B** represents a cone with base radius r, **C** represents a truncated cone with base radius r_b and top radius r_t. Each shape has height h (parallel to gravity), length L, and is subject to weight load ρg. 68

9 Alveolar deformation from original position against gravity (mm), in the upright (black) and supine (red) positions. **A** represents the cylinder analogy, **B** represents the cone analogy and **C** represents the truncated cone analogy. 71

10 Comparison of regional lung characteristics in the upright position. **A** displays the model's calculated number of alveolar units per cm of total lung height for the cylinder, cone, and truncated cone analogies. **B** presents data from Hopkins et al. [13] on the regional density of lung tissue in a human subject, derived from MRI imaging. The truncated cone analogy (A) most accurately reflects the physiological distribution seen in human data (B). . . 73

11 Alveolar deformation from original position against gravity (mm), in the upright (black) and supine (blue) and prone (red) positions, using the truncated cone shape analogy. 76

12 Comparison of lung function between upright,supine and prone positions. **A** displays the relative volume of each alveolar unit. **B** displays the relative ventilation of each alveolar unit. **C** displays the relative perfusion of each alveolar unit. **D** displays the ventilation-perfusion ratio as a function of total lung height. . . . 82

13 Visual representation of Terzaghi's consolidation problem, depicting a soil sample confined by an impermeable ring with a closed base. The sample is submerged in water, allowing fluid to drain freely from its exposed upper boundary, and subjected to a constant perpendicular stress. 87

14 Analytical solution for Terzaghi's consolidation problem, illustrating the relative change in pore pressures $p/p0$ against relative height z/h for various values of the time parameter $c_v t/h^2$. The graph shows higher pore pressures towards the base $z/h = 0$ and a reduction to near-zero pressures as the time parameter increases, indicating full consolidation of the sample 93

15 Reference diagram for the proposed one-dimensional poroelastic model of the lung. The lung is represented as a structure with pores aligned against gravity, where u denotes the deformation of pores at a specific gravitational plane (height x) over time t. . 94

16 Visual representation of the Crank-Nicolson method, a finite difference scheme used for solving partial differential equations in a one-dimensional problem. The grid shows spatial index i and time index j, illustrating how the method achieves second-order convergence in both space and time. 99

17 Initial displacement and pressure solutions for the swelling problem, where fluid is introduced only at the base $x = 0$ via a constant input function (right-most plot). Displacements and pressures are plotted for all pores on each isogravitational plane. The red line indicates the base of the lung at $x = 0$. Note the significant, unnatural fluctuations observed in the pressure field, indicating numerical instability. 103

18 Flow diagram illustrating the iterative methods implemented to solve the poroelastic model. The process includes solving matrix equations using Gauss-Seidel iterations for initial predictions, followed by a relaxation loop to ensure convergence and remove unnatural pore-pressure oscillations, repeating until the maximum time steps are reached. 105

19 Displacement and pressure solutions to the swelling problem using a relaxation iteration with the relaxation factor set to 0.7. The input is set to a constant as in the right-most plot. Displacements and pressures are plotted for all pores on each isogravitational plane. The red line represents the base of the lung at $x = 0$. 106

20 Displacement and pressure solutions to the source problem using a relaxation iteration with the relaxation factor set to 0.7. Simulations are shown for three different input functions, shown in the right-hand column. Displacements and pressures are plotted for all pores on each isogravitational plane. In each instance, the base of the lung at $x = 0$ is plotted in black, the first iteration up from the base is plotted in blue, and the apex of the lung at $x = n$ is plotted in red. All other internal nodes are plotted in grey. 109

21 Final displacement in the steady-state scenario with no input source, depicting the lung deforming under its own weight in the upright position. The analytical steady-state solution (solid line) is plotted against the results from the numerical finite-difference approach (dashed line), demonstrating good approximation between the two methods. 116

22 Final displacement in the steady-state scenario with no input source, showing lung deformation under its own weight in the upright, supine, and prone positions. The lung deforms most significantly in the upright position, while the prone position exhibits the smallest deformation, approximately half that of the upright orientation. 117

23 Final displacement in the steady state scenario with constant source and 'leaky' boundary in the upright position. The analytical steady state solution is plot against the results from the numerical finite-difference approach. 119

24 Final displacement in the steady-state scenario with a constant source and 'leaky' boundaries, across upright, supine, and prone positions. The lung exhibits the most significant deformation in the upright position, whereas the prone position demonstrates the smallest deformation, roughly a 50% reduction compared to the upright orientation. 120

25 Simulated ventilator waveform data for the source problem using a relaxation iteration with relaxation factor 0.7. Row A is upright, row B is supine, row C is prone. 123

26 Visual representation of the virtual trajectory along which alveolar coordinate x moves between the limits 0 (fully closed) and 1 (fully open) with respect to the current airway pressure P_{aw} and the critical opening and closing pressures P_o and P_c. As depicted in [72]. 129

27 Visual representation of the rate of change of x, $\frac{dx}{dt}$, as a function of pressure. Constants s_o and s_c give the slopes for this rate increase once P_{aw} passes the critical pressures P_o and P_c. As depicted in [72]. 129

28 The regional recruitment of alveoli represented by the percentage of each plane open in different test scenarios. A depicts complete uniformity in the lung and the threshold pressures. B samples threshold pressures from a normal distribution to introduce some randomness. C adds spatial variation in both the thresholds and in the local compartmental pressures, to explore higher heterogeneity. 131

29 The S-shaped pressure-volume curve generated by the simulated waterfall model, incorporating full spatial heterogeneity in alveolar pressures and threshold opening/closing pressures. The curve exhibits a lower inflection point (LIP) at low volumes where alveoli non-linearly recruit, a linear middle portion as more alveoli open, and an upper inflection point (UIP) at high volumes where compliance decreases due to full inflation. 133

30 Simulated ventilator waveform data for non-linear neo-Hookean hyperelastic model of porosity and permeability, compared to the linear model. Lung is in the upright position and simulated over two breathing cycles. Linear is the top row and non-linear is the bottom. 138

31 Average values for permeability (m^2) and porosity across the lung, over a two-breath cycle. 140

32 Pressure-volume curve for the poroelastic lung with non-linear porosity and permeability. Region A is the alveolar recruitment zone and region B is the alveolar over-distension zone. The red dotted line represents a theoretical pressure-volume curve taken from [78]. 143
33 Simulated ventilator waveform data for fully non-linear neo-hookean hyperelastic model of the lung. Lung is in the upright position and simulated over two breathing cycles. 150
34 Pressure-volume curve for the fully non-linear poroelastic lung with non-linear porosity and permeability and neo-Hookean hyper-poroelastic elasticity. Region A is the alveolar recruitment zone and region B is the alveolar over-distension zone. The red dotted line represents a theoretical pressure-volume curve as in [78]. . . 152
35 Alveolar compliance plotted against volume in the fully non-linear model. Section A shows gradual increase in compliance as alveoli open (recruitment zone). Section B represents a linear relationship where all alveoli are open and compliance increases with expansion. Section C demonstrates decreasing compliance as alveoli become over-distended, reflecting the stiffening of alveolar tissue. 153
36 Graph of the representative data of the respiratory tract of an average adult with a lung volume of $4800cm^3$ at roughly 75% total lung capacity, with respect to the tree generation. Top left: The number of segments in each generation. Top right: The average length at each generation. Bottom left: The average diameter at each generation. Bottom right: The total surface area at each generation. Adapted from Weibel 1991 to include the endotracheal tube [86]. 161

37 Average pressure in each of the branch generations down the airway tree. 164

38 Average resistance in each of the branch generations down the airway tree. 164

39 Visual representation of airflow through the branching airway network in an intubated patient. Airflow originates from the ventilator P_vent, passes through the endotracheal tube (ETT, generation -1), and continues through successive airway generations to the terminal branch ($P_term - 1$) and ultimately the alveoli (P_term), assuming conservation of flow throughout the system. 166

40 Relative airflow in the alveoli as a function of vertical height, at FRC, TLC and 50% inflation. Lung is in the upright position. . . 171

41 Relative perfusion in the alveoli as a function of vertical height, at FRC, TLC and 50% inflation. Lung is in the upright position. 173

42 Ventilation/perfusion ratio as a function of vertical height, at FRC, TLC and 50% inflation. Lung is in the upright position . . 175

43 Simulated ventilator waveform data for the source problem in a fully non-linear neo-Hookean model. Row A is upright, row B is supine, row C is prone. 178

44 Ventilation at FRC as a function of lung height, in the upright, supine and prone positions. 180

45 Perfusion at FRC as a function of lung height, in the upright, supine and prone positions. 181

46 Ventilation/perfusion ratios at FRC as a function of lung height, in the upright, supine and prone positions. 183

47 The impacts of ventilator settings on the calculated mechanical power, varying a single parameter at a time. Top left shows the inspiratory:expiratory ratio (I:E), top right shows the tidal volume (TV), bottom left shows the PEEP, and bottom right shows the respiratory rate (RR). When not being varied, parameters are set as followed: I:E = 1, TV = 9ml/kg, PEEP = 5cmH2O, RR = 12bpm. All calculated from Eq 189. 189

48 The relationship between mechanical power and calculated mechanical strain in the lung. 194

49 The relationship between mechanical power and calculated mechanical stress in the lung. 196

50 The local mechanical power delivered to the alveoli in each gravitational plane, at functional residual capacity, total lung capacity and 50% inflation. Lung is in the upright position. %Total lung height goes from 0% at the bottom to 100% at the top. 200

51 The local mechanical power delivered to the alveoli in each gravitational plane at total lung capacity, with the lung in the upright position, supine position and prone position. A maximum safe threshold of $15 J/min$, taken from experimental findings [102, 103, 104], and the theoretical "Safe Zone" is highlighted green. %Total lung height goes from 0% at the bottom to 100% at the top. 201

Glossary of Terms

Term	Full form
ARDS	Acute respiratory distress syndrome
COPD	Chronic obstructive pulmonary disease
FEV	Forced expiratory volume
FIO_2	Fraction of inspired oxygen
FRC	Functional respiratory capacity
FVC	Forced vital capacity
MAP	Mean airway pressure
PaO_2	Partial pressure of oxygen
PEEP	Positive end-expiratory pressure
PIP	Peak inspiratory pressure
TLC	Total lung capacity
VC	Vital capacity
VILI	Ventilator-induced lung injury
Ventral	The front portion of the lungs, or the part of the lungs that faces the front of the body
Dorsal	The back portion of the lungs, or the part of the lungs that faces the back of the body
Dependent Lung	The lowest part of the lung in relation to gravity
Non-dependent Lung	The highest part of the lung in relation to gravity

*All code used in this thesis was implemented in MATLAB [1]

1 Abstract

This thesis explores the impact of body positioning on pulmonary mechanics in critically ill patients, particularly those requiring mechanical ventilation for conditions like ARDS. Changing a patient's posture, such as moving them from supine to prone, can enhance lung function by improving ventilation and perfusion distribution and reducing the risk of Ventilator-Induced Lung Injury (VILI). The primary goal of this research is to identify key parameters influenced by body positioning and to develop a mathematical model that simulates lung behaviour under different conditions.

Central to this thesis is the understanding of how gravity influences lung tissue deformation, a phenomenon directly affecting airflow and blood flow within the lungs. Through detailed analyses, we identify that alveolar displacement is more pronounced when a patient is upright, and less pronounced in the prone, compared to the supine. We demonstrate that lung deformation due to gravity is a critical factor in the observed differences in pulmonary function between positions.

After an in-depth review of the current and historic literature, we begin by modelling the lung as a static object using solid mechanics, to determine the deformation of lung tissue when fully deflated. This model will then inform the governing equations of a poroelastic model, coupling the solid tissue with the intricate airflow through the system. We will look at this from its simplest linear approximation, increasing complexity until a fully non-linear physiologically accurate model is realised. Finishing this thesis, we will connect the non-linear poroelastic model to the branching upper airways and blood column, in order to assess the spatial ventilation and perfusion mismatch of the lung in different orientations.

This approach validates the concept that mathematical models can accu-

rately capture multi-variate lung behaviour, with demonstrated predictive fidelity, and can be used for in-silico experimentation to provide clinical inference and aid decision making.

2 Impact Statement

The research presented in this thesis has the potential to significantly impact both academic scholarship and clinical practice, particularly in the field of pulmonary mechanics and critical care. By developing an advanced mathematical model that simulates lung deformation and function across various body positions, this work sheds light on the relationship between gravity, patient positioning, and pulmonary mechanics. This understanding is crucial for improving care in patients requiring mechanical ventilation, especially those suffering from acute respiratory distress syndrome (ARDS), chronic lung diseases, or severe respiratory failure as seen during the COVID-19 pandemic.

From an academic perspective, the contributions of this thesis extend across multiple disciplines, including applied mathematics, biomedical engineering, and pulmonary physiology. The integration of poroelasticity into lung mechanics modelling is novel, offering a detailed mathematical framework for understanding how lung tissue deforms under different gravitational and mechanical forces. This interdisciplinary approach could stimulate further research in computational biology, particularly in refining mathematical models that account for individual patient variability, an area of increasing importance in precision medicine.

Beyond academia, the clinical implications of this work are substantial. The mathematical models developed offer new tools for understanding how patient positioning impacts lung function, particularly in the distribution of ventilation and blood flow to different lung regions. This knowledge is highly relevant for optimising treatment strategies in the ICU, where patients often need mechanical ventilation to survive. By better understanding the mechanics of lung deformation, clinicians can tailor patient positioning to improve lung function and reduce the risk of VILI, a common complication in mechanically ventilated patients.

One of the most immediate potential impacts of this research lies in its application to patients with ARDS, a condition exacerbated by improper ventilation strategies. By using the models developed in this thesis, clinicians could simulate the effects of various positioning strategies before applying them in practice, potentially lowering mortality rates and shortening ICU stays. Additionally, the insights from this work could lead to more personalised treatment protocols, accounting for individual variations in lung structure and response to gravity.

In the broader healthcare context, the findings from this thesis could inform public health policy and clinical guidelines. For example, during the COVID-19 pandemic, prone positioning became a widely adopted strategy to improve lung function in critically ill patients. Insights into the extent and distributions of VILI in different positions demonstrate a clear area for treatment development. Over time, this research could help shape ventilator management protocols, reduce healthcare costs associated with prolonged ICU care, and ultimately improve the quality of life for patients suffering from severe respiratory conditions.

3 Introduction

The CHIMERA (Collaborative Healthcare Innovation through Mathematics, EngineeRing and AI) hub at UCL aims to use mathematical modelling and critically-ill patient data to improve health care protocols and overall improve the treatment of patients. In an intensive care setting, many patients require intervention using a mechanical ventilator in order to maintain normal lung function and ensure the best possible outcome. The programming and proper utilization of mechanical ventilators relies on an accurate understanding of pulmonary physiology, and this has been an area of significant research in recent years. Collecting patient data has allowed for the creation of mathematical models of the human lung which can be experimented with in order to explore possible strategies for effective treatment. A number of models of mechanical ventilation have been explored in this hub, however, there are many areas that are still to be developed. One such area is the influence of patient positioning on pulmonary function. There is evidence that the position of a patient, as well as the time spent in that position can drastically improve the expected outcome [2]. Manoeuvring the posture of a patient is a common treatment strategy in the ICU, and a number of positions are regularly used [3]. The upright position sees a patient either stood up or sat at a 90° angle such that their torso is completely vertical. The supine position has the patient lay flat on their back, which is one of the most commonly seen positions due to comfort for the patient and ease of access for the clinicians. Equally, Fowler's position is often utilised and sees the patient sat at a 45% incline from horizontal. The prone position (laying a patient flat on their front) has garnered increasing interest and is associated with a measurable improvement in patient condition. This position has been associated with a significant improvement in patient condition [4]. The attention on this position in particular has come with the emergence of Covid-19 in 2019 which resulted in a global pandemic [5]. Evidence of survival improvement in non-Covid patients was applied to Covid-diagnosed patients, such as the 2021 study which found that in patients with hypoxaemic respiratory failure due to COVID-19, awake proning reduced the incidence of treatment failure and the need for intubation [6].

Although the benefits of altering patient position are known, the precise mechanics behind the differences in pulmonary function between postures are still being explored. One key concept is deformation of lung tissue under gravity, and how this moves and redistributes the length of the lung. The substantial volume of soft tissue in the lungs will predictably be influenced by gravity to a quantifiable degree. Past work in this area has focused on animal studies for data collection [7, 8, 9], with results indicating a significant correlation between height of the lung against gravity and a number of key indicators of lung health, such as blood flow and gas volume. Recently, work has been undertaken to explore this phenomenon in humans, with interesting results ranging from external pressures placed on the lung due to gravity [10] and deformation of lung tissue due to its own weight. The data collected in these studies have given results that clearly indicate the importance of including such phenomena when treating a patient. For example, tissue stress and strain occur in a vertical gradient with highest levels at the apex of the lung [11], resulting in alveoli at the top of the lung being over-distended and those at the bottom being compressed [12, 13]. It has also been shown that these gradients result in a regional distribution of airflow and bloodflow to the alveoli, which in turn alters the ventilation/perfusion match and the efficiency of gas exchange across the lung [14]. This project will collate the current works on body positioning and gravity as they relate to pulmonary function, and use findings to create a mathematical model which can accurately replicate human physiology. Such a model allows the simulation of possible treatment strategies in order to understand not only the expected outcome for the patient, but also the individual mechanics that are contributing to the outcome.

3.1 Literature Review

The primary purpose of this research is to create a model which can explore the intricate effects of body positioning on pulmonary function, and the subsequent outcome for the patient. However, lung function cannot be defined by one single variable, and so it is important to evaluate the contributions of various pulmonary factors to overall lung health. Therefore, the literature will be presented in sections. First, we will establish the clinical context and motivations behind the thesis, exploring the use of patient positioning in the ICU. We will then go into detail on the precise mechanisms that are influenced by shifting positions, and how these contribute to the overall function of the lung and health of the patient. At this point we will evaluate the current modelling efforts, both their successes and limitations, before finally diving into the poroelastic framework.

3.1.1 Clinical Context and Motivation: Patient Positioning in Critical Care

It is widely accepted that altering a patient's position can significantly affect their pulmonary function. A 2014 study by Naitoh and collaborators [2], involving twenty healthy individuals, investigated the impacts of body position on pulmonary function and chest wall motion. They found that forced expiratory volume (FEV) measurably decreased by an average of $0.4L$/s when subjects moved from a sitting position to any of the six recumbent positions. Thoracic expansion also declined by approximately 30% in all recumbent positions compared to sitting, with similar changes observed in both supine and prone positions. However, this study had limitations, including a small and skewed sample size (15 out of 20 subjects were male), and the use of only young, healthy participants (between the ages of 20 and 43), making its direct applicability to critically ill ICU patients limited due to substantial differences in pulmonary function associated with age and underlying lung conditions.

A systematic review by Mezidi and Guérin in 2018 [15] assessed available data on the effects of body position in mechanically ventilated Acute Respiratory Distress Syndrome (ARDS) patients. Their general findings indicated an increase in functional residual capacity (FRC) when patients moved from supine to either sitting or prone, as well as an increase in oxygenation. Respiratory resistance was found to decrease in an upright stance and increase in lateral positions, while prone positioning showed either a decrease or no significant change. The review highlighted variations in methodology between studies, such as the time patients were left in prone position (from 'a few minutes' to 2 hours) and cohort sizes (from ten to 41 patients). A deeper dive into the papers included in the meta-analysis expands on these findings: Blanch et al. [16] observed a 15% rise in PaO_2/FIO_2 (a measure of oxygenation) in 16 out of 23 ARDS patients when moved from supine to prone, an improvement more pronounced in patients receiving ventilation for a shorter duration since ARDS diagnosis. Servillo (1997) also reported increased oxygenation in 10 out of 12 ARDS patients when moved from dorsal to ventral decubitus (supine to prone) $\dot{\text{H}}$owever, this study had a small sample size and included patients with various other diagnoses that could impact lung function. Measurements were also taken after only 15 minutes in the prone position, a much shorter duration than in other studies. A meta-analysis by Munshi (2017), involving over 2000 patients, reinforced the importance of proning duration, finding a significantly lower risk of mortality and higher PaO2/FIO2 on Day 4 in patients who received at least 12 hours of proning. Despite variations in methodology and duration across studies, the consistent finding was an improvement in oxygenation when patients were moved to the prone position. It is also noted that the current health of the patient significantly impacts the expected results of proning, necessitating the incorporation of specific and localised impacts of different conditions into any clinically relevant model.

The prone position has garnered increasing interest due to its association with significant improvement in patient condition. The emergence of the SARS-CoV-2 (COVID-19) virus in 2019, leading to a global pandemic, brought particular attention to proning, as many patients developed severe breathing difficulties, pneumonia, and ARDS. Evidence suggests that proning may markedly improve the survival of COVID-19 patients. A large multinational meta-trial by Ehrmann and colleagues (2021) [6] studied 1121 awake COVID-19 patients and found that awake prone positioning reduced the risk of treatment failure (defined as death or requiring intubation) from 46% in standard care to 40% in the proned group. Patients proned for at least 8 hours per day showed a significantly lower treatment failure rate (17%) compared to those proned for less than 8 hours (48%). Ghelichkhani and Esmaeli [17] suggested that prone positioning is effective in COVID-19 due to the prevalence of ARDS among patients (up to 17% of cases). Proning improves ARDS outcomes by increasing recruitment in dorsal regions, improving chest wall elastance, enhancing tidal volume, and increasing end-expiratory lung volume. It also reduces over-distension in dorsal (non-dependent) lung regions, improving oxygenation. While Li and Ma [18] noted key distinctions between COVID-19-related ARDS and non-COVID ARDS (e.g., longer time before symptom onset), they suggested similar treatment methods should be effective. Park et al. [19] found that prone positioning had the same effectiveness in treating COVID ARDS as in standard ARDS, though improvements in oxygenation and static respiratory compliance were initially higher in COVID ARDS patients. However, debates persist, with Gattinoni and Marini [20] highlighting unique characteristics of COVID ARDS, such as unusually high lung compliance, which questioned whether standard ARDS treatments (e.g., high PEEP levels) were always appropriate. This debate underscores the continuing progress and evolving understanding in pulmonary physiology, suggesting that the precise mechanics behind positional changes still require deeper exploration.

Ultimately, while the benefits of altering patient position are known and increasingly applied in clinical practice, the precise underlying mechanisms that drive the differences in pulmonary function between postures are still being explored. This highlights the critical need for a comprehensive and detailed mathematical model that can accurately replicate human physiology and provide insights into these mechanisms, not only to understand the expected outcome but also the individual mechanics contributing to it.

3.1.2 Physiological Mechanisms Influencing Regional Pulmonary Mechanics

Understanding the spatial and temporal variability of pulmonary mechanics is essential for developing physiologically accurate models of lung behaviour. This section explores the fundamental physiological mechanisms that govern regional differences in lung deformation, ventilation, and perfusion, with a particular emphasis on the influence of gravity, body position, and external mechanical forces. These factors interact with the intrinsic material properties of lung tissue and the complex geometry of the pulmonary system to produce highly heterogeneous mechanical behaviour. A detailed review of how gravitational gradients, pleural pressures, and anatomical constraints affect lung mechanics—alongside their implications for ventilation-perfusion (V/Q) matching—provides critical context for modelling the lung as a deformable medium. This understanding lays the groundwork for transitioning from classical solid mechanics approaches to more advanced poroelastic models, where both tissue deformation and fluid transport are tightly coupled within a unified framework.

In the study of pulmonary mechanics, the understanding of regional lung function, particularly ventilation and perfusion distribution, has evolved significantly, moving beyond initial gravity-centric models to incorporate complex structural and mechanical factors. Early investigations, such as those by West and Dollery [7, 14, 21], established that in erect humans, pulmonary blood flow decreases from the base to the apex. There are critiques that can be made of these early works, such as the use of a canine lung as a proxy, or the use of radioactive Xenon 133 which has made the experiments un-replicable within modern ethical guidelines. The groundwork for pulmonary bloodflow distribution however, has been crucial in the ongoing study of regional lung mechanics. This distribution was traditionally explained by West's three-zone model [7], which posits that flow is determined by the interplay of pulmonary arterial, alveolar, and venous pressures.

West depicted that the lung should be separated into three 'zones', as shown in Figure 1. Zone 1 occurs above the point at which pulmonary arterial pressure and alveolar pressure are equal. In this zone, alveolar pressure is such that it exceeds perfusion pressures. This results in blood flow being completely restricted, and no perfusion is seen in this zone. Zone 2 occurs below the point at which pulmonary arterial pressure and alveolar pressure are equal, but above the point at which pulmonary venous and alveolar pressure are equal. In this zone, blood flow increases down the lung in a linear pattern due to the steady increase in arterial pressure. Finally, zone 3 occurs below the point at which

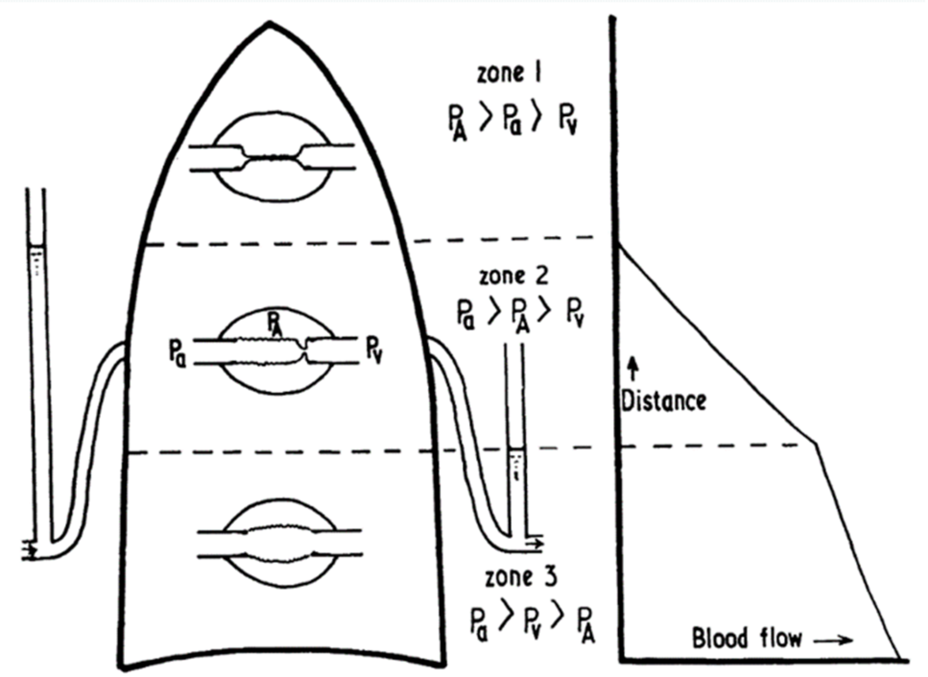

Figure 1: Diagram representing West's theoretical three-zone model, which posits that pulmonary blood flow distribution is determined by the interplay of pulmonary arterial P_a, alveolar P_A, and pulmonary venous P_v pressures, with zones aligning vertically parallel to gravity. Zone 1 $P_A > P_a > P_v$ restricts blood flow, Zone 2 $P_a > P_A > P_v$ shows linear blood flow increase, and Zone 3 $P_a > P_v > P_A$ also shows linear blood flow increase but with a shallower gradient. [7].

pulmonary venous pressure and alveolar pressure are equal. This zone also sees a linear relationship between distance down the lung and blood flow, but with a significantly shallower gradient than in zone 2. The boundaries for the zones were stated to be as follows:

$$\begin{aligned} Zone1 &\Rightarrow P_{Alv} > P_{art} > P_{ven} \\ Zone2 &\Rightarrow P_{art} > P_{Alv} > P_{ven} \\ Zone3 &\Rightarrow P_{art} > P_{ven} > P_{Alv} \end{aligned} \tag{1}$$

where P_{Alv}, P_{art} and P_{ven} represent alveolar pressure, pulmonary arterial pressure and pulmonary venous pressure respectively. Zones align vertically parallel to gravity.

Critiques have been made that gravity alone cannot account for the heterogeneity in pulmonary bloodflow. For instance, Hughes et al. (1968) challenged the sufficiency of West's model, observing that in the bottom (dependent) zones of the upright lung, blood flow decreases despite increasing hydrostatic pressure [22]. They argued that this phenomenon "is impossible to explain" solely on the basis of pulmonary arterial, alveolar, and venous pressures, suggesting instead that added resistance to flow lies in larger, extra-alveolar vessels influenced by interstitial pressure. This extended model, incorporating interstitial pressure effects, provided a more comprehensive explanation for blood flow distribution, particularly at lower lung volumes where this added resistance was more marked. This discourse highlights the need for a coupled model which can incorporate both the gravitational gradients of bloodflow as well as the complexity of the vascular structures.

Further on from perfusion variation, significant work has gone into the understanding of the mechanics present in the lung tissue itself, and how this contributes to spatial heterogeneity. The concept of the "Slinky effect" has emerged to explain how lung tissue deforms under its own weight, impacting perfusion measurements, shown in Figure 2 [12]. In the upright position, the lung's own weight causes the apex to be more expanded and the base to be more compressed. This results in a vertical gradient of tissue deformation, with greater alveolar distension at the apex and smaller, denser alveoli at the base. The term captures how gravity causes a progressive increase in tissue compression and pleural pressure from top to bottom, influencing both ventilation distribution and regional lung mechanics. Hopkins et al. (2007) utilised

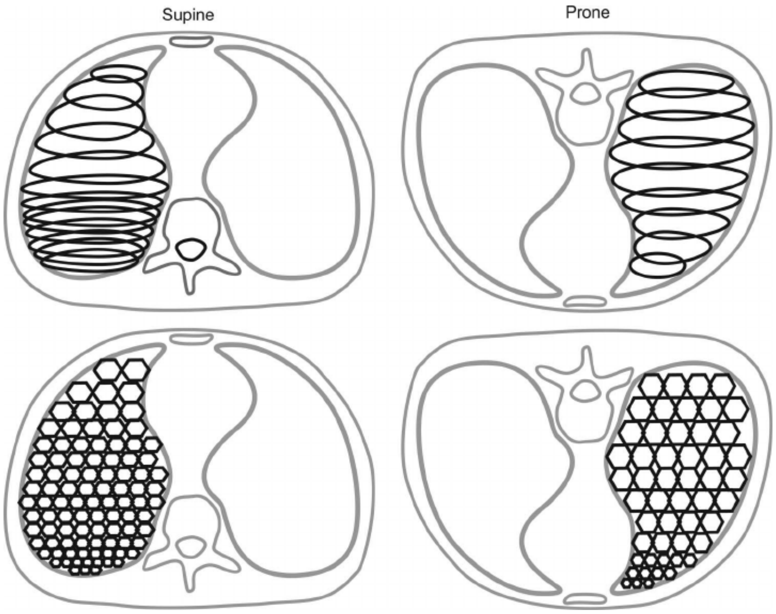

Figure 2: Schematic representation of strain-stress distribution and its impact on alveolar size distribution between the supine and prone position. The Slinky effect of a triangular-shaped spring suspended from its apex (supine position) causes higher strain and larger variation in the distribution of alveolar sizes due to the effects of gravity and a steeper stress production during mechanical inspiration in the upper lung regions. In contrast, suspending the spring by its base across a wider surface area (prone position) produces a more even strain and more homogeneous distribution of alveolar size that lessens inhomogeneity in stress development throughout the lungs during mechanical inspiration. Taken from [23].

functional MRI in supine humans to demonstrate that both perfusion and lung density exhibit vertical gradients [13]. However, when perfusion was normalised for regional lung density, the apparent vertical gradient in perfusion was not significantly different from zero. This key insight suggests that a substantial part of the observed vertical perfusion gradient in intact lungs is an artefact of measurement arising from the gravitational compression of dorsal (dependent) lung regions, which increases local tissue (and thus capillary) density. The importance of gravity in lung density distribution has been explored between horizontal patient positions as well as in the upright. In the upright position, the lungs are suspended vertically, allowing gravity to act directly along their long axis. This results in a pronounced deformation gradient, where the apex is more distended and the base is more compressed, leading to significant differences in alveolar size, compliance, and ventilation. In the supine position, the lungs lie horizontally and gravity acts from the ventral to the dorsal [24]. This shifts the deformation gradient dorsally, compressing the posterior lung regions and reducing ventilation there. While the Slinky effect persists in supine, the gradient is less steep than in upright. In the prone position, although the lungs remain horizontal, due to the anatomical shape of the lungs and reduced influence from the heart and abdominal contents, tissue deformation is more evenly distributed. As a result, the Slinky effect is minimized in prone, leading to more uniform tissue density and ventilation [24]. This position-dependent variation in the Slinky effect has important implications for ventilation–perfusion matching and clinical strategies such as prone positioning in respiratory failure.

Patient positioning profoundly influences lung mechanics and gas exchange, with studies consistently showing a more uniform distribution of ventilation and perfusion in prone compared to supine postures. Bryan et al. (1964) initially demonstrated that while upright subjects exhibit apex-to-base gradients in ventilation and perfusion, these distributions become "much more uniform" in the supine position, although a front-to-back perfusion gradient persists [25]. More recently, Henderson et al. [24], using functional MRI, confirmed that gravitational gradients in both ventilation and perfusion are indeed less pronounced in the prone posture than in the supine. However, it is noteworthy that their study found the overall heterogeneity (relative dispersion) of ventilation, perfusion, and regional ventilation-perfusion ratio ($\dot{V}_A/\dot{Q}$) was not statistically significantly different between postures in healthy lungs. This particular finding is crucial when looking toward ICU integration, as stark contrasts have been found between healthy and diseased lungs.

V/Q ratio heterogeneity is a crucial indicator of impaired lung function in non-healthy lungs, reflecting an imbalance between regional airflow and blood flow. In morbidly obese individuals, reduced lung volumes and elevated pleural pressures can lead to airway closure, causing abnormalities in V/Q distribution and hypoxaemia [26, 27, 28, 29]. For patients with ARDS and lung injury, there is significant topographic heterogeneity, with dependent lung regions often derecruited or filled with fluid due to increased lung weight from oedema, leading to greater V/Q mismatch [30]. However, prone positioning in ARDS can significantly improve V/Q matching by promoting a more uniform distribution of alveolar size and tissue stress, thereby mitigating the gravitational and compressive effects and reducing the non-uniform risk of ventilator-induced lung injury [23]. Additionally, factors like heterogeneous hypoxic pulmonary vasoconstriction and the varied impact of positive end-expiratory pressure (PEEP) on perfusion distribution in different postures further contribute to V/Q mismatching in injured lungs.

In conclusion, the interplay between gravity, body positioning, and external mechanical forces shapes a highly heterogeneous landscape of lung deformation, ventilation, and perfusion. These physiological mechanisms—while fundamentally grounded in classical principles of fluid and solid mechanics—are modulated by the lung's complex geometry, compliant tissue structure, and dynamic interactions with surrounding organs. Clinical studies and imaging data underscore the importance of these factors in both healthy and diseased lungs, revealing how regional mechanics influence gas exchange and injury susceptibility. However, to translate this physiological understanding into predictive capability, it must be formalized through robust mathematical frameworks.

3.1.3 Physiological Models of the Pulmonary System

Our continuing progression in the improvement of healthcare rests on centuries of research, whether it be through the recorded experimentation of live patients, or the post-mortem study of deceased individuals. This however, comes with many drawbacks as it is often slow, ethically complex and requires expensive equipment. This is why theoretical modelling is so valuable. Using mathematics, we can simulate experimental ideas through models, and test theories without the need for extensive human trials. Physiological models use mathematics to replicate human anatomy, through equations and iterative systems fitted to parameters collected from real medical data [31]. The computational modelling of human processes is an ever-growing field, with new and intriguing works being published rapidly. A search for “physiological model” on PubMed yields over 250,000 results, with over half of these being published in the last decade [32]. This progression is driven by an increasing demand for in-silico experimentation of human physiology, and supported by the constantly advancing mathematical tools and techniques at our disposal [33].

Due to the complexities of modelling lung mechanics, a number of different pressure measurements can be used. For reference, a visual diagram of these pressures can be seen in Figure 3, and can be referred to throughout the thesis if needed.

We can use these models to explore the underlying mechanisms of human physiology, and predict the response behaviour to a particular treatment strategy. In pulmonary medicine, mathematical models have successfully been used to better understand lung function and have resulted in a notable improvement to patient outcomes. In 2017, Rahaman used a simplistic approximation of viscoelastic lung behaviour to explore the effects of mechanical ventilation and the contributing factors to ventilator induced lung injury (VILI) [35]. They found

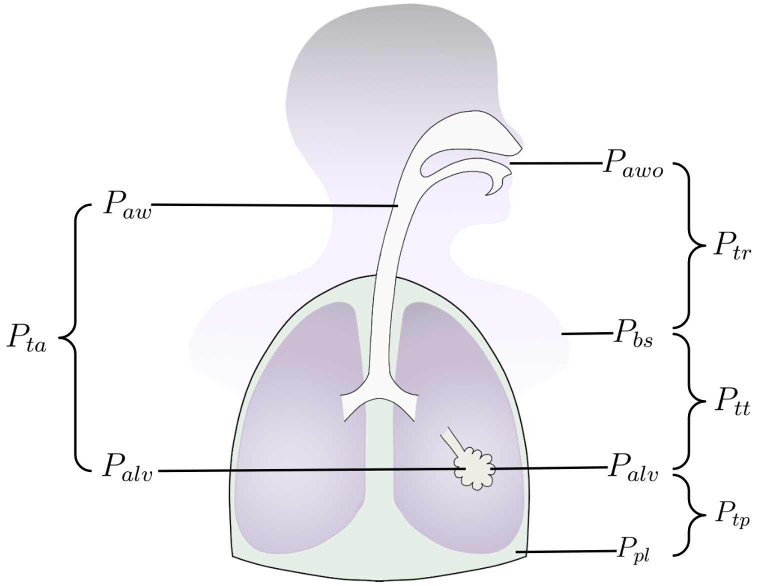

Figure 3: Reference diagram detailing various respiratory system pressures relevant to lung mechanics modelling. Key pressures include:,
P_{awo} - airway opening pressure.
P_{alv} - alveolar pressure.
P_{pl} - intra-pleural pressure.
P_{bs} - body surface pressure.
P_{aw} - airway pressure.
$P_{tp} = P_{alv} - P_{pl}$ - transpulmonary pressure.
$P_{tt} = P_{alv} - P_{bs}$ - trans-thoracic pressure.
$P_{ta} = P_{aw} - P_{alv}$ - trans-airway pressure.
$P_{tr} = P_{awo} - P_{bs}$ - trans-respiratory pressure.
taken from [34]

that in the ARDS lung, the forced pressures of mechanical ventilation caused significant stress in the system, but these could be minimised with the correct treatment strategies, such as proning the patient, and recommended that targeting transpulmonary pressure would be an effective strategy to limit VILI. The focus on minimising VILI is a key area in pulmonary modelling. In a highly-cited paper by Gattinoni et al, it was posited that the ventilator-associated causes of lung injury could be evaluated as a single parameter, the so-called mechanical power [36]. They computed the following equation for mechanical power:

$$Power_{rs} = RR \cdot \left\{ \Delta V^2 \cdot \left[\frac{1}{2} \cdot EL_{rs} + RR \cdot \frac{(1 + I:E)}{60 \cdot I:E} \cdot R_{aw} \right] + \Delta V \cdot PEEP \right\} \tag{2}$$

where ΔV is the tidal volume, $EL_{rs}$is the elastance of the respiratory system, $I : E$ is the inspiratory-to-expiratory time ratio, RR is the respiratory rate, and R_{aw} is the airway resistance. They found that mechanical power increased exponentially by adjusting the settings for tidal volumes, airway pressure and respiratory rate. This equation utilises the values set at the ventilator itself. By programming this into ventilators, clinicians can easily see how adjustments they are making are affecting mechanical power and how this increases injury risk for the patient.

This is the primary goal for mechanistic models, to give clinicians insight into the under-lying mechanics of the system such that they can tailor care for the best possible outcome. Creating the most accurate possible lung analogy through mathematics and simulation, gives the best chance of accurately predicting a patient's response to a particular treatment.

The mechanical behaviour of lung tissue under various forces has been modelled using diverse approaches that elucidate the intricate balance of stresses and strains governing pulmonary function. These models aim to capture the deformation of lung parenchyma due to gravity, internal pressures, and external mechanical forces. The following section focuses on mechanical models that describe the deformation of lung tissue, highlighting key studies and their contributions to the field.

Continuum mechanics models treat the lung as a deformable solid, using mathematical descriptions of stress and strain distributions. This approach is exemplified by the work of Hubmayr et al. [30], who analysed the interplay of regional mechanical properties in healthy and injured lungs. They argued that the lung's response to deformation could vary significantly depending on localized tissue damage, a key consideration for designing protective ventilation strategies.

One of the earliest and most influential works in this area was by West and Matthews in 1972 [11], who modelled the lung parenchyma using a finite element approach to explore the distribution of stress and strain due to its own weight in the upright position. The model consisted of a solid elastic structure using a round-topped trapezoid as a lung-shaped analogy. This shape was assessed at two different widths to find the most physiologically relevant model. The derived equations for stiffness were solved using a finite element approach, dividing the lung into 864 elements for the wider shape, and 444 for the narrower shape, in which The stiffness of each element is determined and then assembled to represent the complete structure, allowing the calculation of internal stress and strain. For the three-dimensional bodies, the elements used were tetrahedrons. Loads were assumed to act at the corner points, or nodes, of these elements. A non-linear stress-strain relationship was used, giving elasticity described by the equation

$$E = 0.8E_0/(0.8 - \epsilon),$$

where E_0 is the modulus at zero strain and ϵ is the strain. This closely matched experimental data from excised dog lung strips [37]. Specific constraints were applied to the nodes (corner points) of the model elements to simulate the lung's support and symmetry within the chest cavity; some nodes were fixed, some could only move vertically, and nodes on the surface were constrained not to move perpendicular to the boundary but were free to slide tangentially.

The main findings highlight the significant impact of the lung's weight on regional stresses, strains, and surface pressures, particularly in the upright position. In the upright lung, the parenchyma was found to be most expanded at the apex and least at the base. This regional difference was substantial, with apical units being about 3.7 times larger by volume than basal units for a lung model with an elastic modulus (E_0) of 1.25 g/cm^2. Inflation of the lung dramatically reduced this distortion, with relatively small increases in overall lung volume causing substantial decreases in volume distortion. Tissue displacement also occurred, with maximum sag happening about halfway down the lung. Expanding the lung to 5.5 times its relaxed volume (linear strain of 0.765) significantly reduced the maximum displacement from 2.8cm at FRC to just 0.12cm when weight was applied (for $E_0 = 2.5g/cm^2$. The inverted lung showed less marked regional differences in expansion and displacement compared to the upright posture. The analysis also revealed important distributions of stress and surface pressure. In the upright lung, the largest changes in stress were in the vertical direction, and expanding stresses were maximal at the apex in both vertical and lateral directions. For a lung at FRC with $E_0 = 2.5g/cm^2$, the vertical expanding stress near the apex was $5.52g/cm^2$, over 300% greater than the uniform stress of 1.63 g/cm^2 in the weightless state. The maximum vertical stress at the apex showed a minimum when plotted against lung volume, occurring around 25% of total lung capacity (TLC) for an E_0 of $2.5g/cm^2$, suggesting this is near the normal breathing range. The surface pressure (analogous to intra-pleural pressure) increased near the top and decreased near the bottom when weight was applied. At FRC, for a model with $E_0 = 2.5g/cm^2$, the difference in surface pressure between the apex and base was 4.9cmH2O. This difference was larger when the elastic modulus was smaller, increasing to 7.9cmH2O water when E_0 was $0.63g/cm^2$, contrasting with the prediction of 5.8cmH2O water based solely on specific gravity. Inflation of the lung reduced these regional pressure differences, resulting in a difference of about 2.2cmH2O between apex and base at high lung volumes near TLC. Vertical acceleration amplified these regional differences; for example, under 3 G acceleration (with $E_0 = 2.5g/cm^2$), apical elements became over 5 times larger by volume than those at the base. The study suggests that the high stresses near the upright apex might contribute to the vulnerability of upper lobes in certain lung diseases.

West and Matthews acknowledge several key limitations stemming from the lack of precise data on lung tissue properties and necessary modelling simplifications. A primary assumption was that the lung parenchyma behaves as a homogeneous, isotropic elastic material with uniform properties in all directions. However, the authors note that the real lung is not homogeneous, and while some experiments suggest isotropic behaviour in excised lobes or strips, this isn't definitively known for the whole lung. They used a specific non-linear stress-strain relationship based on tissue strip data, but the crucial elastic modulus at zero strain (E_0) was uncertain, with values chosen to yield reasonable surface pressures at functional residual capacity (FRC). Similarly, data for Poisson's ratio was unavailable, leading to a value of 0.3 being used, although varying it significantly altered stress and strain magnitudes, not just the pattern. The analysis also didn't account for the fact that an unevenly expanded material becomes anisotropic at large strains, particularly at the apex with low E_0, introducing inconsistencies where strain in one direction exceeds others. Time-dependent behaviours like hysteresis and adaptation were also omitted, presumed to cause small errors in equilibrium states. Furthermore, the model assumed the entire weight of the lung is supported at its periphery, despite some evidence suggesting the chest wall provides partial support. The analysis also simplified the scenario by keeping the external shape of the lung and chest cage constant during expansion, though real shapes change, and it did not include the additional increase in dependent density caused by increased regional blood volume due to lack of data. While a modification was made to account for high bulk modulus under compression (analogous to airway closure), the authors found it had "little difference apart from reducing the compression of the most dependent regions at very low volumes". These factors mean that while the study provides valuable insights into the pattern of gravity's effects, the precise magnitudes calculated are dependent on the chosen parameters and inherent modelling simplifications.

As data on these tissue properties has become more readily available, models have been created with expand on West and Matthew's foundation. Tawhai et al. (2009) employed a finite element analysis of the left human lung, with model geometries derived from multi-detector row computed tomography (MDCT) imaging of two subjects at functional residual capacity (FRC). One subject was a healthy male (subject 1), and the other a female with small airway disease (subject 2). A key methodological point was creating a prone model by simply reversing gravity on the supine lung shape, thus deliberately isolating the effect of gravity direction from confounding factors like displacement of the heart, chest wall, or diaphragm. The lung tissue was assumed to be a compressible, non-linearly elastic continuum with homogeneous and isotropic properties. Simulations were performed by first expanding the lung model in zero gravity and then incrementally adding the gravitational load. The primary results focused on regional tissue density and elastic recoil pressure (analogous to pleural pressure) gradients in the dorsoventral (gravitational) axis at FRC. The study found that the magnitude of the density gradient in supine was approximately double that of the prone lung, specifically -4.33%$/cm$ for subject 1 and -4.96%$/cm$ for subject 2 in supine, compared to -2.72%$/cm$ for subject 1 and -2.51%$/cm$ for subject 2 in prone. Correspondingly, the estimated pleural pressure gradients (Ppl) were also larger for supine, at 0.54$cmH2O/cm$ (subject 1) and 0.56$cmH2O/cm$ (subject 2) for supine, versus 0.29$cmH2O/cm$ (subject

1) and $0.27 cmH2O/cm$ (subject 2) for prone. These findings indicated that a smaller prone gradient was predicted even without shape changes of the chest cavity or the effect of heart support. The model estimates for supine density and the trend of smaller gradients prone were consistent with measurements from the MDCT imaging of the subjects and independent studies.

Despite its advancements, the Tawhai et al. study acknowledged several limitations inherent in the modelling approach. A primary limitation was that the model, by design, considered the effect of posture on density distribution independent of the displacement of the chest cavity, diaphragm, and heart that would typically accompany a change in posture. While this isolated the effect of gravity direction and shape, it did not represent the full physiological scenario. The model also did not account for potential shifts in regional blood content that occur with postural changes. The analysis assumed lung tissue was a homogeneous and isotropic elastic material, an assumption the authors note is not fully accurate for real lung tissue, which is heterogeneous and whose isotropy is not definitively known, particularly in relation to airway and vessel orientation. This assumption may be especially problematic when extending the model to disease states, where regional properties can vary significantly. The modelling of the left lung neglected the oblique fissure, which could affect tissue displacement and potentially regional heterogeneity. The material law used lumped together tissue elasticity and surface forces and was only applied to the static condition at FRC, not accounting for the interplay between these forces during dynamic processes. The coefficients in the strain energy density function were chosen to produce physiologically reasonable pressures rather than being directly derived from experimental measurements. Lastly, the specific choice of the reference state volume might not be perfectly accurate but was selected to facilitate comparison between subjects. While the study was an important step, particularly for understanding mechanical factors in injured lungs, the authors noted the model was not yet complete for studying disease states which involve regional pathology and potentially independent lobe motion.

Another study by Swan, Clark, and Tawhai (2012) aimed to develop a mathematical model to predict the topographic distribution of ventilation in the upright healthy human lung [38]. This was motivated by the technical difficulties in obtaining high-resolution imaging of lung function in the upright posture. The model integrates several factors: an anatomically based structure, tissue deformation due to gravity, and airway resistance. Subject-specific structural models for the lungs and conducting airways were derived from MDCT imaging of a healthy male subject, initially acquired in the supine position at Total Lung Capacity (TLC) and then scaled to the subject's upright Functional Residual Capacity (FRC) volume. The model assumed the lung tissue behaves as a compressible, non-linearly elastic continuum with homogeneous and isotropic properties. Tissue deformation under gravity was predicted using a continuum model, which in turn determined the initial pre-inspiratory configuration of the lung and the elastic recoil pressure and compliance of individual acini. Airflow was simulated in an anatomically based conducting airway tree coupled to geometrically simplified terminal acinar units, each represented as an individual compartment with varying volume-dependent compliances. The airflow in conducting airways was modelled primarily as Poiseuille flow with an additional correction for energy losses at bifurcations based on experimental data. The model coupled flow and tissue elasticity, with the flow driven by a temporally changing pleural pressure applied uniformly across the pleural surface.

The primary findings of the study confirmed experimental evidence that in the healthy lungs, tissue compliance has a far greater effect than airway resistance on the spatial distribution of ventilation. The model predicted significant spatial variation in intrinsic tissue properties. Due to gravitational deformation of the lung tissue within the curvilinear lung shape, the acini in the apical region of the upright lung were predicted to be, on average, more expanded at FRC than those in the basal region. This differential expansion results in a non-uniform distribution of acinar compliance, with less compliance in the more expanded apical units. The model predicted that ventilation to bottom (dependent) regions was greater than to top (non-dependent) regions, exhibiting a gravitational gradient, quantified as 1.4% or 1.5% per cm depending on the calculation method. An iso-gravitational heterogeneity was also imposed on this distribution due to the complex deformation of the curvilinear geometry. The study demonstrated that assuming a uniform or linear distribution of tissue compliance, rather than one derived from soft tissue mechanics, significantly reduced predicted ventilation heterogeneity. The minimal effect of airway resistance on the spatial ventilation distribution was attributed to the low viscosity of air.

Despite its advancements, the model has several acknowledged limitations. The model assumed that each acinus functions mechanically independently of its neighbours, which may not be accurate. The simulation of the upright posture used a lung shape derived from supine MDCT data, not accounting for the typical postural changes in the chest wall, diaphragm displacement, or heart support. While the study isolated the effect of gravity direction, it did not represent the full physiological scenario where these structures change shape with posture. The model also assumed that the change in pleural pressure is uniform at all locations during breathing, whereas in reality, it may vary regionally. The lung tissue was assumed to be a homogeneous and isotropic elastic material, despite known heterogeneity and potential anisotropy in real lung tissue, especially in disease. The modelling of the left lung neglected the oblique fissure, which could influence tissue displacement. The coupling between the tissue mechanics model (determining pre-inspiratory volumes and compliance) and the airflow model was described as "weak," as they were not solved concurrently, and the airflow model assumed isotropic acinar expansion during breathing. The study lacked direct subject-specific validation data for the upright posture, relying instead on comparisons with population data trends. Finally, while the model included a correction for flow disturbances at bifurcations based on experimental data, it still relied on assumptions of laminar flow and did not fully account for factors like the turbulent laryngeal jet or the wide variation in airway geometries

In summary, modelling lung tissue as a solid continuum has provided valuable insights into its deformation under physiological loading, capturing essential mechanical behaviours such as elasticity, anisotropy, and large deformations. However, this approach inherently neglects the complex structures and heterogeneity present in the lung. To more accurately represent the complex biomechanical environment of the lung, particularly the interactions between tissue deformation and airflow or fluid movement, a poroelastic framework becomes a natural and necessary extension. This transition enables the coupling of solid mechanics with fluid transport, offering a more comprehensive and physiologically relevant model of lung function.

3.1.4 Poroelasticity and its Application to Pulmonary Mechanics

Poroelasticity is a framework used to describe the mechanical response of materials that contain a freely moving fluid within a porous structure [39]. It models these materials as a coupled system consisting of a solid skeleton and the pore fluid. The theory accounts for fundamental coupled mechanisms: an increase in pore pressure can induce a dilation (expansion) of the solid material, and conversely, compression of the solid material can cause a rise in the pore pressure, particularly if the fluid is prevented from escaping. These interactions between the interstitial fluid and the porous solid bestow an apparent time-dependent character to the mechanical properties of the material. The theory defines key quantities including the solid displacement vector and the specific discharge vector (fluid motion relative to the solid), as well as stress quantities like the total stress tensor and the scalar pore pressure. The core of the theory lies in its constitutive equations, which are based on assumptions of linearity and reversibility, relating stress and strain (solid strain and the variation of fluid content). To form a complete mathematical system, these constitutive laws are combined with balance laws for mass (continuity equation for the fluid phase) and momentum (equilibrium equations for the bulk material), and a transport law like Darcy's law for fluid flow in the porous media. These governing equations are often formulated as coupled field equations, such as Navier-type equations for displacement and diffusion-type equations for pore pressure or variation of fluid content, which contain coupling terms reflecting the interaction between the solid deformation and the fluid dynamics.

The theoretical basis of poroelasticity originates in the early 20th century with the pioneering work of Karl Terzaghi (1923) [40], who formulated the theory of one-dimensional consolidation to describe the time-dependent settlement of saturated soils under mechanical loading. Terzaghi introduced the principle of effective stress, asserting that the deformation of a porous medium is governed not by the total applied stress, but by the portion transmitted through the solid skeleton—termed the effective stress. This is given by

$$\sigma^{'} = \sigma - p, \tag{3}$$

where $\sigma^{'}$ is the effective stress, σ is the total stress, and p is the pore pressure of the interstitial fluid. Terzaghi's model assumes a fully saturated, incompressible fluid and a linear elastic solid matrix, and it describes fluid flow using

Darcy's law under the assumption of small deformations and uniaxial strain. While powerful, this model is limited to one-dimensional, quasi-static scenarios, and does not account for the dynamic interactions between the solid and fluid phases in a general three-dimensional setting.

A major advance came with Maurice Biot's formulation of the general theory of poroelasticity in 1941, which extended Terzaghi's [40] ideas to a fully coupled, three-dimensional dynamic theory for fluid-saturated porous media [41]. Biot derived a set of governing equations that couple the linear elasticity of the porous solid skeleton with Darcy's law for fluid flow, and incorporated inertial effects of both the solid and fluid phases. This theory introduces a second-order partial differential equation system that simultaneously conserves linear momentum and mass for each phase, under the assumption of small deformations. The solid and fluid motions are interdependent: deformation of the porous matrix generates pore pressure gradients, which in turn drive fluid flow and further influence the stress state of the solid.

Biot's theory also introduced constitutive relations that link stress and strain in the solid matrix with pore pressure and fluid content variations, leading to the formulation of Biot's modulus and other poroelastic parameters. Importantly, Biot's framework reduced to Terzaghi's one-dimensional consolidation theory as a special case, but extended its applicability to a broad range of problems including wave propagation in saturated soils, hydro-mechanical coupling in geotechnical systems, and, more recently, soft tissue biomechanics.

Together, the contributions of Terzaghi and Biot laid the theoretical groundwork for modern poroelastic models, enabling a more comprehensive understanding of fluid-structure interactions in porous, deformable media—a potentially influential framework for modelling physiological tissues such as lung parenchyma, where the interplay between airflow and tissue deformation is fundamental.

Biological tissues are multi-phasic materials composed of a solid phase (structural macromolecules, cells) and a fluid phase (water, solutes, blood, air) [42], making poroelastic modelling a logical framework for their mathematical exploration. Considering that over 60% of cellular content is water, treating living cells as single-phase materials is counter-intuitive. Recent work suggests that the cytoplasm of living cells behaves as a poroelastic material [43]. In this framework, the cytoplasm is viewed as a biphasic material: a porous elastic solid meshwork (cytoskeleton, organelles, macromolecules) bathed in an interstitial fluid (cytosol). The rate of cellular shape change is thought to be limited by the rate at which intracellular water can redistribute within the cytoplasm.

Moeendarbary et al. (2013) investigated this using AFM micro-indentation tests on various cell types, including HeLa and MDCK cells [43]. Their experiments, applying rapid force (<35-100ms rise time), showed that cellular force-relaxation at short timescales (<0.5s) exhibited characteristics consistent with a poroelastic response. They found that the poroelastic diffusion constant D_p scaled with changes in cell volume induced by osmotic pressure, which modulated cytoplasmic pore size without altering the cytoskeleton. For HeLa cells, D_p was around 41 ± 11 m^2/s. They also probed the influence of the cytoskeleton, finding that F-actin strongly affected both cellular elasticity E and hydraulic pore size ξ, with the change in pore size dominating in setting D_p. Microtubules and keratin intermediate filaments were found to play a less significant role. Their study validated that, at short timescales, cellular responses are consistent with poroelastic behaviour driven by water redistribution. A key insight was that the hydraulic pore size (ξ) is distinct from the cytoskeleton entanglement length (λ), and ξ is influenced by both the cytoskeleton and macromolecular crowding. Limitations discussed include that previous studies using shear rheology or lower sampling rates might have missed these poroelastic effects.

Poroelasticity has also been used in the modelling of large and complex organs such as the heart. Chapelle et al. (2010) developed a poroelastic model for cardiac perfusion valid for large strains and compatible with incompressibility [44], deriving their formulation from a free energy function for thermodynamic consistency. The model treats the myocardium as an active poroelastic material, combining a passive poroelastic component with an active contractile component. The fluid (blood) in small arteries and capillaries is modelled as flowing through a single poroelastic compartment, with the venous network represented as a sink term. Fluid enters via a distributed source (small arteries) and leaves via a distributed sink (small veins).

Simulations using this model on an idealized left ventricle geometry with active fibres reproduced several key phenomena observed in cardiac perfusion. During contraction, the myocardium volume decreases, pressure rises, and flow from small arteries is significantly reduced (flow impediment). Simultaneously, blood is squeezed out of the capillaries into the small veins (rise of venous flow). Conversely, during relaxation, flow into capillaries increases, filling their capacitance. The model correctly showed that flow is mainly during the systolic phase in small arteries and mainly during the diastolic phase in small veins, characteristic of the coronary network. It also reproduced the fact that flow impediment is higher in the sub-endocardium than the sub-epicardium, showing pressure and flow vary non-linearly across the myocardium wall.

The application of poroelasticity to lung modelling offers a sophisticated biomechanical framework for understanding the complex interplay between tissue deformation and air flow during respiration. This approach is particularly well-suited to the lung because the parenchyma, the spongy tissue responsible for gas exchange, can be effectively idealised as a saturated porous medium, due to the dense network of alveoli and capillaries [45]. In this idealisation, the solid phase is represented by the tissue network, which includes the alveolar walls, capillaries, and structural fibres like collagen and elastin, while the fluid phase filling the pores is the air within the alveoli and ducts. The large difference in scale between the microscopic structure of individual alveoli (around 0.02 cm) and the macroscopic scale of lung segments (around 4 cm) supports the use of a continuum model based on averaging techniques, such as poroelasticity [46].

Berger et al. (2015) developed a novel lung ventilation model that tightly couples tissue deformation with ventilation. The model represents the lung parenchyma as a continuum poroelastic material [46]. In this framework, the tissue forms the solid phase and the air in the alveoli is the fluid phase. Key assumptions include the incompressibility of both phases and neglecting accelerations and viscous stress compared to drag forces. The model uses a Neo-Hookean strain-energy law for tissue elasticity and Darcy's law for fluid flow through the porous parenchyma. The conducting airways are modelled as a pipe network where flow is assumed to be laminar (Poiseuille flow). The coupling between the poroelastic parenchyma and the airway network is achieved by dividing the lung into subdomains, each linked to a terminal branch of the airway tree. The fluid flux from a distal airway branch serves as a source term for the porous medium in its subdomain. Conversely, the pressure at the end of a distal airway branch determines the average pressure within the tissue of that subdomain.

The model equations are solved numerically using the Finite Element Method (FEM) with a stabilised mixed formulation. The model utilises anatomical data from CT scans for lung geometry and airway tree structure, with distal airways generated algorithmically. Instead of prescribing pleural pressure, which is difficult to measure, the model is driven by deformation boundary conditions on the lung surface, estimated from image registration between respiratory phases. Simulations using this coupled model produced physiologically realistic results for global lung mechanics during normal breathing. A significant finding was the strong correlation between airway resistance and regional tissue expansion (ventilation); increased airway resistance led to decreased ventilation. Similarly, pressure in the poroelastic tissue became more negative with increasing airway resistance, creating pressure gradients that can drive collateral ventilation. Simulations of pathological conditions provided valuable insights. Localised airway constriction resulted in decreased mean tissue expansion and increased heterogeneity within the constricted region, with surrounding tissue compensating by expanding more. This regional difference created large elastic stresses near the boundary of the constricted area. Localised reduction in tissue elasticity led to increased expansion (hyper-inflation) and decreased elastic stress within the weakened region, but dramatically increased heterogeneity and resulted in under-inflation of the immediately surrounding tissue. The model also revealed dynamic hysteresis in the pressure-volume curves, especially at faster breathing rates. This hysteresis is attributed to the delayed filling and emptying of different lung regions due to heterogeneity in airway resistance, leading to increased work of breathing and greater pressure heterogeneity at higher frequencies.

The Berger et al. (2015) model, while advanced, presents several limitations. Firstly, the model relies on simplifying assumptions about lung tissue and air flow behaviour, such as assuming both solid and fluid phases are incompressible. Secondly, the choice of a Neo-Hookean strain-energy law for tissue mechanics means the model does not produce classical hysteresis effects attributed to the viscoelastic properties of lung tissue components like elastin and collagen, although it does show dynamic hysteresis from delayed regional filling/emptying.

Thirdly, the model's boundary conditions are derived from image registration between different respiratory phases rather than direct measurement of pleural pressure, with the paper noting the use of a simple registration method. Fourthly, the model incorporates a realistic airway tree geometry from CT data for proximal airways, but the distal airway tree is generated algorithmically rather than being patient-specific, requiring inferred parameters like radii. Additionally, the numerical solution employs an approximate linearization in the Newton algorithm, only treating the elasticity term as non-linear. Finally, the current model does not include gas exchange, and achieving patient-specific parametrisation for tissue elasticity and distal airway properties using advanced imaging is identified as necessary future work.

Seyfi et al. (2016) presented a biomechanical model for predicting breathing-induced human lung deformation, validated using data from human subjects undergoing radiotherapy [47]. The model uses a subject-specific poroelastic framework where the lung parenchyma is treated as a continuous poroelastic medium composed of a solid tissue matrix and air in the pores (alveoli and ducts). The simulation employs a porous fluid-structure interaction (PFSI) technique to solve the coupled airflow and structural dynamics, incorporating Darcy's law for fluid flow and a Lagrangian formulation for the solid structure. A key methodological contribution is the use of patient-specific lung geometry derived from 4DCT scans of two patients, and estimating heterogeneous, spatially-dependent elastic properties for each patient's lung using an inverse analysis methodology that integrates 4DCT registration data and pulmonary function tests. Boundary conditions included a periodic pressure profile on the lung surface derived from pressure-volume curves and a stress-free inlet at the hilum, with gravity considered in the supine position relevant to radiotherapy.

The Seyfi et al. (2016) model successfully predicts lung displacement during the breathing cycle, showing good agreement with displacement data derived from 4DCT image registration of the same patients. The predicted absolute displacement typically increases from the lung's interior to its surface and from top to bottom. Validation showed the average prediction error over most of the lung was within 3mm, considered clinically acceptable for radiotherapy. Crucially, the model's accuracy was significantly improved by incorporating the heterogeneity of lung tissue properties, resulting in substantially lower errors compared to a homogeneous model. Compared to the Berger et al. (2015) model [46], Seyfi's work distinguishes itself by its explicit subject-specific parametrisation of tissue elasticity derived from patient imaging data using an inverse method, whereas Berger's model used uniform values and noted patient-specific parametrisation as future work. Seyfi also performed direct validation of predicted tissue displacement against image registration data, while Berger used image registration to define surface deformation boundary conditions, but validated primarily against global physiological measures and correlations. Furthermore, Seyfi used pressure boundary conditions on the lung surface, contrasting with Berger's use of deformation boundary conditions. The application focus of Seyfi's model is specifically on tumour localization and motion management for radiotherapy, whereas Berger's focus was broader, aiming to understand coupled mechanics in health and disease states like COPD and fibrosis.

These poroelastic models have demonstrated the ability to produce physiologically realistic results for global lung mechanics, such as tidal volume and flow rates during normal breathing. More importantly, they provide coupled insights into regional ventilation and tissue deformation. Simulations have revealed correlations between airway resistance and regional tissue expansion, showing that ventilation decreases as resistance increases, while tissue pressure becomes more negative. The models can capture phenomena like collateral ventilation, driven by pressure gradients between well-ventilated and less-ventilated regions. Furthermore, simulating pathological conditions such as localised airway constriction or tissue weakening provides insights into the mechanics of respiratory diseases, showing how changes in mechanical properties lead to decreased ventilation, increased heterogeneity, altered stress distributions, and hyperinflation in affected regions. The heterogeneity of lung properties and airway resistance can also lead to dynamic hysteresis in pressure-volume curves, particularly at faster breathing rates, caused by the delayed filling and emptying of different lung regions.

While powerful, the application of poroelasticity to lung modelling faces challenges. Some models make simplifying assumptions about material linearity or the absence of classical tissue viscoelasticity. Patient-specific parametrisation of material properties and the detailed structure of the distal airway tree, often beyond the resolution of standard clinical imaging, remains a significant hurdle. Accurately modelling the mechanical interaction between the lung and the chest wall, as well as the influence of heart motion, is also necessary to improve model accuracy, particularly in regions near these structures. The high detail of data required for the parametrisation of these models makes them very computationally involved beyond the scope of bedside ICU study. In order to make the findings of these papers relevant clinically, a simplified model is required that can make quick and effective predictions.

3.1.5 Concluding Remarks

This literature review has explored the multifaceted physiological, clinical, and mathematical foundations necessary for understanding pulmonary mechanics in critically ill patients, particularly those undergoing mechanical ventilation. A clear consensus has emerged from clinical studies: patient positioning, especially transitioning from supine to prone, can significantly improve lung function by promoting more homogeneous distributions of ventilation and perfusion, thereby mitigating the risk of ventilator-induced lung injury (VILI) and improving patient outcomes in conditions such as Acute Respiratory Distress Syndrome (ARDS).

The physiological underpinnings of these observations—namely gravitational gradients in tissue deformation, regional differences in alveolar mechanics, and the dynamic coupling between ventilation and perfusion—demonstrate a complex interplay that is not easily captured by empirical study alone. Traditional solid mechanics models of lung deformation, while useful, are inherently limited in their ability to represent fluid-structure interactions essential to respiratory dynamics.

Poroelastic theory provides a compelling framework for bridging this gap, offering a mathematically rigorous approach to modelling the lung as a biphasic system of deformable tissue and air. Recent advances in poroelastic modelling have shown promise in simulating both global and regional lung mechanics, yet these models are often computationally intensive and require simplification for bedside clinical application.

Moving forward, the development of a physiologically realistic yet computationally tractable mathematical model of lung tissue mechanics, grounded in poroelastic theory, is not only a logical extension of current research but a necessary step toward personalised critical care. Such a model would allow for predictive simulations of patient-specific responses to positioning and ventilation strategies, thereby equipping clinicians with a powerful tool to optimise treatment plans, reduce the risk of iatrogenic injury, and ultimately improve outcomes for mechanically ventilated patients.

3.2 Outline of Modelling Chapters

Moving forward from the literature review, the clear clinical consensus regarding the significant impact of patient positioning on lung function, particularly in critically ill mechanically ventilated patients, underscores a critical gap in our understanding. While empirical studies consistently demonstrate that postures like prone positioning can improve ventilation and perfusion distribution and mitigate ventilator-induced lung injury, the precise underlying mechanisms that drive these differences remain under-explored. Traditional solid mechanics models, while valuable for understanding tissue deformation, inherently lack the capacity to represent the complex fluid-structure interactions essential to respiratory dynamics. Therefore, the subsequent chapters of this thesis are driven by the urgent need to develop a comprehensive and detailed mathematical model that can accurately replicate human physiology and provide deep insights into these mechanisms, moving beyond mere observation to predictive capabilities for personalised critical care.

The remainder of this thesis will present a series of progressively complex mathematical models, each building upon the insights of the last, to mechanistically explore the effects of gravity and patient positioning on lung mechanics.

Chapter 4: Static Modelling of Lung Tissue Deformation

This chapter initiates the mathematical modelling framework by focusing on the static deformation of lung tissue due to gravity. It aims to determine how different simplified lung shape analogies (cylinder, cone, and truncated cone) can represent the gravitational influence on alveolar displacement in upright, supine, and prone positions. The chapter derives the Bar Equation to calculate tissue deformation and demonstrates that the truncated cone most accurately reflects physiological distribution seen in human data, leading to its selection for subsequent modelling. Initial insights into regional alveolar volume, ventilation, and perfusion distributions across positions are also established.

Chapter 5: Linear Poroelastic Lung Model

This chapter transitions from static analysis to a dynamic framework by introducing a linear poroelastic model. The model couples solid tissue deformation with fluid (air) flow to simulate lung dynamics across the breathing cycle and assess the initial effects of patient positioning. It establishes the governing equations for the system, incorporating Terzaghi's consolidation problem as a foundational concept. The chapter details the Finite Difference Method (Crank-Nicolson approach) for solving these coupled equations, addressing and resolving numerical instabilities through relaxation methods. Results demonstrate that the model can accurately replicate lung behaviour under ventilator waveforms, showing that the prone position leads to more uniform pore pressures and reduced inspiratory pressure spikes compared to upright and supine positions.

Chapter 6: Non-linear Poroelastic Lung Model

Recognizing the limitations of linear assumptions, this chapter develops a fully non-linear poroelastic model. It incorporates strain-dependent elastic properties, including time-dependent alveolar recruitment and de-recruitment, which are influenced by threshold opening and closing pressures and spatial heterogeneity. Neo-Hookean hyperelasticity is integrated to model non-linear porosity and permeability interactions, which are dynamically linked to tissue deformation. The model successfully reproduces the characteristic S-shaped pressure-volume curve of the lung, including the lower and upper inflection points, which are crucial for understanding alveolar recruitment and over-distension.

Chapter 7: A Coupled Pulmonary Model based on Non-linear Poroelastics

This final modelling chapter synthesizes previous advancements by integrating the non-linear poroelastic lung tissue model with key external physiological systems. It connects to the branching upper airways to account for resistance and flow dynamics. The model also incorporates pulmonary blood circulation and external thoracic pressures to predict regional ventilation-perfusion (V/Q) ratios across different patient positions. A significant focus is placed on assessing localized mechanical power delivery and its role in ventilator-induced lung injury. Findings demonstrate that prone positioning substantially reduces the proportion of lung tissue at high risk of VILI and promotes more uniform mechanical power distribution.

4 Static Modelling of Lung Tissue Deformation

4.1 Introduction

This chapter initiates the development of a foundational mathematical model by focusing on the static deformation of lung tissue due to gravity. The primary objective is to evaluate how different simplified lung shape analogies (cylinder, cone, and truncated cone) can represent the gravitational influence on alveolar displacement in upright, supine, and prone positions. We hypothesize that gravity plays a significant role in lung tissue deformation, even in a static state, and that selecting the most physiologically accurate geometric analogy is crucial for subsequent dynamic modelling. The key clinical questions this chapter addresses is: How does a patient's body position influence the static gravitational deformation of their lung tissue, and can a simplified anatomical representation capture this effect in a succinct and reliable way to give real-world clinical applicability? This foundational step is necessary to establish a reliable baseline for understanding gravity's impact before integrating more complex physiological dynamics observed during breathing and mechanical ventilation.

4.2 Tissue Deformation

The first aspect to be modelled is the deformation of the alveoli due to the weight of the lung. It has been well documented that the distortion of lung tissue due to gravity has a measurable impact on alveolar parameters, such as volume, resistance and vertical position [10, 11, 12, 13], and so this mechanism must be developed to begin with, before alveolar parameters are calculated and used as a measure of lung function. When studying deformation as a direct result of gravity, it is possible to simplify the elements involved to a one-dimensional approach, as discussed in the literature review portion of this

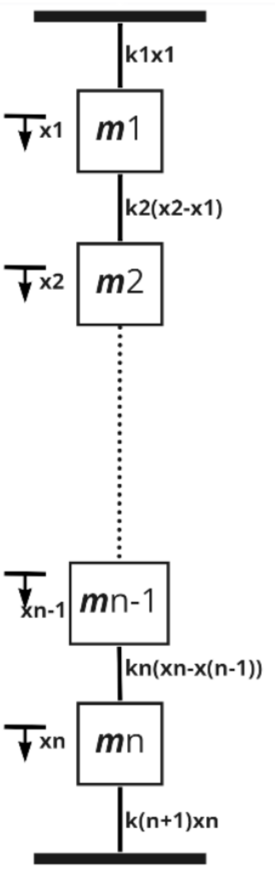

Figure 4: A simplistic model illustrating lung tissue deformation, representing the lung as a series of discrete alveolar sacs (masses m) connected by elastic springs, with deformation (x) occurring vertically. This model assumes the top and bottom of the lung are fixed, confining deformation internally.

thesis. In this model all measurements are taken vertically with respect to each isogravitational plane. In order to select the best approach, a number of model types were explored before selecting the most appropriate for the study question.

One of the more simplistic model set-up of tissue deformation likens the lung components to a series of weights and springs connected in series. Represented in Figure 4, this model equates the alveolar sacs to weights of mass m, connected via elastic springs. The top and bottom of the lung are fixed in place by setting all deformation at the boundaries to zero, as to ensure that all deformation occurs within the lung and does not affect the overall lung size.

Due to the immense count of alveoli (274-790 million) in an adult human lung, it is impractical to model each alveolus as a separate mass. Therefore, the masses instead represent all the alveoli on an isogravitational plane denoted here as “alveolar zones” for simplicity. The number of zones can be increased or decreased to adjust model complexity and biological accuracy. It should be noted that summarising all alveoli in the same plane into one unit nullifies the within-plane heterogeneity discussed in the review above. Therefore it is more sensible to treat the alveolar units in the model as the average value of all alveoli in that plane. Here, x represents the displacement of each zone vertically, and k represents the spring constant as denoted in Hooke's Law.

The issue with this model however, is that it equates the lung to a series of discrete compartments. This is not the case, as deformation is seen as a continuous phenomenon across the lung [13]. Although the number of masses in the system could theoretically be increased until results mimic those of the continuous deformation seen experimentally, this would make the model unnecessarily complex and computationally far more time consuming. Hence, a model is required which can represent the lung as a continuous object in which deformation is not assessed discretely. An appropriate method for this is a continuum approach that incorporates solid mechanics.

Solid mechanics studies the deformation of solid materials in which forces act along the entire body continuously. Although often used to assess rigid materials such as metals and plastics, the use of solid mechanics to explore biological soft tissues has been well documented and verified [48]. Figure 5 represents the lung as a solid bar with a volume load $k(x)$ which acts across the entirety of

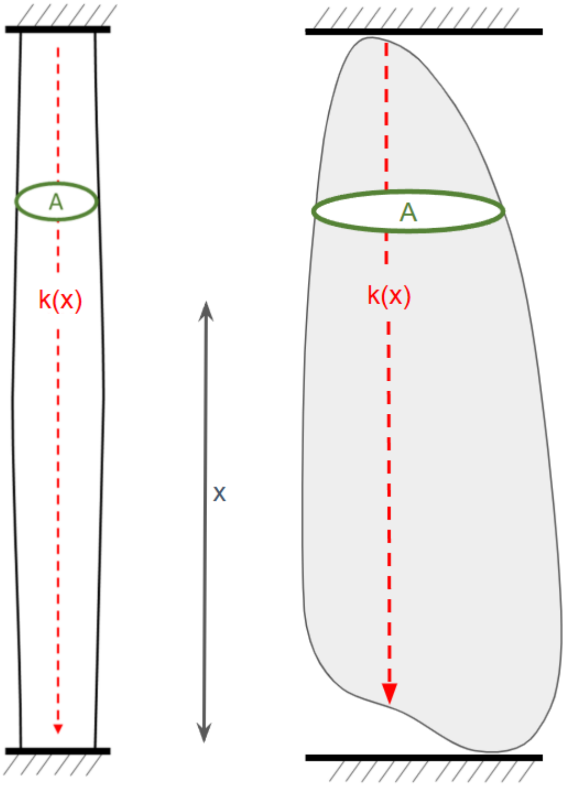

Figure 5: Representation of lung deformation using a solid mechanics continuum approach. The left image shows the typical bar analogy, where the lung is modelled as a continuous solid bar with a volume load acting across its entirety, and fixed at both ends to ensure internal deformation. The right image provides a visual comparison to an anatomical lung shape.

the structure. The bar has a variable cross-sectional area A and tissue elasticity E. As with the model in Figure 4, the bar is fixed at both ends such that deformation is all internal. In this model however, the "alveolar zones" are not expressed discretely, and so each isogravitational plane can be assessed continuously across the lung, allowing for a more realistic representation of lung tissue. The solid mechanics approach also allows far greater customisation, creating the ability to explore the impacts of minute details in the lungs structure. It is this ease of tailoring the model to a specific research question that makes it such an effective choice for this study, and as such is the one used going forward.

4.3 Derivation of the Bar Equation

Due to the continuous nature of the solid mechanics model, lung tissue deformation can be calculated using differential equations. Taking the bar representation in Figure 5, the equation for the bar can be derived using three components that describe it's behaviour.

Firstly, finding the equilibrium of the bar. Take some random element from the bar, with a normal force acting upon it N, and the force of it's own weight load $k(x)A$, as illustrated in Figure 6.

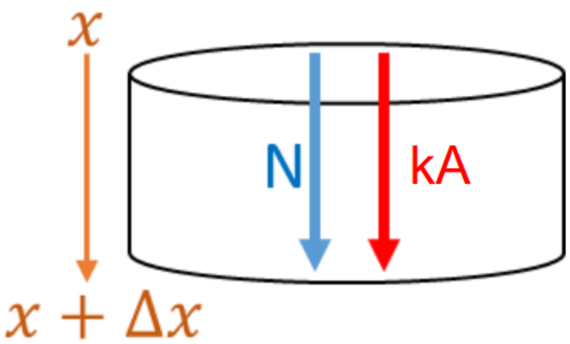

Figure 6: A random, infinitely small element of the solid bar model, illustrating the normal force (N) acting upon it and the force of its own weight load $k(x)A$, used to derive the equilibrium equation for lung tissue deformation.

Here x is the original position of the element and Δx represents the distance that x is displaced downwards. The equilibrium of this element occurs when the normal force acting upon it N plus the force of it's own weight $k(x)A$ equal zero. Taking this across the distance $x + \Delta x$ gives the equation:

$$N(x+\Delta x) - N(x) + \int_{x}^{x+\Delta x} k(x)A\,dx \;= 0 \qquad (4)$$

If this element is set to be infinitely small, it can be assumed that both cross-sectional area and volume load are constant across it's length, thus the equation becomes:

$$N(x+\Delta x) - N(x) + k(x)A\Delta x = 0 \tag{5}$$

and is subsequently rearranged to

$$\frac{N(x+\Delta x) - N(x)}{\Delta x} + k(x)A = 0 \tag{6}$$

Finally, to assess this element as infinitely small, take the limit of the expression as Δx tends to 0.

$$\lim_{\Delta x \to\ 0} \frac{N(x+\Delta x) - N(x)}{\Delta x} + k(x)A \tag{7}$$

$$\therefore N^{'} + k(x)A = 0 \tag{8}$$

This gives our equation for the equilibrium of the bar as 8. The second component required to derive the bar equation is Hooke's Law, which states that stress σ equals strain ϵ multiplied by elasticity E. This gives the equation for normal force of the bar as:

$$N(x) = E(x)A(x)\epsilon(x) \tag{9}$$

The final component required is the definition of normal strain which states that strain ϵ equals the derivative of displacement $u(x)$, such that:

$$\epsilon(x) = \frac{du(x)}{dx} \tag{10}$$

When taking these three components together, combine equations 8, 9 and 10 to give:

$$N^{'} + KA = \frac{d}{dx}(EA\epsilon) + k(x)A = \frac{d}{dx}\left(EA\frac{du}{dx}\right) + k(x)A = 0 \tag{11}$$

In the case of the lung model deforming under gravity, our volume load simply represents the force of the lungs own weight and can therefore be expressed as the density ρ multiplied by gravity g, where ρ and g are constants in height. Which gives the final Bar Equation as:

$$\frac{d}{dx}\left(EA\frac{du}{dx}\right) + \rho g A = 0 \tag{12}$$

This differential equation can be used to calculate the deformation across the bar and is now ready to be modified to represent a physiological model of the lung.

4.4 Lung Deformation in the Upright Position

In order to use the bar equation to calculate tissue deformation in the lung, an appropriate shape must be selected as a lung analogy. CT scans along with other imaging techniques are regularly used to assess the shape and condition of a patient's lungs, and these have been incorporated into mathematical models of lung mechanics effectively [10, 38]. However, the use of imaging data to build an anatomical lung model is very computationally intense, which can make the model too slow for real-time decision making. For simplicity, the lung can instead be equated to a 3-dimensional shape. The literature presents three commonly used shapes to represent the lung for study purposes: the cylinder, the cone, and the truncated cone [49, 50]. In order to create the most informed model possible in this study, each of these shapes is used to model the

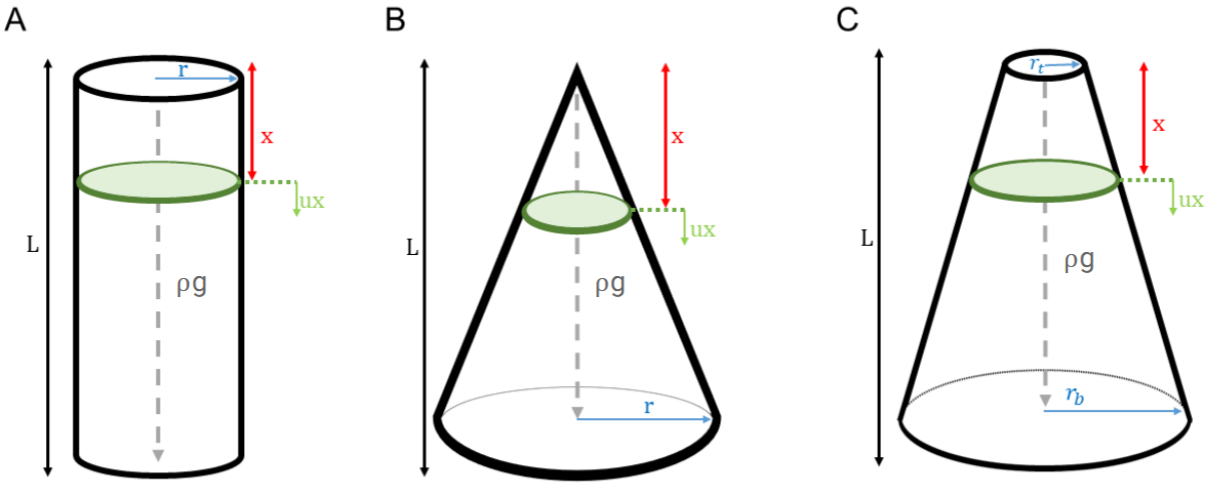

Figure 7: Three analogies for lung shape used in this paper. **A** represents a cylinder with radius r, **B** represents a cone with base radius r, **C** represents a truncated cone with base radius r_b and top radius r_t. Each shape has height L and is subject to weight load ρg.

deformation throughout the lung before selecting the most appropriate shape to proceed with the project. The set up of these shapes can be seen in Figure 7

To begin, the cylinder, being most simplistic shape, was assessed using the bar equation. The cylinder is created as shown in Figure 7A, with radius r, height L and subject to the weight load ρg. The deformation of the element at distance x from the top of the lung is denoted as $u(x)$. For the purposes of this section of the report, elasticity is constant across the length of the lung. The cylindrical shape also means that cross-sectional area is constant across the length as well. This allows the Bar Equation to be simplified as such:

$$\frac{d}{dx}\left(EA\frac{du}{dx}\right) + \rho g A = (EAu^{'})^{'} + \rho g A = 0 \tag{13}$$

Which is rearranged to

$$u^{''} = -\frac{\rho g}{E} \tag{14}$$

This can then be integrated twice to find u

$$u(x) = -\frac{\rho g}{2E}x^2 + c_1 x + c_2 \tag{15}$$

To find the values of terms c_1 and c_2 we fix the top and bottom of the lungs such that all deformation occurs within the shape, as discussed previously. To achieve this, set boundary conditions at $u(0) = 0$ and $u(L) = 0$. This gives deformation in a uniform cylinder as:

$$u(x) = -\frac{\rho g}{2E}x^2 + \frac{\rho g L}{2E}x \tag{16}$$

The second shape modelled was the cone, as can be seen in Figure 7B. The cone has base radius r, height L and again has the weight load ρg. Unlike the cylinder however, the cross-sectional area A is no longer constant across the shape, and is instead a function of distance from the apex x. This means the Bar Equation cannot be simplified in the same way as seen in 13, instead giving:

$$\frac{d}{dx}\left(EA\frac{du}{dx}\right) + \rho g A = E(A(x)u^{'})^{'} + \rho g A(x) = 0 \tag{17}$$

Using the Quotient Rule this becomes

$$u^{''}AE + u^{'}A^{'}E + A\rho g = 0 \tag{18}$$

Due to the nature of a cone, the function $A(x)$ can be determined as a circle at distance x from the apex of the shape, which is simply calculated as

$$A(x) = \pi\left(\frac{rx}{L}\right)^2 \tag{19}$$

Substituting $A(x)$ into 18 gives

$$u^{''}\pi\frac{r^2}{L^2}x^2E+u^{'}2\pi\frac{r^2}{L^2}xE+\pi\frac{r^2}{L^2}x^2\rho g=0 \tag{20}$$

Simplified to

$$u^{''}+\frac{2}{x}u^{'}+\frac{\rho g}{E}=0 \tag{21}$$

When solving this second order differential equation, boundary conditions are once again needed. However, the pointed top of the cone creates some issue, as cross-sectional area is assumed to be zero and so the finite solution cannot be sustained at an infinitesimally small point. To fix this, boundary conditions are instead set at $u(1) = 0$ and $u(L) = 0$. Solving for u using these boundary conditions gives the deformation equation for a cone as:

$$u(x)=\frac{\rho g(x-1)(L^2+L-x^2-x)}{6Ex} \tag{22}$$

Despite this being a relatively common analogy for lung shape, the harsh point at the top of the cone is far from physiologically accurate and forces assumptions to be made, which may affect results. To fix this, the final shape analysed is the truncated cone, as shown in Figure 7C, which mimics the nature of the cone but with the top point being removed. Again, the truncated cone has height L and the weight load ρg. This time though there is both a base radius r_b and a top radius r_t, which can easily be adjusted to replicate physical lung shape as closely as possible.

Taking the Bar Equation for a non-constant cross-sectional area as in 18, the function for $A(x)$ can be derived as the area of the circle at a distance x from the apex of the shape. For the truncated cone, $A(x)$ becomes:

$$A(x)=\pi\left(\frac{xr_b-xr_t+Lr_t}{L}\right)^2 \tag{23}$$

Substituting into (17) gives

$$u'' = -2u' \left(\frac{r_b - r_t}{xr_b - xr_t + Lr_t} \right) - \frac{\rho g}{E} \tag{24}$$

Now that point has been removed from the cone, there is now a definable area at both the base and apex of the shape, and so the boundary conditions can once again be set to $u(0) = 0$ and $u(L) = 0$, fixing the lung far more accurately in the chest cavity. This gives the final equation for deformation in the truncated cone as:

$$u(x) = \frac{\rho g x(L - x)(Lr_b + 2Lr_t + xr_b - xr_t)}{6E(Lr_t + xr_b - xr_t)} \tag{25}$$

4.5 Lung Deformation in the Horizontal Position

Placing the patient flat on their back in the supine position is a common manoeuvrer in the ICU [51], and has been shown in the literature review portion of this paper to significantly alter lung function. In order to model this position, each of the three shapes is turned 90° on to their side. Deformation is once again measured in the direction of gravity. Thus, a new variable is required for the height of the lung against gravity, denoted h. Variables and measurements are adjusted accordingly. Figure 8 contains the visual representation of the three shapes in supine position.

For each of the three shapes, there is a non-constant cross-sectional area; therefore we take the bar equation in the form shown in 18.

To evaluate deformation in shapes with non-constant cross-sectional area, a finite difference method was employed. The governing differential equation was discretised using central difference approximations for both first and second derivatives, resulting in a second-order accurate scheme. This approach yields a tridiagonal system of linear equations, which captures the spatial variation in

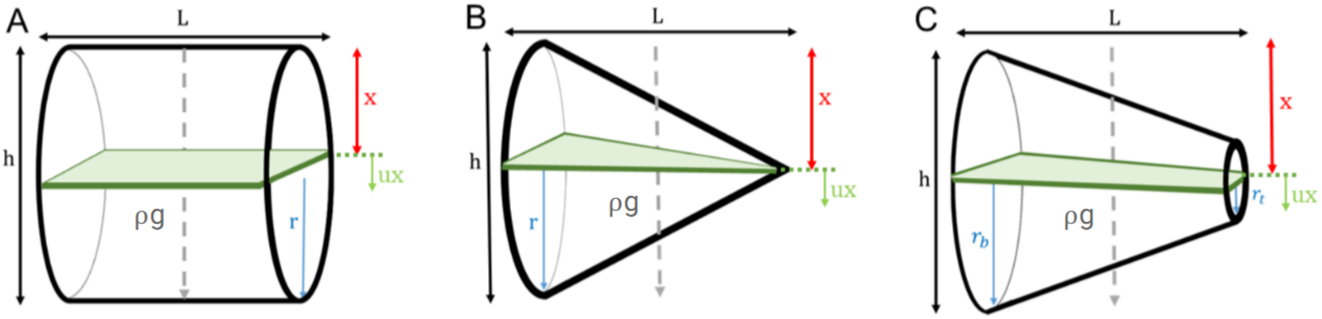

Figure 8: Three analogies for lung shape used in this paper in the horizontal positions. **A** represents a cylinder with radius r, **B** represents a cone with base radius r, **C** represents a truncated cone with base radius r_b and top radius r_t. Each shape has height h (parallel to gravity), length L, and is subject to weight load ρg.

geometry through the coefficients. The method is well-suited for solving boundary value problems involving variable material properties or geometry, such as those encountered in structural and physiological modelling. This method is detailed below.

First taking the equation

$$Au^{''} + A^{'}u^{'} = -\alpha A \tag{26}$$

where $\alpha = \frac{k}{E}$. Expanded at x_i with interval Δ gives

$$A_i\left(\frac{u_{i+1} - 2u_i + u_{i-1}}{\Delta^2}\right) + \left(\frac{A_{i+1} - A_{i-1}}{2\Delta}\right)\left(\frac{u_{i+1} - u_{i-1}}{2\Delta}\right) = -\alpha A_i \tag{27}$$

Separating variables gives

$$u_{i-1}\left(A_i + \frac{\Delta}{2}\left(A_{i-1} - A_{i+1}\right)\right) + u_i\left(-2A_i\right) + u_{i+1}\left(A_i + \frac{\Delta}{2}\left(A_{i+1} - A_{i-1}\right)\right) = -\alpha\Delta^2 A_i \tag{28}$$

This can be rewritten in matrix form as:

$$\begin{bmatrix} 1 & 0 & 0 & \cdots & 0 \\ a & b & c & \cdots & 0 \\ & \ddots & \ddots & \ddots & \\ 0 & \cdots & a & b & c \\ 0 & \cdots & 0 & 0 & 1 \end{bmatrix} \begin{bmatrix} u_0 \\ u_1 \\ \vdots \\ u_{N-1} \\ u_N \end{bmatrix} = \begin{bmatrix} 0 \\ -\alpha\Delta^2 A_1 \\ \vdots \\ -\alpha\Delta^2 A_{N-1} \\ 0 \end{bmatrix} \tag{29}$$

where

$$a = A_i + \frac{\Delta}{2}\left(A_{i-1} - A_{i+1}\right) \tag{30}$$

$$b = -2A_i \tag{31}$$

$$c = A_i + \frac{\Delta}{2}\left(A_{i+1} - A_{i-1}\right) \tag{32}$$

Setting the first and last entries in the tri-diagonal matrix to 1, and the first and last entries in the constant matrix to 0, produces the boundary conditions $u_0 = 0$ and $u_N = 0$. N is the number of points between 0 and h with the interval Δ.

This method is consistent for each shape, with A_i being the cross-sectional area at a distance x from the top of the lung. For the horizontal cylinder, the cross-sectional area will be a rectangle with the area

$$A(x) = 2L\sqrt{x(h-x)} \tag{33}$$

For the cone, when turned to it's side the function for cross-sectional area becomes more complex such that

$$A(x) = \begin{cases} L\frac{h}{2}\left(\sqrt{1-k_1^2} - k_1^2 cosh^{-1}\frac{1}{k_1}\right), & x < \frac{h}{2}. \\ \frac{Lh}{2}, & x = \frac{h}{2}. \\ L\frac{h}{2}\left(\sqrt{1-k_2^2} - k_2^2 cosh^{-1}\frac{1}{k_2}\right), & x > \frac{h}{2}. \end{cases} \tag{34}$$

Where $k_1 = 1 - 2\frac{x}{h}$ and $k_2 = 1 - 2\frac{h-x}{h}$.

Similarly for the truncated cone in the horizontal position

$$A(x) = \begin{cases} L(b-t)\left(\sqrt{1-k_1^2} - k_1^2 cosh^{-1}\frac{1}{k_1}\right), & x < b-t. \\ \frac{L}{2}\left(2\sqrt{t^2-(b-x)^2} + 2\sqrt{b^2-(b-x)^2}\right), & b-t \le x \le b+t \\ L(b-t)\left(\sqrt{1-k_2^2} - k_2^2 cosh^{-1}\frac{1}{k_2}\right), & x > b+t. \end{cases} \tag{35}$$

where $k_1(x) = 1 - \frac{x}{b-t}$ and $k_2(x) = 1 - \frac{2b-x}{b-t}$. These can then be solved as a series of linear equations, using the Tridiagonal Matrix Algorithm (TMA) often referred to as the Thomas algorithm - a streamlined version of Gaussian elimination specifically designed for tridiagonal matrices. It performs a forward elimination followed by back substitution in linear time, making it ideal for large one-dimensional problems.

4.6 Comparing Deformation For Each Shape

In order to choose the most physiologically accurate shape to take forward in this project, each shape is compared in both the upright and supine position. Making the model as effective as possible for clinical decision making relies on a deformation simulation method that most accurately mimics results collected from patients in previous studies.

Figure 9 shows the deformation from the original position in mm for each shape in both the upright and supine positions. One clear observation from the graphs is that deformation levels are consistent between shapes in the supine

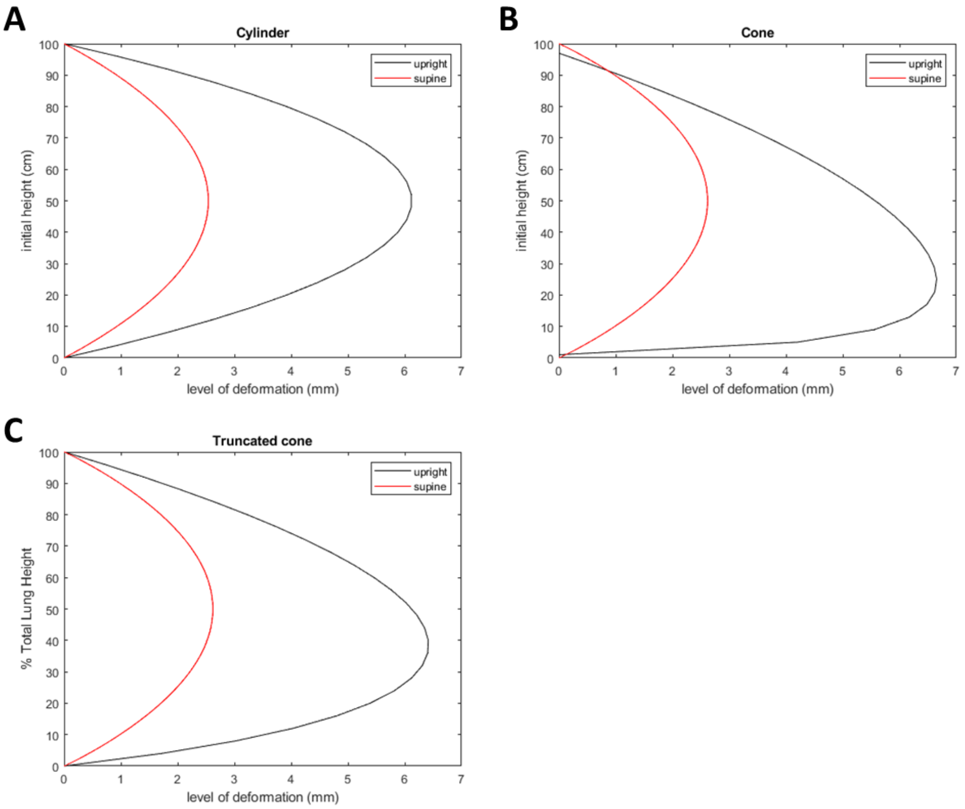

Figure 9: Alveolar deformation from original position against gravity (mm), in the upright (black) and supine (red) positions. **A** represents the cylinder analogy, **B** represents the cone analogy and **C** represents the truncated cone analogy.

position. This is due to the shapes all being symmetrical about their midline when placed horizontally. Deformation is maximal at 50% of total lung height, with roughly a $2.5mm$ displacement downwards. There is a much more noticeable difference between the shapes in the upright position. The constant cross-section of the cylinder results in a symmetrical deformation curve, with maximal displacement of $6mm$ occurring at 50% of total lung height. This is not what we would expect of the lung under the Slinky Effect [23,24,25], in which we expect to see a bottom heavy deformation curve. The cone shape results in the bottom heavy curve as expected, with a far more skewed displacement. Maximal displacement is 6.75mm occurring at 25% of total lung height. It must be noted that due to the boundary condition for the cone being set at 1cm from the apex (as discussed previously), the deformation curve does not start at 100% of total lung height, which may produce inaccurate results. For the truncated cone in the upright position, deformation is slightly skewed towards the bottom of the lung, but to a lesser extent than the cone. Maximal displacement is 6.5mm at 40% of total lung height. In order to choose the most physiologically accurate shape for the model, these curves must be compared to data collected in humans. Tissue displacement due to gravity is impossible to directly measure without comparing to a gravity-free environment, but can be assessed by measuring regional tissue density of the lung.

As a representation of regional tissue density, the model was used to calculate the number of alveolar units at a particular height up the lung. The lung was separated into cm increments, with 100 alveolar units per cm spread uniformly before the addition of gravity. When gravity was added, the new positions of each alveolar unit was calculated and the number in each cm of lung height was recorded. Note, the actual number of alveoli in the human lungs can vary from 274-790 million [52]. In order to model the alveoli effectively as a 1-D approximation, a single alveolar unit represents all the alveoli within the same iso-gravitational plane.

Figure 10A illustrates the number of alveolar units at each level of the total lung height for the three shapes in the upright position. To compare with this, Figure 10B is taken from a 2007 paper by Hopkins et al [13], in which the regional tissue density of a human subject was calculated from MRI imaging. Included here are the range of densities within a single iso-gravitational plane, and the average density in a single plane. The cylinder results in a large number

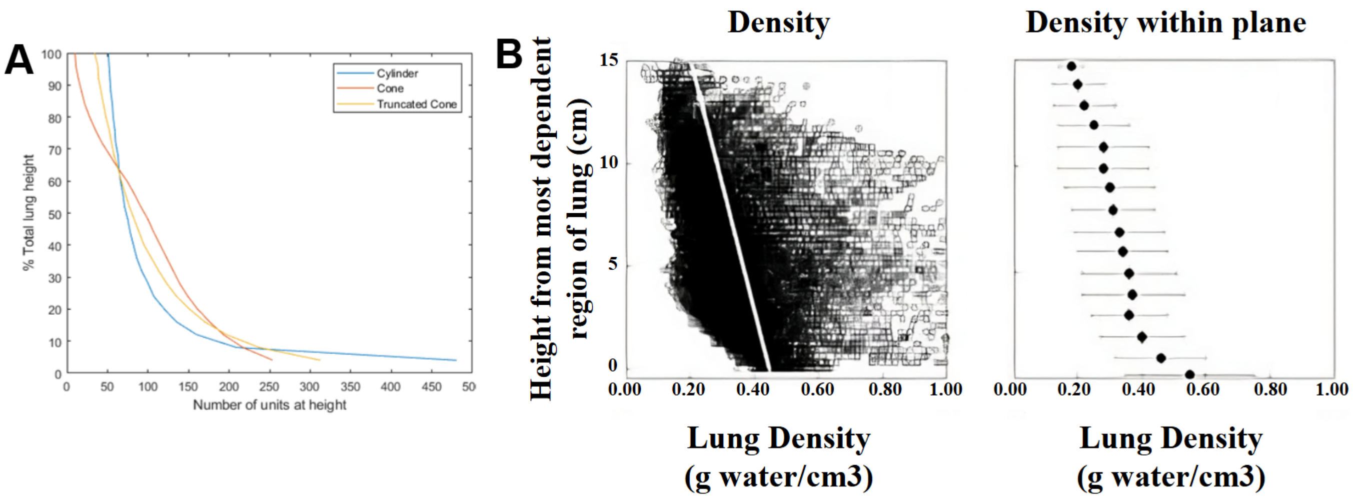

Figure 10: Comparison of regional lung characteristics in the upright position. **A** displays the model's calculated number of alveolar units per cm of total lung height for the cylinder, cone, and truncated cone analogies. **B** presents data from Hopkins et al. [13] on the regional density of lung tissue in a human subject, derived from MRI imaging. The truncated cone analogy (A) most accurately reflects the physiological distribution seen in human data (B).

of alveoli being present in the bottom 10% of the lung, significantly more than is observed in the human subject or the other two shapes. The cone can be seen to give an extremely small number of alveolar units in the top $10 - 20\%$ of the lung, which is physiologically inaccurate when Figure 10B is used as a comparison. The most accurate shape is the truncated cone, which does not show the extremes at the top and bottom of the lung. When this result is combined with the deformation curves, it becomes clear that the truncated cone represents the most physiologically relevant model and as such will be the one used going forward.

The truncated cone model is used to determine the new height of each alveolar unit, as the initial distance from the top of the lung ($x$cm), added to the level of displacement downward due to gravity ($u(x)$mm). This gives the new height as:

$$i = x + u(x) \tag{36}$$

where i is the index for the new alveolar height.

4.7 Prone position

The current model framework does not contain a distinction between Supine and Prone positions, instead modelling the overall mechanics of the lung perpendicular to gravity. Therefore, equations must be expanded to replicate the observed differences between these horizontal positions. From the literature review of this thesis, the observable changes from supine to prone position have been discussed, with the primary finding being the differing uniformity of certain mechanics. When compared to the supine position, prone position is found to reduce the level of alveolar distension in the ARDS lung [17], resulting in a more uniform distribution of ventilation and perfusion across all tissue [24]. Aside from the external pressures of the chest wall and organ placement, Tawhai in 2009 attributed this uniformity to a more consistent elastic gradient in prone position [10]. To model deformation in the proned lung, the tissue elasticity is to be made non-constant, such that this relationship can be replicated.

Taking the initial derived bar equation as in 12, a non-constant cross-sectional area will be set according to the truncated cone reference shape, proven the most physiologically accurate analogy in Figures 9 and 10. Tissue elasticity (E) is now also variable in space, and so must be reassessed as a function of x. This gives the new bar equation as

$$\frac{d}{dx}\left(E(x)A(x)\frac{du}{dx}\right) + \rho g A(x) = 0 \tag{37}$$

Which expanded becomes

$$E^{'}Au^{'} + EA^{'}u^{'} + EAu^{''} + \rho g A = 0 \tag{38}$$

As before, using the second order centred finite difference method to assess the equation at x_i with interval Δ gives

$$\begin{aligned} &A_iE_i\left(\frac{u_{i+1} - 2u_i + u_{i-1}}{\Delta^2}\right) + E_i\left(\frac{A_{i+1} - A_{i-1}}{2\Delta}\right)\left(\frac{u_{i+1} - u_{i-1}}{2\Delta}\right) + \\ &A_i\left(\frac{E_{i+1} - E_{i-1}}{2\Delta}\right)\left(\frac{u_{i+1} - u_{i-1}}{2\Delta}\right) = -\alpha A_i \end{aligned} \tag{39}$$

This can be rewritten in matrix form as:

$$\begin{bmatrix} 1 & 0 & 0 & \cdots & 0 \\ a & b & c & \cdots & 0 \\ & \ddots & \ddots & \ddots & \\ 0 & \cdots & a & b & c \\ 0 & \cdots & 0 & 0 & 1 \end{bmatrix} \begin{bmatrix} u_0 \\ u_1 \\ \vdots \\ u_{N-1} \\ u_N \end{bmatrix} = \begin{bmatrix} 0 \\ -\alpha\Delta^2 A_1 \\ \vdots \\ -\alpha\Delta^2 A_{N-1} \\ 0 \end{bmatrix} \tag{40}$$

where

$$\begin{aligned} a &= A_iE_i - \frac{\Delta}{2}\left(A_i\left(E_{i+1} - E_{i-1}\right) + E_i\left(A_{i+1} - A_{i-1}\right)\right) \\ b &= -2A_iE_i \\ c &= A_iE_i + \frac{\Delta}{2}\left(A_i\left(E_{i+1} - E_{i-1}\right) + E_i\left(A_{i+1} - A_{i-1}\right)\right) \end{aligned}$$

As before, setting the first and last entries in the tri-diagonal matrix to 1, and the first and last entries in the constant matrix to 0, produces the boundary conditions $u_0 = 0$ and $u_N = 0$. Using the horizontal cross-sectional area for the

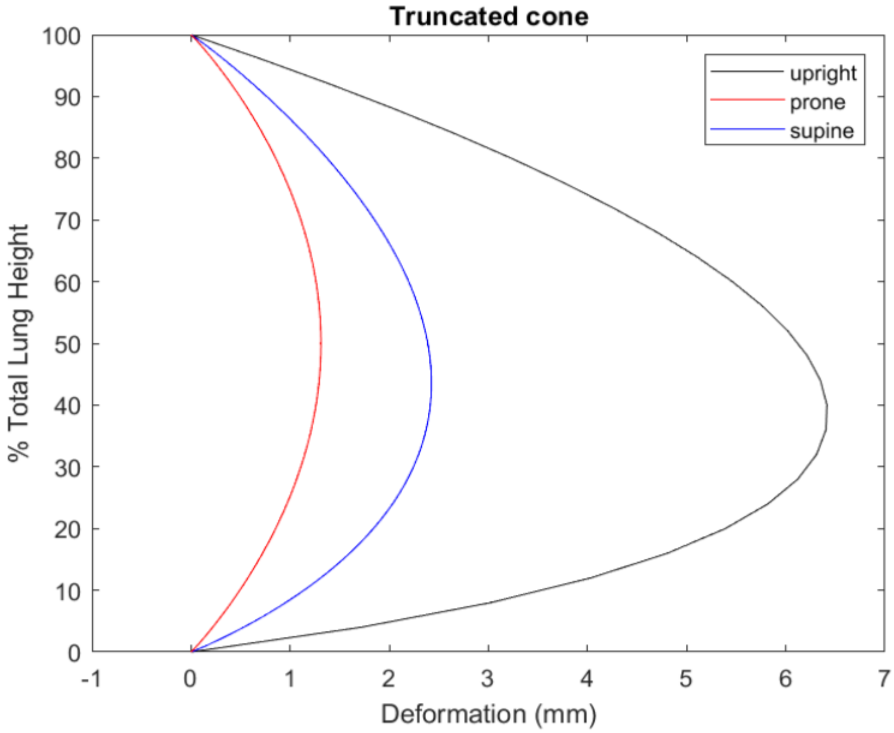

Figure 11: Alveolar deformation from original position against gravity (mm), in the upright (black) and supine (blue) and prone (red) positions, using the truncated cone shape analogy.

truncated cone as in 35. In order to differentiate between supine and prone elasticity, E is set to 1 for all values of x in prone position, and as a linear gradient from 0 to 1 in supine. This is based on experimental findings which suggest lung tissue elasticity is more uniform in the prone position than in the supine, such as in mechanically ventilated pigs [53] and estimates for multidetector row computed tomography imaging in humans [10]. The system of equations created in the matrix notation are again solved using the Tridiagonal Matrix Algorithm (Thomas algorithm).

Figure 11 depicts the deformation from the reference position of the lung against gravity in the upright, supine and prone positions. There are two main observations that can be made for prone position. Firstly, the overall level of deformation is significantly shorter, reaching a maximum displacement half of that in the supine position. The other observation is that the shape of the deformation curve is more uniform in the prone position, not displaying the obvious bottom-heavy curve as seen in the upright position.

Petersson et al. (2007), a study on healthy volunteers, utilized quantitative Single Photon Emission Computed Tomography (SPECT) with fixed radiotracers to assess how changes in posture affect regional lung tissue distribution [54]. Their research explicitly concluded that a change from the supine to the prone posture primarily causes a change in the vertical distribution of lung tissue. Quantitatively, they found that the gradient in lung density was consistently smaller in the prone posture compared to supine, with mean gradients of 0.027 in prone versus 0.051 in supine. This demonstrates that the density gradient in the prone posture was approximately half the magnitude of the supine gradient, directly aligning with the static model prediction that prone deformation is roughly half that of supine. The smaller density gradient in prone also indicates a more uniform tissue distribution, as seen in the model.

Tawhai et al. (2009) further validates these points through finite-element analysis of human lung mechanics, deliberately isolating the effect of gravity by modelling the prone lung as a gravity-reversed supine shape, thereby excluding confounding factors like heart or diaphragm displacement [10]. Their simulations confirmed that the magnitude of the density gradient in the supine lung was nearly twice as large as for the prone lung (e.g., Subject 1 showed $-4.33\%/cm$ in supine vs. $-2.72\%/cm$ in prone; Subject 2 showed $-4.96\%/cm$ in supine vs. $-2.51\%/cm$ in prone). Importantly, they observed that displacements due to gravity in the prone model were smaller than prone throughout most of the tissue compared to supine. Their findings also explicitly state that an underlying feature of the normal lung in the prone posture is a more uniform density distribution and less heterogeneity in density or elastic recoil pressure than when in the supine posture. This provides strong empirical and conceptual backing for the modelling assumption that tissue elasticity is more uniform in the prone position, leading to the observed smoother and less exaggerated deformation curve in Figure 11.

4.8 Alveolar Ventilation

Each alveolar unit now has a distinct location, with parameters relative to its vertical height against gravity. These parameters can then be used to calculate regional ventilation across the lung. To ensure that this model can be easily integrated into a larger model of mechanical ventilation, such as a digital twin, calculations are made using equations similar to those found in the literature. Set values were taken from a theoretical "healthy patient", not affected by ARDS or other pulmonary conditions [55].

For a single alveolar compartment i, the ventilation is defined as the volume of air moving in/out of the i^{th} alveolus in a single sampling interval. This is calculated as:

$$Flow_{comp_i} = \frac{P_{Trachea} - P_{comp_i}}{R_{UpperAirway} + R_{comp_i}} \tag{41}$$

where $P_{Trachea}$ is the tracheal pressure and is set to $100cmH_20$, $R_{UpperAirway}$ is the upper airway resistance and is set to $0.004kPaL^{-1}min^{-1}$, R_{comp_i} is the inlet resistance of the i^{th} compartment and is set to $0.001kPaml^{-1}min^{-1}$, in accordance with the "healthy patient" subject. P_{comp_i} is determined as

$$P_{comp_i} = ST_{alv_i} \left(V_{comp_i} - V_{col}\right)^2 - P_{ext_i} \tag{42}$$

Here ST_{alv_i} is the stiffness of the i^{th} alveolar compartment and is set to $0.05cmH_20$. V_{col} is the constant collapse volume of the unit, i.e. the volume threshold at which the unit closes, and is set to $6ml$. V_{comp_i} is the volume of air inside the i^{th} alveolar unit, and P_{ext_i} is the external pressure applied to the i^{th} compartment, which are determined by the displacement model.

4.9 Alveolar Perfusion

As with alveolar ventilation, alveolar perfusion can also be calculated using parameters derived from the displacement model. As before, set values are chosen in accordance to the "healthy patient" subject model.

For a single alveolar compartment i, the perfusion is defined as the volume of blood passing through the i^{th} capillary unit in a single sampling interval. This can be calculated as:

$$Q_{comp_i} = \frac{CO_{non-shunted} \cdot PVR_{total}}{Ri} \tag{43}$$

where $CO_{non-shunted}$ is the non-shunted bloodflow, PVR_{total} is the total pulmonary vascular resistance, and Ri is the resistance of the i^{th} capillary unit. Although an accurate equation, this version does not allow the integration of elements seen to influence regional perfusion in the literature, and as such has been modified for better manipulation of displacement-influenced variables. The perfusion equation used is instead

$$Q_{comp_i} = \frac{\Delta P}{Ri} \tag{44}$$

Here bloodflow to the i^{th} capillary unit is determined by the dominant pressure gradient ΔP between the pulmonary artery P_a, the pulmonary vein P_v, and the i_{th} alveolar unit P_{comp_i}. Pulmonary arterial and venous pressures are set using a hydrostatic gradient vertically down the lung. This phenomena is well observed [7] and values are set to linear gradients $7-24mmHg$ and $6-12mmHg$ from apex to base for P_a and P_v respectively. The dominant pressure gradient is determined by the inequalities defined by West, such that the bloodflow in the i_{th} capillary unit is calculated by the difference between the two interacting pressures in a a particular zone. This is defined as:

$$Q_{comp_i} = \begin{cases} 0, & \text{if } P_{comp_i} > P_a > P_v. \\ \frac{P_a - P_{comp_i}}{PVR_{comp_i}}, & \text{if } P_a > P_{comp_i} > P_v. \\ \frac{P_a - P_v}{PVR_{comp_i}}, & \text{if } P_a > P_v > P_{comp_i}, \end{cases} \tag{45}$$

which is in accordance with West's Zones of the lung [21]. When alveolar pressure is larger than pulmonary arterial and venous pressures, the capillary collapses and so bloodflow is zero. When pulmonary arterial pressure exceeds alveolar pressure, but pulmonary venous pressure does not, bloodflow is determined by the gradient between the pulmonary artery and the capillary unit. Finally, when both pulmonary arterial and venous pressures exceed alveolar pressure, bloodflow is simply determined by the gradient between the pulmonary artery and vein.

4.10 V/Q Ratio

As discussed earlier in the literature review section of this report, ventilation-perfusion matching is an observable parameter often used by clinicians to monitor lung condition [56]. Given that ventilation and perfusion have been determined as above, the ventilation-perfusion ration can simply be calculated as:

$$\left(\frac{V}{Q}\right)_{comp_i} = \frac{Flow_{comp_i}}{Q_{comp_i}} \tag{46}$$

4.11 Results

Figure 12 displays various indicators of lung function relative to patient positioning and percentage of total lung height. Note, results are displayed relative to the average value across the lung, for a clearer visual representation of changes due to height up the lung (1 on the x axis represents the average). The relative volume of the alveolar units is shown in Figure 12A. In all positions, alveoli are smaller towards the base of the lung, as is expected from the Slinky Effect [12, 13, 38], however the range in alveolar sizes varies significantly. In the upright position, the bottom 45% of the lung is comprised of much smaller than average alveoli, with the bottom 30% being over half the size of average. On the other hand, from 60% of total lung height upwards, alveolar size increases drastically from double the average volume to 6 times the average volume. This is consistent with the large distension expected at the apex of the lung. In supine position, alveolar unit volumes are far more consistent, increasing to only 2.5 times the average volume at the apex of the lung. This observation is even more prominent in the prone position, in which alveolar size varies only 50% from the average.

The model's demonstration of significantly smaller alveoli at the lung base in the upright position, coupled with drastic over-distension at the apex, provides a crucial static baseline for understanding regional lung injury risk. In the ICU, this gravitational predisposition suggests that dependent lung regions may be more prone to collapse (atelectasis) and derecruitment, while non-dependent regions face higher risk of over-distension and subsequent ventilator-induced lung injury (VILI) even before dynamic breathing is considered. The greater uniformity in alveolar size observed in supine and, especially, prone positions highlights why these postures are clinically favoured to mitigate such regional disparities and promote more homogeneous lung mechanics.

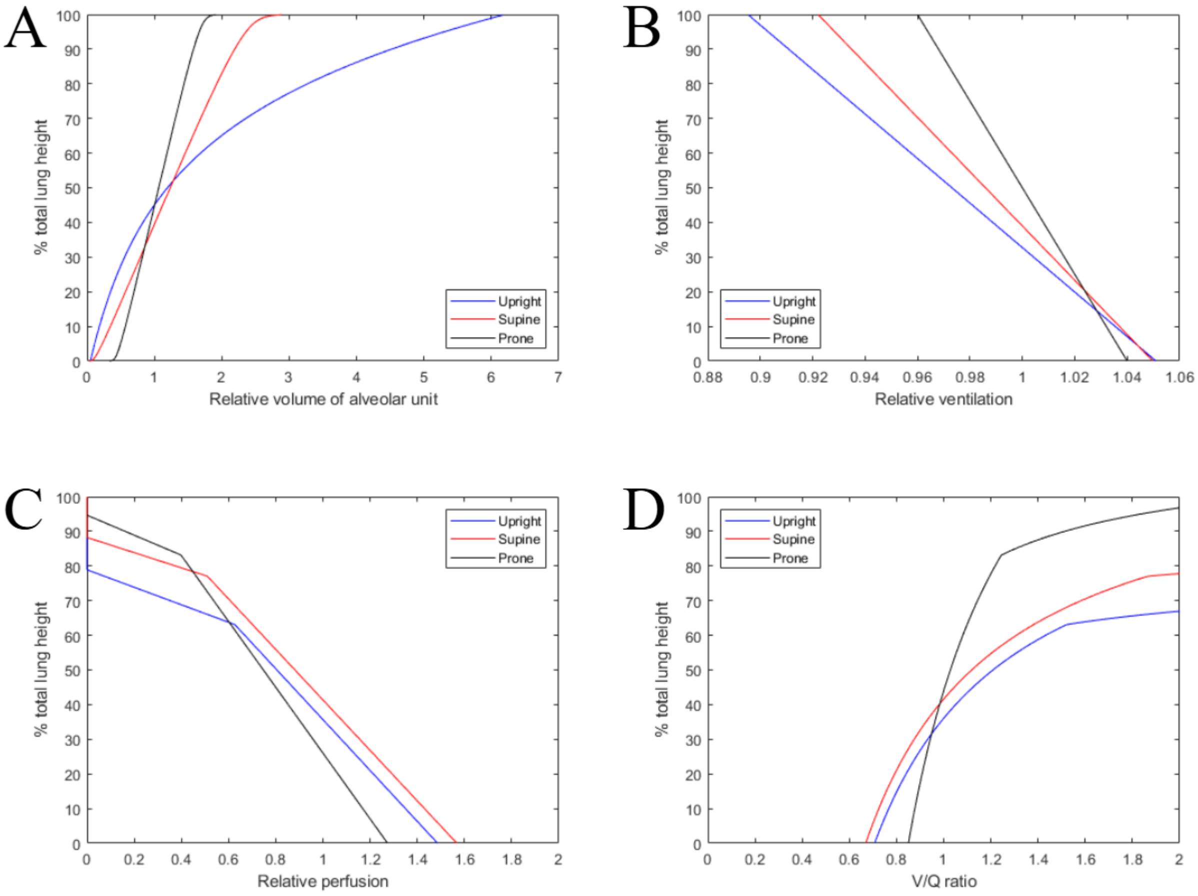

Figure 12: Comparison of lung function between upright,supine and prone positions. **A** displays the relative volume of each alveolar unit. **B** displays the relative ventilation of each alveolar unit. **C** displays the relative perfusion of each alveolar unit. **D** displays the ventilation-perfusion ratio as a function of total lung height.

Figure 12B displays the relative ventilation of the alveolar units across the lung height. The primary difference between positions is the variation from the average ventilation, which is noted here as the mean ventilation value across the whole lung height. For upright this is from 90% of the average at the apex of the lung, to 105% at the base. For supine position, variation is slightly smaller, from 94% at the apex to 105% at the base. For prone position, the smallest variation in ventilation is seen, from 97% at the apex to 104% at the base. In each case, this gradient of increasing ventilation towards the base of the lung is to be expected [24, 25, 57].

Figure 12C displays the relative perfusion of the alveolar units across the lung height. For all positions, the three Zones of the lung [7, 21] can be clearly seen. Zone 1, in which no blood flow can occur, exists at the apex of the lung, with Zone 2 towards the centre and Zone 3 at the base. The positioning differences are seen at the heights at which these zones occur. In the prone position, Zone 1 is smallest, only seen in the top 5% of the lung compared to 10% in the supine position and 20% in the upright position. This is of significant importance, as Zone 1 is expected only to occur during mechanical ventilation [58], and therefore minimising this zone will reduce the number of un-perfused alveoli and increase gas-exchange. In all positions, Zone 2 occurs for roughly 10% of the total lung height. Zone 3 is seen through the bottom 85% in the prone position, 80% in the supine position and the bottom 65% in the upright position. In this zone there is a clear linear relationship between lung height and perfusion as is expected [7]. In prone position, this gradient is steeper, meaning a more uniform perfusion throughout the lung. The main finding of this simulation is that prone position results in more of the lung being well-perfused, with more consistent perfusion levels across the lung.

Finally, Figure 12D shows the ventilation-perfusion ratio across the lung. The theoretical ideal ventilation-perfusion ratio is 1, such that blood flow and air flow are equal and maximal gas exchange can occur [56]. Although 1 is considered a theoretical ideal, in healthy individuals the average ratio is closer to 0.8 [59]. This of course, is not constant across the entirety of the lungs, but is expected to occur at roughly 50% of total lung height. This can be seen accurate in all positions. Due to the mechanical ventilation used in this simulation, perfusion is zero at the top of the lung, and as such the ventilation-perfusion ratio is undetermined, resulting in the curve tapering off at 85% total height in prone 75% total height in supine and 65% total height in upright.

4.12 Concluding Remarks

This chapter established a crucial foundation for the thesis by introducing the mathematical modelling framework through the lens of gravity-induced static deformation of deflated lung tissue. Before progressing to the complex dynamics of breathing and mechanical ventilation, it was essential to first isolate and understand the passive mechanical effects of gravity.

To address the limitations of simplistic discrete models—such as mass-spring systems, which fail to capture continuous tissue behaviour, a continuum approach grounded in solid mechanics was employed. This led to the derivation of the Bar Equation, offering improved physiological accuracy and computational efficiency for describing deformation along isogravitational planes. A central goal was to compare three simplified lung geometries—cylinder, cone, and truncated cone—across multiple body positions (upright, supine, prone), enabling selection of the most anatomically faithful model for use in later dynamic simulations.

The static model developed here is particularly relevant for passive or sedated patients, such as those under mechanical ventilation, general anaesthesia, or neuromuscular blockade. In these contexts, gravitational pre-deformation of lung tissue significantly affects subsequent mechanical behaviour. By quantifying spatial strain heterogeneity across different postures, this chapter provides a mechanistic explanation for observed clinical phenomena such as regional ventilation-perfusion mismatch and dependent collapse. These insights support early interventions, such as pre-emptive prone positioning, to distribute stress more evenly and preserve alveolar integrity from the outset of care.

While the model is less applicable to awake, spontaneously breathing patients, where diaphragm motion, chest wall mechanics, and muscular compensation play major roles, it nevertheless offers a baseline understanding of the passive gravitational component shaping lung configuration in all individuals.

Beyond ARDS management, this framework has implications for surgical positioning and secretion clearance. In procedures requiring prolonged prone or lateral decubitus positioning, understanding deformation patterns can guide posture to preserve pulmonary function. Similarly, gravitational effects on tissue shape impact mucus distribution; prone positioning can enhance drainage from posterior regions, offering therapeutic value in diseases such as bronchiectasis or cystic fibrosis.

The chapter's novelty lies in its systematic evaluation of simplified lung geometries under gravitational load across multiple postures, setting it apart from prior models such as the spring-mass system by Swan et al [38]. This comparative analysis informs both the anatomical assumptions and governing equations for the advanced poroelastic models that follow. By explicitly linking posture, geometry, and gravitational mechanics in a static state, this work forms a coherent and physiologically grounded precursor to dynamic respiratory modelling and reinforces the thesis's broader emphasis on patient positioning as a determinant of lung function.

5 Linear Poroelastic Lung Model

5.1 Introduction

Building upon the static analysis of lung deformation, this chapter introduces a dynamic framework using linear poroelasticity to model the lung's mechanical behaviour. The objective is to establish a basic poroelastic model that couples solid tissue deformation with fluid (air) flow, capable of simulating lung dynamics across the breathing cycle and assessing the initial effects of patient positioning. I hypothesize that a linear poroelastic approach, despite its simplifications, can effectively represent the fundamental interaction between lung tissue and airflow, offering initial insights into how gravity and posture influence internal lung pressures and displacements during ventilation. The central clinical question explored is: Can a simplified (linear) poroelastic model adequately capture how patient positioning affects lung deformation and internal pressures throughout the breathing cycle, and how do these effects compare across upright, supine, and prone postures? This phase is essential as it transitions from a static understanding to a dynamic system, providing a preliminary computational tool to explore time-dependent lung function under mechanical ventilation.

Poroelasticity is a field in mechanics which defines a material as consisting of two separate phases, a deformable solid skeleton interspersed with fluid filled pores [39]. The efficacy of using a poroelastic approach to model soft tissues has been well-established in recent years, and is now being used to explore full organ systems such as the lungs [42, 43, 44, 46]. Further details of this have been discussed previously in the Literature Review section of this thesis. In this chapter, I will establish the basis for a poroelastic model of the lung using linear relationships, before expanding into different patient positions across the breathing cycle.

5.2 Terzaghi's Problem

The poroelastic framework has been used in the field of geomechanics with great success since the early 20^{th} century. In 1923, Terzaghi posited his theory of consolidation, stating that deformations in an element of soil were controlled solely by the flow of fluid through the pores between the solid particles, resulting in both the solid and fluid portions of the system being incompressible [40]. He modelled this as a one-dimensional linear problem, providing a starting point to explore a better understanding of the one-dimensional lung deformation model.

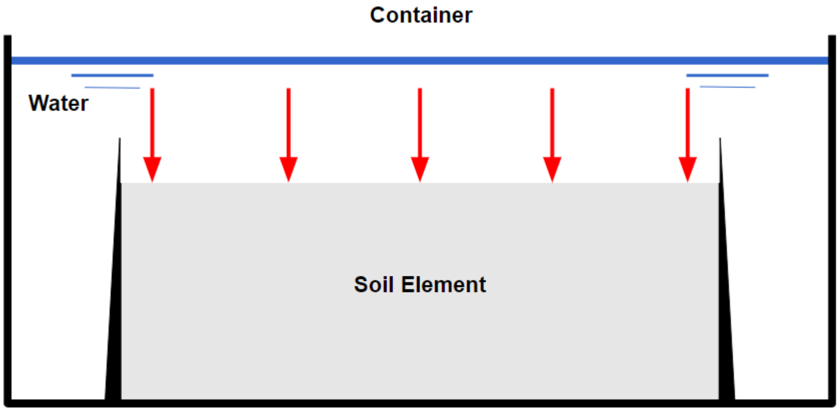

Figure 13: Visual representation of Terzaghi's consolidation problem, depicting a soil sample confined by an impermeable ring with a closed base. The sample is submerged in water, allowing fluid to drain freely from its exposed upper boundary, and subjected to a constant perpendicular stress.

Terzaghi's consolidation problem is set out as follows: a soil sample is confined by an impermeable ring with a closed base, such that there is only one direction for displacement to occur. This ring is then submerged into a container of water, allowing water to be in direct contact with the exposed boundary of the soil. The boundary is said to be fully drained, meaning water is allowed to escape freely. The soil sample is loaded at this boundary with constant perpendicular stress. A visual representation of this can be seen in Figure 13.

In modelling the lung as a poroelastic organ, particularly in scenarios involving interstitial fluid dynamics such as pulmonary oedema or mechanical ventilation, it is instructive to draw on analogies from classical porous media theory. In Terzaghi's consolidation problem, an applied external load is initially supported by the pore fluid, resulting in elevated pore pressure. As fluid slowly drains through permeable boundaries, the pore pressure dissipates and the load is gradually transferred to the soil skeleton, causing consolidation. This process mirrors the behaviour of lung parenchyma when conceptualized as a saturated, deformable "wet sponge": the tissue matrix (analogous to the soil skeleton) is immersed in interstitial fluid, and under external loading—such as gravity, postural changes, or ventilator-induced pressures—fluid pressure initially increases within the lung. Over time, interstitial fluid redistributes or drains (via lymphatic pathways or local permeation), and the mechanical load is transferred to the tissue structure itself. Key parameters in both systems—such as permeability, compressibility of the solid matrix, and fluid viscosity—govern the rate and pattern of pressure dissipation and deformation. Thus, by demonstrating Terzaghi's problem within a mathematical lung model, we capture the essence of time-dependent fluid-structure interactions, providing a physically grounded framework to explore pulmonary mechanics under both physiological and pathological conditions.

This is an example of confined compression, and should result in fluid being expelled from the soil element. This system can be mathematically represented using the storage equation.

$$\alpha \frac{\partial \varepsilon}{\partial t} + S \frac{\partial p}{\partial t} = \nabla \frac{\kappa}{upsilon} \left(\nabla p - \rho_f \underline{g} \right) \tag{47}$$

where α is Biot's coefficient, ε is the volume change of the solid material, S is the storativity of the system, p is the pore pressure, κ is the permeability coefficient, υ is the unit weight of the fluid, ρ_f is the density of the pore fluid, and $\underline{g}$ is the applied force vector. ∇ is shorthand for $\frac{\partial}{\partial z}$. As the soil is confined on all but one side, the applied force vector can be assumed to be a gravitational force in z, such that

$$\underline{g} = \begin{bmatrix} 0 \\ 0 \\ -g \end{bmatrix} \tag{48}$$

Assuming flow only on the vertical z axis, 47 becomes

$$\alpha \frac{\partial \varepsilon}{\partial t} + S \frac{\partial p}{\partial t} = \nabla \frac{\kappa}{\upsilon} (\nabla p) \tag{49}$$

For a one-dimensional problem, the volume change of the system is equal to the vertical strain. As the system is linear, the elastic behaviour of the material can be assessed using the vertical effective stress as

$$\frac{\partial \varepsilon}{\partial t} = -\frac{1}{K + \frac{4}{3}G} \left(\frac{\partial \sigma_{zz}}{\partial t} - \alpha \frac{\partial p}{\partial t} \right) \tag{50}$$

where K is the compression modulus of the porous medium, G is the shear modulus of the porous medium and σ_{zz} is the total stress of the system. Substituting this into 49 gives

$$\left(S + \alpha^2 \frac{1}{K + \frac{4}{3}G} \right) \frac{\partial p}{\partial z} = \alpha \cdot \frac{1}{K + \frac{4}{3}G} \cdot \frac{\partial \sigma_{zz}}{\partial t} + \frac{\partial}{\partial z} \left(\frac{\kappa}{\upsilon} \cdot \frac{\partial p}{\partial t} \right) \tag{51}$$

this is the general equation for consolidation in one-dimension.
For Terzaghi's problem, at time $t = 0$, a vertical load is applied of magnitude q. For $t > 0$, σ_{zz} is constant and so 51 simplifies to

$$\frac{\partial p}{\partial t} = c_v \frac{\partial^2 p}{\partial z^2}, \tag{52}$$

where c_v is the consolidation coefficient such that

$$c_v = \frac{\kappa}{\upsilon\left(S + \alpha^2 \cdot \frac{1}{K+\frac{4}{3}G}\right)} \tag{53}$$

For the initial condition, assumed to be at the moment of loading, there has not yet been any fluid lost from the soil. This gives the condition

$$t = 0: \quad p = p_0 = B \cdot q = \frac{\alpha \cdot \frac{1}{K+\frac{4}{3}G}}{S + \alpha^2 \cdot \frac{1}{K+\frac{4}{3}G}} \cdot q \tag{54}$$

where B is Skempton's coefficient. Boundary conditions need to be defined at the base of the soil, $z = 0$, and at the top free-boundary of the soil, $z = h$. Boundary conditions are

$$t > 0, z = 0 : \frac{\partial p}{\partial z} = 0 \tag{55}$$

$$t > 0, z = h : p = 0 \tag{56}$$

With the initial problem set up, the system can now be solved. We begin by taking the Laplace transform as suggested by Carslaw and Jaeger in 1948 [60].

$$\overline{p} = \int_0^\infty p e^{-st}\, dt \tag{57}$$

that transforms the one-dimensional consolidation equation 51 into

$$\frac{d^2\overline{p}}{dz^2} = \lambda^2 \left(\overline{p} - \frac{p_0}{s}\right) \tag{58}$$

where $\lambda^2 = \frac{s}{c_v}$. The solution of this equation will be in the form

$$\overline{p} = \frac{p_0}{s} + Acosh(\lambda z) + Bsinh(\lambda z) \tag{59}$$

where A and B are integration constants. From the boundary conditions set up in 55 we can calculate constants as

$$t > 0, z = 0, \frac{\partial p}{\partial z} = 0 : B = 0 \tag{60}$$

$$t > 0, z = h, p = 0 : A = -\frac{p_0}{cosh(\lambda h)} \tag{61}$$

Giving the solution as

$$\overline{p} = \frac{p_0}{s} - \frac{p_0}{s} \cdot \frac{cosh(\lambda z)}{cosh(\lambda h)} \tag{62}$$

To invert the transformed solution, Churchill in 1972 suggested using the complex inversion integral

$$p = \frac{1}{2\pi i} \int_{\gamma - i\infty}^{\gamma + i\infty} p \cdot e^{st} \, ds \tag{63}$$

with γ set to insure there are no singularities to the right of the integration [61].

This integral can be can be calculated by using a half-circle closed contour to the left of the integration path, as dictated by Churchill. Assuming that the integrand is singular, and that half-circle itself does not contribute to the integral solution. Using residue-theorem, the integral can be defined as the sum of the poles within the contour such that

$$p = \sum_{\psi}^{N} R \left\{ \overline{p} e^{st} \right\} \tag{64}$$

where R is the corresponding residue. Finding the poles of 62 requires looking at the terms separately. The first term is simple in that it has one pole at $s = 0$ with a residue of p_0. The second term also has a pole at $s = 0$ with a residue of $-p_0$, cancelling out the residue of the first term. The second has poles at all zeros of $cosh(\lambda h)$:

$$\lambda_\psi = \pm \left(2\psi - 1\right) \frac{i\pi}{2h} \tag{65}$$

$$s_\psi = - \left(2\psi - 1\right)^2 \frac{c\pi^2}{4h^2} \tag{66}$$

For all positive integer values of ψ.

For the simple pole at $s = s_\psi$, the residue can be defined

$$R_\psi = \left\{ -\frac{p_0 \cosh(\lambda x) e^{st}}{\frac{d}{ds} s \cdot \cosh(\lambda h)} \right\}_{s=s_\psi} \tag{67}$$

Evaluating the differential and using the poles at the zeros of $\cosh(\lambda h)$, the residue becomes

$$R_\psi = \frac{4p_0}{\pi} \cdot \frac{(-1)^{\psi-1}}{2v-1} \cdot \cos\left((2\psi - 1)\frac{z\pi}{2h}\right) \cdot e^{-(2\psi-1)^2 \cdot \frac{c_v t \pi^2}{4h^2}} \tag{68}$$

Using the definition set in 64, the final solution can thus be taken in the standard used form of p/p_0 as

$$\frac{p}{p_0} = \frac{4}{\pi} \sum_{\psi=1}^{\infty} \frac{(-1)^{\psi-1}}{2\psi - 1} \cdot \cos\left((2\psi - 1)\frac{z\pi}{2h}\right) \cdot e^{-(2\psi-1)^2 \cdot \frac{c_v t \pi^2}{4h^2}} \tag{69}$$

Figure 14 shows the analytical solution for Terzaghi's problem for varying values of the time parameter $\frac{c_v t}{h^2}$. The relative change in pore pressures p/p_0 are plotted against the relative height of the pore z/h. For reference the top of the soil sample is at $z/h = 1$ and the base at $z/h = 0$. This shows that the relative pressure of the pores is higher towards the base of the sample, as is expected [62]. The other interesting observation from this graph, is that as $\frac{c_v t}{h^2}$ increases, pore pressures have been reduced to almost zero, suggesting the sample has been fully consolidated.

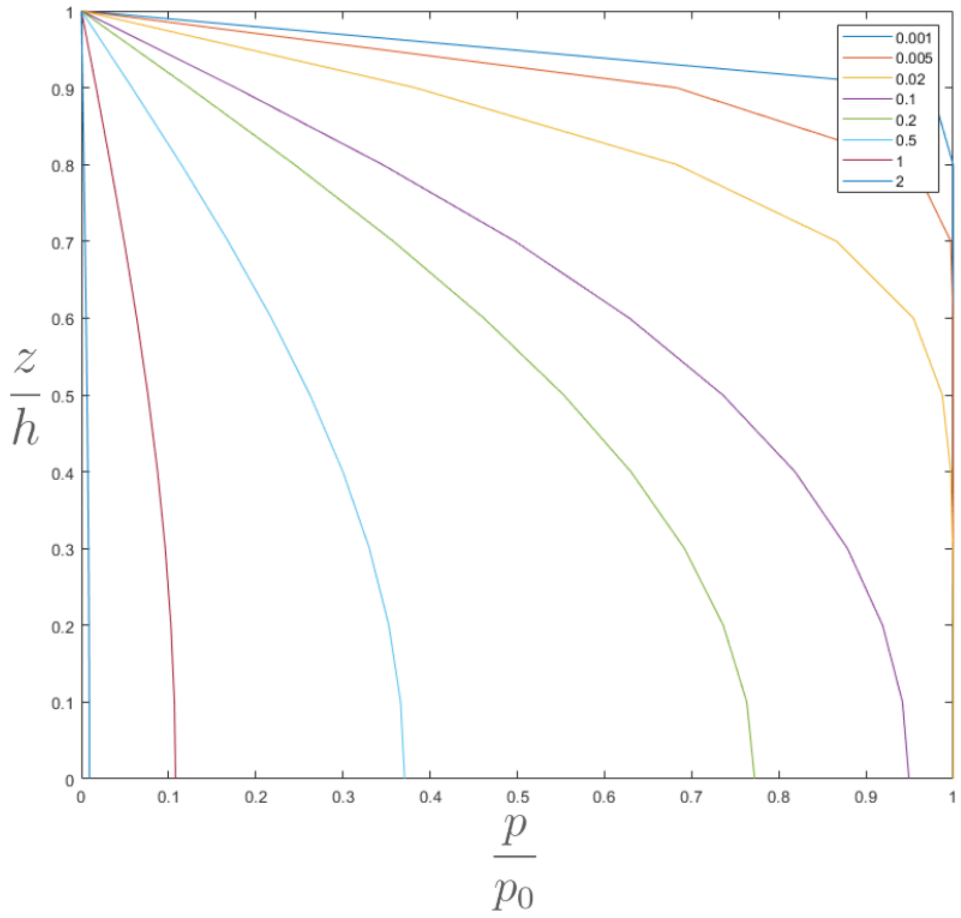

Figure 14: Analytical solution for Terzaghi's consolidation problem, illustrating the relative change in pore pressures $p/p0$ against relative height z/h for various values of the time parameter $c_v t/h^2$. The graph shows higher pore pressures towards the base $z/h = 0$ and a reduction to near-zero pressures as the time parameter increases, indicating full consolidation of the sample

Although the concept of consolidation itself is not directly applicable to a deforming soft tissue structure such as the lung, Terzaghi's Problem does present a very clear symmetry to the pore behaviour of the alveoli. The increasing pressures towards the base of the sample here, can be assumed a direct result of the applied vertical load at the top of the sample. In a spontaneously breathing subject, it is the load applied by the chest wall and diaphragm which forces air out of the alveoli [63]. Terzaghi's theories of consolidation thus raise an interesting question on how these external forces effect the pressures of the alveoli based on their vertical height within the lung. The next portion of this project will therefore focus on using a one-dimensional theory of poroelasticity to model the soft tissues of the lung with the alveolar pores.

5.3 Derivation of The Governing Equations

The basis for a poroelastic framework relies on the conservation of the full system. For this one-dimensional lung model, the governing equations are the conservation of mass of the material, the conservation of the air in the pores and the conservation of momentum of the solid skeleton.

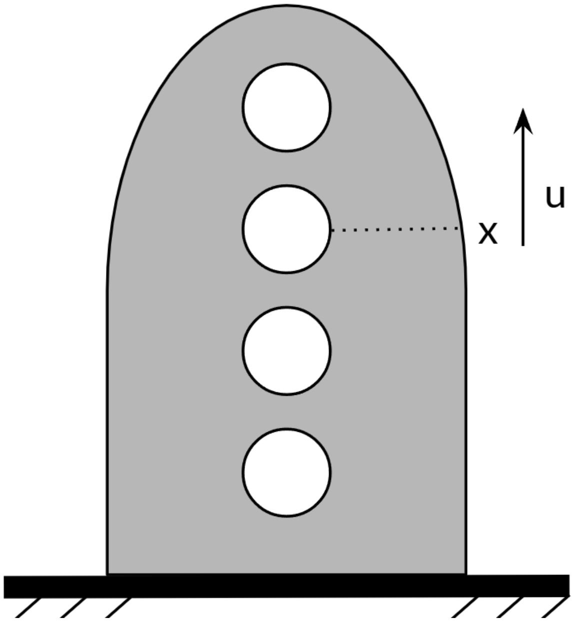

Figure 15: Reference diagram for the proposed one-dimensional poroelastic model of the lung. The lung is represented as a structure with pores aligned against gravity, where u denotes the deformation of pores at a specific gravitational plane (height x) over time t.

For reference, Figure 15 depicts a visual representation of the proposed model. The lung will be modelled as a one-dimensional structure with pores aligned against gravity. The deformation of pores at a particular gravitational plane, height x, is denoted as u over time t.

The mass balance for the solid phase of the system can be defined as

$$\frac{\partial(1-\phi)\rho^s}{\partial t} + \nabla \cdot ((1-\phi)\rho^s \underline{v}^s) = 0 \tag{70}$$

where ϕ is the porosity, ρ^s is the density of the solid and v^s is the velocity of the solid skeleton. In this 1-D problem, ∇ represent the partial derivation $\frac{\partial}{\partial x}$. For this model, the density of the solid tissue is assumed constant, and as such can be factored out, making the mass balance for the solid phase

$$\frac{\partial(1-\phi)}{\partial t} + \nabla \cdot ((1-\phi)\underline{v}^s) = 0 \tag{71}$$

The mass balance for the fluid phase is given as

$$\frac{\partial \phi \rho^f}{\partial t} + \nabla \cdot \left(\phi \rho^f \underline{v}^f\right) = \rho_f S(x,t) \tag{72}$$

Where ρ_f is the density of the fluid and v^f is the velocity of the fluid. $S(x,t)$ is some input source term. Again, assuming the density of the air in the system is constant, this can be factored out yielding the equation

$$\frac{\partial \phi}{\partial t} + \nabla \cdot \left(\phi \underline{v}^f\right) = S(x,t) \tag{73}$$

Adding together 71 and 73 gives

$$\nabla \cdot ((1-\phi)\underline{v}^s) + \nabla \cdot \left(\phi \underline{v}^f\right) = S(x,t) \tag{74}$$

By defining fluid flux $\underline{z}$ to be

$$\underline{z} = \phi \left(\underline{v}^f - \underline{v}^s \right), \tag{75}$$

74 can be simplified to

$$\nabla \cdot (\underline{v}^s + \underline{z}) = S(x, t). \tag{76}$$

We restate the velocity of the solid skeleton in terms of deformation according to

$$\underline{v}^s = \frac{\partial}{\partial t} \left(u(\underline{X}, t) \right), \tag{77}$$

where X is the position of the particle in the reference state. This gives the final equation for the balance of mass of the system as

$$\nabla \left(\frac{\partial}{\partial t} \left(u(\underline{X}, t) \right) + \underline{z} \right) = S(x, t) \tag{78}$$

The conservation of fluid momentum in the system can be simulated using Darcy's Law, such that

$$\kappa^{-1} \underline{z} + \nabla p = \rho^f g, \tag{79}$$

where κ is the permeability, p is the pressure and g is the applied acceleration, in this case gravity. It can be argued that $\rho^f g$ is negligible in the system as the direct impacts of gravity on air in the lung can be assumed zero. This makes the equation for the conservation of fluid momentum

$$\kappa^{-1} \underline{z} + \nabla p = 0 \tag{80}$$

Finally, the conservation of solid momentum of the system can be thought of as the deformation of the lung tissue with time. This can be taken directly from the model derived previously in Chapter 4 of this thesis. However, interpreting this to allow displacement over time requires some adjustments. The density must now be refined to specifically the density of the solid portion of the system. There must also be the inclusion of a pressure input that can force deformation based on in/out flow of air. Over the breathing cycle this is defined as a pressure input for the inhalation phase, and output for the exhalation phase. This gives the equation of solid momentum for this model as

$$\frac{\partial}{\partial x}\left(EA\frac{\partial u}{\partial x} - pA\right) = -A\rho^s(1-\phi)g \tag{81}$$

Where E is tissue elasticity, A is the cross-sectional area of the tissue, and g is the acceleration due to gravity. For the purposes of the model going forward, 78 and 80 will be combined by substituting the fluid flux $\underline{z}$ such that

$$\nabla \cdot \left(\frac{\partial u}{\partial t} - \kappa \cdot \nabla p\right) = S(x,t) \tag{82}$$

To begin, the model will be set up according to the cylinder analogy in the upright position, such that the equations can be solved with a constant cross-sectional area A and tissue elasticity E. Expanding the derivatives for the model 81 and 82, gives the final series of equations for the linear poroelastic model.

$$\frac{\partial^2 u}{\partial x \partial t} - \kappa\frac{\partial^2 p}{\partial x^2} = S(x,t) \tag{83}$$

$$\frac{\partial}{\partial x}\left(E\frac{\partial u}{\partial x} - p\right) = -\rho^s(1-\phi)g \tag{84}$$

5.4 Non-Dimensionalisation of the Equations

Due to the large number of parameters in this lung model, variables are non-dimensionalised for easier computation by scaling them to realistic physiologically relevant values. Variables are non-dimensionalised as follows:

$$x^* = H^* x \tag{85}$$

$$t^* = T^* t \tag{86}$$

$$u^* = H^* u \tag{87}$$

$$p^* = P^*_\infty + MAP^* p \tag{88}$$

where H^* is the total height of the lung, T^* is the maximum time for the simulation, P^*_∞ is the maximum pressure in the alveolar pores and MAP^* is the mean airway pressure. This gives the non-dimensionalised differentials as

$$\frac{\partial u^*}{\partial x^*} = \frac{H^*}{H^*} \cdot \frac{\partial u}{\partial x} \tag{89}$$

$$\frac{\partial p^*}{\partial x^*} = \frac{MAP^*}{H^*} \cdot \frac{\partial p}{\partial x} \tag{90}$$

$$\frac{\partial^2 u^*}{\partial x^{*2}} = \frac{1}{H^*} \cdot \frac{\partial^2 u}{\partial x^2} \tag{91}$$

$$\frac{\partial^2 p^*}{\partial x^{*2}} = \frac{MAP^*}{H^{*2}} \cdot \frac{\partial^2 p}{\partial x^2} \tag{92}$$

$$\frac{\partial^2 u^*}{\partial x^* \partial t^*} = \frac{1}{T^*} \cdot \frac{\partial^2 u}{\partial x \partial t} \tag{93}$$

Substituting these normalisations into the model 83 and 84

$$\frac{1}{T^*} \cdot \frac{\partial^2 u}{\partial x \partial t} - \frac{\kappa MAP^*}{H^{*2}} \cdot \frac{\partial^2 p}{\partial x^2} = S(x,t) \tag{94}$$

$$\frac{E}{H^*} \cdot \frac{\partial^2 u}{\partial x^2} - \frac{MAP^*}{H^*} \cdot \frac{\partial p}{\partial x} = -\rho^s (1-\phi) g \tag{95}$$

For the remainder of this thesis, we assume that all variables have been normalized in this manner.

5.5 The Finite Difference Method

Due to the complexity of these coupled equations, iterative methods will be employed. The finite difference method used here is the Crank-Nicolson approach for partial differential equations, as published by J. Crank and P.Nicolson in 1947 [64]. This method gives second-order convergence in both time and space. A visual representation of the method can be seen in Figure 16.

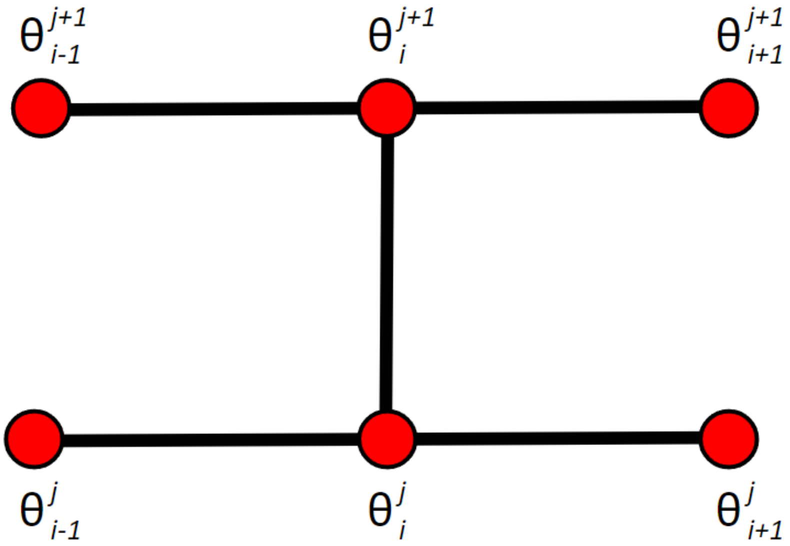

Figure 16: Visual representation of the Crank-Nicolson method, a finite difference scheme used for solving partial differential equations in a one-dimensional problem. The grid shows spatial index i and time index j, illustrating how the method achieves second-order convergence in both space and time.

For any variable $\theta_i^j = \theta(x_i, t_j)$ the finite expansion can be written as

$$\theta \approx \frac{\theta_i^j + \theta_i^{j+1}}{2} \tag{96}$$

$$\frac{\partial \theta}{\partial x} \approx \frac{\theta_{i+1}^{j+1} + \theta_{i+1}^j - \theta_{i-1}^{j+1} - \theta_{i-1}^j}{4\Delta x} \tag{97}$$

$$\frac{\partial^2 \theta}{\partial x^2} \approx \frac{\theta_{i-1}^{j+1} - 2\theta_i^{j+1} + \theta_{i+1}^{j+1} + \theta_{i-1}^j - 2\theta_i^j + \theta_{i+1}^j}{2\Delta x^2} \tag{98}$$

$$\frac{\partial^2 \theta}{\partial x \partial t} \approx \frac{\theta_{i+1}^{j+1} - \theta_{i+1}^j - \theta_{i-1}^{j+1} + \theta_{i-1}^j}{2\Delta x \Delta t} \tag{99}$$

Substituting in the finite difference approximations to 94 yields

$$\begin{aligned} &\frac{1}{T^*}\left[\frac{u_{i+1}^{j+1} - u_{i+1}^j - u_{i-1}^{j+1} + u_{i-1}^j}{2\Delta x \Delta t}\right] - \\ &\frac{\kappa MAP^*}{H^{*2}}\left[\frac{p_{i-1}^{j+1} - 2p_i^{j+1} + p_{i+1}^{j+1} + p_{i-1}^j - 2p_i^j + p_{i+1}^j}{2\Delta x^2}\right] = S_{i,j} \end{aligned}$$

This can be rearranged in order to solve using the Gauss-Seidel method by moving all $j+1$ terms to the left hand side of the equation, and all j terms to the right. This gives

$$\begin{aligned} &\frac{1}{T^*}\left[\frac{u_{i+1}^{j+1} - u_{i-1}^{j+1}}{2\Delta x \Delta t}\right] - \frac{\kappa MAP^*}{H^{*2}}\left[\frac{p_{i-1}^{j+1} - 2p_i^{j+1} + p_{i+1}^{j+1}}{2\Delta x^2}\right] = \\ &S_{i,j} - \frac{1}{T^*}\left[\frac{u_{i+1}^j - u_{i-1}^j}{2\Delta x \Delta t}\right] + \frac{\kappa MAP^*}{H^{*2}}\left[\frac{p_{i-1}^j - 2p_i^j + p_{i+1}^j}{2\Delta x^2}\right] \end{aligned}$$

For ease of notation going forward, constants can be grouped to give

$$\alpha(u_{i+1}^{j+1} - u_{i-1}^{j+1}) - \beta(p_{i-1}^{j+1} - 2p_i^{j+1} + p_{i+1}^{j+1}) = S - \alpha(u_{i+1}^j - u_{i-1}^j) + \beta(p_{i-1}^j - 2p_i^j + p_{i+1}^j) \tag{100}$$

where $\alpha = \frac{1}{T^* \cdot 2\Delta x \Delta t}$, $\beta = \frac{\kappa MAP^*}{H^{*2} \cdot 2\Delta x^2}$ and $S = S_{i,j}$.

Similarly, substituting the finite difference approximations into 95 gives

$$\frac{E}{H^*}\left[\frac{u_{i-1}^{j+1}-2u_i^{j+1}+u_{i+1}^{j+1}+u_{i-1}^{j}-2u_i^{j}+u_{i+1}^{j}}{2\Delta x^2}\right]-$$
$$\frac{MAP*}{H^*}\left[\frac{p_{i+1}^{j+1}+p_{i+1}^{j}-p_{i-1}^{j+1}-p_{i-1}^{j}}{4\Delta x}\right]=-\rho^s(1-\phi)g$$

As before, moving $j+1$ terms to the left hand side gives

$$\frac{E}{H^*}\left[\frac{u_{i-1}^{j+1}-2u_i^{j+1}+u_{i+1}^{j+1}}{2\Delta x^2}\right]-\frac{MAP*}{H^*}\left[\frac{p_{i+1}^{j+1}-p_{i-1}^{j+1}}{4\Delta x}\right]=$$
$$-\rho^s(1-\phi)g-\frac{E}{H^*}\left[\frac{u_{i-1}^{j}-2u_i^{j}+u_{i+1}^{j}}{2\Delta x^2}\right]+\frac{MAP*}{H^*}\left[\frac{p_{i+1}^{j}-p_{i-1}^{j}}{4\Delta x}\right]$$

Collecting constants to give

$$\Gamma\left(u_{i-1}^{j+1}-2u_i^{j+1}+u_{i+1}^{j+1}\right)-\Xi\left(p_{i+1}^{j+1}-p_{i-1}^{j+1}\right)=\zeta-\Gamma\left(u_{i-1}^{j}-2u_i^{j}+u_{i+1}^{j}\right)+\Xi\left(p_{i+1}^{j}-p_{i-1}^{j}\right) \tag{101}$$

where $\Gamma=\frac{E}{H^*\cdot 2\Delta x^2}$, $\Xi=\frac{MAP^*}{H^*\cdot 4\Delta x}$ and $\zeta=-\rho^s(1-\phi)g$.

100 and 101 can now be solved as a coupled system for the unknowns u and p. In order to solve this using Gauss-Seidel iteration, a reference solution is required for time $t_0=0$, and 4 boundary conditions must be set for the values at which $i=0,n$. The boundaries here are for the pressure and deformation at the base and apex of the lung vertically. These conditions are set based on the problem being explored.

5.6 Model Validation

The simplest demonstration of this model is through the Swelling Problem. In this test fluid is only introduced to the system at a single location, and then can spread throughout the system (taken from a 2010 example by Chapelle [44]). In this case, air will only be allowed to enter/exit the lung at the base ($x = 0$). The source must be set to zero for every value of x such that the fluid flow is driven only by the imposed pressure gradient. This gradient is imposed by setting the pressure to zero at the top boundary and to some input function $f_n(t)$ at the base boundary. Displacement is set to zero at the base and as a stress-free boundary at the apex. The boundaries can be then set up as follows.

$$\begin{aligned} p(0,t) &= f_n(t) \\ p(n,t) &= 0 \\ u(0,t) &= 0 \\ \frac{\partial u}{\partial x}(n,t) &= 0 \end{aligned}$$

The Dirichlet boundaries can be substituted in to 100 and 101 immediately. The Neumann boundary however, must be expanded to fit the finite difference scheme. This is done using a one sided expansion such that

$$\frac{\partial \theta}{\partial x}(n,t) \approx \frac{3\theta_n^j - 4\theta_{n-1}^j + \theta_{n-2}^j}{2\Delta x} = 0$$

The equations can now be coupled and solved using Gauss-Seidel iterative methods in the form of the matrix equation

$$A\lambda^{j+1} = B\lambda^j + C \tag{102}$$

Here, A is a matrix containing the parameters for the $j+1$ terms, B is a matrix containing the parameters for the j terms, and C is a solution vector containing the constants. λ is a vector containing the unknowns u and p at $t = j, j+1$ respectively. The problem is initialised by setting displacement and pressures to zero across the system.

Figure 17 shows the results to the swelling problem as set out above. The most pressing observation here is the significant fluctuations in the pressure field, which are not to be expected from the iterative methods used.

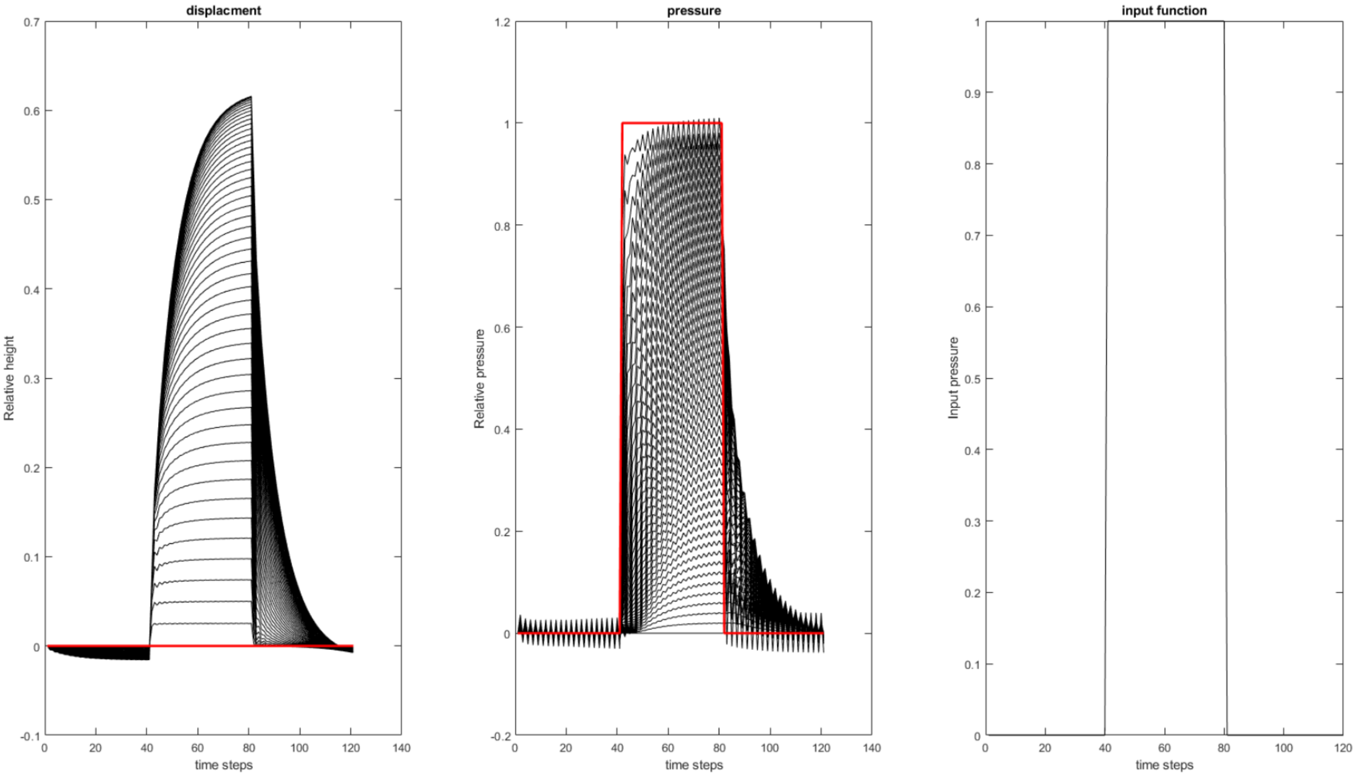

Figure 17: Initial displacement and pressure solutions for the swelling problem, where fluid is introduced only at the base $x = 0$ via a constant input function (right-most plot). Displacements and pressures are plotted for all pores on each isogravitational plane. The red line indicates the base of the lung at $x = 0$. Note the significant, unnatural fluctuations observed in the pressure field, indicating numerical instability.

Poroelastic computations have been found to exhibit these unnatural pore-pressure oscillations when solved using finite methods. A 1981 paper aimed to explore the impacts of mesh size on the extent of these fluctuations in one-dimensional consolidation problems [65]. They found that there is a minimum time-step criteria that when broken can result in violent fluctuations in the pressure field. Further to this, a 1994 paper determined the stability and convergence of Biot's consolidation problem when using finite element approximations [66]. They found that these pressure oscillations are caused by instability in the approximation of compressiblity in the initial conditions, and can be seen to decay in time.

In order to overcome these instabilities and remove the pore pressure oscillations, a relaxation method is proposed. Here the values calculated from the Gauss-Seidel method will be used to incrementally increase the values from the previous time-step until a designated convergence is achieved. The relaxed values are calculated as

$$\psi_{j+1} = \psi_j + RF \cdot \left(\psi_{(j+1)^*} - \psi_j\right) \tag{103}$$

where ψ_{j+1} is the new used value, ψ_j is the previous used value, ψ_{j+1^*} is the new predicted value, and RF is the relaxation factor. $RF = 1$ indicates no relaxation. $RF < 1$ indicates under-relaxation. This process is repeated until a set convergence is reached, such that the norm of the difference between the predicted and relaxed values is below a given error tolerance.

A visual representation of the iterative methods used is shown using the flow diagram in Figure 18. Here both the Gauss-Seidel iterations and the relaxation methods can be seen, from $t = 0$ until the max time steps have been reached. The model initializes the reference state with zero displacements and pressures across the system at $t = 0$. Subsequently, the current value of the input wave-

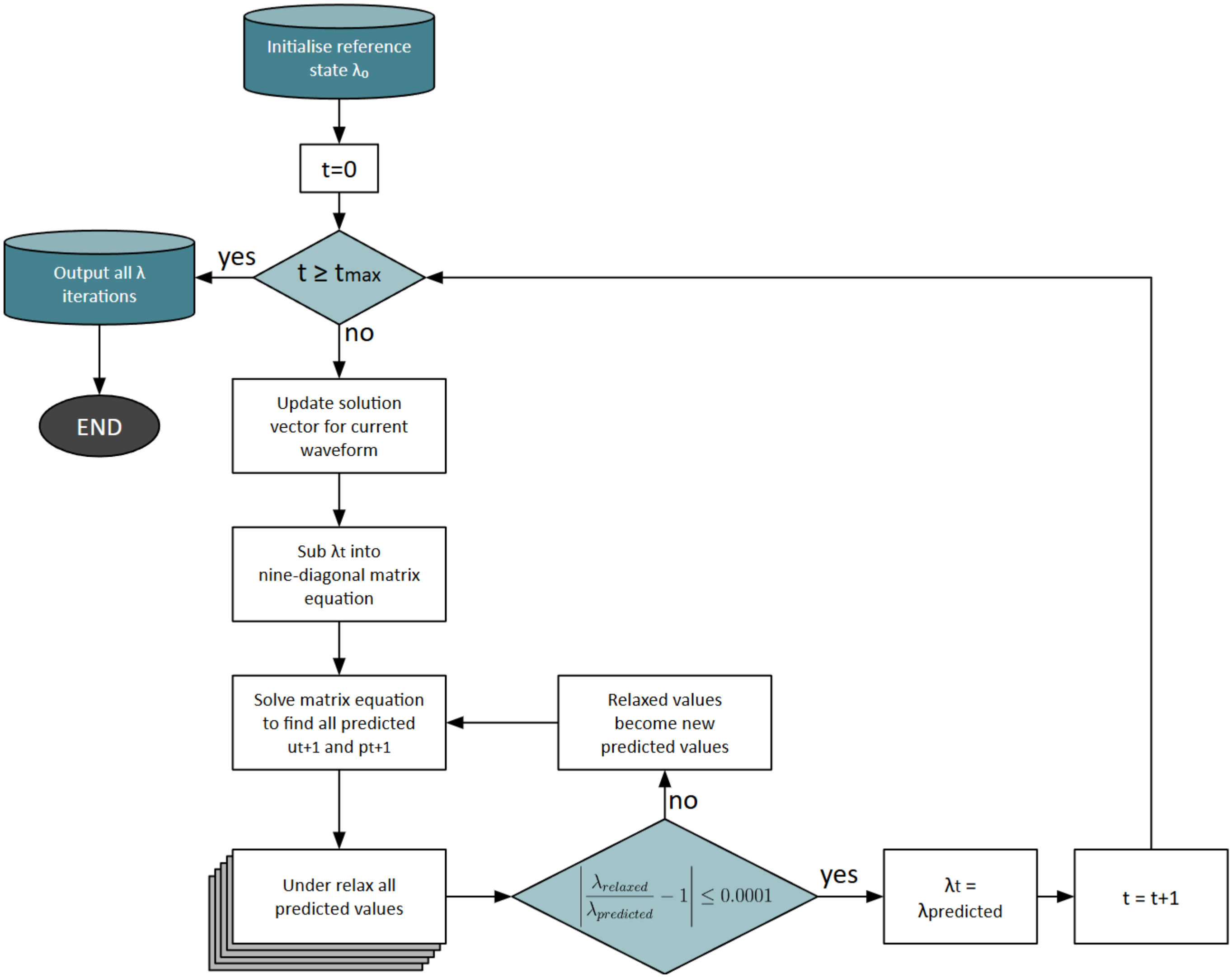

Figure 18: Flow diagram illustrating the iterative methods implemented to solve the poroelastic model. The process includes solving matrix equations using Gauss-Seidel iterations for initial predictions, followed by a relaxation loop to ensure convergence and remove unnatural pore-pressure oscillations, repeating until the maximum time steps are reached.

form is substituted into solution vector C, and parameter matrices A and B are updated as required. The matrix equation is solved using a Gauss-Seidel iteration to obtain the initial prediction, which then enters the relaxation loop.

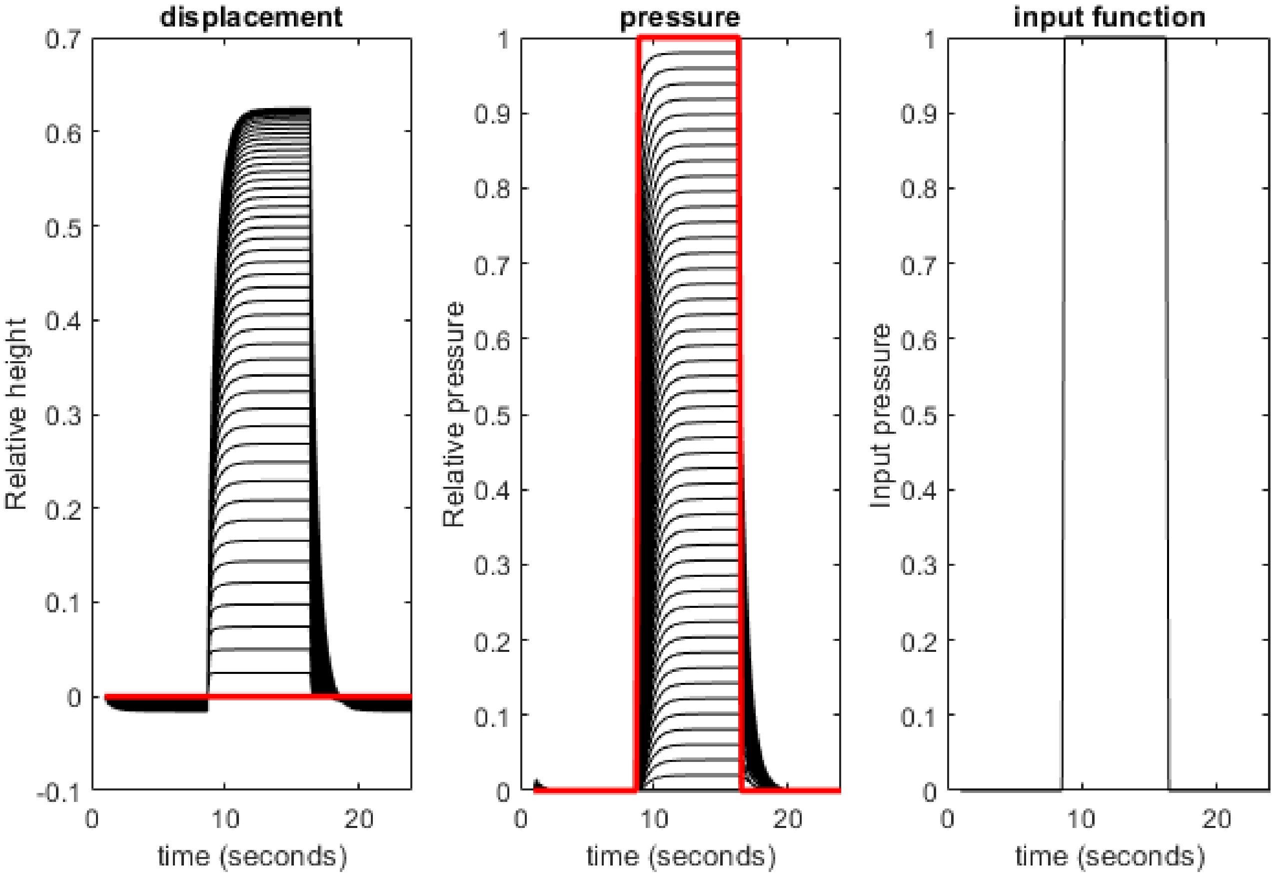

Figure 19: Displacement and pressure solutions to the swelling problem using a relaxation iteration with the relaxation factor set to 0.7. The input is set to a constant as in the right-most plot. Displacements and pressures are plotted for all pores on each isogravitational plane. The red line represents the base of the lung at $x = 0$.

Relaxed values iteratively replace predicted values until the norm of the difference between these vectors falls below the predefined error tolerance. Upon achieving convergence, the predicted value is adopted as the final solution, and the simulation advances to the next time-step, repeating until the maximum simulation time is reached.

Using the relaxation methods to solve the swelling problem, the unnatural pore-pressure oscillations are removed. The relaxation factor RF is set here to 0.7 representing under-relaxation of the predicted solution. Figure 19 shows the relaxed solutions to the swelling problem. With the unnatural oscillations removed, the behaviour of the system can be observed more accurately. In the pressure field (middle plot) the base of the lung at $x = 0$ can be seen to mirror the input function exactly, as is to be expected from the set up of the swelling problem. Through the rest of the lung, pressures increase rapidly until plateauing after 20 inflation steps. At this point, pressures are uniformly distributed across the height of the lung. Upon removal of the input, pressures quickly return to zero. In the displacement field, there is a small settling of the lung before the introduction of any input, this is analogous to the results from the solid mechanics static deformation model presented earlier in this thesis, and represents the 'Slinky Effect' of the lung under it's own weight. After the input function is switched on, the lung displaces rapidly until plateauing after 20 inflation steps as in the pressure waves. Here, it can be seen that relative displacement is greater at the base of the lung, as is expected from a single-point inflation source. The displacement at the base of the lung is shown in red, and is fixed to zero throughout. This swelling experiment provides useful insight into the mechanical behaviours of the lung, however, is not an accurate representation of mechanical ventilation. In order to create a more physiologically relevant simulation, the model must be returned to an input source effecting each alveolar unit on every iso-gravitational plane.

5.7 Source Problem

The reintroduction of the source can be achieved by setting new boundary conditions. As before displacement is set to zero at the base of the lung and is imposed as a stress-free boundary at the apex. Here, the pressure conditions must be set to contain all air within the system and not to allow any to escape through the boundaries. This is achieved by setting the fluid flux z to zero. From 80, we can rearrange to find z such that

$$\underline{z} = -\frac{\nabla p}{\kappa^{-1}} \tag{104}$$

$\therefore$ for the zero flux we have

$$-\frac{\nabla p}{\kappa^{-1}} = 0 \tag{105}$$

Given that permeability κ is set to be a non-zero constant we can take that ∇p must equal zero for this condition to be enforced. This gives the boundary conditions as

$$\begin{aligned} u(0,t) &= 0 \\ \frac{\partial u}{\partial x}(n,t) &= 0 \\ \frac{\partial p}{\partial x}(0,t) &= 0 \\ \frac{\partial p}{\partial x}(n,t) &= 0 \end{aligned}$$

The three Neumann boundary conditions must be expanded via the finite method as before such that

$$\begin{aligned} \frac{\partial \theta}{\partial x}(0,t) &\approx \frac{-3\theta_0^j + 4\theta_1^j - \theta_2^j}{2\Delta x} = 0 \\ \frac{\partial \theta}{\partial x}(n,t) &\approx \frac{3\theta_n^j - 4\theta_{n-1}^j + \theta_{n-2}^j}{2\Delta x} = 0 \end{aligned}$$

Solving using Gauss-Seidel iterations and implementing the relaxation iterative method as shown previously in Figure 18, the source problem can be simulated.

Figure 20 depicts the simulations of the source problem for three different input functions. The first row models the lung mechanics with a constant source

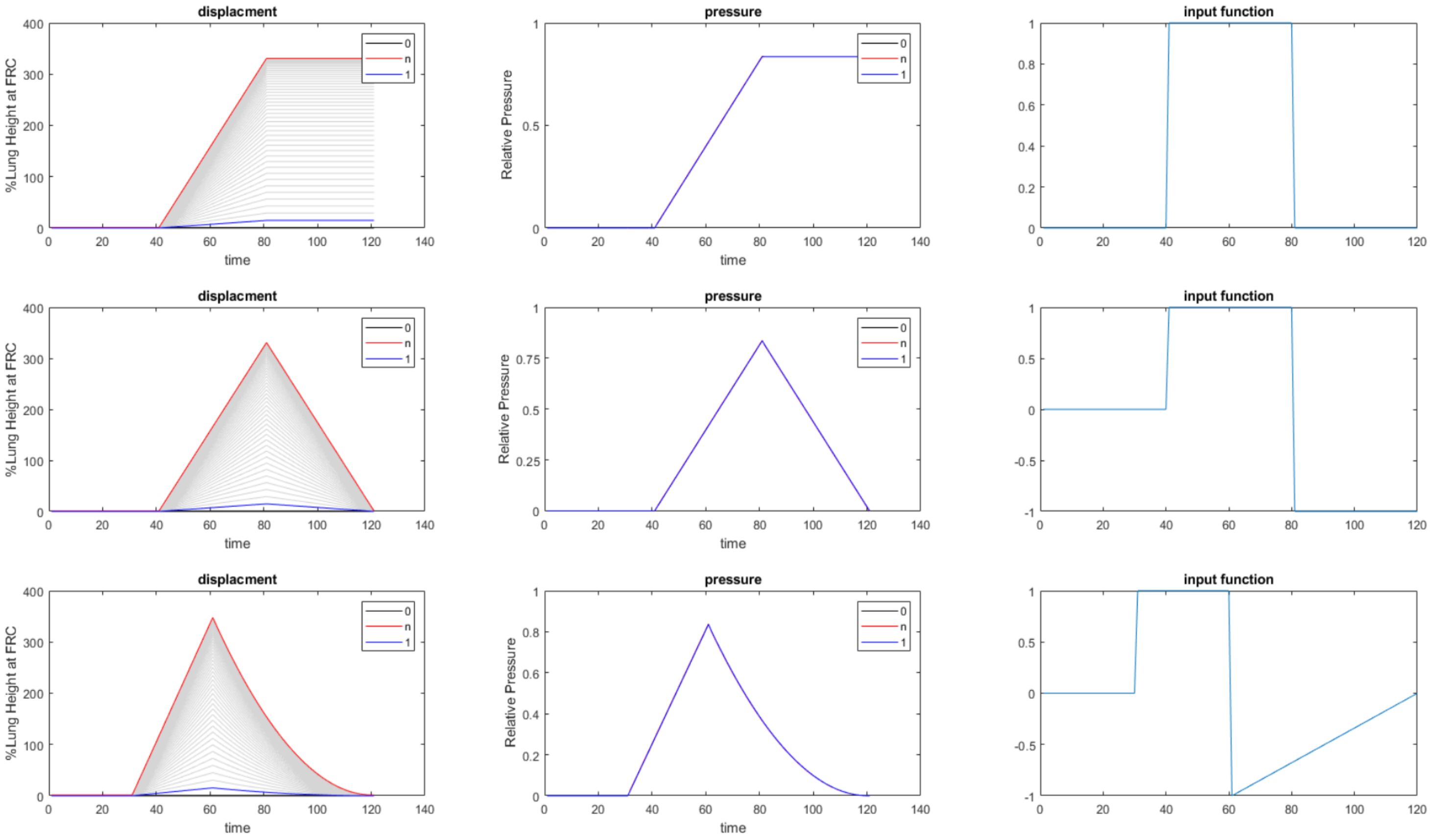

Figure 20: Displacement and pressure solutions to the source problem using a relaxation iteration with the relaxation factor set to 0.7. Simulations are shown for three different input functions, shown in the right-hand column. Displacements and pressures are plotted for all pores on each isogravitational plane. In each instance, the base of the lung at $x = 0$ is plotted in black, the first iteration up from the base is plotted in blue, and the apex of the lung at $x = n$ is plotted in red. All other internal nodes are plotted in grey.

pressure applied for 20 iterations. Here both the displacement and pressures can be seen to increase linearly after inflation is begun, and then remain constant when input is returned to zero. This is due to the lack of an exit for the air in the system. The zero-flux boundaries are set such that no fluid can enter or escape the lung, unless it is done via the source function itself. This means that a deflation function is required in the input. The second row of plots adds a deflation in the form of a negative constant, equal to that of the inflation. The displacement can now be seen to return to zero after the complete deflation. At it's maximum inflation, the n^{th} node reaches a displacement of 350% the lung height at FRC, which represents an increase in total lung size to 3 times that at functional residual capacity. In the last row of plots, the input function is set to more accurately mimic the real functions used by mechanical ventilators for ICU patients. Here deflation is a linear increase from -1 to 0, such that the total area under the curve is equal to that of the inflation function and therefore the total amount of air entering the system is the same as the total amount of air leaving. This is done by doubling the number of iterations for the deflation portion. Here the displacements and pressures return to zero in a sloping descent,as opposed to the linear descent in the middle row plots.

A one-dimensional poroelastic model of the lung connected to a mechanical ventilator input waveform has now been established. In its current form, the model does not have the capacity to vary the patient position, as it assumes a constant cross-sectional area. In order to be used for the exploration of lung mechanics in different body positions, the governing equations must be adjusted to account for lung shape and elasticity variations in space.

5.8 Patient Positioning in the Poroelastic Framework

The purpose of this project is to explore the impacts of patient positioning on lung function, by ways of the specific effects of gravity on underlying tissue mechanics. In order to adjust the current model to include the different body positions, the governing equations must be modified. The differences between the two positions can be equated to two factors, the changes in cross-sectional area of the lung as the shape is oriented against gravity, and the change in elasticity of the lung [10]. This means that equations must include a non-constant cross-sectional area A and tissue elasticity E, such that they are both functions of space.

The equation for the conservation of mass of the system 78 and for the conservation of the fluid momentum 80 do not contain any variables for the cross-section or tissue elasticity, and so remain unchanged. The equation for the conservation of solid momentum however, must be updated. Setting both A and E to functions of x, means 81 must be written in the form

$$\frac{\partial}{\partial x}\left(E(x)A(x)\frac{\partial u}{\partial x} - pA(x)\right) = -A(x)\rho^s(1-\phi)g \tag{106}$$

Expanding by the product rule, this becomes

$$E(x)A(x)\frac{\partial^2 u}{\partial x^2} + \frac{\partial u}{\partial x}\cdot\left(E(x)A^{'}(x) + E^{'}(x)A(x)\right) - pA^{'}(x) - p^{'}A(x) = -A(x)\zeta \tag{107}$$

where $\zeta = \rho^s(1-\phi)g$. The normalisation of the parameters as before is stated in 85-93. Setting A and E to functions of x means these must also be non-dimensionalised, such that

$$A^* = \hat{A}^* A \tag{108}$$

$$E^* = \hat{E}^* E \tag{109}$$

$$\frac{\partial A^*}{\partial x} = \frac{\hat{A}^*}{H^*}\cdot\frac{\partial A}{\partial x} \tag{110}$$

$$\frac{\partial E^*}{\partial x} = \frac{\hat{E}^*}{H^*}\cdot\frac{\partial E}{\partial x} \tag{111}$$

This makes the non-dimensionalised equation for the conservation of solid momentum as

$$\begin{aligned}\frac{\hat{E}^* E \cdot \hat{A}^* A}{H^*} \cdot u^{''} + \left(\frac{\hat{E}^* E \cdot \hat{A}^* A^{'}}{H^*} + \frac{\hat{E}^* E^{'} \cdot \hat{A}^* A}{H^*} \right) u^{'} - \\ \frac{(P^*_\infty + MAP^* p) \cdot \hat{A}^* A^{'}}{H^*} - -\frac{MAP^*}{H^*} \cdot p^{'} \hat{A}^* A = -\hat{A}^* A \zeta\end{aligned}$$

which can be simplified to

$$\hat{E}^* E \cdot A u^{''} + \left(\hat{E}^* E A^{'} + A \hat{E}^* E^{'} \right) u^{'} - \left(P^*_\infty + MAP^* p \right) A^{'} - MAP^* p^{'} A = -H^* A \zeta \tag{112}$$

This is expanded as before using a Crank-Nicholson approach visually shown in Figure 16, according to 96-99, again moving all $j+1$ terms to the left-hand side.

$$\begin{aligned}
& u^{j+1}_{i-1} \cdot \left[\frac{\hat{E}^* E A}{2\Delta x^2} - \frac{\hat{E}^* E A^{'} + \hat{E}^* E^{'} A}{4\Delta x} \right] - u^{j+1}_{i} \cdot \left[\frac{\hat{E}^* E A}{\Delta x^2} \right] + \\
& u^{j+1}_{i+1} \cdot \left[\frac{\hat{E}^* E A}{2\Delta x^2} + \frac{\hat{E}^* E A^{'} + \hat{E}^* E^{'} A}{4\Delta x} \right] + p^{j+1}_{i-1} \cdot \left[\frac{MAP^* A}{4\Delta x} \right] - \\
& p^{j+1}_{i} \cdot \left[\frac{MAP^* A^{'}}{2} \right] - p^{j+1}_{i+1} \cdot \left[\frac{MAP^* A}{4\Delta x} \right] = \\
& u^{j}_{i-1} \cdot \left[-\frac{\hat{E}^* E A}{2\Delta x^2} + \frac{\hat{E}^* E A^{'} + \hat{E}^* E^{'} A}{4\Delta x} \right] + u^{j}_{i} \cdot \left[\frac{\hat{E}^* E A}{\Delta x^2} \right] + \\
& u^{j}_{i+1} \cdot \left[-\frac{\hat{E}^* E A}{2\Delta x^2} - \frac{\hat{E}^* E A^{'} + \hat{E}^* E^{'} A}{4\Delta x} \right] - p^{j}_{i-1} \cdot \left[\frac{MAP^* A}{4\Delta x} \right] + \\
& p^{j}_{i} \cdot \left[\frac{MAP^* A^{'}}{2} \right] + p^{j}_{i+1} \cdot \left[\frac{MAP^* A}{4\Delta x} \right] - H^* A \zeta + P^*_\infty A^{'}
\end{aligned}$$

Cross-sectional area and tissue elasticity are both functions of x that are assumed to remain constant in time, they can therefore be determined by preset functions in this model. This allows us to group terms in the equation for simplicity to become

$$\begin{aligned}&(\Omega-\delta)u_{i-1}^{j+1}-2\Omega u_i^{j+1}+(\Omega+\delta)u_{i-1}^{j+1}+\omega p_{i-1}^{j+1}-\mu p_i^{j+1}-\omega p_{i+1}^{j+1}=\\&(\delta-\Omega)u_{i-1}^{j}+2\Omega u_i^{j}+(-\Omega-\delta)u_{i-1}^{j}-\omega p_{i-1}^{j}+\mu p_i^{j}+\omega p_{i+1}^{j}+\chi\end{aligned}\tag{113}$$

Where notation $\Omega = \frac{\hat{E}^*EA}{2\Delta x^2}$, $\delta = \frac{\hat{E}^*EA^{'}+\hat{E}^*E^{'}A}{4\Delta x}$, $\omega = \frac{MAP^*A}{4\Delta x}$, $\mu = \frac{MAP^*A^{'}}{2}$ and $\chi = -H^*A\zeta + P^*_{\infty}A^{'}$.

The functions for cross-sectional area will be set using the truncated cone shape analogy as in Sections 4.4-4.5 of this thesis, shown in 23 for the upright position, and in 35 for the prone and supine positions. Tissue elasticity will be set as before, as constant in the upright and prone positions, and a linear gradient from 0 to 1 in the supine position.

5.9 Steady-State Solutions

The governing equations for the linear poroelastic model with non-constant area and tissue elasticity are set above. The complexity of these equations when coupled, given the two unknown variables p and u, makes a numerical solution the most appropriate method for solving the system. However, there are a number of theoretical solutions that can be verified analytically. These exist at the points where the model converges in time and reaches a point of equilibrium in both the pressure and displacement fields. These are defined as steady-state scenarios.

The first steady-state scenario exists when there is no air introduced to the lung, such that the source is zero throughout. This is comparable to the scenario in which the lung is simply allowed to deform under it's own weight, as discussed previously in the slinky effect. The equations for this system are

$$\frac{\partial^2 u}{\partial x \partial t} - \kappa \frac{\partial^2 p}{\partial x^2} = S(x,t) \tag{83}$$

$$\frac{\partial}{\partial x}\left(E(x)A(x)\frac{\partial u}{\partial x} - pA(x)\right) = -A(x)\rho^s(1-\phi)g \tag{106}$$

for reference, setting $S(x,t) = 0$. As the system is assumed to have reached equilibrium, there is no time variation remaining. Subsequently, derivatives in time become zero, making 83

$$-\kappa p^{''} = 0 \tag{114}$$

As κ is defined as a non-zero constant, we have that $p^{''}$ must equal zero in this steady state. This implies that p must be a linear function of x and will be chosen here to be the simplest linear function such that $p = x$. Substituting this into 106 gives

$$\frac{\partial}{\partial x}\left(E(x)A(x)\frac{\partial u}{\partial x} - xA(x)\right) = -A(x)\rho^s(1-\phi)g \tag{115}$$

which can be fully expanded to

$$EAu^{''} + \left(EA^{'} + E^{'}A\right)u^{'} - xA^{'} = A - A\rho^s(1-\phi)g \tag{116}$$

Solving for u requires set boundary conditions, given here as a fixed boundary at the base, $u(0) = 0$ and a stress-free boundary at the apex, $u^{'}(n) = 0$. The normalised system sets the maximum height of x to 1, such that $n = 1$. Using these conditions, u' can be found as

$$u'(x) = \frac{1-\rho^s(1-\phi)g}{E}x + \frac{\rho^s(1-\phi)g}{EA}\int xA'dx + \frac{C}{EA} \tag{117}$$

In order to find a solution for u, we must know explicitly the function A(x) and

E(x). These are taken according to the functions set in sections 4.4 and 4.5 of this thesis. The full workings for these solutions for general linear functions $A(x) = ax + b$ and $E(x) = cx + d$ are shown in Appendix A1.

To validate the finite-difference approximations for the model in the chosen positions here, they will be compared to the steady state solution. This is done by setting up the initial problem in the same manner, with no source function, and allowing the simulation to run for a long period of time until convergence is reached.

Figure 21 shows the analytical solution to the steady state scenario with no input source, plotted against the finite-difference approximate solution to the same scenario, in the upright position. Plotted are the final displacements of each alveoli against their height in the reference position. Displacements are the total distance moved, not inclusive of the direction. In this scenario with the lung settling under its own weight, displacement will always be in a downward direction with gravity. It can be clearly observed that the finite difference approach demonstrates high fidelity with the analytical solution.

Figure 22 shows the steady state solutions to the no-source problem for the upright, supine and prone positions. It can clearly be seen that the lung deforms most significantly in the upright position, with the prone position being the smallest deformation, roughly half of that seen in the upright orientation. This is comparable to the results seen in Figure 11, which uses a solid mechanics approach to model lung deformation, however with the notable difference that the lung is fixed and both the top and the bottom, unlike in this poroelastic approach, which sees the lung fixed only at the bottom.

A second steady state scenario exists when the source is reintroduced to the system. When the input is set to a positive constant, the lung can be expected to continue deforming as pressures increase, as air is trapped within the lung.

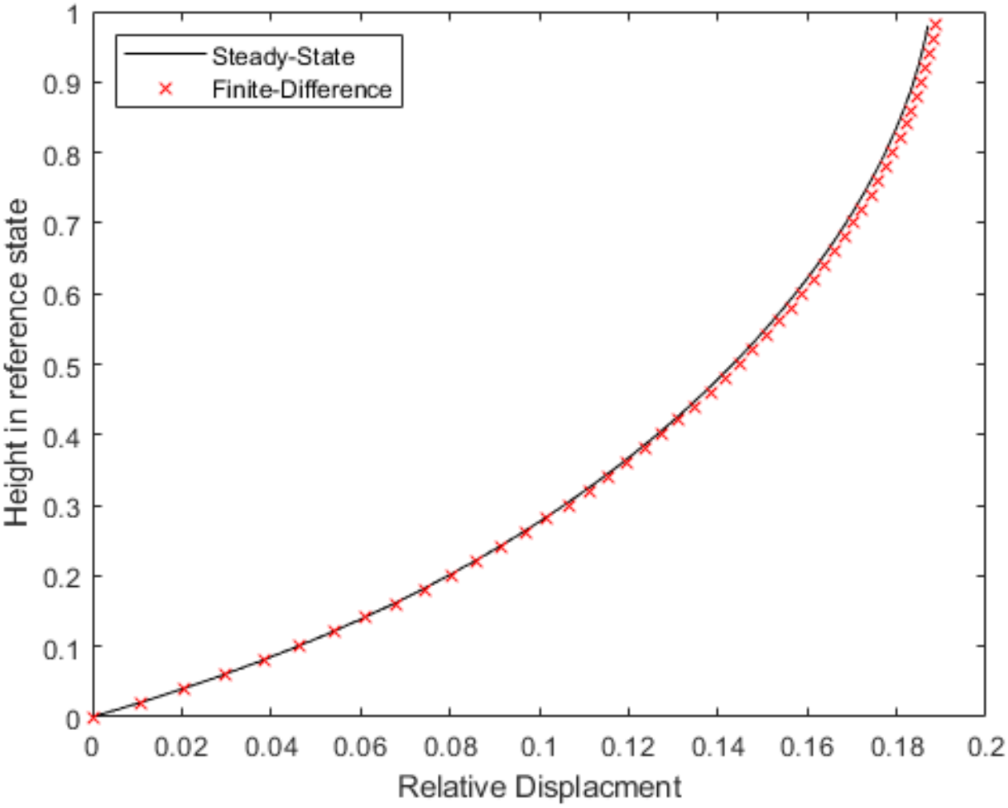

Figure 21: Final displacement in the steady-state scenario with no input source, depicting the lung deforming under its own weight in the upright position. The analytical steady-state solution (solid line) is plotted against the results from the numerical finite-difference approach (dashed line), demonstrating good approximation between the two methods.

If however, the lungs boundaries are considered 'leaky' in that air is able to pass out of the system at the extremities, then the system will eventually reach a state of convergence. In order to set this, the zero-flux boundary conditions must be removed, and replaced with one zero-pressure boundary. This gives the conditions as

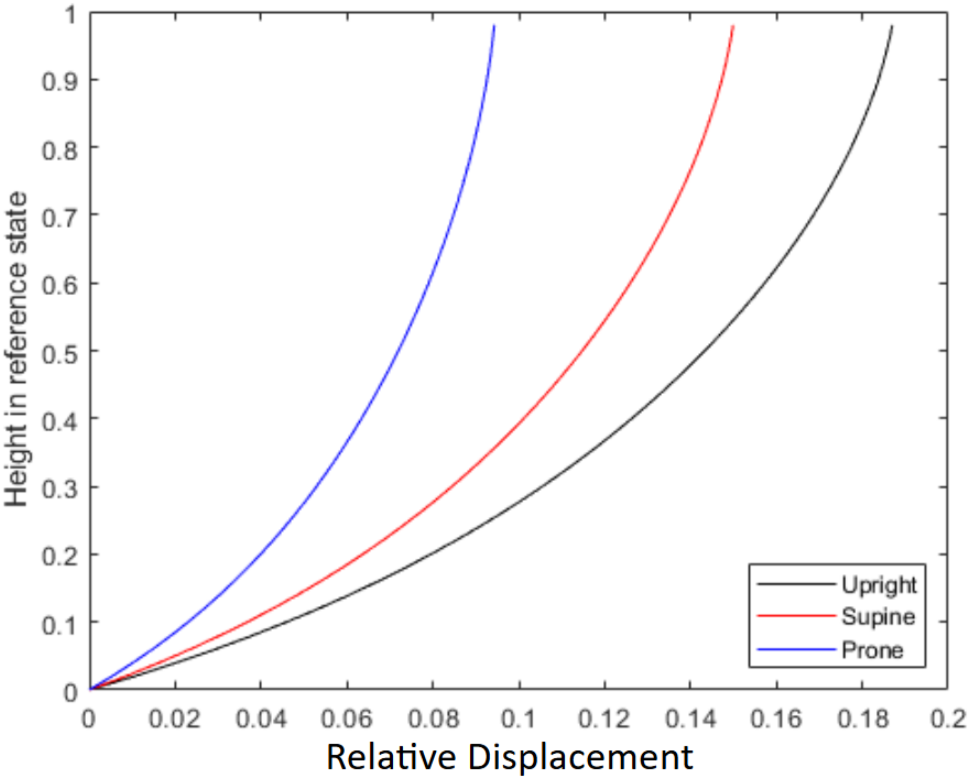

Figure 22: Final displacement in the steady-state scenario with no input source, showing lung deformation under its own weight in the upright, supine, and prone positions. The lung deforms most significantly in the upright position, while the prone position exhibits the smallest deformation, approximately half that of the upright orientation.

$$p(0,t) = 0$$

$$p(n,t) = 0$$

$$u(0,t) = 0$$

$$\frac{\partial u}{\partial x}(n,t) = 0$$

Again taking 83 and 106, assume to variation in time and setting the source to a constant of 1. When normalised, 83 becomes

$$\frac{-\kappa MAP^{*}}{H^{*2}} \cdot p^{''} = 1 \tag{118}$$

Integrating twice to find p using boundary conditions to determine constants of integration, with the maximum height $n = 1$.

$$p = \frac{H^{*2}}{2\kappa MAP^{*}} \left(x - x^{2}\right) \tag{119}$$

Substituting this into 106 and expanding this fully gives

$$\begin{aligned} E\hat{E}^{*}Au^{''} + \left(\hat{E}^{*}EA^{'} + \hat{E}^{*}AE^{'}\right)u^{'} + \left(\frac{AH^{*2}}{\kappa} - \frac{H^{*}}{2\kappa}\right)x + \frac{A^{'}H^{*2}x^{2}}{2\kappa} = \\ -H^{*}A\rho^{s}(1-\phi)f + P^{*}_{\infty} + \frac{AH^{*}}{2\kappa} \end{aligned} \tag{120}$$

Using the displacement boundary conditions to solve for u we get a general solution in the form of an integral equation

$$u(x) = \int \frac{1}{\alpha(x)} \left(\int_{0}^{x} \alpha(s) \cdot \beta(s) ds - \int_{0}^{n} \alpha(s) \cdot \beta(s) ds \cdot \frac{\alpha(x)}{\alpha(n)}\right) dx \tag{121}$$

where

$$\begin{aligned} \alpha(x) &= e^{\int \frac{E^{*}EA' + E^{*}E'A}{E^{*}EA} dx} \\ \beta(x) &= \frac{P^{*}_{\infty} - H^{*}A\rho^{s}\left(1-\phi\right)g + \frac{AH^{*}}{2\kappa} - \left(\frac{AH^{*2}}{\kappa} - \frac{H^{*}}{2\kappa}\right)x + \frac{A'H^{*2}x^{2}}{2\kappa}}{E^{*}EA} \end{aligned} \tag{122}$$

This can then be solved with the explicit functions for cross-sectional area and elasticity stated above.

Figure 23 shows the analytical steady state solution to the 'leaky' boundary problem, plotted against the numerical finite-difference approximation of the same problem. Again the plots are essentially identical, and thus the finite

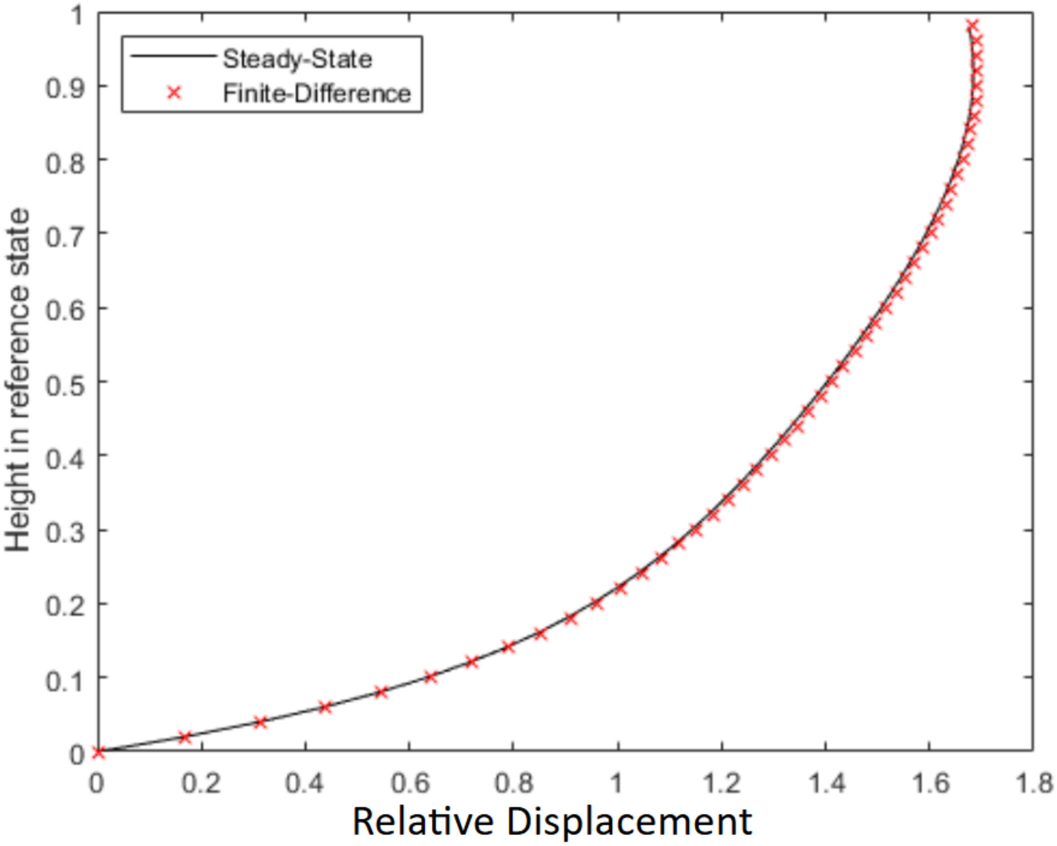

Figure 23: Final displacement in the steady state scenario with constant source and 'leaky' boundary in the upright position. The analytical steady state solution is plot against the results from the numerical finite-difference approach.

difference approximation is a good representation of the full model.

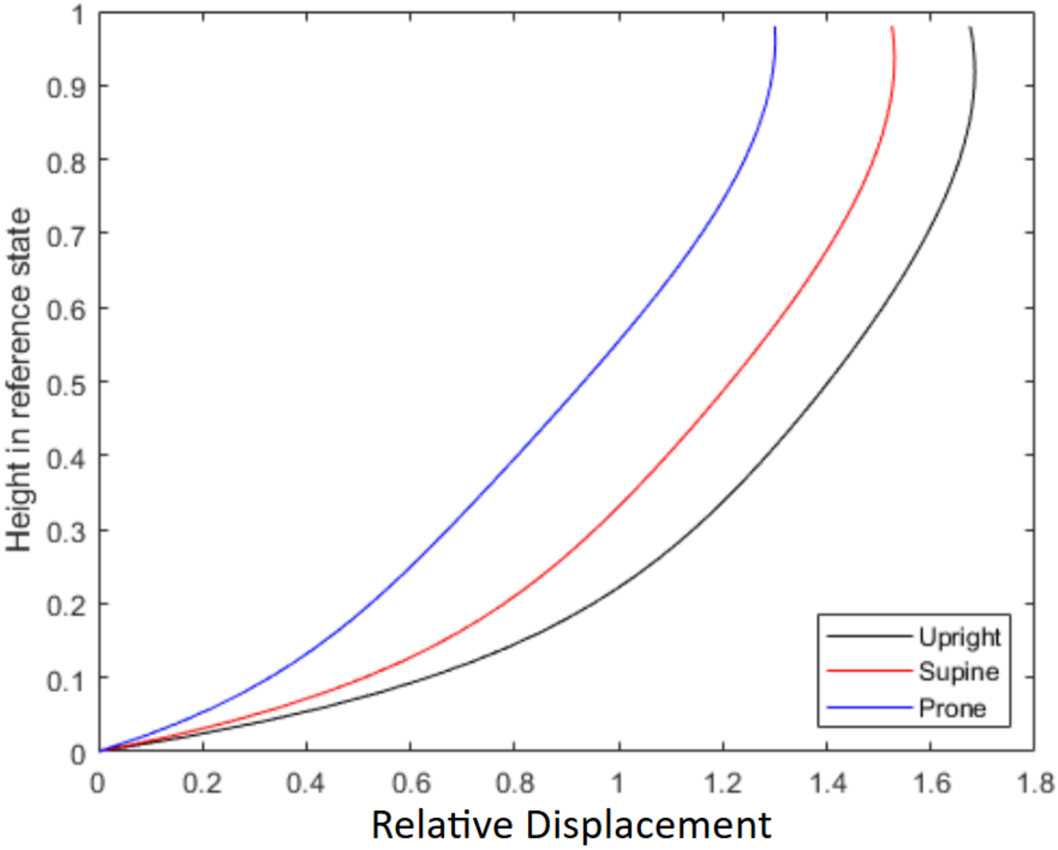

Figure 24: Final displacement in the steady-state scenario with a constant source and 'leaky' boundaries, across upright, supine, and prone positions. The lung exhibits the most significant deformation in the upright position, whereas the prone position demonstrates the smallest deformation, roughly a 50% reduction compared to the upright orientation.

Figure 24 shows the steady state solutions to the 'leaky' boundary problem for the upright, supine and prone positions. It can clearly be seen that the lung deforms most significantly in the upright position, with the prone position being the smallest deformation, a roughly 50% reduction of that seen in the upright orientation.

The final scenario to be discussed in this chapter involves the re-introduction of the zero-flux boundaries such that air is trapped within the lung, and can only enter/exit based on the input source given. As long as there is a positive source, the lung should continue expanding and pressures should continue to increase, meaning no steady-state solution can exist. Proof of this can be completed using the normalisation of 83 with time dependency removed such that

$$\frac{-\kappa MAP^{*}}{H^{*2}} \cdot p^{''} = S \tag{123}$$

This can be rearranged to find $p^{'}$ giving

$$p^{'} = -\frac{H^{*2}S}{\kappa MAP^{*}} \cdot x + C \tag{124}$$

Solving this requires the boundary conditions, which for a zero-flux boundaries are given as $p^{'}(0) = p^{'}(n) = 0$. The $x = 0$ boundary gives $C = 0$. With $n = 1$ this would mean

$$\frac{H^{*2}S}{\kappa MAP^{*}} = 0 \tag{125}$$

Given that H^{*}, κ and MAP^{*} are all non-zero constants, the equation is only solvable an the instance that $S = 0$. Therefore, there is no steady-state scenario with a non-zero constant source.

5.10 Results for Patient Positioning

Having proved the efficacy of a numerical approximation to deformation in the poroelastic framework when using a non-constant cross-sectional area and tissue elasticity, the model can be used to explore the system with realistic ventilator waveforms. The governing equations have been expanded using a Crank-Nicholson approximation and normalised. These can now be set up in the form of the matrix equation

$$A\lambda^{j+1} = B\lambda^{j} + C$$

and then solved using the Gauss-Seidel iterative method. As before the cross-sectional areas are set to the truncated cone analogy.

Figure 25 plots the numerical solution to the problem in the upright, supine and prone positions, over a two-breath cycle. The breath cycle is set using a common ventilator waveform as the input function, shown in the final plot for reference. In the displacement field, in all positions the lung can be seen to expand to TLC at just under 4 times the size at FRC. However, it is important to note that the reference lung height is the measurement parallel to gravity, and as such is larger in the upright position than in the supine and prone positions (25cm to 16cm respectively, from average lung measurements [67]). This means that overall displacement is much higher in the upright position than in the horizontal positions.

The model suggests that while the lung expands to approximately four times its Functional Residual Capacity (FRC) in all positions, the overall displacement is notably higher in the upright position compared to horizontal positions (supine and prone) due to a larger reference lung height parallel to gravity. Several studies corroborate these findings. Yamada and colleagues in 2020 conducted a study using CT scans in healthy subjects to measure lung volumes [68]. They found that inspiratory and expiratory bilateral upper lobe, lower lobe, and total lung volumes, were significantly higher (5.3 to 14.7% increases) in standing and sitting positions compared to the supine position. Volume changes from expiration to inspiration were also significantly higher in standing and sitting positions for the total lung and its lobes. Similarly, a 2022 study in patients with Idiopathic Pulmonary Fibrosis (IPF), total lung and lobe volumes were consistently larger in the standing position than in the supine position [69]. In

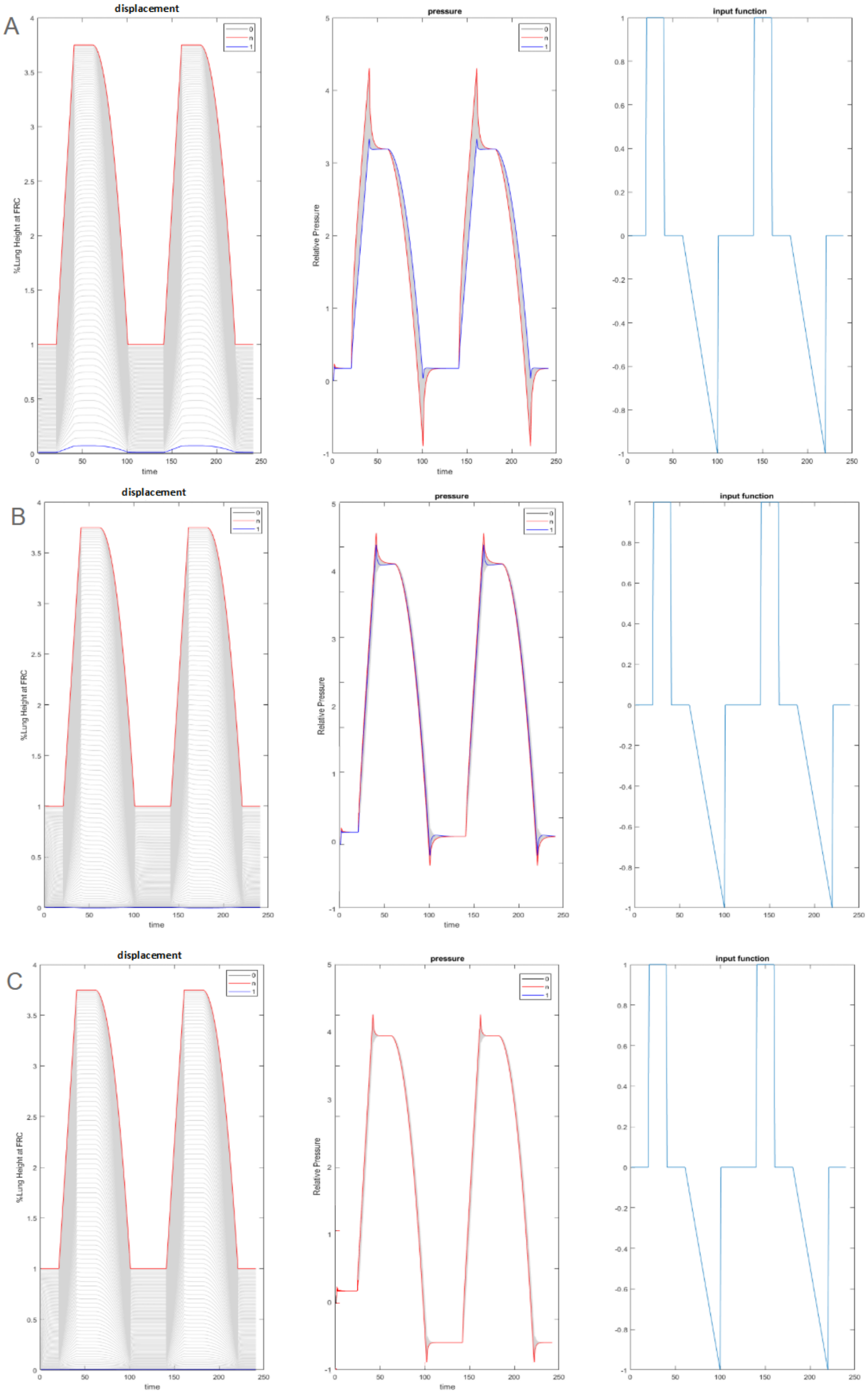

Figure 25: Simulated ventilator waveform data for the source problem using a relaxation iteration with relaxation factor 0.7. Row A is upright, row B is supine, row C is prone.

this linear poroelastic model, there is negligible difference in displacements and volumes between the supine and prone positions.

In the pressure field however, there is a clear difference between positions. The plots included highlighted lines for the apex and base of the lung, such that the spatial variation in pore pressures can be monitored. In the upright position, there is a significant difference between the pore pressure at the base and at the apex, with the apex pore pressure spiking at maximum inflation. The largest observed variation here is of 25% of the maximum. In the supine position, this is reduced to 5% variation at the maximum inflation spike. In prone position, variation is negligible, with the base and apex pore pressures being observably identical. The spatial uniformity of alveolar mechanics in prone position is well documented, and generally credited as the contributing factor to improved lung function in this position [10, 24, 17]. Maximum pressures in prone are also less than those in the upright and supine positions, a roughly 10% decrease. This is an interesting observation given the link between reduction in airway pressures and decreased risk of ventilator induced lung injury in the prone position [70].

The significant reduction in the inspiratory pressure spike and the remarkable uniformity of pore pressures observed in the prone position (Figure 25C) compared to upright (Figure 25A) and supine (Figure 25B) positions offers quantitative support for its clinical efficacy in reducing ventilator-induced lung injury (VILI). Lower peak alveolar pressures and reduced spatial pressure gradients directly translate to decreased mechanical stress on the delicate lung parenchyma, potentially minimizing barotrauma and volutrauma in critical care patients. This linear model, despite its simplifications, provides initial mechanistic insight into why prone positioning is a valuable strategy for clinicians aiming to distribute ventilatory forces more evenly and protect the lung from injurious pressures.

5.11 Concluding Remarks

This chapter explored the applicability of the poroelastic framework to modelling lung mechanics under gravity. The findings demonstrate that the lung is well suited to a poroelastic approach, with model outputs replicating experimental observations across various patient positions. Numerical approximations of the linear poroelastic model proved highly accurate in this context and were validated against analytical steady-state solutions.

However, the current model's reliance on linear assumptions represents a significant limitation. Linear poroelasticity assumes small, proportional tissue deformations and uniform material properties—assumptions that do not reflect the large, heterogeneous, and non-linear strains observed in real lungs during breathing, especially in pathological conditions such as pulmonary oedema or fibrosis. These simplifications exclude critical phenomena like alveolar recruitment/derecruitment, airflow resistance changes, and surface tension-driven mechanics—key components of dynamic lung behaviour and disease progression in conditions such as ARDS.

Despite these limitations, the model yields clinically relevant insights, particularly for sedated or mechanically ventilated patients. It quantitatively illustrates how body position affects internal pressure gradients and stress distributions, showing that upright and supine positions produce steep vertical gradients, while the prone position equalizes these forces, reducing mechanical heterogeneity. This provides a mechanistic explanation for the protective effect of prone positioning, widely adopted in ARDS to mitigate local overdistension and collapse.

From a clinical standpoint, the linear poroelastic model offers a conceptual framework for several key applications:

- COVID-19 management: In early-phase COVID-19 ARDS characterized by relatively preserved compliance, steep pressure gradients can exacerbate patient self-inflicted lung injury (P-SILI). The model supports early proning as a means to blunt vertical pressure disparities and reduce regional strain.

- Secretion clearance and chest physiotherapy: By illustrating how gravity and air pressure interact, the model reinforces the physiological basis for postural drainage techniques that use body orientation to assist mucus mobilization and clearance.
- Ventilator-induced lung injury (VILI) prevention: For patients with asymmetric lung injury (e.g., post-surgical or unilateral disease), the model aids in predicting how positioning influences local stress patterns—potentially guiding strategies to avoid secondary trauma in compromised regions.

Although its simplifications limit direct application to awake, spontaneously breathing patients—where active diaphragm and chest wall mechanics are significant—the model still contributes an understanding of passive gravitational effects in the lung during ventilation.

In conclusion, this chapter validates the potential of poroelastic modelling as a predictive and explanatory tool in critical care. The insights gained establish a strong foundation for more advanced simulations. The next phase of this project will extend the framework into the non-linear regime, aiming to capture the complex, patient-specific dynamics of the ventilated lung with greater precision and clinical relevance.

6 Non-linear Poroelastic Lung Model

6.1 Introduction

Recognizing the limitations of linear models in capturing the intricate mechanical behaviour of lung tissue, this chapter aims to develop a fully non-linear poroelastic model. The objective is to incorporate strain-dependent elastic properties and account for geometrical and material non-linearities, such as time-dependent alveolar recruitment/derecruitment and variable porosity and permeability. I hypothesize that introducing Neo-Hookean hyperelasticity and non-linear porosity/permeability will significantly enhance the physiological accuracy of the model, particularly in replicating complex phenomena like the S-shaped pressure-volume curve and accurately depicting alveolar recruitment and over-distension during the breathing cycle. The clinical question driving this chapter is: How do the inherent non-linear mechanical properties of lung tissue, including alveolar recruitment and stiffening, influence lung mechanics during mechanical ventilation across different patient positions, and how can a more accurate representation of these non-linearities inform protective ventilation strategies? This advancement is crucial for moving beyond simplified assumptions towards a more realistic and clinically applicable model, capable of informing precision medicine approaches in critical care.

Non-linear poroelasticity incorporates strain-dependent elastic properties and accounts for geometrical and material non-linearities, providing a more realistic representation of lung tissue behaviour, especially when subjected to high levels of stress or strain [47]. This non-linear approach also considers the non-uniform distribution of air and fluid within the lung tissue, which can significantly affect mechanical responses.

6.2 Time-dependent Alveolar Recruitment

One phenomena that requires non-linear dynamics is alveolar recruitment. Alveolar recruitment refers to the process of reopening collapsed alveoli, during breathing or mechanical ventilation [71]. In a non-linear system, this process is particularly complex, as the mechanical behaviour of lung tissue deviates from simple linear elasticity, especially under high strain conditions. Alveoli open in a highly non-linear manner due to factors such as surface tension, tissue elasticity, and fluid dynamics within the lung.

In a non-linear model, alveolar recruitment is influenced by the threshold pressures required to overcome the collapse, which vary non-linearly with lung volume and applied forces. As the lung inflates, recruitment occurs more dynamically, with individual alveoli or groups of alveoli opening suddenly, rather than uniformly across the lung. This non-linear behaviour is crucial for accurately capturing the lung's mechanical response, as it affects gas exchange efficiency and the overall distribution of ventilation. Modelling alveolar recruitment in a non-linear framework provides a more realistic understanding of lung function, especially in pathological conditions such as acute respiratory distress syndrome (ARDS), where the recruitment dynamics are significantly altered.

Modelling alveolar recruitment as a time-dependent phenomenon has been well established in literature, and has been validated in both human trials and mouse models [72, 73, 74]. Bates and Irvin in 2002 created a mathematical model of alveolar recruitment and de-recruitment, which gives room for significant expansion into a spatially heterogeneous system as required for this project [75]. In this model, each alveolus can be either fully open or fully closed, which is analogous to the alveolar popping seen in experimental study. The trajectory of each individual alveolus between these states is determined by the addition of a new coordinate between 0 and 1, shown in Figure 26, where 0 is fully closed and 1 is fully open.

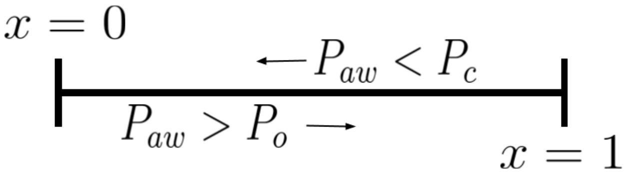

Figure 26: Visual representation of the virtual trajectory along which alveolar coordinate x moves between the limits 0 (fully closed) and 1 (fully open) with respect to the current airway pressure P_{aw} and the critical opening and closing pressures P_o and P_c. As depicted in [72].

The alveoli can move along the trajectory based on the compartmental pressure P_{aw}, but will remain in the same state until it hits 0 or 1. The direction x moves along the trajectory is based on where the compartmental pressure sits with respect to the threshold opening P_o and closing pressures P_c. The coordinate will move towards 0 when P_{aw} falls below P_c, and will move towards 1 when P_{aw} rises above P_o.

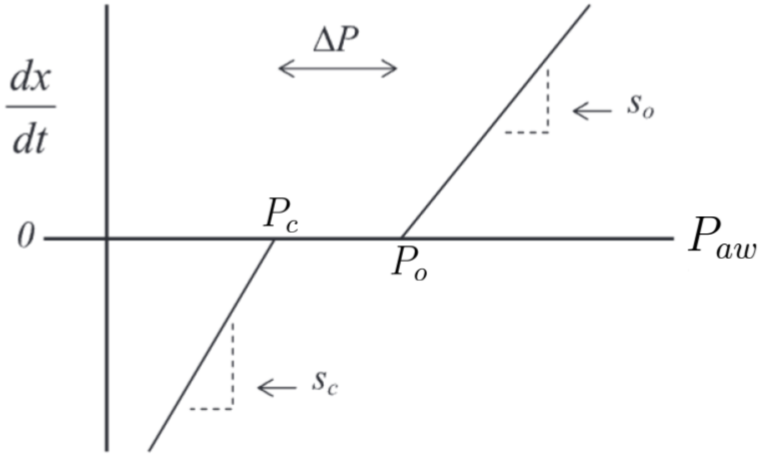

Figure 27: Visual representation of the rate of change of x, $\frac{dx}{dt}$, as a function of pressure. Constants s_o and s_c give the slopes for this rate increase once P_{aw} passes the critical pressures P_o and P_c. As depicted in [72].

The speed with which x moves along the virtual trajectory is proportional to the difference between P_{aw} and the threshold pressures. The more P_{aw} drop below P_c, the quicker it moves, for example. Constants of proportionality are s_o for opening directions and s_c for closing directions. This is represented in Figure 27. This can be summarised by the equation for the rate of change of x at the i^{th} alveolus with respect to time as:

$$\frac{dx_i(t)}{dt} = \begin{cases} s_{o_i}\left(P_{aw} - P_{o_i}\right), & \text{if } P_{aw} > P_{o_i}. \\ s_{c_i}\left(P_{aw} - P_{c_i}\right), & \text{if } P_{aw} < P_{c_i}. \\ 0, & \text{otherwise.} \end{cases} \tag{126}$$

The new value for x at the i^{th} alveolus at each time step is calculated using a first-order Euler integration as

$$x_i(t) = x_i(t - \Delta t) + \frac{dx_i(t)}{dt}\Delta t \tag{127}$$

The result of this setup is that there is a time delay between an alveolus reaching a threshold pressure and it changing state, which is much more analogous to the waterfall phenomena observed in the lungs [76]. This model setup allows for significant manipulation of pressures and threshold, which makes it a perfect test system for the importance of spatial heterogeneity in recruitment. We used a number of test scenarios to explore the importance of this phenomena in regional recruitment behaviour.

Figure 28 shows three scenarios simulated using this time-dependent recruitment model. In each case, the input pressure wave from the ventilator remains the same, and is simulated for two breaths. The count of open alveoli per unit area at each iso-gravitational plane is determined and utilized to calculate the percentage of the plane open at any particular time-step. Figure 28A depicts the results simulated when there is no regional variation in alveolar pressure, and threshold opening and closing pressures are constant throughout the lung.

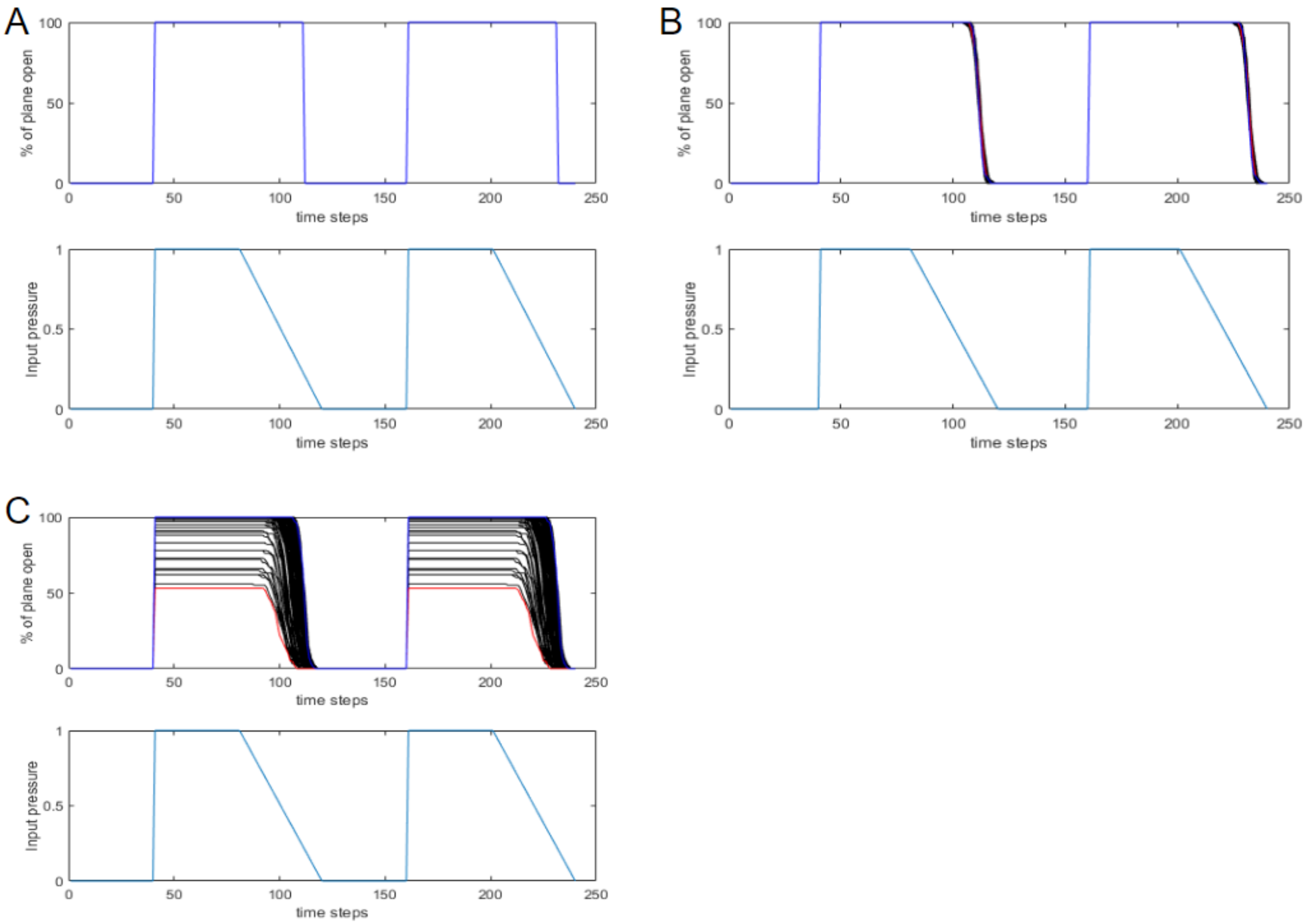

Figure 28: The regional recruitment of alveoli represented by the percentage of each plane open in different test scenarios. A depicts complete uniformity in the lung and the threshold pressures. B samples threshold pressures from a normal distribution to introduce some randomness. C adds spatial variation in both the thresholds and in the local compartmental pressures, to explore higher heterogeneity.

It can clearly be seen that the whole lung pops open and closed as a single unit, with the increase and decrease of input pressure. Figure 28B introduces an element of randomness into the threshold opening and closing threshold pressures, where the exact values for each alveolar unit is taken from a normal distribution about the average, such that:

$$P_{o_i} \in \mathcal{N}(\mu_{P_o}, \sigma_{P_o})$$

$$P_{c_i} \in \mathcal{N}(\mu_{P_c}, \sigma_{P_c})$$

where $N(\mu, \sigma)$ is the normal distribution with mean μ and standard deviation σ. Here there is a minimal degree of observable variation in the closing of the alveoli, indicating negligible heterogeneity.

In Figure 28C, the model now incorporates more significant spatial heterogeneity. Here, the threshold opening pressures are not only drawn from a normal distribution, they are also at a gradient from the bottom (dependent) to the top (non-dependent) region of the lung. This is in accordance with the results found by Scaramuzzo et al in 2020 [77], who used electrical impedance tomography to quantify the regional distribution of opening and closing pressures due to gravity in the lung parenchyma. Their finding being that the alveoli in the bottom (dependent) region of the lung have a higher opening and closing threshold than those in the top (non-dependent). This simulation also includes a gradient in the local alveolar pressure according to the results shown in the linear poroelastic model in Figure 25. This results in variation in the total percentage of open lung tissue. When the model begins with a full closed lung, the most dependent regions only open to 50%, where as the least dependent region open up to 100%, with all internal point spread between.

Visualising the impact of this waterfall alveolar model on the lung as a whole is best achieved by modelling the total volume of the lung against the airway pressures. To calculate the total lung volume in this model, we use the cylinder analogy as proposed in Chapter 4 of this thesis. Here, however, at each plane of the lung, the height of that particular section is determined by the percentage of open alveoli. The pressure is taken as the Mean Airway Pressure of the system.

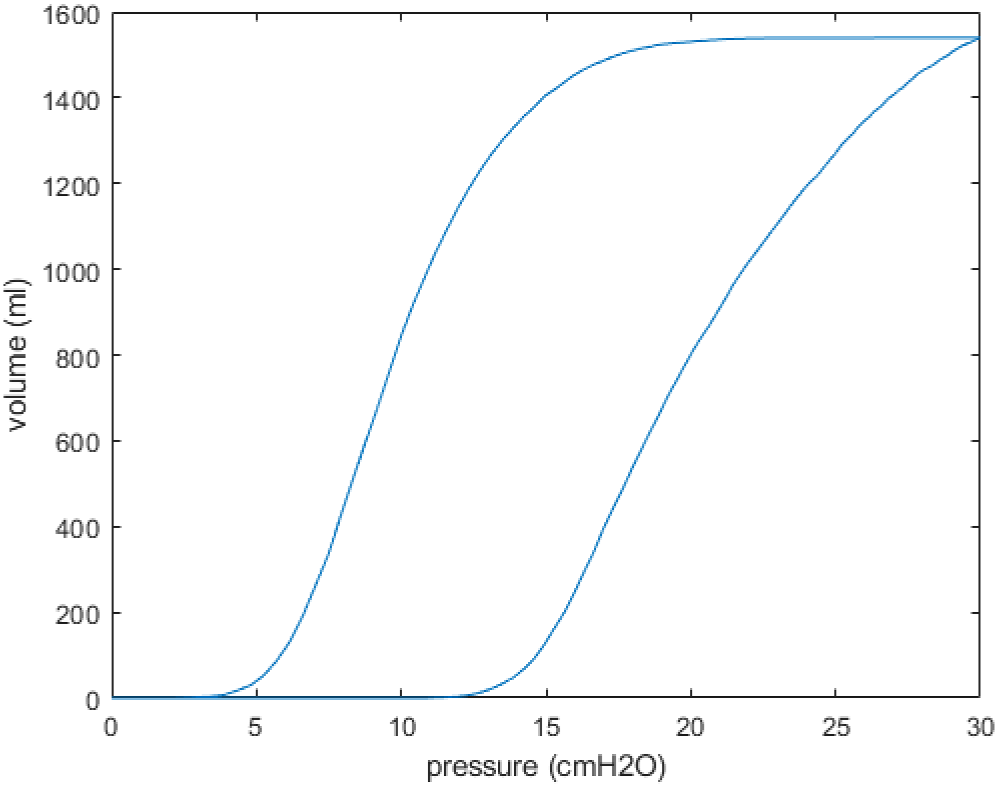

Figure 29: The S-shaped pressure-volume curve generated by the simulated waterfall model, incorporating full spatial heterogeneity in alveolar pressures and threshold opening/closing pressures. The curve exhibits a lower inflection point (LIP) at low volumes where alveoli non-linearly recruit, a linear middle portion as more alveoli open, and an upper inflection point (UIP) at high volumes where compliance decreases due to full inflation.

Figure 29 shows the pressure-volume curve created by the waterfall model with full spatial heterogeneity in alveolar pressures and in threshold opening and closing pressures. The shape of this curve is accurate to the "S-shaped" curve we generally expect in the lung [78], and is characterised by three regions. The lowest volumes and pressures of this graph are referred to as the lower inflection point (LIP). At low lung volumes, most alveoli are collapsed (atelectasis). This portion of the curve is flat, indicating that increasing pressure does not significantly increase lung volume. The gradual popping open of the alveoli in this section is highly non-linear. The second region is the Linear middle portion. As pressure increases, more alveoli are recruited, and the lung becomes more compliant. Here, the curve rises steeply as lung volume increases with relatively smaller increases in pressure. In the final section, the increasing pressures are no longer opening new alveoli, and dynamics become non-linear again. This is the upper inflection point (UIP). At high lung volumes, the lung is fully recruited, and compliance decreases again. This part of the curve flattens, indicating that further increases in pressure lead to little increase in lung volume, as most alveoli are already inflated.

Replicating these findings within a poroelastic framework is going to require significant alterations to the equations and constitutive relationships between parameters. The model must be expanded to include the specific dynamics observed in the lower inflection point and the upper inflection point of the pressure-volume curve.

6.3 Non-Linear Porosity and Permeability Interactions

The lower inflection point is the region in which alveolar recruitment is the dominant relationship. In the waterfall model, this was achieved by measuring the percentage of alveoli open in each region of the lung based on their threshold pressures. Within the poroelastic framework there are two underlying parameters that control this phenomenon, this is porosity ϕ and the permeability κ. Porosity refers to the fraction of the lung tissue that is occupied by air-filled spaces (alveoli and airways). It indicates how much space is available for air or fluid to occupy. Permeability refers to the ability of the porous tissue to allow fluids (air or liquid) to flow through it, influenced by the structure of the alveolar-capillary network. These are both well-embedded into the governing equation for the linear system (83-84). Previously, these have both been set as constants in space and time, which means that the percentage of the lung comprised of air remains constant throughout the breathing cycle; this is far from reality. Instead, the ratio of air to tissue should be determined by the amount of air already in the system, and how far the alveoli themselves have expanded from a reference position. The permeability of the lung, will in turn be affected by this non-linearity as the greater the void spaces in the tissue, the easier it is for fluid to be transmitted.

There are a number of models that have been proposed to incorporate non-linearity into the porosity and permeability variables. For this paper, I have chosen the Neo-Hookean Hyperelastic framework. Neo-Hookean hyperelasticity is a fundamental model in the theory of nonlinear elasticity, particularly describing the behaviour of rubber-like materials. It was introduced by Ronald Rivlin in the mid-20^{th} century as an extension of Hooke's law to large deformations [79, 80]. Unlike linear elasticity, which assumes small strains, neo-Hookean materials can undergo significant stretches while maintaining elasticity. Rivlin's contribution established the neo-Hookean model as a baseline for understanding more complex hyperelastic models, as it provides an essential framework for rubber elasticity and large strain mechanics.

The model is based on a strain-energy function W, which describes the energy stored in the material as a function of its deformation. For a neo-Hookean material, the strain-energy function depends only on the first invariant I_1 of the deformation tensor, and here shall take the form

$$W = \frac{\Lambda}{2}\left(I_1 - 3\right) - \Lambda \ln\left(J\right) \tag{128}$$

Where

$\Lambda =$ Lame 1st parameter, shear modulus

$I_1 =$ First invariant of the right Cauchy-Green deformation tensor $\mathbf{C}$

$J = \det \mathbf{F}$

$\mathbf{F} =$ deformation gradient tensor $= \left(\frac{\partial u_i}{\partial X_j} \right)_{ij}$

$u =$ deformation

$X =$ reference coordinate

Under the additional assumption of isotropy

$$I_1 = \|\mathbf{F}\|^2 = tr\mathbf{C} \tag{129}$$

where $\|\cdot\|$ denotes the Frobenius norm such that tr is the matrix trace. This gives the right Cauchy-Green tensor as

$$\mathbf{C} = \mathbf{F}^T\mathbf{F} \tag{130}$$

and the left Cauchy-Green tensor, referred to as the Finger deformation tensor, as

$$\mathbf{B} = \mathbf{F}\mathbf{F}^T \tag{131}$$

In order to integrate the hyperelastic relationships into a poroelastic model, porosity and permeability will need to be recalculated based on the given strain-energy function in 128. They can be updated to a hyperelastic context as deformation-dependent tensors. These coefficients depend on the skeleton deformation. Since its walls are incompressible, we can write:

$$\phi = 1 - \frac{1-\phi_0}{J} \tag{132}$$

Assuming further that the deformation of parenchyma is mainly volumetric and that the walls are thin (so that the shape of the pores remains the same, the only change being its size), we can also write:

$$\kappa = J^{\frac{2}{3}} \cdot \kappa_0 \tag{133}$$

where ϕ_0, κ_0 are the reference state values for the porosity and permeability respectively.

These new formulas can now be incorporated into the governing equations 83 and 84, and solved using the numerical methods as set out in section 6.5 of this thesis. Figure 30 shows the simulated waveform data for both this model and the linear equivalent, with the lung in the upright position. Reference state values at $t = 0$ are $\phi_0 = 0.7$ and $\kappa_0 = 10^{-5} m^3 s kg^{-1}$ as in [46]. A porosity value of 0.7 is analogous to 70% of the total lung volume comprising of air cavities, which concurs with experimental findings for the lung at FRC [49].

When we compare this simulation to the upright linear model, as in Figure 25A, there are a number of observable differences as well as important similarities. The total displacement magnitude remains consistent between the models, and alveolar distribution between the base and apex is unchanged. The primary difference lies in pressure distributions across the lung. In the non-linear model, pressures exhibit visibly greater spatial consistency across the lung. There is also a substantial reduction in the magnitude of the inspiratory spike, referred to as the pure resistive pressure drop [81]. The pure resistive pressure drop in the context of pulmonary mechanics refers to the region of the lung where significant resistance to airflow occurs due to various factors, including the me-

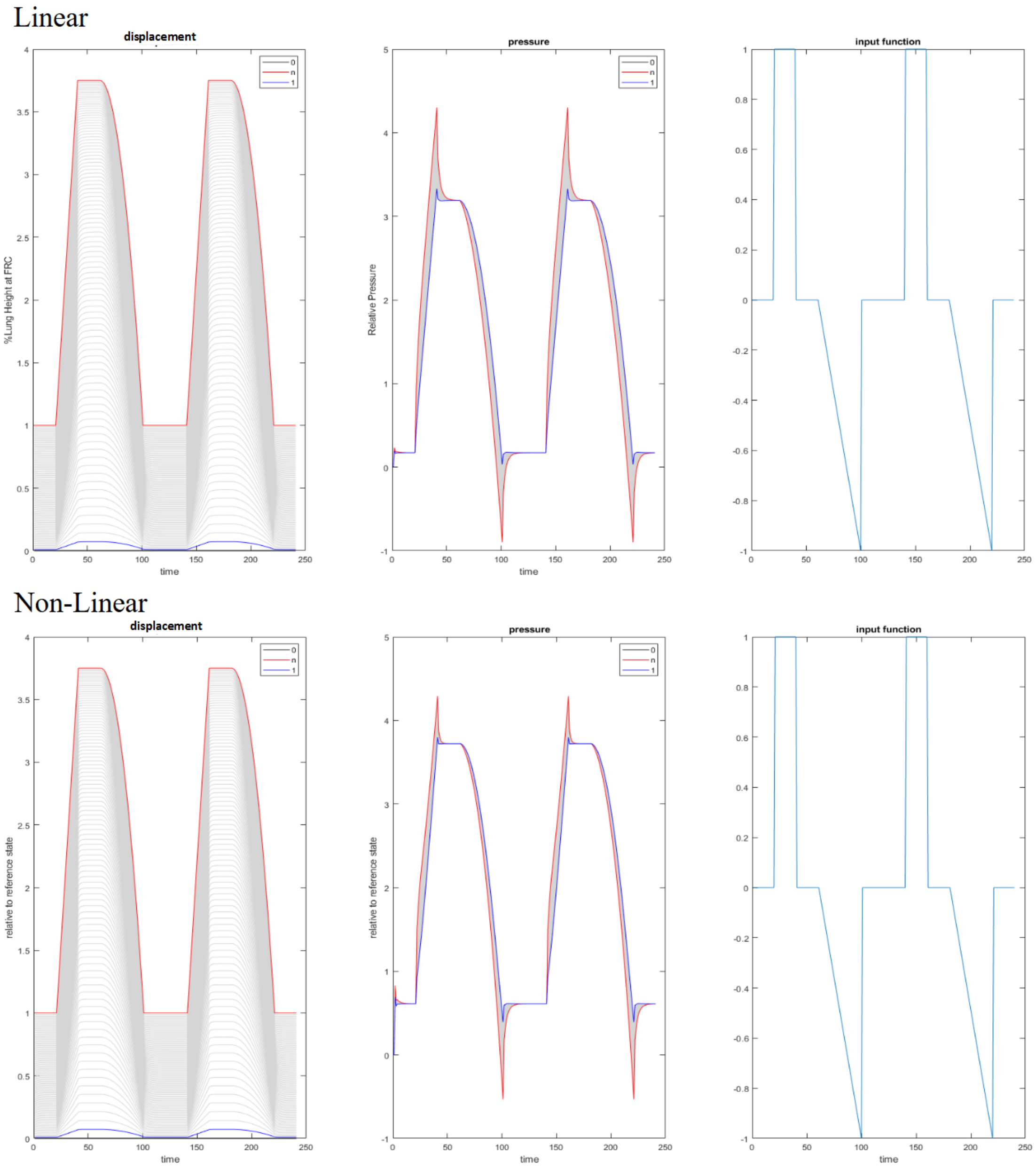

Figure 30: Simulated ventilator waveform data for non-linear neo-Hookean hyperelastic model of porosity and permeability, compared to the linear model. Lung is in the upright position and simulated over two breathing cycles. Linear is the top row and non-linear is the bottom.

chanical properties of the lung tissue and the airways. There are a number of reasons for these observations.

Non-linear poroelasticity accounts for strain-dependent stiffness: as the lung inflates, the tissue becomes stiffer, leading to more gradual and controlled deformation. In contrast, linear model assumes constant stiffness, which overestimates stress concentrations near high-flow zones and underestimates it elsewhere. This means non-linear models distribute ventilation and interstitial pressures more evenly, especially at moderate to high lung volumes. In the linear model, the material does not stiffen as it deforms. Thus, during rapid inflation (like inspiration), it tends to accumulate stress quickly at boundaries, causing a sharp spike in airway/alveolar pressure. The non-linear model naturally damps this response. As the tissue stiffens with volume, it limits the rapid volume-dependent increase in stress, creating a smoother, slower rise in pressure, i.e., no sudden spike. Also, porosity–strain coupling in non-linear poroelastic models buffers abrupt volume transitions, distributing pressure over time and space. Although the macroscopic (global) deformation is matched between models (same tidal volume/displacement), the non-linear model requires more local pressure to reach those deformations—because stiffness increases with stretch. This means at higher lung volumes, non-linear models reflect the increased alveolar recoil pressure that is physiologically observed, resulting in higher local and average pressures, even if displacement is similar.

We can explore this further by tracking the average values for porosity and permeability throughout the breathing cycle.

Figure 31 illustrates the dynamic changes in average permeability and porosity over a two-breath cycle. It indicates that porosity, which represents the fraction of lung tissue occupied by air-filled spaces, increases from approximately 0.7 at functional residual capacity (FRC) to 0.92 at the end of inspiration. The

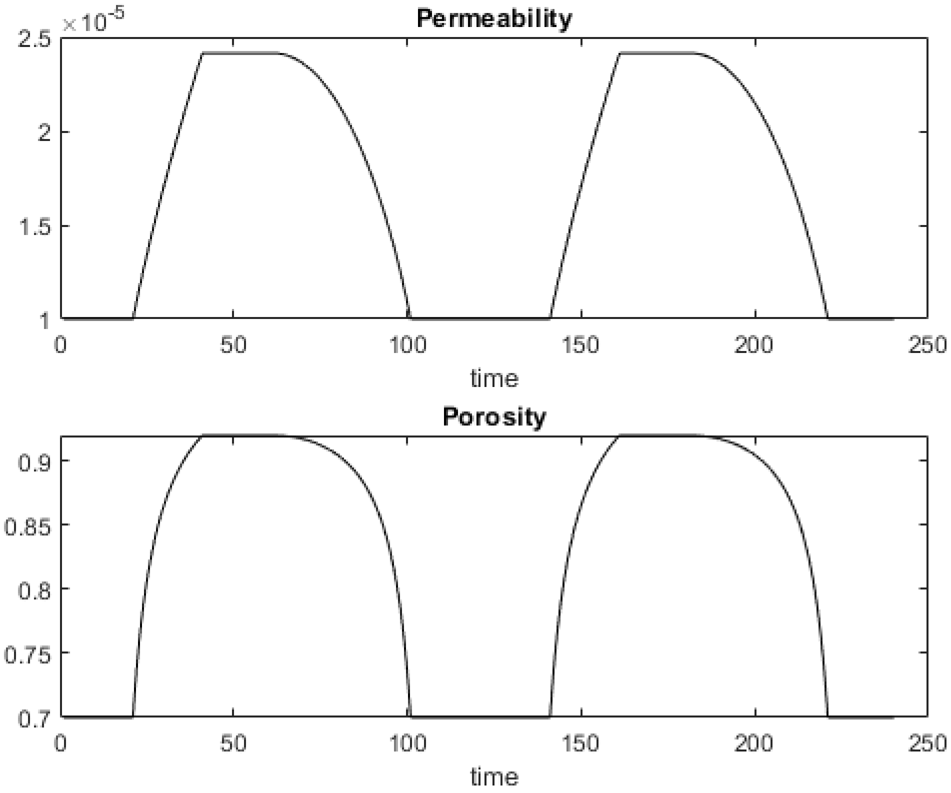

Figure 31: Average values for permeability (m^2) and porosity across the lung, over a two-breath cycle.

model also shows that permeability increases to 2.5 times its reference value during inspiration. These dynamic changes are strongly supported by specific experimental findings from medical imaging and morphological studies.

The dynamic behaviour of porosity is directly reinforced by studies quantifying lung density and volume changes. For instance, Brown et al. (2015) utilized CT scans to measure lung tissue density in a large cohort of human subjects at both full inspiration (total lung capacity, TLC) and end expiration (FRC) [82]. Their results revealed a strong correlation, with larger lungs exhibiting lower mean lung density. Critically, they found that the mean lung density decreased as the lung inflated from FRC to TLC. Since Hounsfield units (HU) directly measure tissue density, with -1000 HU representing air and 0 HU representing water, a decrease in density signifies an increase in air content, or porosity. The theoretical curve presented by Brown et al., which modelled lung density changes based on air inflation while assuming a fixed tissue volume of 900 mL, remarkably closely matched their empirical data from 500 subjects at both FRC and TLC. This finding robustly supports the non-linear model's premise that overall lung volume changes are primarily accommodated by variations in air volume (porosity) rather than changes in tissue volume or the formation of new alveoli. Converting Brown et al.'s observed HU ranges to porosity (using the approximation $\phi = -HU/1000$ as HU approaches -1000 for air and 0 for water, simplifying the fraction calculation with given HU values [83]), the visually estimated FRC densities of approximately -650 to -800 HU correspond to porosities of 0.65 to 0.80, which encompasses this model's initial porosity value of 0.7. Similarly, their observed TLC densities, ranging from roughly -800 to -900 HU, correspond to porosities of 0.80 to 0.90, aligning well with this model's end-inspiratory porosity of 0.92.

Further validation for porosity dynamics comes from Choi et al. (2013), who employed a mass-preserving image registration technique on CT images of human lungs at TLC and FRC [83]. Their research explicitly demonstrated that the difference in tissue volume (TV) between TLC and FRC was negligible, approximately 0.03 to 0.04 litres in normal subjects and severe asthmatics, respectively. This supports the fundamental assumption in the non-linear poroelastic model that tissue volume remains largely constant during lung deformation, with changes in total lung volume primarily attributed to changes in air volume (AV). Choi et al. reported average air volumes of 1.57 litres at FRC and 4.14 litres at TLC for normal subjects, representing a significant increase in air content with inflation. Their methodology for calculating air fraction (porosity) using specific Hounsfield unit values (with HUair at -1000 and HUtissue at 55) provides a direct link between CT intensity and porosity, empirically demonstrating that as the lung inflates, the air fraction (porosity) increases. While the sources do not directly provide specific numerical values for permeability, the observed changes in porosity indirectly validate the permeability dynamics in Figure 31. Permeability is inherently linked to the size and connectivity of air spaces; as porosity increases during inspiration (as quantitatively supported by the aforementioned studies), the pathways for airflow naturally become larger and more open, thereby increasing permeability. The non-linear poroelastic model inherently couples porosity and permeability to tissue deformation, establishing a robust physiological basis for the model's dynamic permeability behaviour.

These simulations are a promising result for the neo-hookean non-linear model of the lung, and display more physiologically relevant dynamics than those of the linear model. Porosity and permeability now being coupled to the tissue deformation has resulted in temporal dynamics accurate to those found in experimental literature utilising a range of computer imaging techniques. However, they do not capture all the key features of the lung's complex material mechanics.

Figure 32 shows the simulated pressure-volume curve for the poroelastic lung with non-linear porosity and permeability. Both the values and general shape of this curve are accurate to experimental findings, however two regions are lacking in dynamical complexity. Region A, highlighted in blue, is the area in which alveolar recruitment and airway resistance are the dominant mechanics. This is analogous to the Lower Inflection Point depicted in Figure 29. In this model the region is not changing in a continuous manner. Conversely, region B, highlighted

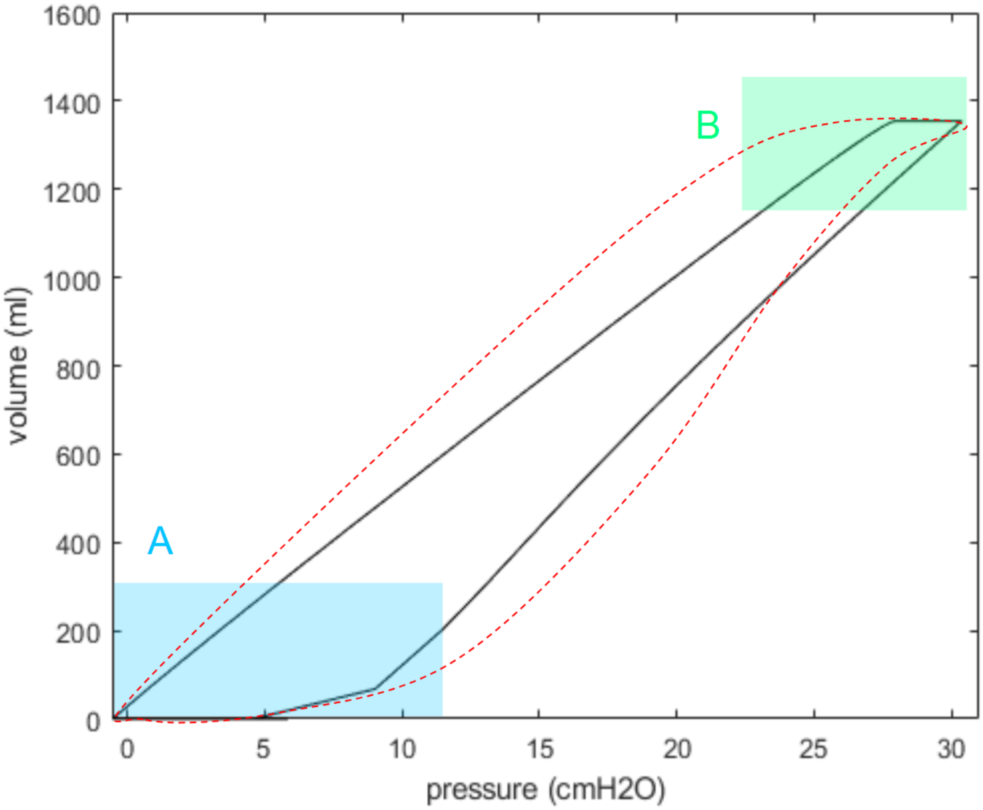

Figure 32: Pressure-volume curve for the poroelastic lung with non-linear porosity and permeability. Region A is the alveolar recruitment zone and region B is the alveolar over-distension zone. The red dotted line represents a theoretical pressure-volume curve taken from [78].

in green, is the area in which alveolar distension is the dominant mechanism. We would expect this region to exhibit the typical "S-shape" commonly associated with the lung pressure-volume curve [78]. This is a complex elastic response in which the alveoli stiffen at higher pressures, and is not captured by porosity-permeability interactions.

Although the inclusion of deformation-dependent permeability and porosity has captured the general relationship between pressure and volume in the lung over the breathing cycle, the more intricate dynamics surround recruitment and over distension are lost. This requires further extension to the non-linear poroelastic model.

6.4 Neo-Hookean Hyperelasticity Governing Equations

In the real world, many materials do not behave linearly under large deformations. If elasticity were constant, as in classical Hookean models, it would fail to capture how materials actually behave under varying loads or strains. Biological tissues, for example, tend to exhibit stiffening as they are stretched to their upper limits [44, 47]. This requires a significant increase in complexity as alveolar elasticity must now not only a function of spatial location, but also of the extent to which that alveolus has already stretched and deformed from it's reference state. In the Neo-Hookean framework, this is achieved by evaluating elasticity as a spatial tensor.

These derivations are based in part on the FEBio: Finite Elements for Biomechanics software suite as presented in [84]. In order to make elasticity deformation-dependent, we first define a new variable $\bar{J}$ which represents the pore volume ratio:

$$\bar{J} = \frac{J - 1 + \phi_0}{\phi_0} \tag{134}$$

which in turn means that

$$\phi = \phi_0 \cdot \frac{\bar{J}}{J} \tag{135}$$

$$\frac{\partial \bar{J}}{\partial J} = \frac{1}{\phi_0} \tag{136}$$

such that when $\phi = 0$ the pore is closed.

We now define a modified deformation gradient

$$\bar{\mathbf{F}} = \left(\frac{\bar{J}}{J}\right)^{\frac{1}{3}} \cdot \mathbf{F} \tag{137}$$

such that $det\left(\bar{\mathbf{F}}\right) = \bar{J}$.

The corresponding modified right Cauchy-Green tensor becomes

$$\bar{\mathbf{C}} = \bar{\mathbf{F}}^T \cdot \bar{\mathbf{F}} = \left(\frac{\bar{J}}{J}\right)^{\frac{2}{3}} \mathbf{C} \tag{138}$$

so that

$$\frac{\partial \bar{\mathbf{C}}}{\partial \mathbf{C}} = \left(\frac{\bar{J}}{J}\right)^{\frac{2}{3}} \cdot \left(\frac{\phi_0^s}{3\left(J - \phi_0^s\right)} \mathbf{C} \otimes \mathbf{C}^{-1} + \mathbf{I} \odot \mathbf{I}\right) \tag{139}$$

where ϕ_0^s is the solid portion of the material such that $\phi_0^s = 1 - \phi_0$.

Using these modified parameters in the constitutive relationship:

$$\bar{W} = \frac{\Lambda}{2}\left(\bar{I}_1 - 3\right) - \Lambda \ln\left(\bar{J}\right) \tag{140}$$

where $\bar{I}_1 = tr\bar{\mathbf{C}}$. This relation shows that the material develops an infinite strain energy density as $\bar{J}$ approaches zero. Λ is Lamé's 1^{st} parameter, referred to as the shear modulus.

From this expression, the 2^{nd} Piola-Kirchhoff stress is given by

$$\mathbf{S} = 2\frac{\partial \bar{W}}{\partial \mathbf{C}} = \Lambda \left[\left(\frac{\bar{J}}{J}\right)^{\frac{2}{3}} \mathbf{I} + \frac{1}{J - \phi_0^s}\left(\phi_0^s \left(\frac{\bar{J}}{J}\right)^{\frac{2}{3}} \frac{I_1}{3} - J\right) \mathbf{C}^{-1}\right] \tag{141}$$

When $\mathbf{C} = \mathbf{I}$, it can be verified that $\mathbf{S} = 0$. The corresponding Cauchy stress is

$$\sigma = \frac{\Lambda}{J}\left[\left(\frac{\bar{J}}{J}\right)^{\frac{2}{3}} \mathbf{b} + \frac{1}{J - \phi_0^s}\left(\phi_0^s \left(\frac{\bar{J}}{J}\right)^{\frac{2}{3}} \frac{I_1}{3} - J\right) \mathbf{I}\right] \tag{142}$$

where $\mathbf{b}$ is the left Cauchy-Green tensor.

The material elasticity tensor is given as

$$\begin{aligned}\mathbb{C} &= 2\frac{\partial \mathbf{S}}{\partial \mathbf{C}} \\ &= \frac{2}{3}g(J)\left(\mathbf{I}\otimes\mathbf{C}^{-1}+\mathbf{C}^{-1}\otimes\mathbf{I}\right)+\left(J\frac{dg}{dJ}\frac{I_1}{3}+J\frac{dh}{dJ}\right)\mathbf{C}^{-1}\otimes\mathbf{C}^{-1} \\ &-2\left(g(J)\frac{I_1}{3}+h(J)\right)\mathbf{C}^{-1}\odot\mathbf{C}^{-1}\end{aligned} \tag{143}$$

where

$$\begin{aligned}f(J) &= \Lambda\left(\frac{\bar{J}}{J}\right)^{\frac{2}{3}} \\ g(J) &= \frac{\phi_0^s}{J-\phi_0^s}f(J) \\ h(J) &= -\mu\frac{J}{J-\phi_0^s}\end{aligned}$$

and

$$\begin{aligned}J\frac{dg}{dJ} &= \Lambda\frac{\left(2\phi_0^s-3J\right)\phi_0^s}{3\left(J-\phi_0^s\right)^2}\left(\frac{\bar{J}}{J}\right)^{\frac{2}{3}} \\ J\frac{dh}{dJ} &= \Lambda\frac{J\phi_0^s}{\left(J-\phi_0^s\right)^2}\end{aligned}$$

The spatial elasticity tensor is thus evaluated as

$$\mathcal{C} = J^{-1}\left[\frac{2}{3}g(J)\left(\mathbf{b}\otimes\mathbf{I}+\mathbf{I}\otimes\mathbf{b}\right)+\left(J\frac{dg}{dJ}\frac{I_1}{3}+J\frac{dh}{dJ}\right)\mathbf{I}\otimes\mathbf{I}-2\left(g(J)\frac{I_1}{3}+h(J)\right)\mathbf{I}\odot\mathbf{I}\right] \tag{144}$$

This tensor is currently configured for a three-dimensional system. However, the poroelastic lung model developed during this project is one-dimensional in order to directly explore the gravitational impacts on lung dynamics. Therefore, 144 must be reduced to a single dimension.

6.5 Reduction to 1-Dimensional System

To reduce 144 from into a single dimension, parallel to gravity, we focus on the scenario where deformations occur only along the vertical (x) axis and set deformations along the other axes to zero.

When confined to one dimension, the deformation gradient tensor F simplifies as follows:

$$F = \begin{pmatrix} \frac{\partial\xi}{\partial X} & 0 & 0 \\ 0 & 1 & 0 \\ 0 & 0 & 1 \end{pmatrix} \tag{145}$$

The Jacobian determinant J becomes:

$$J = \frac{\partial\xi}{\partial X} \tag{146}$$

In this case, there is no deformation in the y- and z-axes, so we simplify the tensors to only reflect changes along the x-axis.

The tensor $b \otimes I + I \otimes b$ reduces to a scalar because only the xx-component remains non-zero. The second term I_1 (the trace of the right Cauchy-Green tensor) simply reduces to $I_1 = (\frac{\partial\xi}{\partial X})^2$.

In one dimension, the Cauchy stress tensor reduces to a scalar stress along the x-axis. The elasticity tensor simplifies, reflecting only the normal stress component along this axis. Thus, 144 becomes a function of only the x-component of the stress and strain, which can be expressed as:

$$C_{1D} = J^{-1}\left[\frac{2}{3}g(J) + \left(J\frac{dg}{dJ}\frac{I_1}{3} + J\frac{dh}{dJ}\right) - 2\left(g(J)\frac{I_1}{3} + h(J)\right)\right] \tag{147}$$

where all quantities are now scalar values related to the deformation along the x-axis; this is a *zeroth* rank tensor.

To fully integrate this with the poroelastic governing equations for the linear system (83,84), we now rewrite this tensor in terms of the deformation u. In one dimension, the deformation gradient tensor F simplifies to:

$$F = \frac{\partial \xi}{\partial X} \tag{148}$$

where $\xi(X,t) = X + u(X,t)$, so:

$$F = 1 + \frac{\partial u}{\partial X} \tag{149}$$

The Jacobian J becomes:

$$J = \det(F) = 1 + \frac{\partial u}{\partial X} \tag{150}$$

Next, we rewrite the first invariant I_1 in terms of $u(X,t)$:

$$I_1 = \left(1 + \frac{\partial u}{\partial X}\right)^2 \tag{151}$$

the reduced form of 144 becomes:

$$C_{1D} = J^{-1}\left[\frac{2}{3}g(J) + \left(J\frac{dg}{dJ}\frac{I_1}{3} + J\frac{dh}{dJ}\right) - 2\left(g(J)\frac{I_1}{3} + h(J)\right)\right] \tag{152}$$

Substitute $J = 1 + \frac{\partial u}{\partial X}$ and $I_1 = \left(1 + \frac{\partial u}{\partial X}\right)^2$, yielding:

$$\begin{aligned} C_{1D} =& \frac{1}{1+\frac{\partial u}{\partial X}}\left[\frac{2}{3}g\left(1 + \frac{\partial u}{\partial X}\right) + \left(\left(1 + \frac{\partial u}{\partial X}\right)\frac{dg}{dJ}\frac{\left(1+\frac{\partial u}{\partial X}\right)^2}{3} + \left(1 + \frac{\partial u}{\partial X}\right)\frac{dh}{dJ}\right)\right. \\ &\left. - 2\left(g\left(1 + \frac{\partial u}{\partial X}\right)\frac{\left(1+\frac{\partial u}{\partial X}\right)^2}{3} + h\left(1 + \frac{\partial u}{\partial X}\right)\right)\right], \end{aligned} \tag{153}$$

where:

$$
\begin{aligned}
f(J) &= \Lambda \left(\frac{J - 1 + \varphi_0}{J} \right)^{2/3} \\
g(J) &= \frac{\varphi_0^s}{J - \varphi_0^s} f(J) \\
h(J) &= -\frac{\Lambda}{J(J - \varphi_0^s)}
\end{aligned}
\tag{154}
$$

Substituting the Jacobian in terms of deformation, these become:

$$
\begin{aligned}
f(u) &= \Lambda \left(\frac{\varphi_0 + \frac{\partial u}{\partial X}}{1 + \frac{\partial u}{\partial X}} \right)^{\frac{2}{3}} \\
g(u) &= \frac{\varphi_0^s}{1 + \frac{\partial u}{\partial X} - \varphi_0^s} \Lambda \left(\frac{\varphi_0 + \frac{\partial u}{\partial X}}{1 + \frac{\partial u}{\partial X}} \right)^{\frac{2}{3}} \\
h(u) &= -\frac{\Lambda}{(1 + \frac{\partial u}{\partial X})(1 + \frac{\partial u}{\partial X} - \varphi_0^s)}.
\end{aligned}
\tag{155}
$$

Moreover, the derivatives become:

$$
\begin{aligned}
\frac{df}{dJ} &= \Lambda \cdot \frac{2}{3} \left(\frac{\varphi_0 + \frac{\partial u}{\partial X}}{1 + \frac{\partial u}{\partial X}} \right)^{-1/3} \cdot \frac{1 - \varphi_0}{\left(1 + \frac{\partial u}{\partial X}\right)^2} \\
\frac{dg}{dJ} &= \frac{\varphi_0^s}{\left(1 + \frac{\partial u}{\partial X} - \varphi_0^s\right)^2} \Lambda \left(\frac{\varphi_0 + \frac{\partial u}{\partial X}}{1 + \frac{\partial u}{\partial X}} \right)^{2/3} + \frac{\varphi_0^s}{1 + \frac{\partial u}{\partial X} - \varphi_0^s} \frac{df}{dJ} \\
\frac{dh}{dJ} &= \Lambda \left[\frac{1}{\left(1 + \frac{\partial u}{\partial X}\right)^2 \left(1 + \frac{\partial u}{\partial X} - \varphi_0^s\right)} + \frac{1}{\left(1 + \frac{\partial u}{\partial X}\right) \left(1 + \frac{\partial u}{\partial X} - \varphi_0^s\right)^2} \right]
\end{aligned}
\tag{156}
$$

By substituting C_{1D} for the constant elasticity E in the governing linear equations, as well as the non-linear porosity and permeability functions described in section 7.3, we can now simulate the full non-linear poro-hyperelastic neo-Hookean model.

6.6 Results for the Neo-Hookean Hyper-poroelastic Model

The non-linear aspects of this model have increased the complexity of the system significantly, and so there are many variables that can now be explored. In order to assess the dynamics of this model against the linear model, we begin by simulating the ventilator waveform data in the upright position.

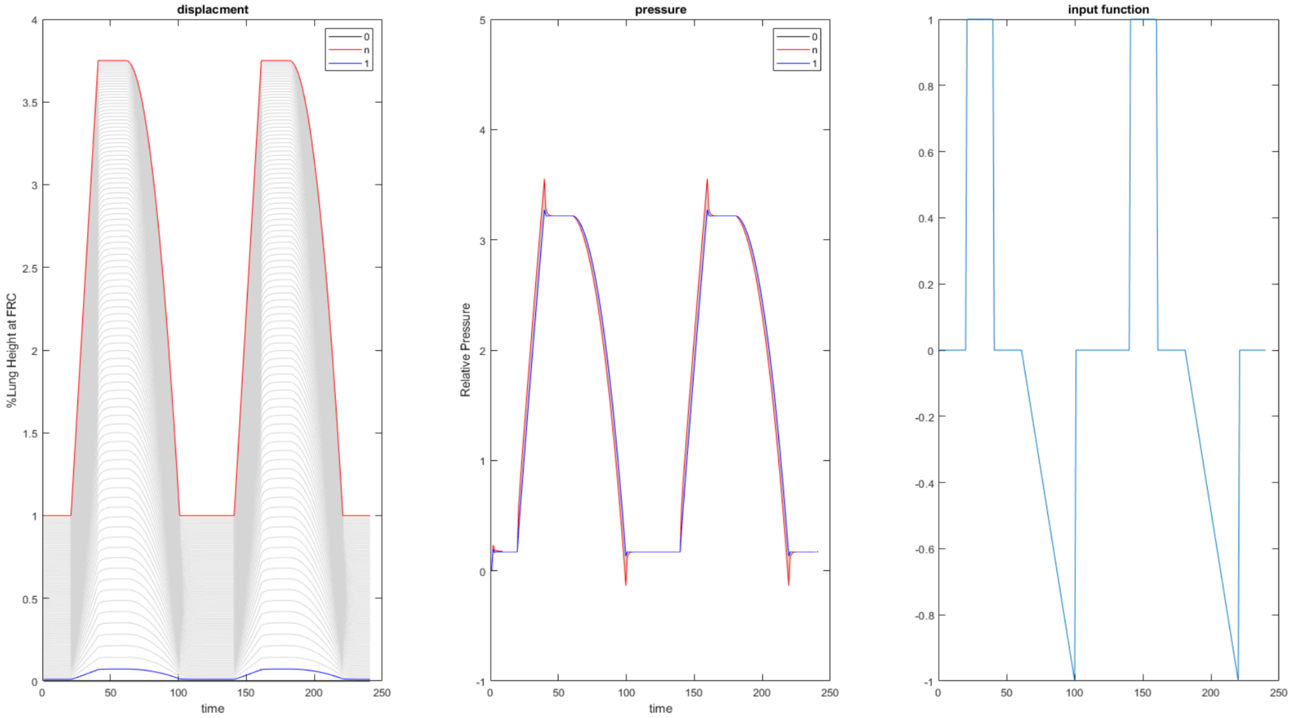

Figure 33: Simulated ventilator waveform data for fully non-linear neo-hookean hyperelastic model of the lung. Lung is in the upright position and simulated over two breathing cycles.

Figure 33 shows the waveform data for the fully non-linear model in the upright position, using the same set up as described for the linear and partially non-linear models shown in Figure 30. As before $\phi_0 = 0.7$ and $k_0 = 10^{-5} m^3 s kg^{-1}$. The overall displacement is unchanged between the models as expected. The most important difference is in the pressure field. In the fully non-linear model, lower relative pressures are required to achieve the same level of displacement we see in the previous simulations, as well as a significant reduction in spatial variation in alveolar pressure at maximum inflation. This is due to the non-linear elastance behaviour, coupled with the specific set up of this model. The alveolar pressure here is calculated only as the internal air pressure resulting from inflation, not including the complexities of pleural pressure and external body pressures which give rise to non-uniformity in the lung experimentally. There is also no accounting for the branching nature of the airways, which naturally deliver a varying airflow to different alveolar regions. As such, we expect to see a smoothing of the alveolar pressures at maximum inflation. This is an important observation in this model, that the poroelastic framework must be coupled with further physiological systems in order to fully capture the total lung dynamics accurately.

Dynamics that are captured extremely well in this model are the non-linear behaviours observed in the pressure-volume curve of the lung. The neo-Hookean hyper-poroelastic elasticity equation contains functions for both the sequential opening and closing of alveoli at low volumes, but also the stiffening of alveolar tissue when they are over-distended at maximum inflation.

Figure 34 shows this pressure-volume curve. As for the partially non-linear model in 32, two regions are highlighted; the region in which alveolar recruitment and airway resistance are the dominant mechanics in region A (blue), and region B (green), in which alveolar distension is the dominant mechanic.

The lower inflection point in region A, is no longer a segmented line, but is now a smooth continuous curve. This means that the alveoli are opening in a sequential waterfall pattern as discussed in section 7.2. Conversely, in region B there is now a smooth descending curve as pressure decreases. This is the area in which alveoli alveoli are becoming less stiff after over-distension, and so

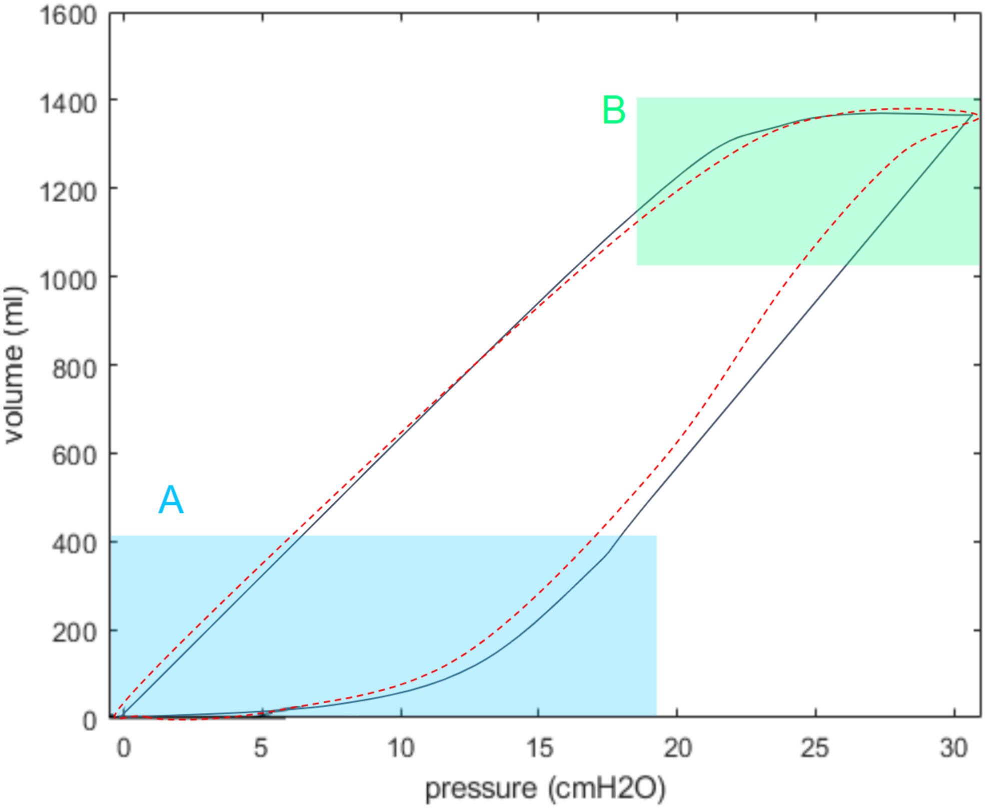

Figure 34: Pressure-volume curve for the fully non-linear poroelastic lung with non-linear porosity and permeability and neo-Hookean hyper-poroelastic elasticity. Region A is the alveolar recruitment zone and region B is the alveolar over-distension zone. The red dotted line represents a theoretical pressure-volume curve as in [78].

volume is decreasing slower than pressure.

The successful replication of the characteristic ’S-shaped’ pressure-volume (P-V) curve, including the smoothly continuous lower inflection point (Region A) and the curvilinear upper inflection point (Region B), is a critical advancement for clinical relevance. In ICU practice, identifying these inflection points is paramount for optimizing Positive End-Expiratory Pressure (PEEP) to maximize alveolar recruitment while avoiding over-distension. This model can serve as an ’in-silico’ tool to predict patient-specific P-V curves, allowing clinicians to tailor PEEP settings to individual lung mechanics, thus minimizing atelectrauma (collapse) at low volumes and volutrauma (over-stretching) at high volumes, crucial for protective ventilation strategies.

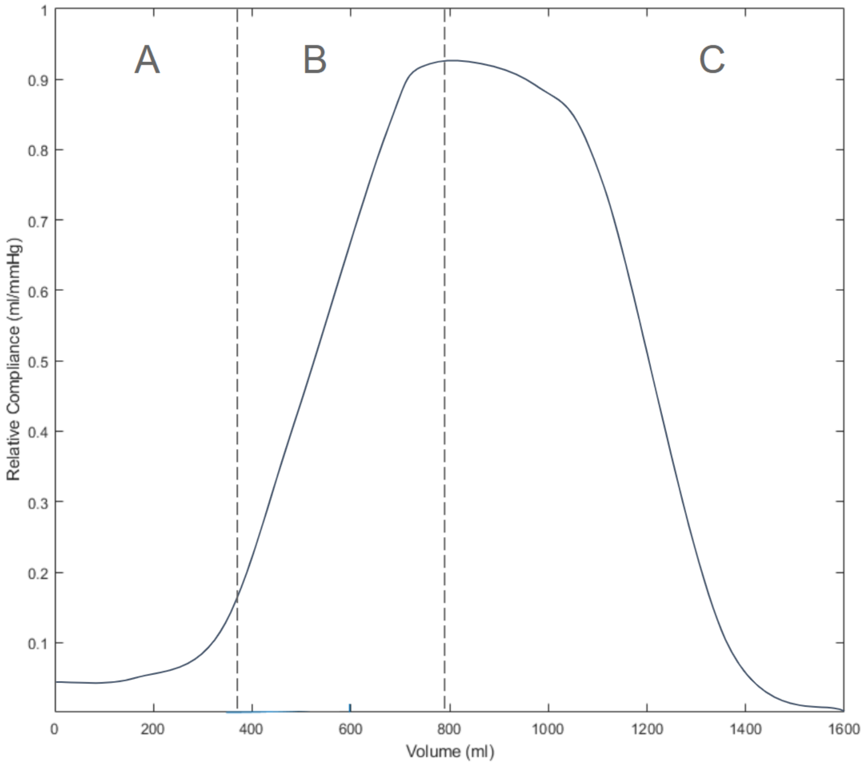

Figure 35: Alveolar compliance plotted against volume in the fully non-linear model. Section A shows gradual increase in compliance as alveoli open (recruitment zone). Section B represents a linear relationship where all alveoli are open and compliance increases with expansion. Section C demonstrates decreasing compliance as alveoli become over-distended, reflecting the stiffening of alveolar tissue.

We can explore this deeper by tracking the change in alveolar compliance as the volume of the alveolus increases. Here compliance is taken as the inverse of elastance calculated using the neo-Hookean hyper-poroelastic equation. Figure 35 displays this dynamic split into three sections. In section A, alveolar compliance gradually increases as the lung expands, with the non-linear curve reflected the popping open of alveoli in this region. This is due to the increased pressure required to open the alveoli from its closed position. In section B, we reach a linear relationship. Here, all alveoli are open and the compliance of the alveoli increases in line with expansion. Finally, in section C we have reached a point where the alveoli are beginning to become over-distended. This results in the stiffening of the alveolar tissue and so compliance decreases again. This is confirmation that alveolar tissue behaves much like that of a rubber balloon. A similar compliance curve is seen in [85], as part of a digital twin model created within the CHIMERA hub.

The dynamic changes in alveolar compliance, exhibiting initial increase (Section A) and subsequent decrease (Section C) at high volumes, directly mirror the 'rubber balloon' analogy of lung mechanics. In a clinical context, understanding this non-linear compliance response is vital for preventing lung injury. The model's ability to show stiffening at high volumes (Section C) suggests that exceeding certain tidal volumes can rapidly increase localized stress, even with seemingly modest volume changes. This reinforces the principle of limiting tidal volumes and using patient-specific data to avoid the injurious 'flat top' of the P-V curve, where further pressure increases yield minimal volume gain but significant mechanical stress.

6.7 Concluding Remarks

This chapter extended the linear poroelastic framework to incorporate non-linear dynamics, emphasizing the necessity of such enhancements for accurately modelling lung tissue mechanics under both physiological and pathological conditions. By integrating neo-Hookean hyperelasticity and non-linear interactions of porosity and permeability, the model captures complex behaviours such as alveolar recruitment, over-distension, and regional compliance changes during the breathing cycle. These features allow the model to reproduce the sigmoidal pressure-volume (P–V) relationship observed experimentally, including critical landmarks such as the lower and upper inflection points—parameters directly relevant to clinical practices such as PEEP titration.

The model's ability to reflect the complex interplay between geometry, time-dependent tissue mechanics, and spatial gradients provides a deeper mechanistic understanding of how ventilation strategies and body positioning influence alveolar dynamics. In particular, the finding that alveolar recruitment is more progressive and uniform in the prone position lends strong support to the clinical use of proning as a lung-protective strategy. This suggests that prone positioning reduces the simultaneous presence of collapsed and overdistended units, minimising mechanical heterogeneity, an insight especially relevant in the management of ARDS and COVID-19-associated ARDS, where lung injury is often patchy and non-uniform. In such cases, the model supports strategies that prioritise position-based optimisation over reliance on aggressive recruitment manoeuvres or high PEEP levels, which carry a risk of further injury through overdistension.

The model also offers predictive insights into the regional risk of ventilator-induced lung injury (VILI), showing how variable tissue properties and gravity-dependent deformation patterns affect local stress distributions. By simulating these complex interactions, the model helps identify vulnerable regions (particularly in non-dependent, hyperinflated areas) and supports individualised adjustment of ventilator pressures based on a patient's postural mechanics and injury profile. These findings reinforce the potential for personalised ventilation strategies that go beyond protocolised care.

Importantly, this framework is also applicable beyond classical ARDS. In patients with traumatic injuries (such as rib fractures or post-lobectomy states), the model enables prediction of regional compliance loss and guides postural strategies to offload or protect compromised regions. Similarly, for obese patients or those recovering from abdominal surgery—where elevated abdominal pressures and diaphragm displacement alter baseline lung mechanics—the model helps anticipate the potential benefits of prone or semi-prone positioning in relieving dependent compression and improving overall ventilation distribution.

Although currently one-dimensional, this model's high spatial resolution enables detailed tracking of clinical parameters as they evolve over time and gravity. This dimensional limitation was a deliberate design choice to ensure computational efficiency and facilitate future integration into digital twin frameworks for real-time clinical decision support. Nonetheless, the lack of heterogeneity in the coronal and axial planes must be acknowledged, particularly for diseases like ARDS that exhibit strong spatial variation in multiple dimensions. The exclusion of chest wall mechanics and interactions with branching airway structures also limits full physiological fidelity, especially for modelling the active mechanics of awake, spontaneously breathing patients.

Despite these constraints, the non-linear model marks a substantial advance over its linear predecessor, more accurately reflecting the underlying biology of alveolar mechanics and providing insights of direct clinical relevance. The successful replication of experimental findings—including improved P–V curves and realistic pressure distributions, such as reduced inspiratory pressure spikes—validates its use as a foundation for future, more comprehensive models.

The final chapter of this thesis will focus on coupling this non-linear poroelastic model with additional physiological subsystems—such as branching airways, vasculature, and chest wall mechanics—to more fully capture the complexity of lung dynamics. Particular emphasis will be placed on how these systems interact across different body positions, enabling high-granularity simulation of regional ventilation and perfusion. By preserving the unique spatial structure of the current model, this future work aims to provide clinicians with precise, position-sensitive tools for optimising respiratory care in diverse and critically ill patient populations.

7 A Coupled Pulmonary Model based on Non-linear Poroelastics

7.1 Introduction

This final modelling chapter synthesizes the advancements from previous stages to create a comprehensive, coupled pulmonary model designed for robust clinical inference. The objective is to integrate the non-linear poroelastic lung tissue model with key external physiological systems, including the branching upper airways and pulmonary blood circulation, while also incorporating external thoracic pressures. I hypothesize that this fully coupled model will accurately predict regional ventilation-perfusion (V/Q) ratios across different patient positions and reliably assess localized mechanical power delivery, thereby identifying areas at risk for ventilator-induced lung injury (VILI). The overarching clinical questions addressed are: How do the complex interactions between mechanical ventilation, airway structure, blood flow, external pressures, and patient positioning collectively influence regional gas exchange efficiency and the localized risk of VILI? This comprehensive model is necessary for translating theoretical understanding into actionable clinical insights, enabling in-silico experimentation to optimize ventilator settings and patient positioning strategies for improved outcomes in mechanically ventilated patients.

The previous chapters of this thesis have focused on building and validating a mathematical model of lung tissue based on biomechanical approaches. It has been shown that these models can accurately replicate the distortion of the alveoli throughout the breathing cycle, including complex phenomena such as the Slinky Effect, alveolar recruitment and over distension. However, in order to use these models for clinical inference, we need to account for the wider picture of factors influencing the measurements taken at the ICU bedside. This will allow the model to eventually be parametrised using individual patient data.

In this chapter, we extend the model to incorporate the interaction between the upper airways and the deeper pulmonary structures, critical in understanding how the ventilator moves air through the respiratory system and to the alveolar units. This allows for a more detailed exploration of ventilation and perfusion as it varies spatially, by introducing external pressures, hydrostatic gradients in blood flow, and the intricate nature of the lung's branching airways that give rise to the waveforms we see at the bedside. We also delve into how patient positioning, whether upright, supine, or prone, affects the distribution of ventilation and perfusion within the lung. The differences in these distributions have a direct impact on the ventilation-perfusion (V/Q) ratio, an important indicator of lung efficiency [14, 25]. A mismatch in V/Q can lead to regions of the lung being either over-ventilated or under-perfused, resulting in impaired gas exchange [57]. By analysing these positional effects within the poroelastic model, we aim to provide a clearer understanding of how to optimize patient care through positioning strategies.

Towards the end of this chapter, we will use this model to explore a number of important clinical questions. Of particular interest within pulmonary modelling currently is the concept of mechanical power as it relates to Ventilator-Induced Lung Injury (VILI), and whether the ventilator outputs can be used to predict the risk of damage to a patient's lungs. Here, we will implement the mechanical power formulation presented by Gattinoni in 2016 to assess ventilator-related causes of lung injury [36]. This will then be extended into the poroelastic model, to identify any regions of the lung most susceptible to trauma, and the implications of this trauma on the overall mechanics of the tissue.

7.2 Connection to Upper Airways

Regional ventilation in the lung is in part determined by the amount of air reaching each of the terminal branches in the airway tree. This is due to the complex fractal nature which is notably asymmetric, resulting in heterogeneity in the volume of air arriving to an alveolus [38]. Airway resistances, pressures, and flows all depend on the size and length of each airway segment as it varies through the branch generations, and so a model needs to be able to incorporate this phenomenon.

The branching airways in the human lung consist of over 16 million individual airway segments, and, with the asymmetrical bifurcations, this creates an incredibly complex system. In order to visualise this, data was taken from a paper published by Weibel in 1991, which has been well cited in the literature as a base for the mathematical modelling of the airway tree [86]. This data is a representation of the respiratory tract of an average adult with a lung volume of $4800cm^3$ at roughly 75% total lung capacity.

Figure 36 depicts the key morphological variables of the airway structure, separated into generation number. As standard, the trachea is noted as generation 0, the bronchi from 1-3 and so on until the alveolar sacks at generation 23. As this thesis is concerned with patient receiving mechanical ventilation in the ICU, a generation -1 has been added to represent an endotracheal tube of typical dimensions. The top left graph shows an exponential increase in the number of branches with each successive generation, especially beyond generation 15. The length of airways decreases sharply in the early generations, stabilizing at a relatively small value after around generation 5. There is a notable peak at generation 4, this is due to the specific shape of the pulmonary lobes, requiring this bifurcation to be slightly longer. The average diameter of the airways reduces rapidly through the generations. There is a slight increase from the

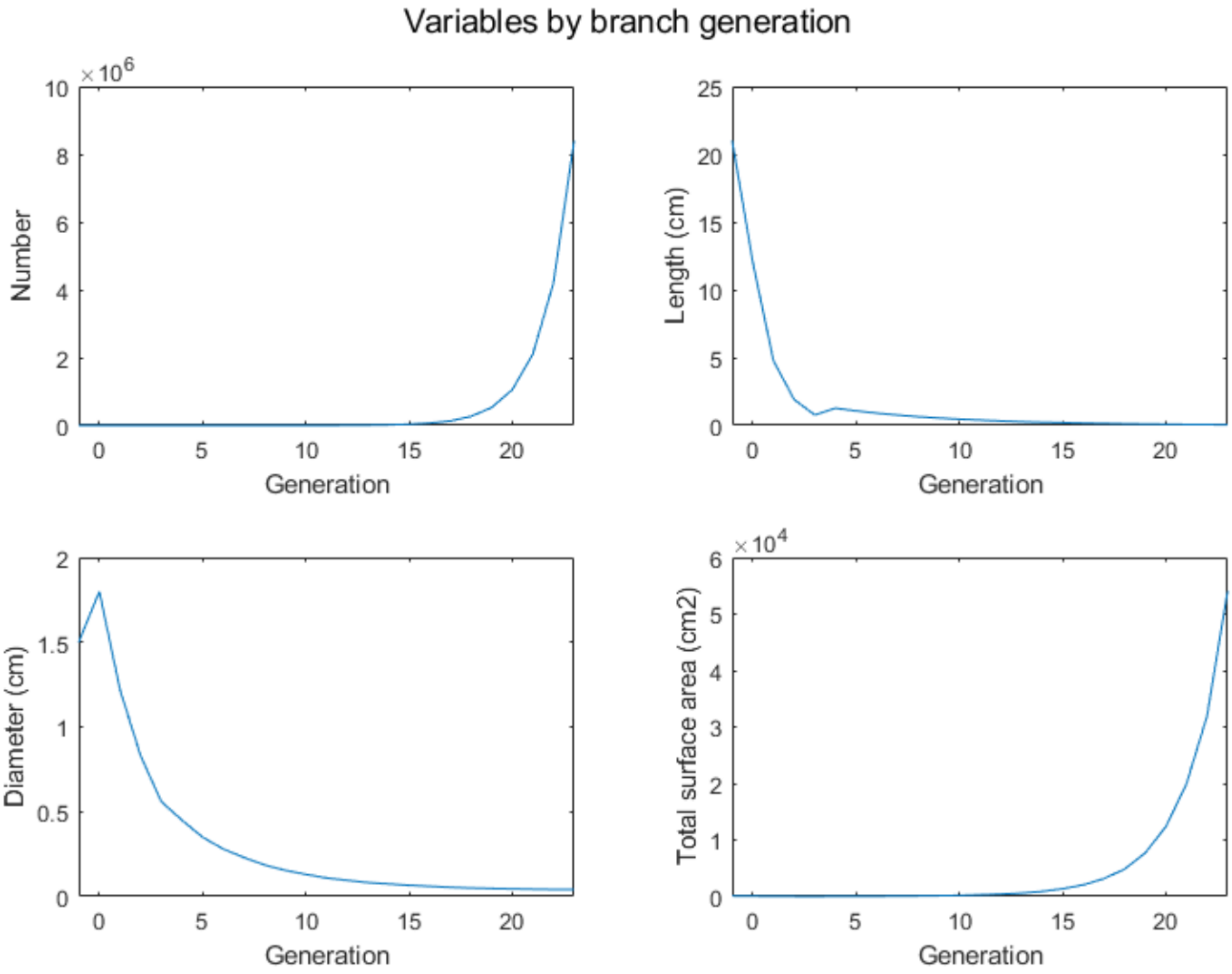

Figure 36: Graph of the representative data of the respiratory tract of an average adult with a lung volume of $4800cm^3$ at roughly 75% total lung capacity, with respect to the tree generation. Top left: The number of segments in each generation. Top right: The average length at each generation. Bottom left: The average diameter at each generation. Bottom right: The total surface area at each generation. Adapted from Weibel 1991 to include the endotracheal tube [86].

endotracheal tube to the trachea, as the tube must be able to fit safely in the trachea during mechanical ventilation. Despite the length and diameter of the airways decreasing as generation number increases, the shear number of segments at each generation increases so quickly that the total surface area of each generation has an exponential increase. This can be seen in the bottom right graph, and is a fantastic visual representation of the vast surface area of the alveolar sacs, as to how the lung maximizes gas exchange so effectively.

It is these specific branching measurements that affect regional airflow to the alveoli, as the varying pipe lengths and diameters significantly alter the local resistance to flow and subsequent drop in pressure. Airflow through the majority of the lung is laminar, with smooth flow and negligible mixing, although can exhibit turbulent flows in the large trachea and main bronchi particularly during high flow rates associated with heavy breathing [87]. For this model we will assume all flow to a laminar approximation for simplicity. This means that the pressure drop from the beginning of a particular segment to the end of that segment can be described by Poiseuille's law, neglecting inertial effects. This law states that laminar flow rate of an incompressible fluid along a pipe is proportional to the fourth power of the pipe's radius [88], such that:

$$\Delta P = \frac{8L\mu q}{\pi r^4}, \tag{157}$$

where ΔP is the pressure difference between the two ends of the pipe segment, is the length of the segment, r is the radius of the segment, μ is the dynamic viscosity of the fluid, and q is the volumetric flow rate of the fluid. We then can take the resistance to flow in that segment as the ratio of the pressure difference to the airflow.

$$R = \frac{\Delta P}{q} \tag{158}$$

Therefore the resistance is written

$$R = \frac{8L\mu}{\pi r^4} \tag{159}$$

In these equations we assume conservation of airflow through throughout the airway tree. In order to complete the branching from the ventilator down to the alveolar sacs, we must calculate the pressure at the end of each segment given the pressure at the beginning, where this end pressure becomes the beginning pressure for the next segment and so on. This allows us to estimate the pressure, resistance and flow at the alveolar sacs, directly from the ventilator settings at the endotracheal tube.

$$P_{i,2} = P_{i,1} - \frac{8L_i\mu}{\pi r_i^4} \cdot q \tag{160}$$

Here $P_{i,1}$ is the pressure at the beginning of the i^{th} pipe segment, and $P_{i,2}$ is the pressure at the end of the i^{th} pipe segment. The length of the i^{th} pipe is L_i and the radius is r_i. Finally, μ is the dynamic fluid viscosity of the air in the branches, and q is the flow rate through the pipe segment. Flow rate is calculated according to the cross-sectional area of the branch segment A_i and the flow velocity v as $q = A_i \cdot v$. We can now plot the pressure and resistance changes through the branches using the data presented in Figure 37 [86].

Pressures and resistances are shown for a single tube at each generation, with the model assuming all branches in the same generation are identical. Figure 37 shows a near linear drop in pressure from the endotracheal tube down to generation 4, and then an exponential decay in pressure down to the parenchyma. This is because, after the 4th generation the pipes begin to become significantly shorter and narrower. The resistances in Figure 38 show some interesting dynamics. We begin with zero resistance at the opening of the endotracheal tube

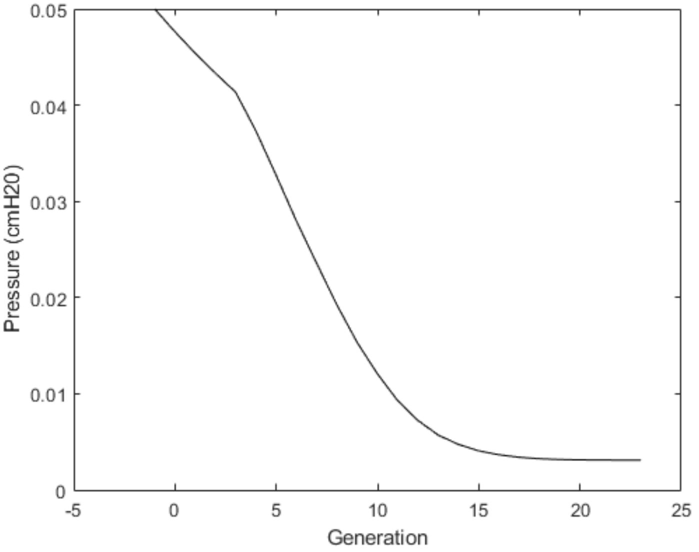

Figure 37: Average pressure in each of the branch generations down the airway tree.

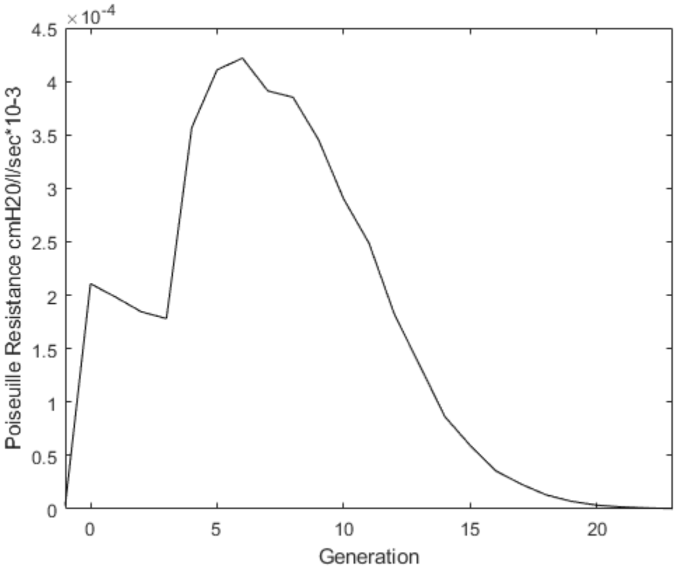

Figure 38: Average resistance in each of the branch generations down the airway tree.

as we assume this is where flow begins, with resistance increasing significantly by the start of the trachea. There is then a slight decline in resistance down to generation 4. This is because the total cross-sectional area in these early generations increases despite the individual airway diameters becoming smaller, as seen in Figure 36. This is due to the multiplicative branching nature of the airway tree. While the diameter of each branch decreases, the number of branches increases, resulting in a larger combined cross-sectional area. After this there is a sharp increase in resistance to the maximum resistance reached at generation 6, the beginning of the terminal bronchioles. This is because the airway diameter has become significantly smaller, but the total cross-sectional area hasn't yet increased enough to offset the narrowing. After this resistance decreases exponentially down to the alveoli, as the total surface area is now increasing rapidly, seen in Figure 36.

Having now proven the importance of airway structure and the precise mechanics apparent in the bifurcating tree, we now need to couple this network into the existing poroelastic model. This can be achieved by replacing the source term in the governing equations to a flux from the airway tree as it reaches the parenchyma such that

$$\frac{\partial^2 u}{\partial x \partial t} - \kappa \frac{\partial^2 p}{\partial x^2} = \Phi(x)_{terminal} \tag{161}$$

where $\Phi(x)_{terminal}$ is the air flux at the terminal node of the branching tree at height x on the isogravitational plane set up.

Using 160 for the pressure drop from the beginning to end of one pipe segment, we can create a summarising equation for the total pressure drop from the ventilator input to these terminal nodes. Summing resistances we can calculate the the total pressure drop from the ventilator to the end of the N^{th} airway generation as

$$\Delta P = q \sum_{i=1}^{N} R_i \tag{162}$$

To find the outlet flux for the terminal branch, we require the pressures at the start and end of this pipe. We assume that all flow is conserved through the system. A visual representation of this is shown in Figure 39. Airflow q travels from the ventilator at P_{vent} through to the endotracheal tube (ETT) at generation -1. From there it travels through each of the airways to the terminating branch at the end of generation 22 P_{term-1}, to the alveoli opening at generation 23 P_{term}.

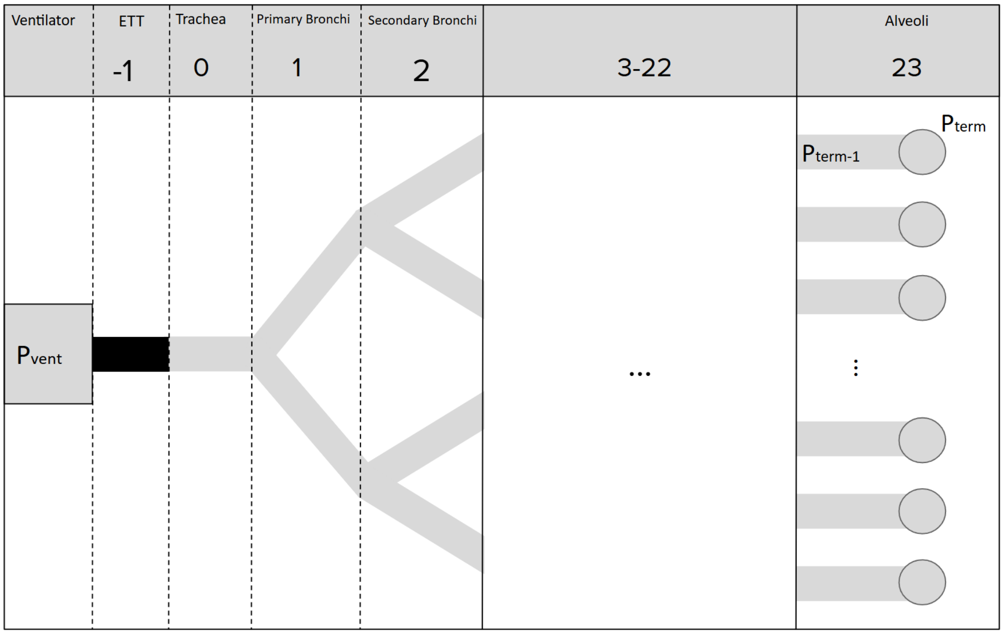

Figure 39: Visual representation of airflow through the branching airway network in an intubated patient. Airflow originates from the ventilator P_vent, passes through the endotracheal tube (ETT, generation -1), and continues through successive airway generations to the terminal branch ($P_term - 1$) and ultimately the alveoli (P_term), assuming conservation of flow throughout the system.

The corresponding equations are

$$P_{term} = P_{vent} - q \sum_{i=1}^{term} R_i \tag{163}$$

$$P_{term-1} = P_{vent} - q \sum_{i=1}^{term-1} R_i \tag{164}$$

Finally, the flux can be calculated using the Poiseuille equation as

$$\Phi_{term} = \left(\frac{A_{term}}{8\pi\mu} \right) \cdot \frac{P_{term} - P_{term-1}}{L_{term}} \tag{165}$$

where A_{term} is the cross-sectional area of the terminal branch, and L_{term} is the length of the terminal branch.

Having now created a more intricate system for the delivery of air from the ventilator to the alveoli, we can extend the model to include spatially varying ventilation in the lung.

7.3 Ventilation and Perfusion

The importance of ventilation and perfusion variation was discussed in detail in the literature review portion of this thesis (Section 3.14), and was modelled briefly in the solid mechanics chapter (Sections 4.8-4.10). However, the temporally dynamic set up of the poroelastic model will require a much more intricate set up. For the alveolar ventilation, we must couple the poroelastic model into the upper airways network.

For a single alveolar compartment i, the ventilation is defined as the volume of air moving in/out of the i^{th} alveolus at a single timestep, according to 41. This is calculated as:

$$Flow_{comp_i} = \frac{P_{Trachea} - P_{comp_i}}{R_{UpperAirway} + R_{comp_i}} \tag{166}$$

where $P_{Trachea}$ is the tracheal pressure, $R_{UpperAirway}$ is the upper airway resistance, and R_{comp_i} is the inlet resistance of the i^{th} compartment. We take the pressure in the i^{th} alveolar compartment P_{comp_i} as the pressure waveform created by the poroelastic matrix, with inclusion for the non-linear stiffness of the alveoli E and external pressure gradients according to

$$P_{comp_i} = E_i \left(V_{comp_i} - V_{col}\right)^2 - P_{ext_i} \tag{167}$$

as in equation 42. $P_{Trachea}$ is calculated using 163 as

$$P_{trachea} = P_{vent} - q \cdot R_{trachea} \tag{168}$$

where

$$R_{trachea} = \frac{8 \cdot L_{trachea} \cdot \mu}{\pi \cdot r_{trachea}^4}$$

P_{vent} is the pressure set at the ventilator; the opening of the endotracheal tube. The resistance of the upper airways is a constant, and the resistance at the i^{th} compartment is calculated as

$$R_{comp_i} = \frac{8 \cdot L_{term} \cdot \mu}{\pi \cdot r_{term}^4} \tag{169}$$

$L_{trachea}$, $r_{trachea}$, L_{term} and r_{term} are the length and radius of the trachea and terminal airway respectively.

Substituting these into 41 gives the updated equation for airflow at the i^{th} compartment as

$$Flow_{comp_i} = \frac{P_{vent} - \frac{q \cdot 8 \cdot L_{trachea} \cdot \mu}{\pi \cdot r_{trachea}^4} - P_{comp_i}}{R_{UpperAirway} + \frac{8 \cdot L_{term} \cdot \mu}{\pi \cdot r_{term}^4}} \tag{170}$$

We finally need to extend the pressure in the i^{th} compartment to include the external pressures (P_{ext}) exerted on the lungs by the rest of the body and gravity. These pressures are taken from experimental studies performed to determine the gradient parallel to gravity of the extrinsic pressures applied to the lung, primarily results from Bryan in 1974 and West in [89, 90]. This gives the final equation as

$$Flow_{comp_i} = \frac{P_{vent} - \frac{q \cdot 8 \cdot L_{trachea} \cdot \mu}{\pi \cdot r^4_{trachea}} - (P_{comp_i} - P_{ext})}{R_{UpperAirway} + \frac{8 \cdot L_{term} \cdot \mu}{\pi \cdot r^4_{term}}} \tag{171}$$

A similar approach can be taken for the updating of the perfusion equation, 43, to fit into the poroelastic framework. For a single alveolar compartment i, the perfusion is defined as the volume of blood passing through the i^{th} capillary unit in a single timestep.

$$Q_{comp_i} = \frac{\Delta P_{vessels}}{PVRi} \tag{172}$$

where $\Delta P_{vessels}$ is the pressure difference between pulmonary artery, vein and the alveolus, according to West's Zones of the lung [7]. The pulmonary vascular resistance of the i^{th} capillary unit which feed the alveolus, $PVRi$, must be calculated as it's own branching tree system.

$$PVRi = \frac{8 \cdot L_{capillary} \cdot \mu}{\pi \cdot r^4_{capillary}} \tag{173}$$

where μ is the dynamic viscosity of the blood, and $L_{capillary}$ and $r_{capillary}$ are the length and radius of the i^{th} capillary respectively.

Combining these gives the overall estimated bloodflow at the i^{th} alveolus as

$$Q_{comp_i} = \frac{\Delta P_{vessels} \cdot \pi \cdot r^4_{capillary}}{8 \cdot L_{capillary} \cdot \mu} \tag{174}$$

Finally, we need to separate this equation by the laws of the West Zones of the lung, such that the dominant pressure interactions are controlling the flow.

$$Q_{comp_i} = \begin{cases} 0, & \text{if } P_{comp_i} > P_a > P_v. \\ \frac{\left(P_a - P_{comp_i}\right)\cdot\pi\cdot r^4_{capillary}}{8\cdot L_{capillary}\cdot\mu}, & \text{if } P_a > P_{comp_i} > P_v. \\ \frac{(P_a - P_v)\cdot\pi\cdot r^4_{capillary}}{8\cdot L_{capillary}\cdot\mu}, & \text{if } P_a > P_v > P_{comp_i}. \end{cases} \tag{175}$$

where P_a is the pressure in the pulmonary artery and P_v is the pressure in the pulmonary vein. This allows us to calculate the ventilation perfusion ratio as

$$\left(\frac{V}{Q}\right)_{comp_i} = \frac{Flow_{comp_i}}{Q_{comp_i}}, \tag{176}$$

and we can now explore the gravitational distribution of perfusion, ventilation and the V/Q ratio at different points in the breathing cycle.

It is important to note that not all air in the lung is contributing to gas exchange. Dead space refers to areas within the respiratory system where ventilation occurs but gas exchange is absent. This includes anatomical dead space, the volume of air in the conducting airways (like the trachea and bronchi) that does not participate in gas exchange, and alveolar dead space, which is the volume of air in ventilated alveoli that are not perfused with blood. A notable example of alveolar dead space occurs in West's Zone 1, where alveolar pressure exceeds perfusion pressures, completely restricting blood flow. The sum of anatomical and alveolar dead space is termed physiological dead space. Conversely, a shunt occurs when blood flows through the pulmonary circulation but does not participate in gas exchange, bypassing ventilated alveoli—effectively, perfusion without ventilation. Understanding these concepts is essential, as the mismatch between ventilation and perfusion (V/Q ratio) directly impacts the efficiency of gas exchange and is a critical indicator of lung function. The model in this thesis focusses only the air flow and blood flow in the lung, not gas exchange explicitly, therefore these features would need to be included if gas exchange were to be modelled.

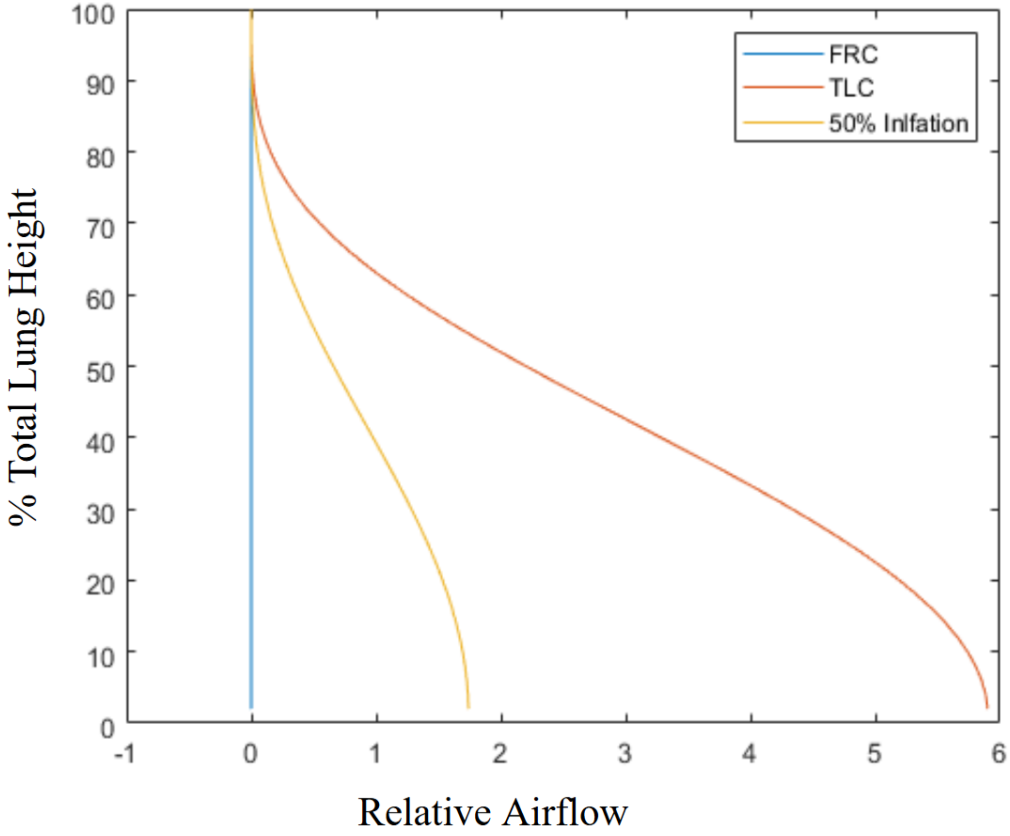

Figure 40: Relative airflow in the alveoli as a function of vertical height, at FRC, TLC and 50% inflation. Lung is in the upright position.

Figure 40 illustrates the distribution of relative airflow as a function of vertical lung height (expressed as a percentage of total lung height) at three different lung volumes: Functional Residual Capacity (FRC), 50% inflation, and Total Lung Capacity (TLC). The x-axis represents relative airflow, while the y-axis represents the vertical position within the lung, with 0% being the base and 100% being the apex. At FRC, airflow is shown as uniform across the lung height, indicating that ventilation is zero throughout, which is characteristic of a resting or end-expiratory state. At 50% inflation, the yellow curve demonstrates a skew in airflow distribution, with greater airflow occurring in the lower (dependent) regions of the lung. This reflects the gravitational gradient of pleural pressure and lung compliance. The base of the lung, being more compliant at mid-inflation, receives more airflow compared to the apex. This is consistent with biological reality: during normal tidal breathing, the lower parts of the lung generally receive better ventilation due to increased compliance and favourable pleural pressure. At TLC, the red curve becomes even more skewed, showing dramatically increased airflow at the base and minimal airflow at the apex. This results from reduced compliance at high lung volumes, particularly in the upper lung regions, which are already near maximal inflation and therefore resist further expansion. Meanwhile, the lower lung regions can still accommodate more volume, leading to a larger airflow directed there. Overall, this graph reflects fundamental principles of pulmonary physiology, including the effects of gravity, regional compliance, and pleural pressure gradients on ventilation distribution. It illustrates how ventilation becomes more heterogeneous with increasing lung inflation, favouring the dependent (lower) lung regions due to their greater capacity to expand.

Figure 41 shows the relative perfusion to the alveoli at each isogravitational plane, at FRC, TLC and 50% inflation. Of important note here are the size and positions of each of the three West Zones, as these dynamics are essential to understanding lung function. At all levels of lung inflation, perfusion is greatest in the dependent (lower) regions of the lung and decreases steadily toward the apex. This distribution pattern is primarily due to the effects of gravity on pulmonary blood flow. Blood is a relatively heavy fluid, and under upright conditions, hydrostatic pressure causes more blood to pool in the lower parts of

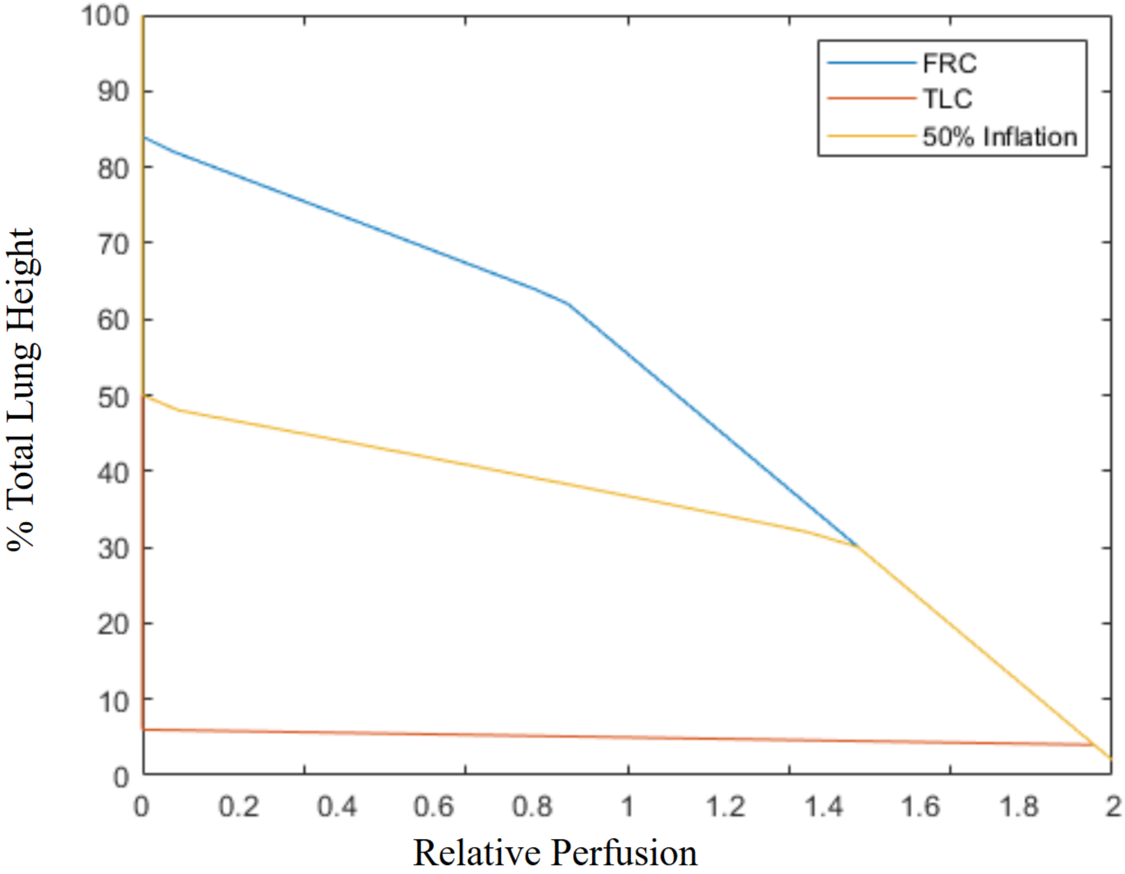

Figure 41: Relative perfusion in the alveoli as a function of vertical height, at FRC, TLC and 50% inflation. Lung is in the upright position.

the lung, enhancing perfusion there. At FRC, blood flow is maximised , with only the top 17% of the lung falling into the Zone 1 category where blood flow is entirely restricted by the size of the alveoli. From 65% to 83% we see Zone 2, where blood flow is controlled by the gradient between the pulmonary artery and the pressure in the alveolus. The bottom 65% of the lung fall into Zone 3, where blood flow is maximised and is simply a gradient between the pulmonary artery and pulmonary vein. This aligns with known physiology: the pulmonary vascular resistance is lower in the bottom (dependent) zones, promoting more blood flow in these regions. As the alveoli expand to the mid-point of inflation, more of the lung enters Zone 1, as the alveoli are now larger and constricting the blood vessels. The top 50% of the lung is now unperfused. Approximately 15% falls into Zone 2 and the bottom 35% is in Zone 3. Finally, at TLC we see almost the entire lung is now exhibiting the behaviour of West Zone 1, with negligible blood flow. This is because nearly all alveoli are fully expanded and blood vessels are being severely compressed. This is a very interesting observation, as the reduction of Zone 1 is one of the primary goals of clinicians when selecting ventilator settings. During spontaneous breathing, Zone 1 is small, but the forced pressures of mechanical ventilation create this dynamic. This graph reflects the classic zone model of pulmonary perfusion [7], where gravity and lung inflation influence vascular pressures and resistances, resulting in perfusion being highest at the base and lowest at the apex. As lung volume increases, overall perfusion decreases, especially in the upper lung, due to stretching and compression of pulmonary vessels. This has direct implications for ventilation-perfusion (V/Q) matching and gas exchange efficiency across different postures and breathing states.

Having now looked at each component separately, we can assess the ratio between ventilation and perfusion as an indicator of gas exchange and overall lung function.

Figure 42 shows the ventilation/perfusion ratio at the three levels of inflation as a function of vertical lung height, in the upright position. The first observation to be made is in comparing this non-linear model to its solid mechanics counterpart in Figure 12. It can clearly be seen that the non-linear framework creates a much smoother curve for the ventilation perfusion ratio than in the static model, where there is a clear disconnect between the three West Zones. This continuity results from the more intricate ventilation relationship. Now

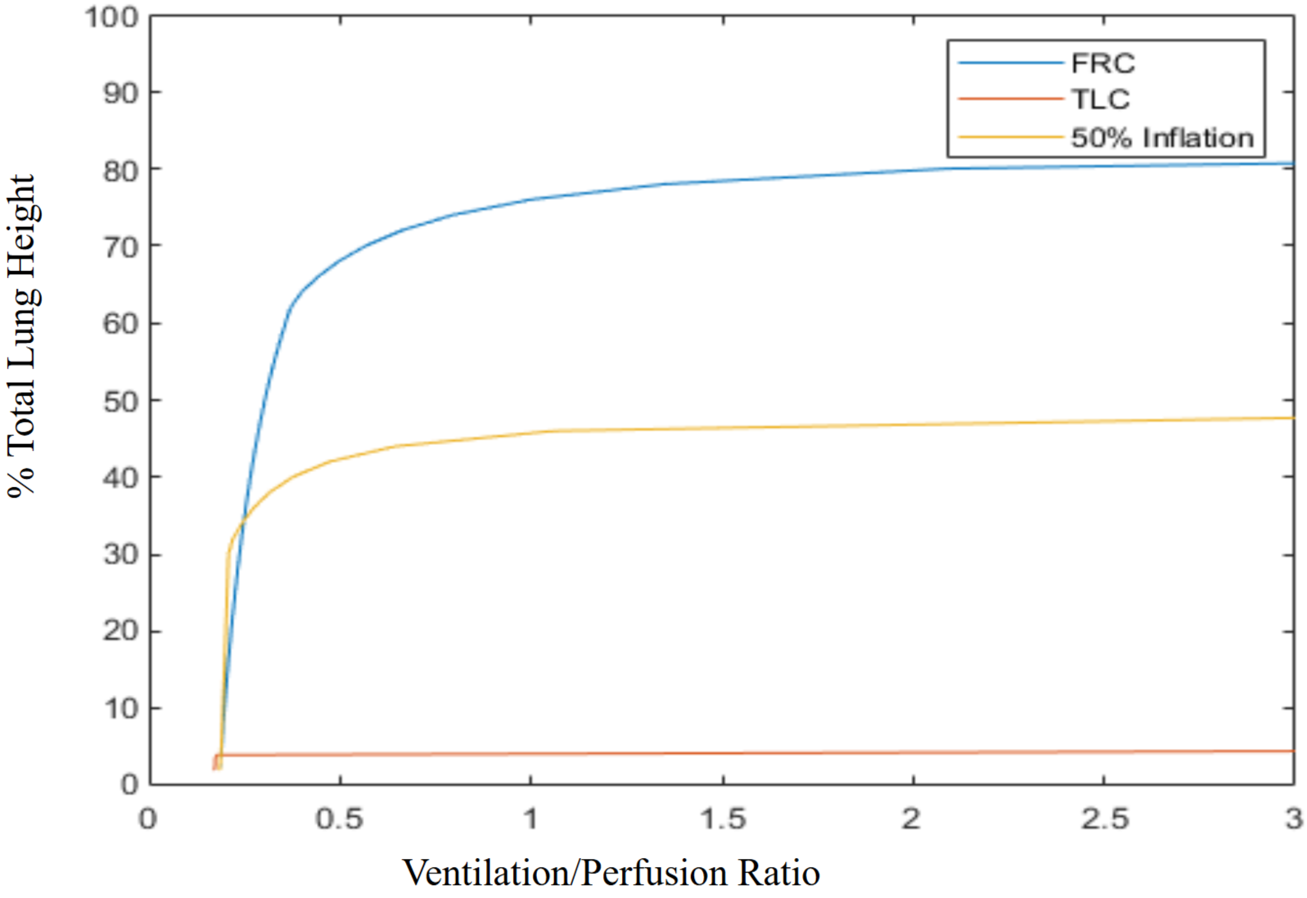

Figure 42: Ventilation/perfusion ratio as a function of vertical height, at FRC, TLC and 50% inflation. Lung is in the upright position

looking at the difference between inflation points, the height at which the curve converges is most significant. At Functional Residual Capacity, the curve flattens at just above 80% of the total lung height, this is because above this is the Zone 1 portion, in which perfusion is zero. Therefore dividing ventilation by perfusion in this area will not give a solution. This is analogous to the alveolar dead space in which the alveoli are ventilated but no gas exchange can occur. This is replicated at 50% inflation, where Zone 1 extends down to the top 50% of the lung, and at Total Lung Capacity where 95% of the lung is in Zone 1.

Theoretically, the ideal V/Q ratio is 1, and this is the aim when a patient is receiving mechanical ventilation. There are many techniques a clinician may implement in order to achieve this, but of primary focus here is in patient manoeuvring. We can now use this non-linear Neo-Hookean Hyper-Poroelastic model to explore the gravitational mechanics that change between positions.

7.4 Positions Comparison

Having coupled the non-linear poroelastic model with the complex structures of the airway and vascular tree, it is now possible to explore in depth the mechanical differences between patient positions that are observed experimentally. In order to do this, a shape must be assigned to the lung model such that it can be rotated accordingly. Here this is chosen to be the truncated cone analogy which was explored in Chapter 4, and shown to be a physiologically relevant shape whilst keeping mathematical complexity minimal.

The equations for the cross sectional area of the truncated cone are

$$A(x) = \pi \left(\frac{xb - xt + Lt}{L} \right)^2 \tag{23}$$

in the upright positions, and

$$A_x = \begin{cases} L(b-t)\left(\sqrt{1-k_1^2} - k_1^2 cosh^{-1}\frac{1}{k_1}\right), & x < b-t. \\ \frac{L}{2}\left(2\sqrt{t^2-(b-x)^2} + 2\sqrt{b^2-(b-x)^2}\right), & b-t \leq x \leq b+t \\ L(b-t)\left(\sqrt{1-k_2^2} - k_2^2 cosh^{-1}\frac{1}{k_2}\right), & x > b+t. \end{cases} \tag{35}$$

Where $k_1 = 1 - \frac{x}{b-t}$ and $k_2 = 1 - \frac{2b-x}{b-t}$, in the horizontal positions. These are shown visually in Figures 7 and 8. b is the radius of the larger base of the truncated cone, and t is the radius of the smaller top. These functions are substituted into the equation for the conservation of solid momentum, 81, as before.

A more significant adjustment is required for the varying elasticity between patient positions, that is highly responsible for the deformation differences between supine and prone position despite the same cross-sectional area. In the linear model, this was achieved by simply adding a spatial gradient to tissue elasticity E, which could be set prior to simulation. In the non-linear model however, elasticity is now a function of deformation itself according to the spatial elasticity tensor of the neo-Hookean hyperelastic model, 144.

The simulated ventilator waveform data is shown in Figure 43. The three positions are compared on total displacement and pressure at each isogravitational plane, with the upright in row A, supine in row B and prone in row C. This is directly comparable to the linear model of the ventilator waveform shown in Figure 25.

If we initially compare the linear and non-linear models, there is a clear difference in the pressure field, with average pressures being higher in the non-linear model across all positions. This is due to the more complex stress-strain behaviours in the non-linear. The relationship between stress and strain is no longer proportional because, as the tissue deforms, the stiffness of the material can increase towards the end of exhalation, requiring higher pressures to achieve the same amount of deformation. The variation in pressure across lung height is also much higher in the linear model, with pressures at each gravitational plane being near uniform in the non-linear system. In the non-linear poroelastic model, the lung tissue becomes stiffer as it stretches, especially at higher volumes. This property allows the tissue to distribute stress more evenly because regions of the lung that are more compliant (or less stiff) initially will gradually stiffen as they expand. This adaptive stiffness limits over-distension in certain areas, redistributing pressure and reducing large regional differences

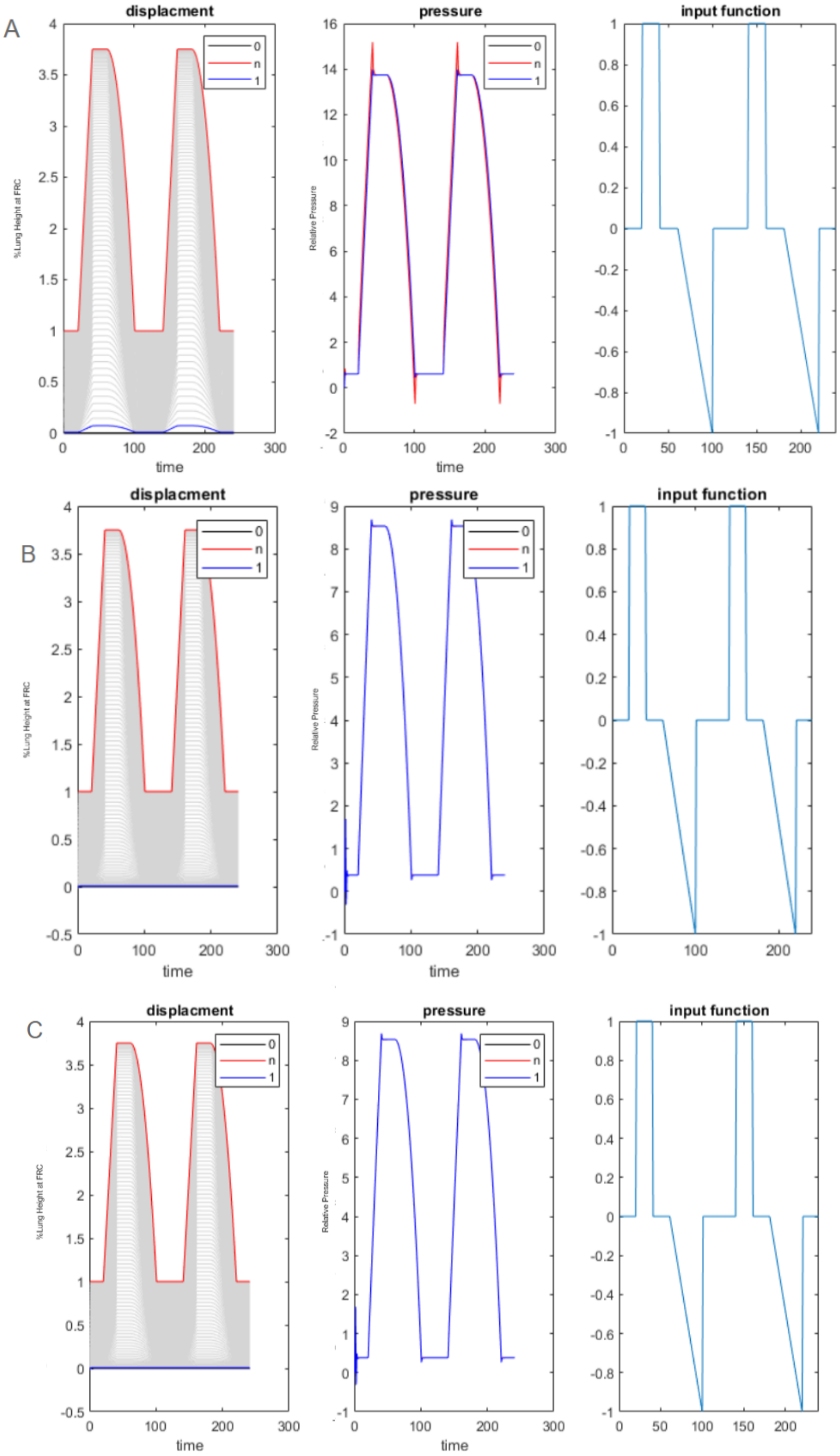

Figure 43: Simulated ventilator waveform data for the source problem in a fully non-linear neo-Hookean model. Row A is upright, row B is supine, row C is prone.

in strain.

Between the positions themselves, the results are inline with the observations from the linear model. Pressures are highest in the upright lung, and there is clear heterogeneity in pressures across the lung height. In the prone and supine positions, the pressures are lower at full inflation, and significantly more uniform across the lung height. There is little to no observable difference between the prone and supine positions here, as the complex elastic behaviour is the dominant factor. In actuality, the differences between the prone and supine positions are heavily influenced by external factors such as extrinsic pressure, and so these must be included for accurate comparison. We therefore add the external pressures discussed in 42 to calculate the effective alveolar pressure.

This can then be extended to include the ventilation and perfusion calculations set in section 8.3 of this thesis. From the results presented in section 8.3, it is shown that regional variation in ventilation/perfusion mismatch is most significant at functional residual capacity, as so position comparisons will be made at FRC.

Figure 44 shows the average ventilation to the alveoli in each isogravitational plane, with the lung at functional residual capacity. In each position, airflow is lowest at the apex and highest at the base, as is expected. Between positions, the difference is in the spatial variation in ventilation. In the upright position, there is a large gradient between the base and apex of the lung, with significantly larger airflows at the base. This variation is marginally reduced in the supine position, and approximately halved in the prone position, where considerably greater uniformity across the lung is observed. In the prone position, the external pressure gradient on the lung is much smaller, which allows air to flow into the alveoli more efficiently. The higher tissue elastance in this position also prevents the over-distension of the top alveoli and promotes recruitment,

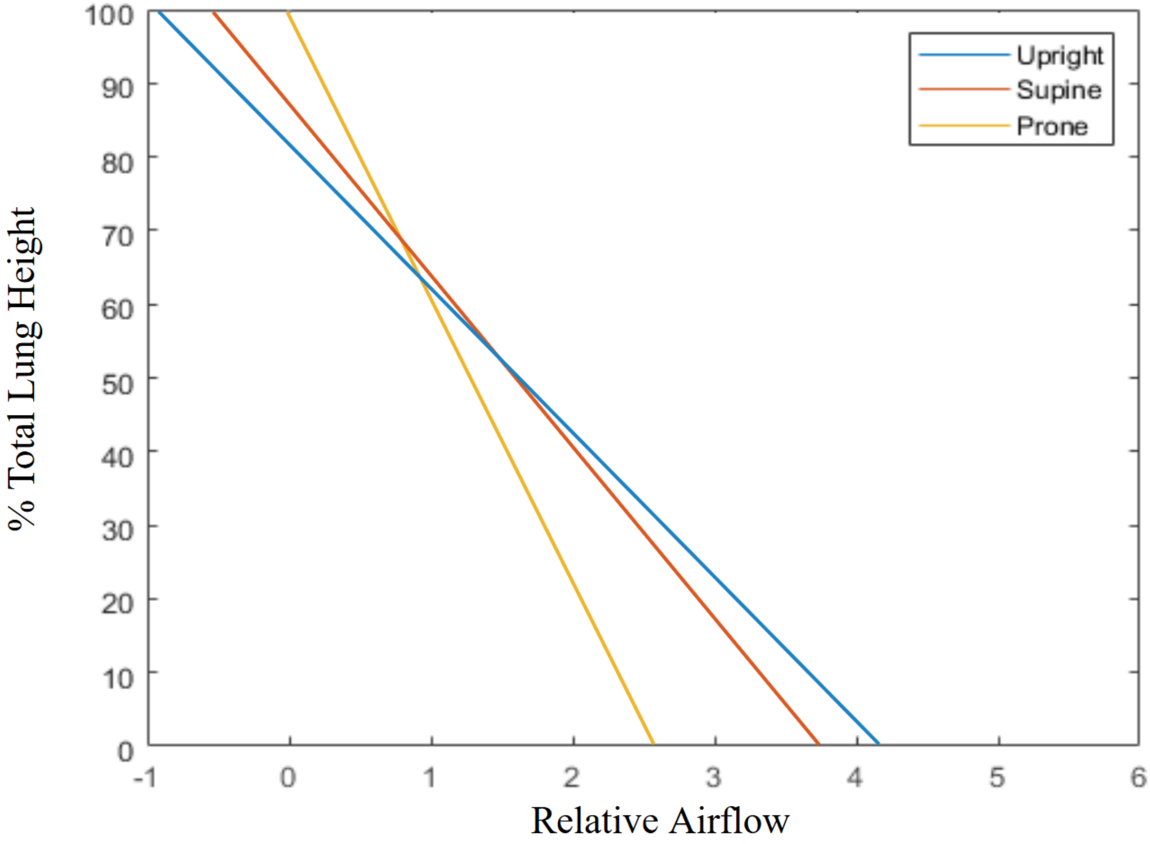

Figure 44: Ventilation at FRC as a function of lung height, in the upright, supine and prone positions.

resulting in more even ventilation. Experimental work has focussed more significantly on the supine and prone positions. Johnson et al (2017) synthesised and reviewed existing research on ventilation differences between pone and supine positions, with highly insightful conclusions [91]. Studies utilising sophisticated imaging techniques observed a much larger gradient in the spine position than in the prone, due to a more homogenous distribution of pleural pressures [92, 93, 94, 95], which the model successfully captures.

Figure 45 shows the average perfusion of the capillaries feeding the alveoli

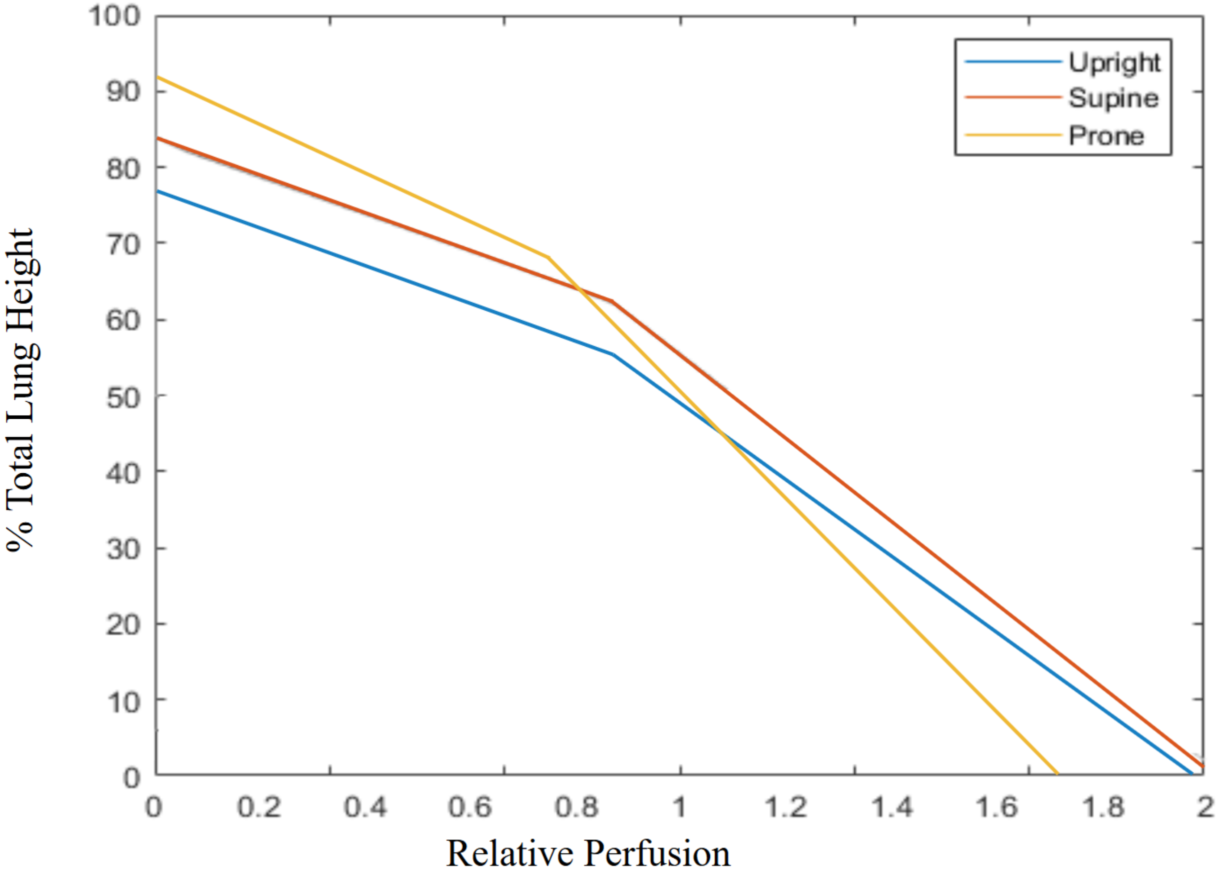

Figure 45: Perfusion at FRC as a function of lung height, in the upright, supine and prone positions.

in each isogravitational plane, with the lung at functional residual capacity. Of most importance here, is the portion of the lung in each of the three West zones in each position. In the upright position, the top 23% of the lung is in zone 1, in which over-distended alveoli prevent all blood flow. Roughly 20% falls into zone 2, where alveolar pressure is the dominant factor, and the rest falls into zone 3. Moving into the supine position, zone 1 and zone 2 are both reduced by 5%, with 67% now exhibiting zone 3 dynamics. Finally, in prone position only the top 9% of the lung is in zone 1, with roughly 20% in zone 2 and 70% in zone 3. This reduction in zone 1 in the prone position is of particular interest in a clinical setting, as we want to minimise the number of alveoli unable to perform gas exchange in order to improve overall lung function. Original research by Glenny and colleagues in 1999, demonstrated that pulmonary perfusion heterogeneity was greatest in the upright posture, averaging 65.3% [96]. In comparison, blood flow variability was significantly less in the supine posture, averaging 52.0%, and even less in the prone posture, averaging 43.8%. This decreasing trend in heterogeneity from upright to supine to prone directly supports the idea of increasing uniformity of perfusion gradients across these positions. Furthermore, the contribution of gravity to this perfusion heterogeneity was estimated to be 25% in the upright posture, 7% in the supine posture, and only 5% in the prone posture, reinforcing that gravity's influence on flow distribution is greatest when upright and least when prone, leading to varying levels of uniformity, as seen in the model.

In order to look in more detail at the gas exchange capabilities throughout the lung in the different positions, we can now look at the ventilation/perfusion ratio.

Figure 46 shows the average V/Q ratio at the alveoli in each isogravitational plane, with the lung at functional residual capacity. As is expected from the size and location of West zone 1, each of these curves plateaus at a certain height up the lung, above which no blood flow is present and the ratio has no solution. The ideal V/Q ratio is 1, at which the airflow and bloodflow to the alveolus are even and gas exchange is most efficient. This however, is not seen in the majority of the lung, and so the clinical goal is to have as much of the lung close to this value as possible. In the prone position, the lowest ratio is at 0.5 at the base of the lung, meaning that bloodflow is double the airflow in this region. This is a much better value than in the upright and supine positions, where the base exhibit

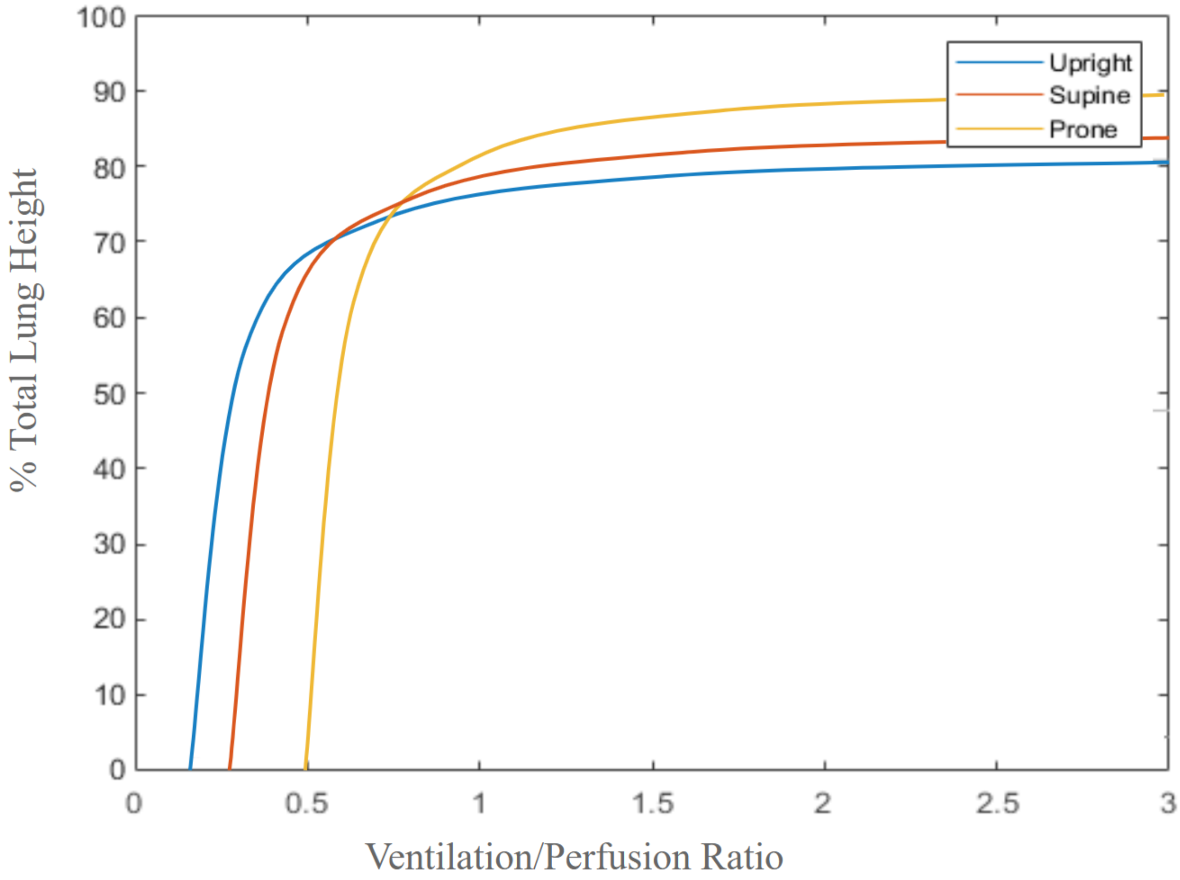

Figure 46: Ventilation/perfusion ratios at FRC as a function of lung height, in the upright, supine and prone positions.

ratios of 0.15 and 0.25 respectively. The height at which the curves converge is akin to the start of zone 1 seen in Figure 45, 77% in the upright position, 82% in the supine position and 90% in the prone position. This is well founded in experimental research. Nyren in 2010 explored V/Q gradients in healthy patients who were anaesthetised and undergoing mechanical ventilation, which is directly comparable to the structure of this model [97]. They found that the vertical heterogeneity in V/Q ratio decreased from 31.4% in the supine position to 16.4% in the prone position.

This section determined that upright positioning results in increased pressure variations across the lung, while supine and prone positions promote a more uniform pressure distribution. Additionally, non-linear stress-strain relationships inherent to lung tissue were noted to impact pressure distribution, with significant increases in pressure at the apex during upright positioning, indicating the potential for over-distension. The prone position demonstrated the most uniform stress distribution, minimizing pressure discrepancies across lung height. Positioning was also shown to impact regional bloodflow to the lung, with large portions of the lung being unperfused in the upright position, and minimal portions unperfused in prone. This observation is important when discussing the mismatch in ventilation and perfusion across the lung, and why certain positions promote more efficient gas exchange than others.

The detailed visualization of West's Zones and the ventilation-perfusion (V/Q) ratio across different lung heights and patient positions is directly actionable for clinicians. The significant reduction of Zone 1 (unperfused, ventilated lung) in the prone position, particularly at FRC and 50% inflation, quantitatively demonstrates how proning can improve overall gas exchange efficiency by recruiting previously unperfused lung regions. This model suggests that clinicians can use patient positioning as a powerful tool to minimize alveolar dead space and optimize V/Q matching, directly contributing to improved oxygenation in critically ill patients, especially those with ARDS. The model's ability to show the V/Q ratio converging closer to the ideal value of 1 in the prone position provides a compelling mechanistic reason for its clinical efficacy. This finding supports the practice of prone positioning to rebalance regional airflow and blood flow, crucial for enhancing gas exchange and reducing hypoxaemia in mechanically ventilated patients.

With the non-linear neo-Hookean hyper-poroelastic model now fully operational and providing insightful and physiologically relevant results, we can begin to use it to explore important clinical questions. The findings from the positional analysis underscore the significance of mechanical factors, such as pressure gradients and tissue elasticity, in determining lung function. But more than this, they can be used to assess the risk to the lung caused by these simulated stresses from the ventilator. With prone positioning offering a balance of stress across lung regions, it emerges as a key configuration for reducing over-distension risks, a factor crucial to mitigating lung injury. This sets the stage for the upcoming discussion on how mechanical power—the combined effect of volume, pressure, and frequency—contributes to ventilator-induced lung injury (VILI), emphasizing the importance of positional adjustments in preventing damage during mechanical ventilation.

7.5 Mechanical Power and VILI

In the management of mechanically ventilated patients, understanding the relationship between mechanical power and lung injury is critical to optimizing ventilator settings and minimizing damage. Ventilator-Induced Lung Injury (VILI) arises from the mechanical forces exerted on lung tissues, which can lead to over-distension and tissue stress [35]. Traditional approaches often focused on controlling specific parameters like tidal volume and airway pressure. However, recent insights have emphasized the role of mechanical power—a holistic measure integrating tidal volume, flow, and airway pressure—as a critical factor in predicting lung damage [36]. The mechanical power risk model provides a particularly effective framework for this study because it captures both the solid and fluid characteristics of lung tissue. The poroelastic model created in this thesis accommodates the unique characteristics of lung deformation under mechanical stress, such as alveolar recruitment and collapse, as well as stress distribution across lung regions. By representing the lung as a poroelastic medium, this study can simulate the nuanced behaviour of lung tissues under varied ventilator settings, offering a more accurate prediction of injury sites and severity. Thus, applying the poroelastic model allows us to better quantify mechanical power's impact on VILI and refine protective ventilation strategies tailored to individual patient conditions.

For this study, the equation for the mechanical power will be derived following the highly-credited work of Gattinoni et al in 2016 [36]. To begin we take the traditional equation of motion for the mechanics of breathing as stated by Otis et al in 1950 [98], and introduce a component for the Positive end-expiratory pressure (PEEP), as determined by Marini and Crooke in 1993 [99].

This gives the pressure for the whole respiratory system P_{RS} as

$$P_{RS} = EL_{RS} \cdot \Delta V + R_{aw} \cdot F + PEEP \tag{177}$$

where EL_{RS} is the elastance of the respiratory system, ΔV is the volume change in the system (tidal volume), R_{aw} is the resistance of the upper airways and F is the airflow through the system. Each of the components in this equation represents some dynamic pressure, such as

$$EL_{RS} \cdot \Delta V = \Delta P \tag{178}$$

$$R_{aw} \cdot F = P_{peak} - P_{plat} \tag{179}$$

$$PEEP = P_{end-expiration} \tag{180}$$

where ΔP is the pressure component generated by elastic recoil alone, P_{peak} is the peak pressure and P_{plat} is the plateau pressure such that $P_{peak} - P_{plat}$ is the pressure component due to the motion of the system, and $P_{end-expiration}$

is the pressure at the end of expiration. There is debate on the inclusion of PEEP in this equation, as it itself is a static pressure [100]. However, PEEP does generate a volume when first applied to the respiratory system, and as such is integral in determining the energy change needed to increase the system volume [101].

The energy required for each breath can be calculated by multiplying the pressure equation 177 by the change in volume ΔV, such that

$$E_{breath} = EL_{RS} \cdot \Delta V \cdot \Delta V \cdot \frac{1}{2} + R_{aw} \cdot F \cdot \Delta V + PEEP \cdot \Delta V \tag{181}$$

The first term in the equation is multiplied by $\frac{1}{2}$ as to approximate the integral of the product $\Delta Px \times \Delta V$, as shown in the linear portion of pressure-volume relationships depicted by Gattinoni [36].

We can now take the flow of air through the system F as the rate of volume change ΔV over the whole inspiratory time period T_{insp}. This gives the updated equation for energy per breath as

$$E_{breath} = \Delta V^2 \cdot \left(EL_{RS} \cdot \frac{1}{2} + \frac{1}{T_{insp}} \cdot R_{aw} \right) + PEEP \cdot \Delta V \tag{182}$$

As to explore the impact of the ventilator settings on the mechanical power output, we can write T_{insp} as a function of respiratory rate RR and inspiratory-to-expiratory ratio $I : E$, where

$$\frac{T_{insp}}{T_{exp}} = \frac{I}{E} \tag{183}$$

$$T_{insp} + T_{exp} = T_{total} \tag{184}$$

$$T_{total} = \frac{60}{RR} \tag{185}$$

$$\therefore \tag{186}$$

$$T_{insp} = T_{total} \cdot \frac{I:E}{1+I:E} \tag{187}$$

Substituting this into 181 gives

$$E_{breath} = \Delta V^2 \cdot \left(EL_{RS} \cdot \frac{1}{2} + RR \cdot \frac{1+I:E}{60 \cdot I:E} \cdot R_{aw} \right) + PEEP \cdot \Delta V \tag{188}$$

In order to convert this to an equation for mechanical power, we express it in J/min, multiplying the product of the volume, expressed in litres, and the pressure, expressed in cmH_2O, by 0.098. This gives the final equation for the mechanical power as

$$Power_{RS} = 0.098 \cdot RR \cdot \left[\Delta V^2 \cdot \left(EL_{RS} \cdot \frac{1}{2} + RR \cdot \frac{1+I:E}{60 \cdot I:E} \cdot R_{aw} \right) + PEEP \cdot \Delta V \right] \tag{189}$$

Within this equation there are multiple parameters that can be altered in the ventilator settings, such as respiratory rate, inspiratory:expiratory ratio, tidal volume and PEEP. Therefore we can explore how changing each of these parameters individually effects the calculated mechanical power.

Figure 47 shows the impacts of various ventilator settings on the calculated mechanical power. For each of the parameters in the mechanical power equation that are directly controllable at the bedside, we cycle through a range of possible

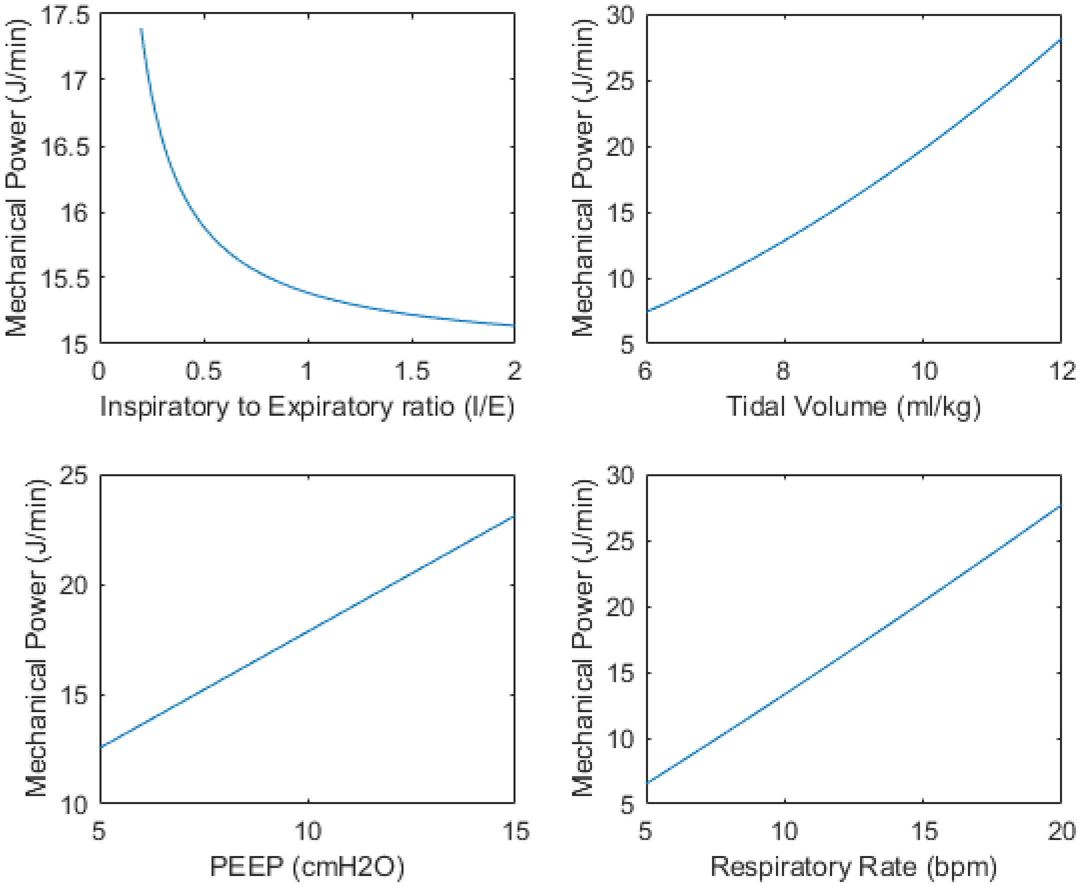

Figure 47: The impacts of ventilator settings on the calculated mechanical power, varying a single parameter at a time. Top left shows the inspiratory:expiratory ratio (I:E), top right shows the tidal volume (TV), bottom left shows the PEEP, and bottom right shows the respiratory rate (RR). When not being varied, parameters are set as followed: I:E = 1, TV = 9ml/kg, PEEP = 5cmH2O, RR = 12bpm. All calculated from Eq 189.

values while keeping all other parameters constant. This ensures any changes in the calculated mechanical power are solely due to the variable being studied. It is generally accepted that a higher mechanical power results in greater risk of lung injury, however the exact thresholds are significantly debated. For example, Guerin et al [102] found that a mechanical power above 12J/min resulted in a worse survival likelihood over a 90 day period. Serpa Neto et al [103] and Xie et al [104] put this threshold higher, suggesting that a mechanical power above 17J/min increased the risk of mortality, where Parhar et al [105] put this threshold even higher at 22J/min. Therefore, here we explore the value of mechanical power directly, without applying a set threshold for risk of VILI.

The top left graph shows the effect of the inspiratory:expiratory ratio on the mechanical power. Here the value of (I:E) plotted is calculated as $\frac{I}{E}$ with inspiratory time set to 1, such that an $\frac{I}{E}$ value of 0.25 correlates to a I:E ratio of 1:4, and a value of 2 corresponds to a ratio of 2:1 and so on. This curve exhibits an exponential decay behaviour, such that as the expiratory time grows significantly larger than the inspiratory time, the mechanical power increases rapidly. Conversely, as the expiratory time falls below the inspiratory time, the mechanical power begins to converge at value 15.4J/min. This relationship is physiologically logical when considering the mechanical definition of power in the respiratory system, which depends on airway pressures, inspiratory flow, and tidal volume. At very low I:E ratios, inspiratory time is extremely short, requiring rapid airflow to deliver the same tidal volume. This high inspiratory flow leads to increased airway resistance and elevated pressure demands, significantly raising the energy required per breath—hence the sharp increase in mechanical power.

Conversely, as the I:E ratio increases, inspiratory time lengthens and the airflow needed per unit time decreases. This reduces both resistive and elastic workload on the lungs, resulting in a corresponding drop in mechanical power. While the model suggests that mechanical power approaches zero at very high I:E ratios, it is important to note that such extremes are not clinically sustainable, as they can compromise gas exchange and lead to issues such as dynamic hyperinflation or CO_2 retention [106, 107]. Nonetheless, the trend highlights the inverse relationship between inspiratory flow demand and mechanical energy expenditure, and emphasizes the potential for optimising I:E ratio as part of lung-protective ventilation strategies.

The top right graph shows the effects of altering the tidal volume on mechanical power. The relationship here is also non-linear due to the second-order ΔV term in 189. At a tidal volume of 6ml/kg, the mechanical power is relatively low, at a value of only 7.5J/min. Doubling the tidal volume to 12ml/kg, increases mechanical power to 28J/min, an almost 4-fold increase. This means that as tidal volume increases further, mechanical power will begin to rise much more rapidly. Mechanical power is influenced by both the elastic and resistive components of the respiratory system, and tidal volume directly affects both. As tidal volume increases, more pressure is required to overcome the elastic recoil of the lungs and chest wall, particularly if lung compliance is limited. Additionally, higher tidal volumes often require increased inspiratory flow, which raises resistive pressure due to airway resistance. Although the increase appears close to linear over the physiological range, the slight non-linearity arises because both pressure and flow—which scale with tidal volume—contribute multiplicatively to the total energy delivered per breath. This reinforces the importance of limiting tidal volume in protective ventilation strategies, as even modest increases can lead to disproportionate rises in mechanical power and, consequently, greater risk of ventilator-induced lung injury.

The bottom left graph shows the effects of increasing PEEP. This relationship is clearly linear, with an increase in PEEP of 10cmH_2O resulting in an increase in mechanical power of 10J/min. This relationship is expected, as PEEP adds a constant baseline pressure to each breath, increasing the total pressure the ventilator must generate throughout the respiratory cycle. Since mechanical power is calculated as the energy transferred to the respiratory system per unit time, and energy is directly related to pressure and volume, an increase in PEEP raises the starting point of each breath's pressure curve, thereby increasing the total work done per breath in a linear fashion. Importantly, this added energy does not contribute to tidal ventilation but rather maintains alveolar recruitment and end-expiratory lung volume. While moderate increases in PEEP can improve oxygenation and prevent alveolar collapse, this linear rise in mechanical power highlights the need to carefully balance PEEP settings to avoid excessive energy delivery and potential lung injury.

Respiratory rate in the bottom right graph also displays a linear relationship with mechanical power. Rising from 6J/min at a respiratory rate of 5 breaths per minute, to 28J/min at 20 breaths per minute. Mechanical power represents the energy delivered to the lungs per unit time, and increasing the respiratory rate means that more breaths—and therefore more energy—are delivered each minute. Assuming tidal volume and pressures remain constant, each breath requires a fixed amount of work, so doubling the respiratory rate effectively doubles the total mechanical power. This linear relationship underscores the role of respiratory rate as a key driver of energy transfer to the lung. While increasing RR can help regulate CO_2 clearance, it also raises the cumulative mechanical stress on the lungs, which may contribute to ventilator-induced lung injury (VILI) if not balanced appropriately with other ventilator settings. Thus, optimizing RR is essential not only for gas exchange but also for minimizing total energy exposure to the respiratory system.

The implications of these simulations are profound, as they demonstrate the substantial impact that clinician-programmed ventilator settings can have on generated mechanical power and, consequently, on patient risk. However, if we wish to quantify the risk, we must chose an adequate parameter to function as a signifier. In order to do this we will asses the mechanical stresses and strains applied to the lung with various settings and the associated mechanical power. Dynamics stresses and strains are calculated as follows [108].

$$strain = \frac{\Delta V}{FRC} \tag{190}$$

$$stress = E \cdot strain \tag{191}$$

In order to create a wide range of possible stresses, strains and mechanical powers, we will systematically cycle through the range of possible values for each of the ventilator settings, at each point mapping the calculated stress, strain and mechanical power according to 189, 190 and 191.

Figure 48 reveals a sigmoidal (S-shaped) relationship between mechanical power and strain, which reflects the non-linear mechanical properties of the lung. Initially, as mechanical power increases from 0 to around 10 J/min, strain rises relatively steadily from 0 to 2. This phase corresponds to the lung's compliant region, where increases in energy (mechanical power) result in effective volume expansion. In this range, the lung is relatively easy to inflate, and small increases in pressure and power produce meaningful increases in volume and strain. Between 10 and 35 J/min, the curve begins to flatten, with strain increasing more slowly from 2 to 3. This plateau represents the transitional phase, where many alveoli are already recruited, and the lung becomes progressively stiffer. Additional energy is now less effective at increasing lung volume, as the lung tissue approaches its elastic limit and compliance decreases. This is often associated with overdistension risk in mechanical ventilation. Beyond 35 J/min, strain begins to increase exponentially, despite further rises in mechanical power. This late steepening suggests a non-physiological or injurious region, where the lung may be forced beyond its safe inflation capacity. In this phase,

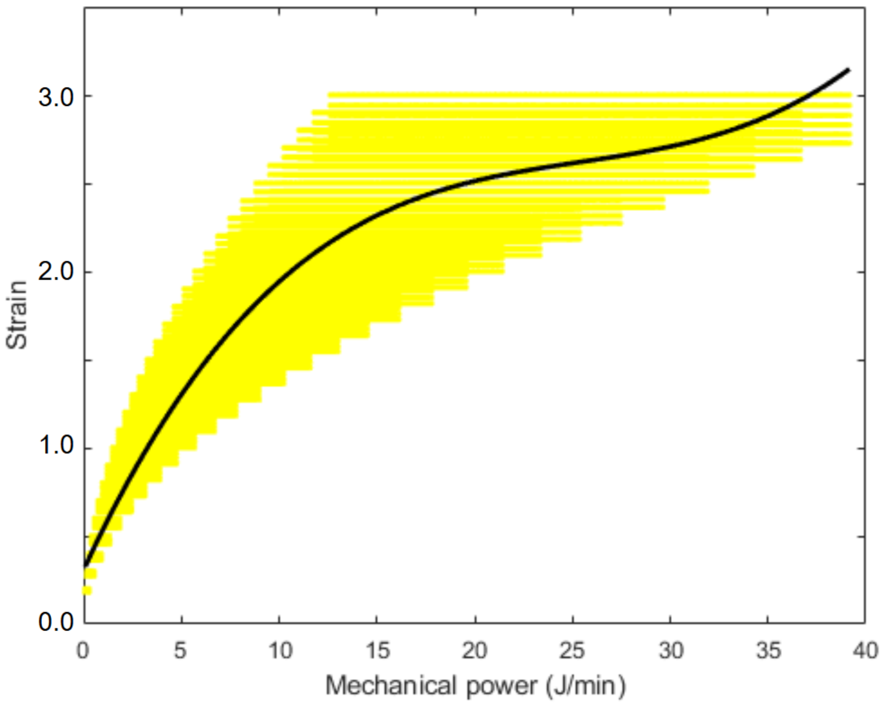

Figure 48: The relationship between mechanical power and calculated mechanical strain in the lung.

even small additional increases in mechanical power result in disproportionately high strain, possibly indicating non-linear tissue stress, microstructural failure, or volutrauma.

Experimental findings have focussed specifically on the normal operating range of mechanical ventilators, which here is the initial slop of the graph before the plateau. Romitti et al investigated mechanical power levels of 3, 7, and 12 J/min in proned healthy pigs, and calculated the resultant strains [109]. In this study, strain never exceeded 1.0. The 7J and 12J groups exhibited strain levels that were approximately 50% and 100% greater than the 3J group, respectively. This means that the Romitti study operated within the initial "compliant region" (where strain rises relatively steadily from 0 to 2 for mechanical power up to around 10 J/min, according to Figure 48). The observation of higher strain at higher mechanical power levels in Romitti's study is consistent with the positive slope in the initial phase the model. A similar result was found in humans with ARDS, over the same mechanical power range. Pistillo et al (2023) designed a prospective cohort study of 18 ARDS patients, adjusting ventilator settings to achieve desired mechanical powers [110]. Specifically, specific lung mechanical power (SLMP), which is transpulmonary mechanical power normalised to end-expiratory lung volume, showed a very strong positive linear correlation with strain ($R = 0.97, R^2 = 0.94, p < 0.00001$). Similarly, specific mechanical power (SMP), which normalises mechanical power of the respiratory system (MPRS) to the compliance of the respiratory system (CRS), also had a positive correlation with strain ($R = 0.68, R^2 = 0.47, p = 0.001$). SLMP was here also only explored between 4.57 and 11J/min. The agreement of the near linear phase of this sigmoid provides significant validation to the model, and subsequently highlights the importance of dynamics outside of these normal operating mechanical powers. Neither study provides data for the non-linear, plateauing (transitional) or exponentially increasing (injurious) phases of the curve, thus highlighting this as an area of particular interest going forward.

Overall, this curve captures the classic pressure–volume nonlinearity of the lung, now expressed through the lens of mechanical power and strain. It highlights how energy delivery becomes inefficient—and potentially harmful—beyond certain thresholds, emphasizing the need to limit mechanical power in clinical settings to avoid entering the exponential, injury-prone region of the curve.

Figure 49 shows the relationship between mechanical power and mechanical stress in the lung. In the initial phase, as mechanical power increases from 0 to around 15 J/min, stress rises steadily from 0 to approximately $4cmH_2O$. This corresponds to the normal elastic behaviour of the lung, where tissue re-

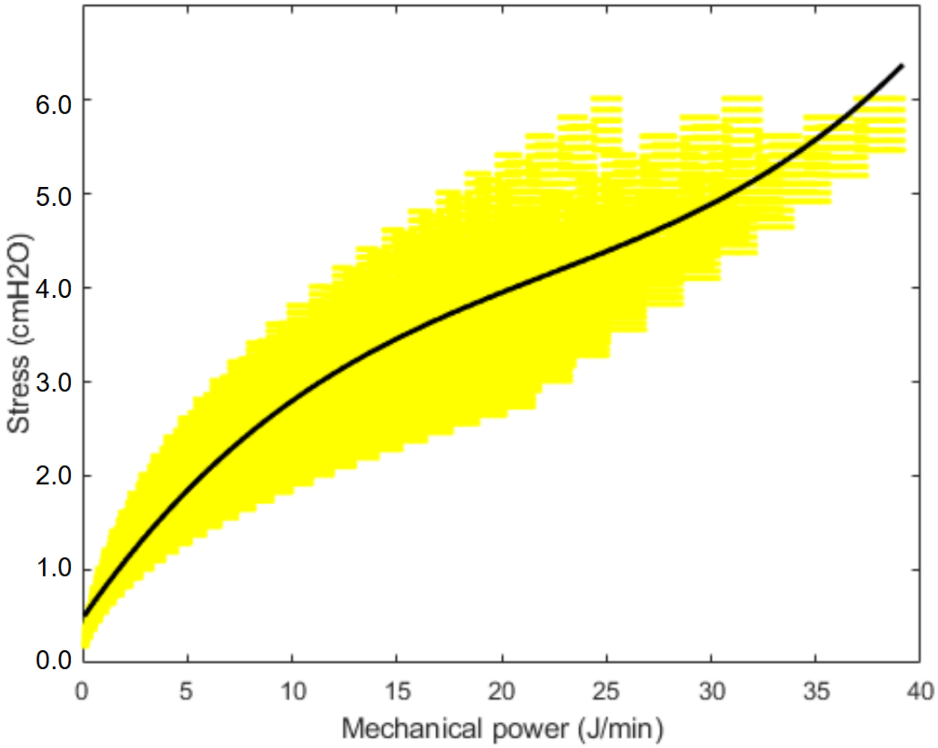

Figure 49: The relationship between mechanical power and calculated mechanical stress in the lung.

sponds proportionally to increased energy input. During this phase, alveoli are recruited efficiently, and lung units expand with relatively low resistance, so increases in mechanical power translate into predictable, moderate increases in tissue stress. Between 15 and 30 J/min, the curve begins to flatten, with stress increasing only slightly from 4 to $5 cmH_2O$. This plateau reflects a transitional zone, where the lung has reached a near-maximal recruitment state, and further expansion becomes increasingly resisted by the stiffer structural elements of the lung. Compliance is reduced in this region, and although energy input continues to rise, much of it is "lost" to overcoming resistive and elastic limits, rather than further stretching the lung. This represents a protective ceiling beyond which the lung resists additional distension. Beyond 30 J/min, stress begins to increase exponentially with further increases in mechanical power. This marks the transition into a potentially injurious regime, where small increases in mechanical power lead to disproportionately large rises in mechanical stress. This steep segment of the curve may reflect overdistension of alveoli, local tissue damage, or nonlinear stiffening of the extracellular matrix. It highlights how exceeding mechanical thresholds can rapidly push the lung into unsafe territory, even if changes in volume (strain) appear modest.

The study discussed previously by Pistillo et al also calculates stress in the lung as a result of mechanical power [110]. They demonstrated strong positive linear correlations between normalised mechanical power and stress: SLMP and stress ($R = 0.9, R^2 = 0.84, p = 0.00004$) and SMP and stress ($R = 0.86, R^2 = 0.75, p = 0.00001$). This supports the fundamental positive relationship between mechanical power and stress. The maximal transpulmonary pressure at the end of inspiration (defined as stress) was 18.1cmH2O, at a specific lung mechanical power (SLMP) measured was 11 J/min/L. These values fall within the initial phase of Figure 49 (0-11 J/min for mechanical power, 0-3 cmH2O for stress). The difference between the model calculation of stress and the measured in the study is a result of differing (but still comparable) stress calculations, as the model calculates the elastic component of stress, a more precise mechanical parameter. The consistently positive, linear correlations observed by Pistillo et al. indicate that within the range of values studied, the relationship generally aligns with the initial rising portion of the model.

Overall, this S-shaped curve illustrates that while the lung can absorb mechanical energy effectively up to a point, there are clear thresholds beyond which additional mechanical power translates to harmful stress, emphasizing the importance of mechanical power as a key determinant of ventilator-induced lung injury risk.

The comprehensive analysis of how ventilator settings (I:E, TV, PEEP, RR) impact mechanical power offers clinicians a quantitative guide for 'lung-protective' ventilation. The non-linear increases in stress and strain with rising mechanical power underscore the importance of strict control over ventilatory parameters to avoid exceeding the lung's elastic limits and inducing injury. This model can serve as a simulation platform for clinicians to predict the mechanical power delivered by specific ventilator settings, allowing for proactive adjustments to minimize VILI risk tailored to a patient's current lung condition.

This section has magnified the use of mechanical power as an indicator of lung injury, and the internal lung mechanics that contribute to this. However, these equations explore the lung as a whole. The stresses and strains in the lung are rarely uniform, which results in certain regions being at higher risk of injury than others. This is where the spatio-temporal poroelastic model is extremely useful, as we have separated these mechanics across the height axis, and so can now calculate how the overall mechanical power effects the lung at high spatial resolution and identify the most at-risk areas.

7.6 Localised damage in the poroelastic model

When exploring the effects of mechanical power on the risk of ventilator-induced lung injury (VILI), it is important to remark that the risk of injury is not uniform across the lung. As the underlying mechanics of the lung tissue vary with height, so does the associated strain delivered from the ventilator. Therefore, using the poroelastic model in order to these strains of immense importance to fully understand patient risk.

Quantifying the regional impacts of ventilator mechanical power requires the conversion of 189 to a spatially explicit equation, such that values are calculated for each alveolus instead of the lung as a whole. The mechanical power delivered to the i^{th} alveolus, $Power_i$, is calculated as follows:

$$Power_i = 0.098 \cdot RR \cdot \left[\Delta V_i^2 \cdot \left(EL_i \cdot \frac{1}{2} + RR \cdot \frac{1 + I:E}{60 \cdot I:E} \cdot R_i\right) + PEEP \cdot \Delta V_i\right] \tag{192}$$

where the tidal volume is replaced by the change in volume of the i^{th} alveolus, ΔV_i, the respiratory system elastance is replaced by the dynamic elasticity of the i^{th} alveolus, EL_i, and the airway resistance is replaced by the resistance of the terminal branch feeding the i^{th} alveolus, R_i. RR, $PEEP$ and $I:E$ remain constant spatially.

As this equation is not coupled into the poroelastic framework, and instead is calculated separately at each time step, the model can be run in accordance to the setup in chapter 7 of this thesis. EL_i is calculated using the neo-Hookean hyper-poroelastic framework set in 128, and R_i is calculated according to 159.

Figure 50 shows the results of this local estimation of mechanical power. Lung is in the upright position and shown at FRC, TLC and 50% inflation. At functional residual capacity, the mechanical power is constant across the lung at 7J/min. This low value is due to the set PEEP which holds the lung open and prevents alveolar collapse. As the lung begins to inflate, we see that mechanical power is not being delivered to the lung evenly, instead showing much higher levels in top (non-dependent) regions. This is understandable, as we see higher pressures and over-distension towards the top of the lung, greatly increasing the stress in those alveoli. At full inflation (TLC), this relationship is more prominent, with the top of the lung receiving a mechanical power of near 30J/min. This supports experimental findings, such as a 2007 study that found top (non-dependent) regions of the lung had greater levels of alveolar injury when mechanical ventilation was increased [111]. This highlights a key

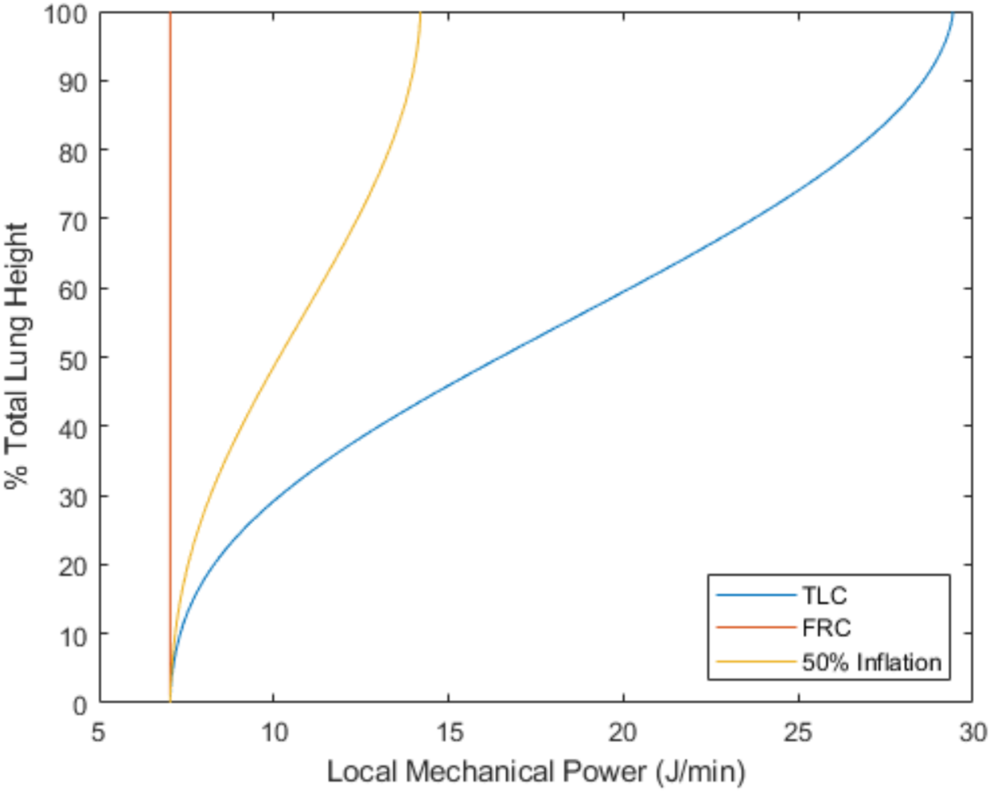

Figure 50: The local mechanical power delivered to the alveoli in each gravitational plane, at functional residual capacity, total lung capacity and 50% inflation. Lung is in the upright position. %Total lung height goes from 0% at the bottom to 100% at the top.

mechanism of regional overdistension, where well-aerated lung zones absorb the majority of ventilatory energy—supporting the concept that ventilator-induced lung injury (VILI) is driven not only by global power but by its uneven regional distribution.

Having established that spatial variation in mechanical power delivery is prominent in the lung, and can be captured using the poroelastic model, we can now explore the impact of patient positioning on this relationship.

Figure 51 shows the variation with height in the local mechanical power

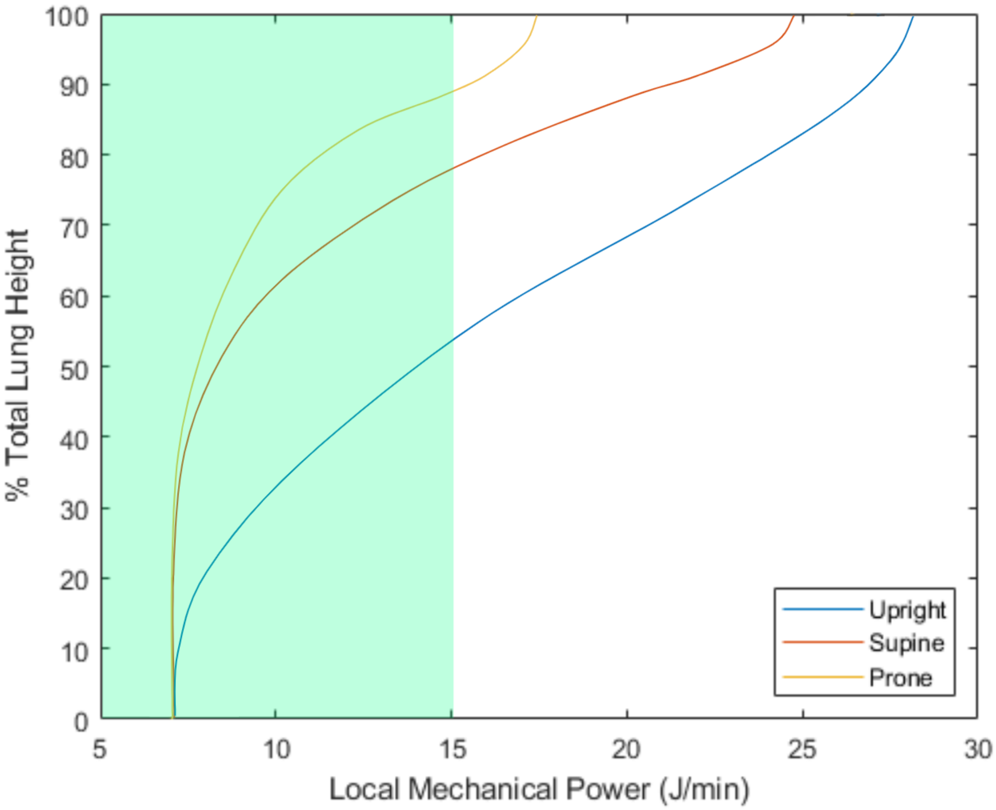

Figure 51: The local mechanical power delivered to the alveoli in each gravitational plane at total lung capacity, with the lung in the upright position, supine position and prone position. A maximum safe threshold of $15 J/min$, taken from experimental findings [102, 103, 104], and the theoretical "Safe Zone" is highlighted green. %Total lung height goes from 0% at the bottom to 100% at the top.

in the upright, supine and prone positions, with the lung inflated to TLC to demonstrate the maximum stress point. In all positions, the lung shows higher mechanical power in the non-dependent regions, however, the maximum mechanical power reached varies greatly between positions. In the upright position, mechanical power reaches a maximum of 27J/min at the apex of the lung. This is reduced to 25J/min in the supine position and further reduced to 17J/min in the prone position. Further to this, if we choose a value of 15J/min as the threshold for safe ventilation, we can assess the proportion of the lung at risk in each position. In the upright, nearly 50% of the lung is above the safe mechanical power threshold. In the supine position this drops to 20% and in the prone position only 10% of the lung is identified as being at risk. This is a highly notable finding, as experimental studies have demonstrated prone positioning to substantially reduce the risk of ventilator-induced lung injury, leading to its frequent proposal as a protective strategy in viable patients [112]. However, this model provides greater insight into the possible distribution of risk between positions which has not yet been explored experimentally. These findings incorporate many of the mechanics which vary between positions, such as pleural pressure gradients, regional inflation levels, differing compliances, and even varying recruitment, highlighting the true complexities that mechanical power can encompass.

Given the known variation in pressure distributions between each isogravitational plane, it is logical to hypothesise that mechanical power and subsequent VILI risk would also vary in directions other than gravitational. Expanding the model into two dimensions could therefore provide unique insights into regional risk for ventilated patients, even further than the insights the model has currently given in one dimension.

A significant novel contribution of this model is its ability to predict localized mechanical power delivery and associated VILI risk across different gravitational planes. The finding that non-dependent lung regions consistently receive the highest mechanical powers, regardless of position, provides crucial insight into regional injury patterns often observed in ARDS. More importantly, the quantitative demonstration that prone positioning substantially reduces the proportion of lung tissue above the 'safe mechanical power threshold' directly supports its use as a powerful protective strategy against VILI. This offers clinicians a data-driven rationale for patient positioning, enabling them to redistribute stresses and protect the most vulnerable lung regions, potentially leading to better patient outcomes and reduced long-term pulmonary complications. This granular spatial resolution allows for a more precise assessment of VILI risk than traditional whole-lung mechanical power calculations, providing a roadmap for future personalized ventilation strategies where 'safe zones' can be dynamically identified and optimized for individual patients.

7.7 Concluding Remarks

This chapter has demonstrated the power and clinical relevance of the fully coupled non-linear poroelastic lung model, which now integrates airway branching geometry, perfusion dynamics, and thoracic pressure influences. This comprehensive framework allows simulation of whole-lung physiology across a variety of clinical conditions and patient positions, capturing how regional lung mechanics interact with vascular and ventilatory inputs to produce spatially heterogeneous function.

By coupling the model with branching airways and blood supply, we showed that regional differences in both ventilation and perfusion are not only measurable but are direct consequences of underlying lung tissue mechanics modulated by gravity, posture, and airway resistance. Critically, this model was able to replicate the known clinical phenomenon whereby prone positioning improves ventilation-perfusion (V/Q) matching, reducing non-perfused (Zone 1) regions and suggesting more efficient gas exchange. This finding provides a mechanistic explanation for the frequently observed increase in PaO_2/FiO_2 ratios following prone positioning in patients with moderate to severe ARDS, particularly when conventional recruitment or neuromuscular blockade strategies have limited effect.

In addition, the model explored one of the most pressing issues in ventilator management: the spatial distribution of mechanical power and its role in ventilator-induced lung injury (VILI). By calculating the time-resolved delivery of mechanical energy to lung tissue, the model revealed a highly heterogeneous pattern of power deposition, with the non-dependent regions (e.g., anterior lung in supine, dorsal in prone) receiving disproportionately high energy loads. This insight is critical: it shows that even in globally "protective" ventilation settings, localised overdistension and stress concentration can persist and drive injury. These findings align with experimental evidence but go beyond it by offering precise, localised predictions of VILI risk that are difficult to measure clinically or experimentally. Importantly, the model also demonstrated that these regional risks are not fixed: by re-positioning the patient (e.g., from supine to prone), the same ventilator settings can result in dramatically different distributions of mechanical power. In prone positioning, the model predicts a more uniform power delivery profile, with reduced overdistension in the previously high-risk non-dependent regions. This supports a more nuanced, position-aware ventilation strategy, where body posture becomes an active tool for reducing local mechanical trauma, alongside ventilator setting adjustments such as PEEP titration and tidal volume modulation.

Beyond ARDS, the model offers explanatory power for conditions like early COVID-19 pneumonia, where severe hypoxaemia may occur despite preserved ventilation. In such cases, upright or supine positions may exacerbate V/Q mismatch due to gravitational perfusion gradients. The model supports the role of awake proning in non-intubated patients by showing how this intervention can improve V/Q balance and oxygenation even in the absence of overt ventilatory failure. This fully coupled model also holds significant value for surgical and interventional planning. In cases such as prone neurosurgery, cardiothoracic procedures, or one-lung ventilation scenarios, understanding how ventilation and perfusion shift with patient positioning is critical. The model offers a predictive tool to anticipate these shifts and optimise intraoperative gas exchange, potentially reducing perioperative complications.

Furthermore, the model's capacity to track mechanical power across the breathing cycle and spatially map regions of elevated stress has no current equivalent in experimental or clinical practice. This opens up opportunities for personalised medicine: clinicians could eventually use model outputs to identify high-risk lung zones in individual patients and implement strategies such as tailored positioning, targeted PEEP adjustments, and selective monitoring to reduce VILI incidence.

For sedated and mechanically ventilated patients, this model offers robust predictive capacity for both V/Q distribution and mechanical energy delivery. It validates the use of prone positioning to minimise perfusion dead space, enhance oxygenation, and reduce VILI risk, offering a solid mechanistic rationale for its early and repeated use in severe respiratory failure. For awake patients, although the model does not explicitly incorporate active respiratory muscle function, it nevertheless provides foundational insights into how gravitational and thoracic pressure gradients shape ventilation and perfusion. These insights support interventions like awake proning, particularly in resource-limited settings or early disease phases where invasive ventilation is not yet required.

Despite its sophistication, the model remains limited by its dimensionality and does not yet include active neuromuscular mechanics or real-time feedback from patient-driven efforts. However, its high granularity and physiologically informed coupling make it an ideal platform for future expansion. The ability to replicate bedside phenomena—such as pressure-volume curves, oxygenation shifts with posture, and regional stress distributions—using only ventilator input parameters affirms its translational potential.

In conclusion, this chapter marks the culmination of the thesis's modelling work by delivering a fully coupled, non-linear poroelastic lung model that mechanistically links ventilation, perfusion, posture, and injury risk. It serves as a powerful research and clinical tool capable of simulating whole-lung behaviour with unprecedented detail. Crucially, it offers the ability not only to explain observed clinical phenomena but to anticipate them—enabling safer, more personalised, and physiologically grounded care strategies for patients with complex respiratory needs.

8 Conclusion

8.1 Review

In this thesis, we explored the impact of patient positioning and gravity on pulmonary mechanics, focusing on critically ill patients who require mechanical ventilation. This study aimed to uncover how different postures may influence lung deformation, and the subsequent ventilation and perfusion across the lung, and how these changes can inform clinical care. By developing a series of increasingly sophisticated mathematical models using incorporating techniques from solid mechanics, poroelasticity, geomechanics and structural engineering, this research provides a framework to analyse and predict pulmonary responses to various clinical conditions and interventions. Below is a summary of the primary findings for each major section of the thesis.

The literature review established the groundwork by analysing existing research on pulmonary function as influenced by body position. Studies indicate that different positions affect lung function significantly, with prone positioning shown to improve oxygenation and ventilation-perfusion matching in critically ill patients. Moreover, it was found that gravity plays a substantial role in the distribution of lung tissue deformation, ventilation, and perfusion. However, there were gaps in the literature regarding the precise mechanics underlying these effects and how they translate into real-world clinical settings. This review highlighted the need for a mathematical approach to model lung behaviour under varying positions, thus guiding the thesis' focus for a comprehensive and detailed mathematical model of lung tissue.

To establish a baseline understanding of lung tissue deformation, we began with a static model that treated the lung as a solid, non-dynamic object. This model provided initial insights into how gravity affects the lung when deflated and allowed us to assess basic tissue deformation patterns in upright, supine, and prone positions. Results from this stage highlighted that the lung tissue experiences increased strain in the upright position, with reduced deformation in the prone orientation. This confirmed that gravity is indeed a significant factor in pulmonary mechanics and laid the foundation for integrating dynamic aspects into the model.

The development of linear and non-linear poroelastic models added complexity, allowing the simulation of lung dynamics with airflow and the intrinsic elasticity of lung tissue. The linear poroelastic model, based on simplified assumptions, showed that lung tissue compliance and resistance varied with patient position, corroborating clinical observations of improved oxygenation and perfusion in the prone position.

Building on this, the non-linear poroelastic model introduced hyperelastic properties and time-dependent recruitment of alveolar units, resulting in a more physiologically accurate depiction of lung behaviour. This advanced model demonstrated that alveolar recruitment is more uniform in the prone position, aligning with clinical findings of improved ventilation-perfusion ratios in this posture. Furthermore, the model indicated that prone positioning could mitigate regions of alveolar collapse and over distension, suggesting potential benefits in reducing ventilator-induced lung injury (VILI). These findings support the clinical practice of prone positioning as a strategy to optimize ventilation in ICU patients. Results from this section provided confidence in the ability of the model to accurately predict lung behaviour throughout the breathing cycle in a mechanically ventilated patient, and opened the way for in silico experimentation and testing clinical theories.

In the final section, the model was extended to incorporate the intricate branching structure of the upper airways, in a way which captured to overall patterns of flows and resistance, without being too computationally complex.

We also added the hydrostatic fluid column associated with pulmonary bloodflow, in order to fully couple the poroelastic model the the cardiac system, with special interest in the influence of external pressures put onto the alveoli by the thoracic contents in different positions. Having established a baseline for the upright lung across the breathing cycle from functional residual capacity to total lung capacity, the lung and surrounding structures were rotated to the prone and supine positions. Findings in this stage were an increases uniformity in alveolar pressures in the horizontal positions, which in turn resulted in a more uniform distribution of airflow and bloodflow. Of particular note here was the impact of patient orientation on the size and location of West's zones of the lung, with the unperfused zone 1 being smallest in the prone position, and largest in the upright. This resulted in a ventilation/perfusion ratio closer to 1 in the prone position, a finding which corroborates clinical and experimental results.

Finally, the model was used to test a scenario of particular clinical importance; the ventilator mechanical power and the subsequent risk of ventilator induced lung injury for the patient. After exploring how each ventilator setting contributes to this calculated mechanical power, we assessed how it impacts the two key indicators of lung damage relevant to the poroelastic model, the dynamic stresses and strains. Findings here were that stress and strain increase in a non-linear manner as mechanical power increases; increasing exponentially after a certain mechanical power value. This not only validates the importance of mechanical power on the risk of lung damage, but also helps to explain the controversy between the exact value for a safe threshold of mechanical power that can be given to a patient. Mechanical power was found to vary greatly with lung height, with the non-dependent regions at the top of the lung receiving the highest power, and subsequently at the greatest risk of injury. However, these risk can be reduced by manoeuvring the patient into the prone position, redistributing the stresses on the alveoli.

Overall, this thesis has provided an in-depth look into the importance of mathematical modelling in aiding clinical decision making, and just how vital it can be for the wellbeing of the patient. Through a series of mathematical models, this thesis contributes a deeper understanding of how these mechanisms work and offers a quantitative tool that could potentially assist clinicians in optimizing patient care. By examining each position and developing models that increasingly reflect physiological complexity, this study confirms the clinical value of prone positioning, provides a framework for individualized patient care, and lays the groundwork for further research in computational pulmonary mechanics.

The progression from static to coupled non-linear models demonstrates a quantitative tool that can bridge the gap between theoretical understanding and actionable clinical guidance. Specifically, the findings on reduced pressure heterogeneity, improved V/Q matching, and diminished localized VILI risk in the prone position provide robust mechanistic support for this widely adopted ICU strategy. This thesis confirms the potential of 'in-silico' experimentation to inform real-time bedside decisions, enabling clinicians to tailor ventilator settings and patient positioning to individual physiological responses.

8.2 Novel Insights and Contributions to the Field of Pulmonary Mechanics

The work presented in this thesis advances the field of pulmonary mechanics by addressing several critical gaps in the existing literature and introducing a novel mathematical framework for modelling lung deformation and function.

The most distinctive feature of this model is its explicit tracking of spatial variations across isogravitational planes. Unlike traditional models that treat the lung as a single, homogeneous entity, this work accounts for regional differences in mechanics and physiology by separately modelling each isogravitational plane. This enables a more precise representation of how gravity and body position influence alveolar mechanics, ventilation-perfusion ratios, and tissue stresses within specific regions of the lung. Most importantly, the model tracks and outputs each of the parameters as they vary in space and time. By incorporating these spatial variations, the model provides a detailed understanding of localized phenomena that are often obscured in whole-lung analyses, such as the distribution of strain and stress, and their implications for ventilator-induced lung injury (VILI).

A novel feature of the model is its ability to capture non-linear time-dependent alveolar recruitment and de-recruitment against gravity. By dynamically linking alveolar opening and closing pressures with regional mechanical properties, the model provides a more accurate representation of lung behaviour under varying ventilatory conditions. This contrasts with many existing models, which often treat recruitment as a static or linear process.

This work introduces a unique capability to simulate the localized effects of mechanical ventilation, particularly the distribution of strain and stress across the lung under different ventilatory settings. By incorporating boundary conditions specific to ventilator-induced pressure and flow, the model offers insights into ventilator-induced lung injury (VILI) and helps identify strategies to minimize mechanical damage.

While previous models often include different postures, this thesis uniquely investigates the internal mechanics of the lung in detail across these positions, focusing on regional mechanics and their implications for ventilation-perfusion dynamics. It also allows for a detailed exploration into the effects of positioning on regional recruitment, distribution of stress and strains, and risk of localised ventilator induced damage.

The explicit tracking of spatial variations across isogravitational planes, combined with the ability to simulate localized mechanical power and VILI risk, represents a significant advancement. This allows clinicians to move beyond 'one-size-fits-all' ventilation by identifying specific vulnerable lung regions and dynamically adjusting strategies. The model's capacity to predict the impact of ventilator settings on localized stress and strain offers a powerful new dimension for developing truly protective and personalized ventilation protocols, aiming to reduce iatrogenic injury and improve long-term outcomes for critically ill patients.

8.3 Future Work

This research has demonstrated the potential of poroelastic modelling to analyse and predict the impact of patient positioning on pulmonary mechanics. However, further work is necessary to enhance the model's precision, clinical applicability, and adaptability to diverse patient profiles. Future research should address limitations identified in this study and extend the model to incorporate additional physiological and mechanical complexities. Several promising directions for future work include enhancing patient specificity, refining mechanical complexity, and broadening the model's clinical applications.

8.3.1 Modelling Complex Fluid Dynamics in the Airways

Currently, the resistance and flow of air to the model is calculated according to Poiseuille's law of fluid dynamics, creating a simple function to summarise dynamics from the ventilator to the terminal branches. However, this is a significant simplification to a very complex system. In reality, the airways are lined with mucus which not only provides a protective barrier, but also greatly impacts the flow of air through the branching network [111]. By assessing the mathematical nature of these secretions, we can create a more accurate model of the airways. This will allow for a more intricate exploration of the local stresses and strains in the airways to explore injury and damage. Moreover, this will allow for the modelling of fluid build up and clinical removal techniques such as suctioning, which are very common in mechanically ventilated patients. These areas are currently being explored by members of the CHIMERA team at UCL, including the mathematical modelling of pulmonary secretions as a non-Newtonian fluid, and the analysis of pre and post-suctioning data to establish differences in pressure volume curves. Mucus could be added as an extra phase in the model iteration.

8.3.2 Exploring Additional Patient Positions and Mobility

This thesis has focussed on three primary positions, upright, supine and prone. Although these have provided fantastic insight into pulmonary mechanics due to gravity, the positions most commonly used in the ICU setting differ from these. Prone is being used more regularly since the Covid-19 pandemic, however supine and upright are less common. More routinely used is the Fowler's/Semi-Fowler's positions, a semi-reclined position which has the patient's torso elevated at between 15-30° for low Fowler's, 30-45° for semi-Fowler's, 45-60° for standard Fowler's, and 60-90° for high Fowler's. There is also particular interest in the lateral positions, in which a patient is placed on their side, as this common for a number of surgical procedures and airway clearance techniques, as well as in seizing and unconscious patients as an attempt to keep the airways open. However, the addition of these positions requires a significantly more complex analogy for lung shape, which can be rotated more freely than the current truncated cone. There is also interest in the dynamics created moving between positions, as this is a common approach when attempting to improve lung function. Simulating continuous or frequent positional changes (e.g., rotations every few hours) could help assess the benefits of regular patient repositioning as a strategy to improve lung mechanics and alveolar recruitment, and prevent regional lung collapse.

8.3.3 Increasing Physiological Accuracy of Lung Shape Analogy

This thesis explore three shapes as an analogy to the lung; the cylinder, the cone, and the truncated cone, finding that the truncated cone provided the greatest physiological accuracy of the three. However, this is still a vast oversimplification of the complex geometry of a physical lung. As the cross-sectional area of the lung is computed as a function of x in the current model set-up, it would be possible to import a more realistic set of value for cross-sectional area from data. This would require accurate imaging data of the lung shape in different positions. This concept could also then be expanded to assess patient specific differences in lung shape such as height and width of the lung relative the patient's own physiology.

8.3.4 Heterogeneity Within Each Isogravitational Plane

In Section 3.1 of this thesis, it was shown that multiple parameters that vary in height up the lung, also vary within each isogravitational plane, such as ventilation and perfusion. Expanding the model to 2 dimensions would allow for the exploration of local heterogeneity in lung mechanics influenced by factors other than gravity. In order to do this, we could give each alveolus a second coordinate in the y plane and update equations accordingly. A more simplistic approach however, would be to create a 1.5 dimension model. Here, the existing set up and calculation would remain as presented in this thesis, but each parameter would now be represented as a vector of value ranges in the y axis.

8.3.5 Modelling Different Pathophysiologies with Regional Characteristics

A key direction for future work is adapting the current models to simulate various pathophysiological states, such as ARDS or COPD, with localized alterations in compliance, resistance, and perfusion. Incorporating patient-specific data, such as from personalized imaging (e.g. CT scans) or pulmonary function tests, could enable tailored simulations. This would assist in predicting responses to therapeutic interventions like mechanical ventilation or prone positioning in diverse patient populations. The unique framework of this model allows for local damage to added at any location in the lung, and parameters adjusted accordingly. This means that disease-affected lung regions could be replicated accurately from pulmonary oedema to the stiffening seen in fibrosis.

8.3.6 Chest Wall and Diaphragm Considerations

To significantly enhance the model's precision and clinical applicability, future work must conceptually incorporate the mechanics of the chest wall and the effects of the diaphragm, as these factors are known to profoundly influence positional changes in lung mechanics and are acknowledged as external pressures applied to the lung by the contents of the thorax that require further refinement. This is crucial because pleural pressure gradients and the diaphragm's load directly impact regional lung mechanics and vary with body position, patient age, and conditions such as obesity. Conceptual methods for integration could involve dynamically determining the external pressure term within the model based on a more comprehensive understanding of chest wall and abdominal mechanics, potentially including deformable models of the chest wall and diaphragm themselves, possibly using continuum mechanics or poroelastic principles. Incorporating the chest wall and surrounding muscular systems will also allow for a more precise exploration of lung mechanics in awake ventilated patients, which the current model setup cannot do directly.

8.3.7 Validating with Experimental Data

Validation is crucial for ensuring that the developed models can accurately represent physiological behaviour and support clinical decision-making, particularly as the model progresses from conceptual understanding to aiding real-time clinical inference in an Intensive Care Unit (ICU) setting. While traditional approaches remain vital, future work should prioritize directly comparing model outputs with a diverse range of experimental and clinical datasets to refine and establish the model's reliability. Some possibilities are listed below.

Traditional Experimental Data for Validation

Comparisons with existing experimental datasets, whether derived from imaging studies, cadaver models, or animal experiments, form a foundational aspect of model validation.

Imaging Data (CT/MRI Scans)

- Regional Lung Density and Deformation: High-resolution CT and MRI scans can quantify regional lung tissue density and deformation, confirming phenomena like the "Slinky Effect" where the lung deforms under its own weight, causing varying tissue density from apex to base. The model's predicted displacement and changes in alveolar volume across vertical lung height can be directly compared with these imaging results. For instance, differences in tissue density gradients between supine and prone positions, as observed experimentally, can be a validation target.

- Dynamic Changes (4D CT): More advanced 4D CT provides dynamic information throughout the breathing cycle, which can validate the model's time-dependent poroelastic dynamics, including parameters such as porosity and permeability variations with inflation.

- Alveolar Recruitment and Over-distension: Imaging can visualize regional alveolar opening and closing, especially in diseased states like ARDS, which can be compared to the model's time-dependent alveolar recruitment dynamics. This also extends to validating the model's prediction of alveolar stiffening during over-distension at high lung volumes.

Animal Studies

- Ventilation-Perfusion (V/Q) Distribution: Studies using radioactive tracers (e.g., Xenon 133, radioactive CO_2) in animals have provided extensive data on regional ventilation and perfusion distribution across lung height and between different positions. The model's V/Q ratio predictions, especially the extent and behaviour of West's Zones (Zone 1 where perfusion is zero) at different lung volumes, can be rigorously validated against such findings.

- Gravity's Contribution to Perfusion Heterogeneity: Animal studies have explored the degree to which gravity determines regional blood flow heterogeneity, and whether non-gravitational factors (e.g., vascular structure) play a more significant role. The model's ability to replicate these complex interactions and quantify the relative influence of gravity versus structural heterogeneity would be a strong validation point.

Patient-Specific Data Integration

- Integration into a Digital Twin Framework: A more immediately promising avenue for validation, particularly for clinical applicability, is the integration of the poroelastic lung model into a digital twin framework, such as those developed within the CHIMERA hub. This approach allows for continuous validation and refinement using real-world clinical data.

- Ventilator Waveforms: Comparing simulated pressure-volume (P-V) curves and pressure-time/flow-time waveforms against those measured directly from the mechanical ventilator provides a direct validation of the model's dynamic behaviour during inflation and deflation. This includes assessing the accuracy of the model's representation of the Lower Inflection Point (LIP) and Upper Inflection Point (UIP), which characterize alveolar recruitment and over-distension, respectively.

- Blood Gas Analysis: Clinical measurements of arterial partial pressure of oxygen (PaO2) and fraction of inspired oxygen (FIO2) ratio (PaO2/FIO2) provide a direct measure of gas exchange efficiency. The model's ability to predict improvements in oxygenation with positional changes (e.g., prone positioning) can be validated against this crucial clinical metric.

- Chest Wall Dynamics and Compliance: Patient data on chest wall motion and overall lung and chest wall compliance in different body positions, including variations due to patient age or obesity, can be used to validate the model's incorporation of external pressures and their impact on lung mechanics. This helps validate the conceptual inclusion of chest wall and diaphragm effects.

Predictive Testing and Clinical Trials

Digital twins enable "in-silico experimentation" where different ventilation strategies or postural adjustments can be simulated and their predicted outcomes compared to actual patient responses. This includes evaluating predicted mechanical power and associated VILI risk in different lung regions and positions. Collaborating with clinical teams to incorporate this model into patient-specific care plans and validating its predictive power in pilot studies would represent a significant step forward in establishing the trust and utility of the model in clinical settings. This also supports the model's potential integration into clinical guidelines and decision-support systems, as seen during the COVID-19 pandemic with prone positioning.

Validation with Diseased Lung Data

The model's ability to simulate various pathophysiological states (e.g., ARDS, COPD) and localized alterations in compliance, resistance, and perfusion is critical for its clinical utility. Patient-specific data from diseased lungs, rather than just healthy individuals, will be essential for validating the model's predictions of how lung injury affects tissue deformation, V/Q matching, and susceptibility to VILI.

References

[1] Inc. The MathWorks. *MATLAB R2024a*. Natick, Massachusetts, USA, 2024.

[2] Satoko Naitoh et al. “The effect of body position on pulmonary function, chest wall motion, and discomfort in young healthy participants”. In: *Journal of manipulative and physiological therapeutics* 37.9 (2014), pp. 719–725.

[3] Peter J Thomas et al. “Positioning practices for ventilated intensive care patients: current practice, indications and contraindications”. In: *Australian Critical Care* 19.4 (2006), pp. 122–132.

[4] C Guerin et al. “Effects of prone position on alveolar recruitment and oxygenation in acute lung injury”. In: *Intensive care medicine* 25 (1999), pp. 1222–1230.

[5] Anthony S Fauci, H Clifford Lane, and Robert R Redfield. *Covid-19—navigating the uncharted*. 2020.

[6] Stephan Ehrmann et al. “Awake prone positioning for COVID-19 acute hypoxaemic respiratory failure: a randomised, controlled, multinational, open-label meta-trial”. In: *The Lancet Respiratory Medicine* 9.12 (2021), pp. 1387–1395.

[7] JB West, CTt Dollery, and A Naimark. “Distribution of blood flow in isolated lung; relation to vascular and alveolar pressures”. In: *Journal of applied physiology* 19.4 (1964), pp. 713–724.

[8] ROBB W Glenny et al. “Gravity is a minor determinant of pulmonary blood flow distribution”. In: *Journal of applied physiology* 71.2 (1991), pp. 620–629.

[9] ROBB W Glenny, LINCOLN Polissar, and H THOMAS Robertson. “Relative contribution of gravity to pulmonary perfusion heterogeneity”. In: *Journal of applied physiology* 71.6 (1991), pp. 2449–2452.

[10] Merryn H Tawhai et al. “Supine and prone differences in regional lung density and pleural pressure gradients in the human lung with constant shape”. In: *Journal of Applied Physiology* 107.3 (2009), pp. 912–920.

[11] John B West and Frank L Matthews. “Stresses, strains, and surface pressures in the lung caused by its weight”. In: *Journal of Applied Physiology* 32.3 (1972), pp. 332–345.

[12] G Kim Prisk. “Microgravity and the respiratory system”. In: *European Respiratory Journal* 43.5 (2014), pp. 1459–1471.

[13] Susan R Hopkins et al. “Vertical gradients in regional lung density and perfusion in the supine human lung: the Slinky effect”. In: *Journal of applied physiology* 103.1 (2007), pp. 240–248.

[14] JB West and CT Dollery. “Distribution of blood flow and ventilation-perfusion ratio in the lung, measured with radioactive CO2”. In: *Journal of Applied Physiology* 15.3 (1960), pp. 405–410.

[15] Mehdi Mezidi and Claude Guérin. “Effects of patient positioning on respiratory mechanics in mechanically ventilated ICU patients”. In: *Annals of translational medicine* 6.19 (2018), p. 384.

[16] L Blanch et al. “Short-term effects of prone position in critically ill patients with acute respiratory distress syndrome”. In: *Intensive care medicine* 23 (1997), pp. 1033–1039.

[17] Parisa Ghelichkhani and Maryam Esmaeili. “Prone position in management of COVID-19 patients; a commentary”. In: *Archives of academic emergency medicine* 8.1 (2020), e48.

[18] Xu Li and Xiaochun Ma. “Acute respiratory failure in COVID-19: is it “typical” ARDS?” In: *Critical care* 24.1 (2020), p. 198.

[19] Jimyung Park et al. “Effect of prone positioning on oxygenation and static respiratory system compliance in COVID-19 ARDS vs. non-COVID ARDS”. In: *Respiratory research* 22 (2021), pp. 1–12.

[20] L Gattinoni and JJ Marini. “Isn’t it time to abandon ARDS? The COVID-19 lesson”. In: *Critical Care* 25.1 (2021), p. 326.

[21] JB West and CT Dollery. “Distribution of blood flow and the pressure-flow relations of the whole lung”. In: *Journal of Applied Physiology* 20.2 (1965), pp. 175–183.

[22] JMB Hughes et al. “Effect of lung volume on the distribution of pulmonary blood flow in man”. In: *Respiration physiology* 4.1 (1968), pp. 58–72.

[23] Richard H Kallet. “A comprehensive review of prone position in ARDS”. In: *Respiratory care* 60.11 (2015), pp. 1660–1687.

[24] A Cortney Henderson et al. “The gravitational distribution of ventilation-perfusion ratio is more uniform in prone than supine posture in the normal human lung”. In: *Journal of applied physiology* 115.3 (2013), pp. 313–324.

[25] AC Bryan et al. “Factors affecting regional distribution of ventilation and perfusion in the lung”. In: *Journal of applied physiology* 19.3 (1964), pp. 395–402.

[26] Anne E Dixon and Ubong Peters. “The effect of obesity on lung function”. In: *Expert review of respiratory medicine* 12.9 (2018), pp. 755–767.

[27] GöraN Hedenstierna and Joakim Santesson. “Breathing mechanics, dead space and gas exchange in the extremely obese, breathing spontaneously and during anaesthesia with intermittent positive pressure ventilation”. In: *Acta Anaesthesiologica Scandinavica* 20.3 (1976), pp. 248–254.

[28] Paolo Pelosi et al. “The effects of body mass on lung volumes, respiratory mechanics, and gas exchange during general anesthesia”. In: *Anesthesia & Analgesia* 87.3 (1998), pp. 654–660.

[29] Negin Behazin et al. “Respiratory restriction and elevated pleural and esophageal pressures in morbid obesity”. In: *Journal of applied physiology* 108.1 (2010), pp. 212–218.

[30] Rolf D Hubmayr. “Perspective on lung injury and recruitment: a skeptical look at the opening and collapse story”. In: *American journal of respiratory and critical care medicine* 165.12 (2002), pp. 1647–1653.

[31] Fabrizio Bezzo and Federico Galvanin. “On the identifiability of physiological models: Optimal design of clinical tests”. In: *Computer Aided Chemical Engineering*. Vol. 42. Elsevier, 2018, pp. 85–110.

[32] *PubMed Search*. URL: `https://pubmed.ncbi.nlm.nih.gov/?term=computational+model`.

[33] David Gavaghan et al. “Mathematical models in physiology”. In: *Philosophical Transactions of the Royal Society A: Mathematical, Physical and Engineering Sciences* 364.1842 (2006), pp. 1099–1106.

[34] J.K. Stoller and R.M. Kacmarek. *Fundamentals of Respiratory Care*. Mosby, 2009. ISBN: 9780323046077. URL: `https://books.google.co.uk/books?id=lXDgPAAACAAJ`.

[35] Ubaidur Rahaman. “Mathematics of ventilator-induced lung injury”. In: *Indian Journal of Critical Care Medicine: Peer-reviewed, Official Publication of Indian Society of Critical Care Medicine* 21.8 (2017), p. 521.

[36] Luciano Gattinoni et al. “Ventilator-related causes of lung injury: the mechanical power”. In: *Intensive care medicine* 42 (2016), pp. 1567–1575.

[37] EP Radford. “Recent studies of mechanical properties of mammalian lungs”. In: *Tissue elasticity* 177 (1957).

[38] Annalisa J Swan, Alys R Clark, and Merryn H Tawhai. “A computational model of the topographic distribution of ventilation in healthy human lungs”. In: *Journal of theoretical biology* 300 (2012), pp. 222–231.

[39] Emmanuel Detournay and Alexander H-D Cheng. “Fundamentals of poroelasticity”. In: *Analysis and design methods.* Elsevier, 1993, pp. 113–171.

[40] VON TERZAGHI. “Die Berechnung der Durchassigkeitsziffer des Tones aus dem Verlauf der hydrodynamischen Spannungs. erscheinungen”. In: *Sitzungsber. Akad. Wiss. Math. Naturwiss. Kl. Abt. 2A* 132 (1923), pp. 105–124.

[41] Maurice A Biot. “General theory of three-dimensional consolidation”. In: *Journal of applied physics* 12.2 (1941), pp. 155–164.

[42] Andrea Malandrino and Emad Moeendarbary. “Poroelasticity of living tissues”. In: *Encyclopedia of biomedical engineering* (2019), pp. 238–245.

[43] Emad Moeendarbary et al. “The cytoplasm of living cells behaves as a poroelastic material”. In: *Nature materials* 12.3 (2013), pp. 253–261.

[44] Dominique Chapelle et al. “A poroelastic model valid in large strains with applications to perfusion in cardiac modeling”. In: *Computational Mechanics* 46 (2010), pp. 91–101.

[45] António F Miguel. “Lungs as a natural porous media: architecture, airflow characteristics and transport of suspended particles”. In: *Heat and mass transfer in porous media*. Springer, 2011, pp. 115–137.

[46] Lorenz Berger et al. “A poroelastic model coupled to a fluid network with applications in lung modelling”. In: *International journal for numerical methods in biomedical engineering* 32.1 (2016).

[47] Behnaz Seyfi, Anand P Santhanam, and Olusegun J Ilegbusi. “A biomechanical model of human lung deformation utilizing patient-specific elastic property”. In: *Journal of Cancer Therapy* 7.6 (2016), pp. 402–415.

[48] Amir A Zadpoor. *Mechanics of biological tissues and biomaterials: current trends*. 2015.

[49] Ewald R Weibel, Andre F Cournand, and Dickinson W Richards. *Morphometry of the human lung*. Vol. 1. Springer, 1963.

[50] DL Vawter, FL Matthews, and JB West. “Effect of shape and size of lung and chest wall on stresses in the lung”. In: *Journal of Applied Physiology* 39.1 (1975), pp. 9–17.

[51] Lisa Spruce and Sharon A Van Wicklin. “Back to basics: positioning the patient”. In: *AORN journal* 100.3 (2014), pp. 298–305.

[52] Matthias Ochs et al. “The number of alveoli in the human lung”. In: *American journal of respiratory and critical care medicine* 169.1 (2004), pp. 120–124.

[53] Bhushan H Katira et al. “Positive end-expiratory pressure, pleural pressure, and Regional Compliance during Pronation. An experimental study”. In: *American journal of respiratory and critical care medicine* 203.10 (2021), pp. 1266–1274.

[54] Johan Petersson et al. "Posture primarily affects lung tissue distribution with minor effect on blood flow and ventilation". In: *Respiratory physiology & neurobiology* 156.3 (2007), pp. 293–303.

[55] Sonal Mistry et al. "Validation of at-the-bedside formulae for estimating ventilator driving pressure during airway pressure release ventilation using computer simulation". In: *Respiratory Research* 23.1 (2022), p. 101.

[56] Peter D Wagner. "Ventilation/perfusion relationships". In: *Clinical Physiology* 1.5 (1981), pp. 437–451.

[57] AC Bryan, J Milic-Emili, and D Pengelly. "Effect of gravity on the distribution of pulmonary ventilation." In: *Journal of Applied Physiology* 21.3 (1966), pp. 778–784.

[58] Gary F Nieman, Andrew M Paskanik, and Carl E Bredenberg. "Effect of positive end-expiratory pressure on alveolar capillary perfusion". In: *The Journal of Thoracic and Cardiovascular Surgery* 95.4 (1988), pp. 712–716.

[59] Andrew B Lumb and Elizabeth Horncastle. "Pulmonary physiology". In: *Pharmacology and physiology for anesthesia*. Elsevier, 2019, pp. 586–612.

[60] Horatio Scott Carslaw et al. "Conduction of heat in solids and heat conduction". In: *Physics Today* 1.7 (1948), pp. 24–24.

[61] Ruel Vance Churchill et al. *Operational mathematics*. Vol. 1. McGraw-Hill New York, 1972.

[62] Peter B Flemings. *A concise guide to geopressure: Origin, prediction, and applications*. Cambridge University Press, 2021.

[63] J Nagels et al. "Mechanical properties of lungs and chest wall during spontaneous breathing". In: *Journal of Applied Physiology* 49.3 (1980), pp. 408–416.

[64] John Crank and Phyllis Nicolson. “A practical method for numerical evaluation of solutions of partial differential equations of the heat-conduction type”. In: *Mathematical proceedings of the Cambridge philosophical society*. Vol. 43. 1. Cambridge University Press. 1947, pp. 50–67.

[65] PA Vermeer and A Verruijt. “An accuracy condition for consolidation by finite elements”. In: *International Journal for numerical and analytical methods in geomechanics* 5.1 (1981), pp. 1–14.

[66] Márcio A Murad and Abimael FD Loula. “On stability and convergence of finite element approximations of Biot’s consolidation problem”. In: *International Journal for Numerical Methods in Engineering* 37.4 (1994), pp. 645–667.

[67] Ewald R Weibel and Domingo M Gomez. “Architecture of the human lung: use of quantitative methods establishes fundamental relations between size and number of lung structures”. In: *Science* 137.3530 (1962), pp. 577–585.

[68] Yoshitake Yamada et al. “Comparison of inspiratory and expiratory lung and lobe volumes among supine, standing, and sitting positions using conventional and upright CT”. In: *Scientific reports* 10.1 (2020), p. 16203.

[69] Shotaro Chubachi et al. “Differences in lung and lobe volumes between supine and upright computed tomography in patients with idiopathic lung fibrosis”. In: *Scientific reports* 12.1 (2022), p. 19408.

[70] SD Mentzelopoulos, C Roussos, and SG15738300 Zakynthinos. “Prone position reduces lung stress and strain in severe acute respiratory distress syndrome”. In: *European Respiratory Journal* 25.3 (2005), pp. 534–544.

[71] G Mols, H-J Priebe, and J Guttmann. “Alveolar recruitment in acute lung injury”. In: *British journal of anaesthesia* 96.2 (2006), pp. 156–166.

[72] Christopher B Massa, Gilman B Allen, and Jason HT Bates. "Modeling the dynamics of recruitment and derecruitment in mice with acute lung injury". In: *Journal of Applied Physiology* 105.6 (2008), pp. 1813–1821.

[73] Baoshun Ma, Béla Suki, and Jason HT Bates. "Effects of recruitment/derecruitment dynamics on the efficacy of variable ventilation". In: *Journal of applied physiology* 110.5 (2011), pp. 1319–1326.

[74] Carolin M Geitner et al. "An approach to study recruitment/derecruitment dynamics in a patient-specific computational model of an injured human lung". In: *International Journal for Numerical Methods in Biomedical Engineering* 39.9 (2023), e3745.

[75] Jason HT Bates and Charles G Irvin. "Time dependence of recruitment and derecruitment in the lung: a theoretical model". In: *Journal of Applied Physiology* 93.2 (2002), pp. 705–713.

[76] Scott P Albert et al. "The role of time and pressure on alveolar recruitment". In: *Journal of Applied Physiology* 106.3 (2009), pp. 757–765.

[77] Gaetano Scaramuzzo et al. "Gravitational distribution of regional opening and closing pressures, hysteresis and atelectrauma in ARDS evaluated by electrical impedance tomography". In: *Critical Care* 24 (2020), pp. 1–8.

[78] R Scott Harris. "Pressure-volume curves of the respiratory system". In: *Respiratory care* 50.1 (2005), pp. 78–99.

[79] RS Rivlin. "Pheology Vol. 1 351p (Eirich) Philoso". In: *Trans. Roy. Soc. London A* 240 (1948), pp. 459–491.

[80] Ronald S Rivlin. "Large elastic deformations of isotropic materials IV. Further developments of the general theory". In: *Philosophical transac-*

tions of the royal society of London. Series A, Mathematical and physical sciences 241.835 (1948), pp. 379–397.

[81] Claude Guerin and Jean-Christophe Richard. "Measurement of respiratory system resistance during mechanical ventilation". In: *Intensive care medicine* 33 (2007), pp. 1046–1049.

[82] H Brown Robert et al. "Lung density changes with growth and inflation". In: *Chest* 148.4 (2015), pp. 995–1002.

[83] Sanghun Choi et al. "Registration-based assessment of regional lung function via volumetric CT images of normal subjects vs. severe asthmatics". In: *Journal of applied physiology* 115.5 (2013), pp. 730–742.

[84] Steve A Maas et al. "FEBio: finite elements for biomechanics". In: (2012).

[85] Manuel T Cabeleira et al. "Comparing physiological impacts of positive pressure ventilation versus self-breathing via a versatile cardiopulmonary model incorporating a novel alveoli opening mechanism". In: *Computers in Biology and Medicine* 180 (2024), p. 108960.

[86] Ewald R Weibel. "Design of airways and blood vessels considered as branching trees." In: *The lung* (1991), pp. 711–720.

[87] Abhijit Guha. "Transport and deposition of particles in turbulent and laminar flow". In: *Annu. Rev. Fluid Mech.* 40.1 (2008), pp. 311–341.

[88] J Pfitzner. "Poiseuille and his law". In: *Anaesthesia* 31.2 (1976), pp. 273–275.

[89] A Charles Bryan. "Comments of a devil's advocate". In: *American Review of Respiratory Disease* 110.6P2 (1974), pp. 143–144.

[90] John Burnard West. *Respiratory physiology: the essentials.* Lippincott Williams & Wilkins, 2012.

[91] Nicholas J Johnson, Andrew M Luks, and Robb W Glenny. “Gas exchange in the prone posture”. In: *Respiratory care* 62.8 (2017), pp. 1097–1110.

[92] TC Amis, Hazel A Jones, and JMB Hughes. “Effect of posture on interregional distribution of pulmonary ventilation in man”. In: *Respiration physiology* 56.2 (1984), pp. 145–167.

[93] Eric A Hoffman. “Effect of body orientation on regional lung expansion: a computed tomographic approach”. In: *Journal of Applied Physiology* 59.2 (1985), pp. 468–480.

[94] D Orphanidou et al. “Tomography of regional ventilation and perfusion using krypton 81m in normal subjects and asthmatic patients.” In: *Thorax* 41.7 (1986), pp. 542–551.

[95] Johan Petersson et al. “Physiological imaging of the lung: single-photon-emission computed tomography (SPECT)”. In: *Journal of applied physiology* 102.1 (2007), pp. 468–476.

[96] Robb W Glenny et al. “Gravity is an important but secondary determinant of regional pulmonary blood flow in upright primates”. In: *Journal of Applied Physiology* 86.2 (1999), pp. 623–632.

[97] Sven Nyren et al. “Lung ventilation and perfusion in prone and supine postures with reference to anesthetized and mechanically ventilated healthy volunteers”. In: *Anesthesiology* 112.3 (2010), pp. 682–687.

[98] Arthur B Otis, Wallace O Fenn, and Hermann Rahn. “Mechanics of breathing in man”. In: *Journal of applied physiology* 2.11 (1950), pp. 592–607.

[99] John J Marini and Philip S Crooke. "A general mathematical model for respiratory dynamics relevant to the clinical setting". In: *American Review of Respiratory Disease* 147 (1993), pp. 14–14.

[100] Robert Huhle et al. "Is mechanical power the final word on ventilator-induced lung injury?—no". In: *Annals of translational medicine* 6.19 (2018), p. 394.

[101] Luciano Gattinoni, Francesca Collino, and Luigi Camporota. "Mechanical power: meaning, uses and limitations". In: *Intensive Care Medicine* 49.4 (2023), pp. 465–467.

[102] Claude Guérin et al. "Effect of driving pressure on mortality in ARDS patients during lung protective mechanical ventilation in two randomized controlled trials". In: *Critical Care* 20 (2016), pp. 1–9.

[103] Ary Serpa Neto et al. "Mechanical power of ventilation is associated with mortality in critically ill patients: an analysis of patients in two observational cohorts". In: *Intensive care medicine* 44 (2018), pp. 1914–1922.

[104] Yongpeng Xie et al. "Correlation analysis between mechanical power, transforming growth factor-β1, and connective tissue growth factor levels in acute respiratory distress syndrome patients and their clinical significance in pulmonary structural remodeling". In: *Medicine* 98.29 (2019), e16531.

[105] Ken Kuljit S Parhar et al. "Epidemiology, mechanical power, and 3-year outcomes in acute respiratory distress syndrome patients using standardized screening. An observational cohort study". In: *Annals of the American Thoracic Society* 16.10 (2019), pp. 1263–1272.

[106] PMA Calverley and NG Koulouris. “Flow limitation and dynamic hyperinflation: key concepts in modern respiratory physiology”. In: *European Respiratory Journal* 25.1 (2005), pp. 186–199.

[107] ARIE Oliven et al. “Mechanisms underlying CO2 retention during flow-resistive loading in patients with chronic obstructive pulmonary disease.” In: *The Journal of Clinical Investigation* 71.5 (1983), pp. 1442–1449.

[108] V Modesto I Alapont, M Aguar Carrascosa, and A Medina Villanueva. “Stress, strain and mechanical power: Is material science the answer to prevent ventilator induced lung injury?” In: *Medicina intensiva* 43.3 (2019), pp. 165–175.

[109] Federica Romitti et al. “Mechanical power thresholds during mechanical ventilation: an experimental study”. In: *Physiological reports* 10.6 (2022), e15225.

[110] Néstor Pistillo et al. “Mechanical power correlates with stress, strain, and atelectrauma only when normalized to aerated lung size in patients with acute respiratory distress syndrome”. In: *Critical Care Explorations* 5.10 (2023), e0982.

[111] David B Hill et al. “Physiology and pathophysiology of human airway mucus”. In: *Physiological Reviews* 102.4 (2022), pp. 1757–1836.

[112] Claude Guérin et al. “Prone position in ARDS patients: why, when, how and for whom”. In: *Intensive care medicine* 46 (2020), pp. 2385–2396.

9 Appendices

9.1 Additional workings

Equation 116:

$$EAu'' + (EA' + E'A)\,u' - xA' = A - A\rho^s(1-\phi)g \tag{9.1}$$

In the linear model, we assume $\rho^s(1-\phi)g$ is constant and will be denoted in this solution as γ. From the product rule we can take the first two equation terms as:

$$EA'' + (EA' + E'A)\,u' = (EAu')' \tag{9.2}$$

$\therefore$

$$(EAu')' = xA' + A(1-\gamma) \tag{9.3}$$

Which expands to

$$EAu' = \int xA'dx + \int A(1-\gamma)dx + C \tag{9.4}$$

Where C is a constant of integration. This can be rearranged to find the equation for u' as

$$u' = \frac{1}{EA}\int xA'dx + \frac{1-\gamma}{EA}\int Adx + \frac{C}{EA} \tag{9.5}$$

Using integration by parts this becomes

$$u' = \frac{1}{EA}\left(\int xA'dx + (1-\gamma)\left[xA - \int xA'dx\right] + C\right) \tag{9.6}$$

which cancels down to

$$u' = \frac{1}{EA}\left((1-\gamma)xA + \gamma\int xA'dx + C\right) \tag{9.7}$$

Finally, cancelling out $A(x)$ terms we get the final equation for u' as

$$u' = \frac{1-\gamma}{E}x + \frac{\gamma}{EA}\int xA'dx + \frac{C}{EA} \tag{9.8}$$

In order to find an explicit solution for $u(x)$, we require given functions for cross-sectional area $A(x)$ and elasticity $E(x)$.

As an initial exploration, we will assume both are linear functions of x such that they take the form

$$\begin{aligned} A(x) &= ax + b, \\ E(x) &= cx + d, \\ A'(x) &= a, \\ E'(x) &= c. \end{aligned}$$

where a, b, c and d are constants.

Substituting this into our equation for u' 9.5 we get

$$u' = \frac{(1-\gamma)x(ax+b)}{(ax+b)(cx+d)} + \frac{\gamma}{(ax+b)(cx+d)}\int ax\ dx + \frac{C}{(ax+b)(cx+d)} \tag{9.9}$$

which cancels to

$$u' = \frac{(1-\gamma)x}{(cx+d)} + \frac{\gamma}{(ax+b)(cx+d)}\int ax\ dx + \frac{C}{(ax+b)(cx+d)} \tag{9.10}$$

Solving the integral we get

$$u' = \frac{(1-\gamma)x}{(cx+d)} + \frac{\gamma a x^2}{2(ax+b)(cx+d)} + \frac{\overline{D}}{(ax+b)(cx+d)} \tag{9.11}$$

where the constant $\overline{D} = \gamma D + C$.

In the non-dimensionalised model, x varies from 0 to 1, with $x = 0$ being the base of the lung and $x = 1$ being the top. Therefore, the boundary conditions to the no-input simulation exist at $u(0) = 0$ and $u'(1) = 0$. Substituting $u'(1) = 0$ we can find the constant of integration as:

$$0 = \frac{(1-\gamma)}{(c+d)} + \frac{\gamma a}{2(a+b)(c+d)} + \frac{\overline{D}}{(a+b)(c+d)} \tag{9.12}$$

such that

$$\overline{D} = -(1-\gamma) \cdot (a+b) - \frac{\gamma a}{2} \tag{9.13}$$

This can be substituted back into equation 9.5 to give

$$u' = \frac{(1-\gamma)x}{(cx+d)} + \frac{\gamma a x^2}{2(ax+b)(cx+d)} - \left[\frac{(2-\gamma)a + 2(1-\gamma)b}{2(ax+b)(cx+d)}\right] \tag{9.14}$$

We now need to integrate this again to find the equation for $u(x)$. Each term will be integrated separately, beginning with the first term

$$\int \frac{(1-\gamma)x}{cx+d}\, dx = (1-\gamma) \int \frac{x}{cx+d}\, dx \tag{9.15}$$

which is evaluated as

$$(1-\gamma) \cdot \frac{1}{c^2} \left(cx + d - \ln\left(cx+d\right)\right) + C \tag{9.16}$$

The second term requires a more intricate integration method due to the quadratic denominator.

$$\int \frac{\gamma a x^2}{2(ax+b)(cx+d)}\, dx = \frac{\gamma a}{2} \int \frac{x^2}{(ax+b)(cx+d)}\, dx \tag{9.17}$$

We decompose the denominator such that for some constants A and B

$$\frac{x^2}{(ax+b)(cx+d)} = \frac{A}{ax+b} + \frac{B}{cx+d} \tag{9.18}$$

which is rearranged to give

$$x^2 = A(cx + d) + B(ax + b) \tag{9.19}$$

In order to find the values of A and B we chose values of x which eliminate certain terms, in this case $x = -b/a$ and $x = -d/c$ such that

$$\begin{aligned} A &= -\frac{b^2}{da^2 - bca}, \\ B &= -\frac{d^2}{bc^2 - dac}. \end{aligned}$$

This allows us to write the second term of the equation to be integrated as

$$\frac{\gamma a}{2} \int -\frac{b^2}{(da^2 - bca)(ax + b)} - \frac{d^2}{(bc^2 - dac)(cx + d)} \; dx \tag{9.20}$$

which becomes

$$\frac{\gamma a}{2} \left[-\frac{b^2}{(da^2 - bca)a} \cdot \ln{(ax + b)} - \frac{d^2}{(bc^2 - dac)c} \cdot \ln{(cx + d)} \right] + C \tag{9.21}$$

The final term is solved in a similar manner. Where

$$\int \frac{(2 - \gamma)a + 2(1 - \gamma)b}{2(ax + b)(cx + d)} \; dx = \frac{(2 - \gamma)a + 2(1 - \gamma)b}{2} \int \frac{1}{(ax + b)(cx + d)} \; dx \tag{9.22}$$

We decompose the denominator for the fraction to be integrated such that

$$\frac{1}{(ax + b)(cx + d)} = \frac{A}{ax + b} + \frac{B}{cx + d} \tag{9.23}$$

which is rearranged to give

$$1 = A(cx + d) + B(ax + b) \tag{9.24}$$

As before we chose values of x which eliminate certain terms, $x = -b/a$ and $x = -d/c$ such that

$$\begin{aligned} A &= \frac{a}{da - cb}, \\ B &= \frac{c}{bc - ad}. \end{aligned}$$

These are then substituted back into the original term as

$$\frac{(2-\gamma)a + 2(1-\gamma)b}{2} \int \frac{a}{(da - cb)(ax + b)} + \frac{c}{(bc - ad)(cx + d)} \, dx \tag{9.25}$$

giving the solution

$$\frac{(2-\gamma)a + 2(1-\gamma)b}{2} \left[\frac{\ln{(ax + b)}}{da - cb} + \frac{\ln{(cx + d)}}{bc - ad} \right] + C \tag{9.26}$$

We can now recollect these terms to find the equation for $u(x)$ as

$$\begin{aligned} u(x) = {} & (1-\gamma) \cdot \frac{1}{c^2} \left(cx + d - \ln{(cx + d)} \right) \\ & + \frac{\gamma a}{2} \left[-\frac{b^2}{(da^2 - bca)a} \cdot \ln{(ax + b)} - \frac{d^2}{(bc^2 - dac)c} \cdot \ln{(cx + d)} \right] \\ & - \frac{(2-\gamma)a + 2(1-\gamma)b}{2} \left[\frac{\ln{(ax + b)}}{da - cb} + \frac{\ln{(cx + d)}}{bc - ad} \right] + \overline{C} \end{aligned} \tag{9.27}$$

where $\overline{C}$ is the collected constants of integration, which we find by taking the boundary condition $u(0) = 0$.

$$\begin{aligned} \overline{C} = -\Bigg(& (1-\gamma) \cdot \frac{1}{c^2} \left(d - \ln{d} \right) + \frac{\gamma a}{2} \left[-\frac{b^2}{(da^2 - bca)a} \cdot \ln{b} - \frac{d^2}{(bc^2 - dac)c} \cdot \ln{d} \right] \\ & - \frac{(2-\gamma)a + 2(1-\gamma)b}{2} \left[\frac{\ln{b}}{da - cb} + \frac{\ln{d}}{bc - ad} \right] \Bigg). \end{aligned} \tag{9.28}$$

Thus, the final form solution for $u(x)$ with some linear equation for $E(x)$ and $A(x)$ is

$$\begin{aligned}
u(x) =&(1-\gamma)\cdot\frac{1}{c^2}\left(cx+d-\ln\left(cx+d\right)\right)\\
&+\frac{\gamma a}{2}\left[-\frac{b^2}{(da^2-bca)a}\cdot\ln\left(ax+b\right)-\frac{d^2}{(bc^2-dac)c}\cdot\ln\left(cx+d\right)\right]\\
&-\frac{(2-\gamma)a+2(1-\gamma)b}{2}\left[\frac{\ln\left(ax+b\right)}{da-cb}+\frac{\ln\left(cx+d\right)}{bc-ad}\right]\\
&-\Bigg((1-\gamma)\cdot\frac{1}{c^2}\left(d-\ln d\right)+\frac{\gamma a}{2}\left[-\frac{b^2}{(da^2-bca)a}\cdot\ln b-\frac{d^2}{(bc^2-dac)c}\cdot\ln d\right]\\
&-\frac{(2-\gamma)a+2(1-\gamma)b}{2}\left[\frac{\ln b}{da-cb}+\frac{\ln d}{bc-ad}\right]\Bigg).
\end{aligned} \tag{9.29}$$